Department of Mathematics
University of Bergen, Norway

Nansen Environmental and
Remote Sensing Center

Ambient Noise in the Marginal Ice Zone

by

Hanne Sagen

Dr. Scient. Thesis

May 1998

ACKNOWLEDGMENT.

The Dr. Scient work has been funded by the Norwegian Research Council, project number 101798/410, and the Nansen Environmental and Remote Sensing Center.

My supervisors have been Prof. Sigve Tjøtta, Department of Mathematics at the University of Bergen, and Prof. Ola M. Johannessen, Nansen Environmental and Remote Sensing Center/ Geophysical Institute at the University of Bergen. First I want to thank Prof. Sigve Tjøtta for all support and guidance I have received during my work. Prof. Ola M. Johannessen is acknowledged for introducing me to the field of ambient noise generation in the marginal ice zone, and for providing a wealth of data from the MIZEX and SIZEX acoustic field experiments which I could use in my thesis. Both supervisors have been very enthusiastic and provided constructive criticism, which have made it possible to complete the thesis. Thanks to Stein Sandven, Torill Hamre and Anita Jacob for help with practical and technical solutions during the completion of the thesis. I am very grateful to my father and Melissa who have taken care of Torunn and Håkon Johan during the long days and evenings.

Thanks also to the many colleagues at the Nansen center for their efforts in acoustic data processing, OASES model installation, software development for analysis and presentation of data, use of SAR data, and use of oceanographical and meteorological data, which have made this study possible.

A major part of this thesis has been on the analysis of ambient noise data and environmental data collected during five experiments, which were supported by the Office of Naval Research grant N00014-91-7-1311, the University of Bergen, and by the Norwegian Defence Research Establishment in Horten. Thanks to the many peoples who have taken part in the data collection, data processing, and data presentation. Furthermore, I would like to thank the Norwegian Defence Research Establishment (NDRE) for excellent cooperation in planning and coordinating the acoustic experiment, and during the data processing phase. NDRE is also thanked for lending us the tape recorder equipment. Special thanks to I. Engelsen, NDRE, who died in 1994, who was very actively involved in planning and coordinating the acoustic field experiments in 1989 and 1992. He was responsible for processing the ambient noise and acoustic propagation loss data from SIZEX 89 and 92.

The acoustic data from all the field experiments have been collected by the 333 Squadron of the Royal Norwegian Air Force. Whiteout their outstanding work in the deployment of sonobuoys, recording of ambient noise, taking photographs and writing detailed logs, this study would not have been possible. In particular I would like to thank the squadron leaders for excellent co-operation. Thanks to K. Starke and T.Turner for making sure that the buoys were dropped according to experiment plans.

List of Content.

List of Abbreviations and expressions.

AMOC	Acoustic Monitoring of Ocean Climate
ARGOS	Satellite based positioning system
AXBT	Airborne eXpendable Bathy Thermograph
CTD	Conductivity-Temperature- Density
DATOS Digital	Bottom moored ambient noise buoy containing a Audio Tape Recorder.
HM	Haakon Mosby R/V
HUS	H. U. Sverdrup R/V
MIZ	Marginal Ice Zone
MIZEX	Marginal Ice Zone EXperiment
RF	Radio Frequency
PB	Polarbjørn R/V
PS	Polarsyssel R/V
RBS	Bottom mounted hydrophone and recording system
R/V	Research vessel
SAR	Synthetic Aperture Radar
SAFARI	Seismo Acoustic Fast field Algorithm for Range-independent environments
SIZEX	Seasonal Ice Zone EXperiment
Sonobuoy including	Acoustic buoy, which is dropped from aircraft, hydrophone and antenna.
SUS	Explosive charges dropped from aircraft

1. Introduction

Most underwater acoustic studies have been performed in oceans without sea ice cover (see for example Kerman 1988, 1993; Jensen et al., 1994). The focus of this study is on acoustics in the marginal ice zone (MIZ) which is partly or fully ice covered oceans and where few acoustic investigations have been made because this region is logistically difficult to operate in.

Ambient noise is defined to be sound which is generated by many natural processes at or beneath the sea surface, turbulence in the water column or seismic activity at the sea floor. The ambient noise is, once it is generated, strongly affected by the acoustic propagation conditions, which in the MIZ is characterized by strong surface ducts perturbed by fronts, ice edge eddies in the upper water layer and by highly variable ice cover as well as by variable bottom conditions (Johannessen, 1983; Wadhams, 1986; Squire 1994). Therefore, this thesis will investigate both ambient noise and acoustic propagation in the MIZ.

1.1 State of Art

1.1.1 Sound propagation studies in the MIZ

There are three dominant features of the MIZ which affect sound propagation: 1) the strong surface duct, 2) the horizontal gradients in the oceanographic fields including sound speed structures, and 3) the variable ice conditions and its effect on acoustic propagation. In addition, when the MIZ is located on a continental shelf, the interaction of sound with the sea floor becomes important. A brief review of previous acoustic propagation studies and their main results, including ocean acoustic tomography, are presented in Table 1.1. These investigations have generally used source frequency at a few hundred Hz, except in the MIZEX 84 propagation study and in the numerical study by Mellberg et al. (1987, 1991).

During the Fram Strait Marginal Ice Zone Experiment (MIZEX 84), acoustic waves were transmitted over a 100 km path in order to study the Doppler shifts and fluctuations around these shifts. The fluctuations were attributed to the quasi-steady motion of source and receiver due to dynamic processes, such as internal waves and ice edge eddies in the MIZ (Dyer et al., 1987). Another major acoustic study in the MIZ was the year long tomography experiment in the Greenland Sea in 1988 - 1989 (Worcester et al., 1993). The experiment consisted of six 250 Hz acoustic transceivers; five in a pentagon and the sixth in the center. Results from this experiment show that the acoustic travel times and amplitudes at 250 Hz are sensitive to the depth of the surface duct and to the elastic parameters of the ice cover which is different in the MIZ compared to the interior ice pack (Jin et al., 1994). Transmission loss estimates calculated by Jin et al., (1994) indicated a stronger attenuation coefficient in the MIZ compared to the interior ice pack and in open ocean. Estimated loss per km due to scattering from the ice cover has been shown to increase if the number of edges along a transect increases (Dahl,

1989). The number of edges increases if the ice concentration increases and the floe size decreases, which is often the case when comparing the interior ice pack to the MIZ.

In order to study sound propagation through mesoscale eddies and fronts in the MIZ of the Greenland Sea, Mellberg et al. (1987 and 1991) used traditional ray trace and parabolic equation. The models included range dependence in sound speed profiles, but no ice cover or bottom effects. The low frequency sound is generally refracted below the depth of the receivers due to the warmer water often found in eddies in the Fram Strait (Mellberg et al., 1987). This implies that eddies can affect propagation loss so that 1kHz yields a loss more than 20 dB smaller than at 50 Hz. The sound speed structure and dominant modes of acoustic propagation are entirely different on either side of a frontal zone where fine and mesoscale structures are present. The propagation loss and the modal structure in a frontal zone are therefore very sensitive to source and receiver configuration. A frontal zone can increase the loss by 15 dB over a distance less than 10 km. (Mellberg et al., 1991). The effect of elastic ice cover or sea floor was not included in the studies by Mellberg et al. (1987, 1991).

1.1.2 Ambient noise studies in the MIZ

In a pioneering study by Diachoke and Winokur (1974) the high ambient noise levels in the MIZ was proposed to be generated by the interaction of waves/swell with the ice cover. In addition to waves/swell, ice concentration and acoustic propagation characteristics (sound speed profiles, reflection and scattering from the ice cover) were pointed out as the key components influencing the ambient noise. Generally, later works have supported these hypotheses (Johannessen et al 1988 a, b, 1990, 1992 a, b, 1993 a, 1994 a; Buckingham 1988, 1993; Makris and Dyer, 1991; Lynch et al., 1993).

All ambient noise studies in the MIZ show the importance of the swell interaction with ice on ambient noise (i.e. Rottier, 1990; Makris and Dyer, 1991; Johannessen et al. 1992 b, 1994 a). Investigations have independently documented strong influence of inertial motion or internal waves (Makris and Dyer, 1991); and tidal currents (Johannessen et al. , 1992 a, b; Bourke and Parsons, 1993) on the observed large ambient noise fluctuations at low frequencies. Both Makris and Dyer (1991) and Bourke and Parsons (1993) reported that the long term variations were observed during periods of weak surface wave activity. Other phenomena such as ice-ocean eddies which occur frequently in the ice edge zone (Johannessen, et al. 1983; Johannessen, et al., 1987 a; Johannessen, et al., 1987 b), contribute to large horizontal gradients in the observed ambient noise field (Johannessen et al., 1988 a, 1990, 1992 b, 1993 a). High levels are not necessarily found in the eddy centre, but in shear zones with strong convergence of ice at the periphery of the eddy (Johannessen et al., 1988 a, 1988 b, 1992). A clear minimum in ambient noise level in the ice edge zone is caused by the dampening effect of grease ice (Johannessen et al., 1988 a, 1988 b, 1994). Highlights of ambient noise studies in the MIZ are listed chronologically in Table 1.2.

Table 1.1 Summary of highlights of acoustic propagation studies in the marginal ice zone.

References	Geographical location - Study objective - Data used - Main Results
Dyer et al, 1987	Greenland Sea, (MIZEX 84), 80^0 N 47'N 4^0 19'E. Source onboard ship. Transmitting frequency 20 Hz up to 200 Hz. Receivers onboard another ship. Path length 100 km, which was partly covered with ice. The objective was to study the Doppler shift and fluctuations around these shifts. The study postulated that eddies or other mesoscale motions of comparable scale are important in determining acoustic fluctuations in the MIZ.
Mellberg et al, 1987	Numerical study using oceanographical data from MIZEX 84 as input to a ray model and a standard parabolic equation model. The study does not take reflections from bottom or ice into account. The numerical study showed that low frequency sound is generally refracted below the depth of the receivers due to the warmer water often found in eddies in the Fram Strait. This implies that eddies can affect propagation loss so that 1kHz yields a loss more than 20 dB smaller than at 50 Hz.
Lynch et al, 1987	North of Svalbard, MIZEX 84. An acoustic tomography source was transmitting at 224 Hz center frequency. The signals were recorded at two receivers, one drifting with the ice and one stationary. This was a feasibility study for acoustic tomography in the MIZ and in the Arctic. The feasibility test was generally positive.
Mellberg et al, 1991	Greenland Sea, MIZEX 83. This study is similar to Mellberg et al.,1987, but in this study the frontal zones are considered. A wide angle PE model is used, and only 50 Hz signal is considered. The ice cover /bottom effects are not included. The propagation loss and the modal structure in a frontal zone are very sensitive to source and receiver configuration. A frontal zone can increase the loss by 15 dB over a distance less than 10 km.
Jin et al., 1993	The objective of this study was to investigate the effects of sea ice on acoustic ray travel times, with applications to the Greenland Sea tomography experiment. Travel times were estimated using a generalized ray theory. Results show that the ice thickness and shear wave speed are the two most important ice parameters influencing the travel times.
Sutton, et al.,1993	The Greenland Sea Tomography Experiment 1988 - 1989. Six transceiver in a pentagon configuration with the sixth instrument in the center. Source depth 100 m. Transmitting center frequency at 250 Hz, bandwidth 120 Hz. The ice cover effects are not included in the study. The effect of seasonal changes in surface duct characteristics on acoustic travel time is studied by ray theory and mode theory. The main effect was a delay of the acoustic energy cutoff with several hundred milliseconds of the intermediate profiles (very shallow ducts) compared to the summer and winter profiles
Worcester et al., 1993	The Greenland Sea Tomography Experiment 1988 - 1989. The same acoustic experiment as above. The objective was to study the evolution of the large-scale temperature field. This paper focus on inversions of the averaged travel times giving the range-averaged potential temperature along source-receiver paths. Tomographic inversions are largely consistent with fragmented hydrological data collected during the recordings.
Jin et al., 1994.	The Greenland Sea Tomography Experiment 1988 - 1989. The objective was to study the effect of scattering from the ice cover at 250 Hz. The main result is that part of the amplitude reduction in the data is indeed due to ice, although the exact amount is sensitive to the details of the mixed layer.
Lynch et al., 1996	Tomographic experiment in the Barents Sea, August 1992. The objective was to study the acoustical properties and ocean dynamics of the Barents Sea Polar front close to the Bear Island. Source frequency 225 Hz, 16 element receiver. Acoustic fluctuations due to internal waves and internal tides were monitored. Data and theory (mode and ray) shows good agreement.

Table 1.2 Summary of highlights of ambient noise studies in the marginal ice zone

References	Geographical location - Study objective - Data used - Main Results
Diachoke and Winokur, 1974; Diachoke, 1980	Greenland Sea, July 1971. Averaged ambient noise levels at 100, 315 and 1000 Hz. Sharp peak in ambient noise at the compact ice edge caused by swell. Broader and weaker peak at a diffuse ice edge.
Yang et al., 1987	Greenland Sea, 1983. At 75 N, 9 W. Broad band data 100 - 500 Hz. Local hotspots separated with 50 km along the ice edge were proposed to be caused by ice edge eddies.
Johannessen et al., 1988 a, b	MIZEX 85. Fram Strait, 30 April, 1985, at 78.5 N 0 W. Averaged levels at 40, 100, 315 and 1000 Hz. High ambient noise levels were located within ice edge eddies, but not necessarily in the eddy centre.
Buckingham, Chen, 1988	MIZEX 84. Fram Strait, June 1984, at 80.6 N 8 E. Frequency spectra 10 - 2000 Hz have a exponential decay as f^{-2} from 50 Hz up to 1kHz. The main noise generating mechanism is proposed to be floe-floe collisions.
Johannessen et al., 1990	MIZEX 87. Fram Strait, April 2, at 78 N 4W. Averaged levels and frequency spectra from 20 - 1000 Hz. Data indicated hotspots in relation to eddies and locally very compact ice edge condition due to on ice wind conditions. Variation in averaged ambient noise levels were correlated to ice zones. The effect of swell was clearly observed in the data. Preliminary study of a later experiment in the Barents Sea (SIZEX 89) suggested that sea ice motion driven by tidal currents has strong impact on ambient noise generation. Grounded ice bergs cutting up the ice field was also reported to generate strong noise in the Barents Sea.
Makris and Dyer, 1991	MIZEX 84. Fram Strait, June 1984, at 80.5 N 8.0 E The study considered time series at 25 - 50 Hz. Gravity waves and ice concentration were found to be the main correlates of ice edge noise. During weak swell a 12 hour periodic signature was observed and attributed to the formation of dense ice due to inertial oscillations or internal waves.
Johannessen, et al.,1992 b.	MIZEX 84-87, Fram Strait: 77.5-79.0 N and 2E-5W, SIZEX 89, Barents Sea: 75.5-76 N and 14-16E. The studies used averaged levels at selected frequencies: 40, 100, 315 and 1000 Hz, Frequency spectra at 10-1000 Hz. Hotspots and broad frequency spectra were related to zones of high ice concentration and high internal ice stress as found in relation to ice edge eddies and compact ice edges due to strong on ice winds.
Johannessen et al., 1992 a, b; Nesse et al., 1992.	SIZEX 89. Barents Sea. February-March, 1989, at 75 05 N 23 04 E. Bottom mounted buoys at 20-630 Hz. Long term variation in ice edge ambient noise below 125 Hz was highly correlated to ice motion caused by tidal current. Above 125 Hz, position relative to the ice edge and normal wind speed component normal to local ice edge played the dominant role in prediction of ambient noise levels.
Buckingham, 1993	Greenland Sea at 76 N 5.0W. Frequency spectra 20-2000 Hz. An exact solution for the inverse square sound speed profile was used to explain the ambient noise frequency spectra. The main result was that the shape of the frequency spectra is caused by the upward refracting propagation conditions. Kinks in the exponential decay is present where the local sources become dominant over the more distant sources.
Lynch et al., 1993	Greenland Sea tomography Experiment 1988 - 1989, centred at 75 N 0-5 W. Year long time series at 200-300 Hz. Supports previous results. Large scale wind and wave information can be used to predict the MIZ ambient noise quantitatively at mid frequencies.
Bourke, Parson, 1993	CEAREX. North East Barents Sea. 5-4000 Hz. Semi-diurnal oscillations in sea ice conditions and ambient noise level at 32 Hz. Tidal current or inertial oscillations cause the ice motion.
Johannessen, et al 1994	SIZEX 92. Barents Sea. March 1992. Centered at 77.0 N29 E. Sonogram 20-5000 Hz and averaged levels at 1000 Hz. Hotspots were found in connection to icebergs, and minimum levels were found in grease ice regions. Periodic signatures in ambient noise were observed and related to swell-ice interaction.

The summary in Table 1.2 suggests that the ambient noise characteristics have mostly been described by averaged levels at selected frequencies (Diachok and Winokur, 1974; Johannessen et al; 1988), and by times series in low- and mid frequency band (Makris and Dyer, 1991; Bourke, et al., 1993; Johannessen, 1992; Lynch et al., 1993). Frequency spectra have been used less extensively, although they contain much more information than averaged levels at selected frequencies or narrow band time series. Buckingham (1988, 1993), Johannessen, et al. (1990), Sagen et al. (1992) used ambient noise frequency spectrum in their analyses; and time series of frequency spectra (sonogram) were recently introduced in the MIZ studies (Nesse et al., 1992; Johannessen et al., 1994).

While the traditional objective of ambient noise studies has been to develop ambient noise prediction models, the attention in the last ten years has moved towards using the ambient noise observations as a monitoring tool for environmental parameters such as geoacoustic parameters of the seabed (Buckingham and Jones, 1987; Buckingham, et al., 1994 c) and physical processes related to breaking of waves (Melville, 1994). To our knowledge, not no inversion of ambient noise characteristics to sea ice and ocean parameters has been attempted neither in the MIZ nor the interior of the Arctic Ocean.

1.2 Scientific Rational and motivation

Remote sensing from space has proven to be an excellent tool for sea ice monitoring and localization of mesoscale features such as eddies and vortex pairs (Sandven et al., 1990, Sandven et al., 1993, Johannessen, et al., 1994 b). Since electromagnetic waves are rapidly attenuated in ice and water only limited information about interior of the ice cover or the water masses below the sea surface can be obtained by methods using such waves. However, sound waves propagate in water with very little absorption, and have been used extensively in underwater defense systems for several decades. In oceanography, acoustical methods such as acoustic tomography and thermometry (Munk et al., 1995), have become increasingly important to study physical processes such as surface waves, currents and temperature distribution. These methods employ configurations of sound sources and receivers in arrays.

A proposed concept for Acoustic Monitoring of the Ocean Climate (AMOC) in the Arctic ocean, including the Fram Strait, is under development (Johannessen et al., 1997). The new approach of AMOC is to monitor climate changes by detecting and quantifying global warming in the Arctic Ocean. The method employs gyre scale acoustic long range propagation for ocean basin temperature and ice thickness changes in combination with remote sensing of sea ice from satellites, modeling, and data assimilation. One important specific objective is to study the sensitivity of ocean temperature and ice thickness on acoustic propagation.

The ambient noise recorded at a location contains combined information of the environment in which it was generated and has propagated through. It is therefore a growing interest in using ambient noise as a monitoring concept of oceanographic processes (Mellville, 1994), as well as for bottom conditions (Buckingham, 1987, 1994 c).

There are both economical and environmental benefits of using ambient noise instead of man made acoustic sources. Passive monitoring systems need only configurations of acoustic receivers which will be much cheaper than systems involving intensive sources. Undoubtedly, another benefit of the use of natural ambient noise is that it generates no additional acoustic pollution which can be harmful for the marine environment.

In order to establish inversions of ambient noise to environmental information the acoustic propagation and ambient noise generation in the MIZ has to be better understood, which is the major scientific rational for this thesis.

1.3 Objectives and methods

According to the scientific rationale above the overall objective of this study is to

Improve the understand of acoustic propagation and ambient noise generation in the marginal ice zone

In order to meet the overall objective it is necessary to characterize and analyze the acoustic propagation and ambient noise in the MIZ through field investigations, and relate temporal and spatial variations to oceanographical and meteorological processes and ice conditions.

Previous studies have mainly been carried out by extensive use of statistical description of time series of ambient noise at a few selected frequencies or narrow bands, and by cross-correlation's with environmental conditions (i.e. Makris and Dyer, 1991; Johannessen et al 1992 a; Bourke et al. 1993; Lynch et al., 1993). The main effort in this thesis is to study broadband propagation loss and broad band ambient noise data obtained during the MIZEX and SIZEX experiments (1985, 1987, 1989, and 1992). Overview articles of these experiments are published by Johannessen et al. (1992 c and 1993 b).

Ambient noise data from 82 different locations in the Barents Sea and 72 locations in the Greenland Seaare used in the thesis. Environmental conditions are observed by in situ measurements and remote sensing. Sound propagation is studied using propagation loss data from SIZEX 92 combined with numerical simulations using the wave number integration model OASES. The OASES model is developed and documented by H. Schmidt (1997).

The thesis consists of the following six specific objectives which are analyzed in Chapter 5 - 9:

- **Investigate broad band sound propagation in shallow water MIZ (Chapter 5)**
- **Investigate the hypothesis that hotspots along the ice edge are due to ice edge eddies (Chapter 6)**
- **Investigate the hypothesis that icebergs interacting with the sea ice field is a strong noise generating mechanism (Chapter 6)**
- **Investigate the effect of sound propagation conditions on broad band ambient noise (Chapter 7)**
- **Investigate the effect of swell on ambient noise (Chapter 8)**
- **Investigate why grease ice causes a stronger dampening of the ambient noise close to the sea floor than when the receiver is closer to the surface (Chapter 9)**

Table 1.3 gives an overview of the specific objectives, methods and the main results.

1.4 Organization

In order to understand the effect of the MIZ environment on acoustic propagation and ambient noise generation a general description of sea ice conditions, ocean currents, and mesoscale processes in the Fram Strait and Barents Sea is given in Chapter 2. Acoustic propagation models are briefly discussed for use in the MIZ in Chapter 3. The acoustic experiments during MIZEX and SIZEX campaigns are described in Chapter 4. Results and interpretation from a propagation study in shallow water across the ice edge in the Barents Sea and corresponding numerical simulations are presented in Chapter 5. The remaining chapters deal with ambient noise studies. Spatial variation in averaged ambient noise levels for hotspot studies are presented in Chapter 6. The shape of frequency spectra is discussed and related to propagation effects in Chapter 7. The effect of ocean gravity waves on ambient noise is investigated in Chapter 8 using high resolution time series of frequency spectra (sonogram). Chapter 9 is devoted to a study of dampening of ambient noise by grease ice. Summary and conclusions are given in Chapter 10, which also includes recommendation for future work.

Table 1.3 Overview of the study objectives, methods and main results of the thesis

Chapter	Study Objectives	Method	Main Results
5	Investigate broad band sound propagation in shallow water MIZ.	Analyze broad band propagation loss data and compare to range independent numerical simulations for ice covered shallow water regions using OASES. The source is located at 18 m.	Experiment: A stronger transmission loss pr kilometer is observed in the MIZ than in open ocean or in the interior Arctic. The optimum frequency domain of propagation is between 100 and 400 Hz for long range propagation. Numerical simulations: The reflection coefficient is very sensitive to ice thickness and elastic properties. Sound above 100 Hz is generally trapped in the surface duct where it is strongly exposed to reflection losses from the ice- water interface. The optimum frequency domain is regulated by the bottom interaction, ice thickness and the position of the receiver relative to the source within the surface duct.
6a	Investigate the hypothesis that hotspots along the ice edge are due to ice edge eddies.	Averaged ambient noise levels at selected frequencies.	Large gradients in ambient noise levels are localized to regions of high ice concentration and increased internal ice stress caused either by ice edge eddies or strong on-ice wind conditions.
6b	Investigate the hypothesis that icebergs interacting with the ice field represents strong noise generators.	Averaged ambient noise levels at selected frequencies	Hotspots have been localized to positions close to icebergs in the eastern Barents sea and is caused by the icebergs are cutting up the ice cover.
7.	Investigate the effect of sound propagation on broad band ambient noise.	Ambient noise frequency spectra	The maximum lobe of the frequency spectrum reflects the averaged optimum frequency domain of sound propagation. Kinks and slopes in frequency spectra are related to ice parameters through the reflection coefficients and the scattering from the ice.
8.	Investigate the effect of swell on ambient noise.	Ambient noise sonogram	A scheme for inversion of swell period and wavelength, is developed to retrieve ice thickness.
9.	Investigate why grease ice causes a stronger dampening of ambient noise close to the sea floor than within the surface duct.	Time series at selected frequencies and sonogram, combined with Numerical simulations	Both the surface duct prior to freezing process and wave dampening effect of grease ice causes reduction of ambient noise above 100 Hz for receiver located close to the sea floor.

2. Environmental characteristics of the MIZ

The sea ice in the Arctic ocean is generally described as a mixture of continuous ice cover, which can be broken up by leads, and numerous ice floes of varying size. Average thickness of the multiyear ice, which is the ice surviving one or more summer seasons, is about 3 m, but the maximal thickness can exceed 20 m in areas of heavy ridges and ice keels. The surface topography is determined by the amount and size of ridges and the presence of edges surrounding floes and leads. The marginal ice zone (MIZ) can be "loosely defined" as the transition zone between ice-covered ocean and adjacent ice-free oceans. The MIZ in the Greenland and Barents seas is a dynamic region where several atmospheric and ocean phenomena and processes, such as polar lows, surface waves, eddies and other mesoscale current features have strong impact on the ice cover.

2.1 Ice conditions in the MIZ of the Greenland and Barents seas

2.1.1 Ice zones observed in SAR imagery

The MIZ of the Greenland and Barents seas contain all the main ice types, ranging from newly formed ice (grease ice, pancake ice, etc.), first year (FY) ice and multi-year (MY) ice. The floe size can vary from less than a meter for pancake ice to more than 10 km for MY ice. Based on the ice information obtained by high-resolution ($\approx$ 100 m) Synthetic Aperture Radar (SAR) images, four zones within the MIZ can be defined:

1) the *open ocean* zone is a continuous ice free area located outside the main ice edge. A compact ice edge is defined between the open ocean and the ice pack area when the ice concentration increases rapidly from 0 to 100 %.

2) The *diffuse ice edge zone* is defined as the area where the ice concentration increases more gradually from open water to 100 %.

3) The *compact ice zone* is the region inside the ice edge, with high concentration (> 95 %) of broken-up floes. An example of this zone is clearly seen in the SAR image of April 2, 1987, obtained in the Fram Strait (Figure 2.1), as a 10-20 km wide belt of bright signature inside the main ice edge. In situ observations show that ice concentration is generally high in this zone (90-100%), consisting mainly of broken-up multiyear and firstyear floes which are transported southwards with the East Greenland Current.

4) The *interior ice pack* is the region inside the compact ice zone. In contrast to zone 2 and 3, this area is not affected by wave action which breaks up the ice pack in smaller floes. The area is dominated by large floes of firstyear and multiyear ice and leads which can be open or covered by thin ice.

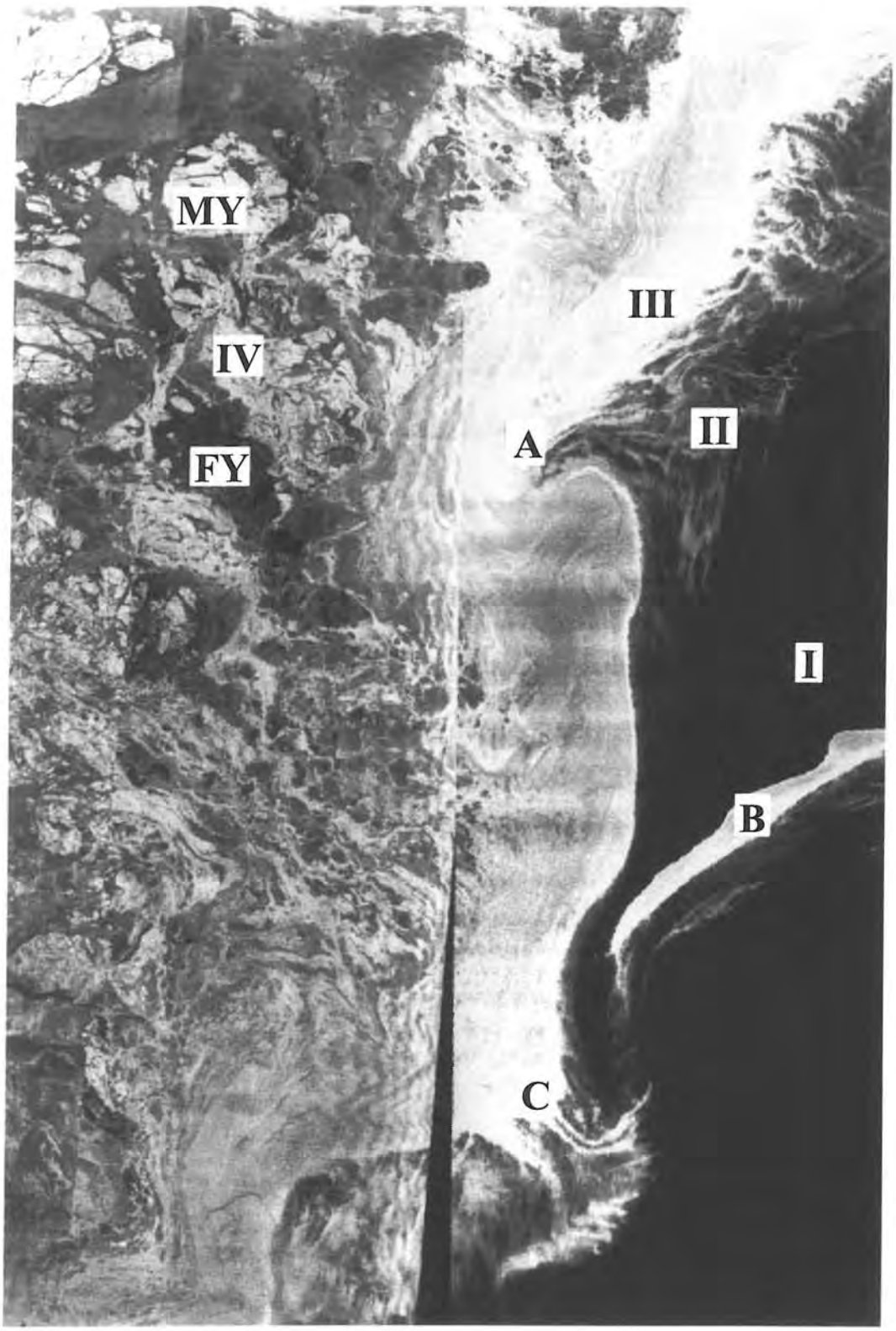

Figure 2.1. Airborne SAR image obtained on April 2 during MIZEX 87, showing a typical winter MIZ in the Fram Strait. The image is centred at 78° N 4°W and covers an area of 150 by 100 km. Four characteristic zones can be identified in the image; **I**: Open ocean, **II**: Diffuse ice zone, **III**: Compact ice zone, and **IV**: Interior ice pack with many multiyear (MY) floes. Three types of meso scale features are shown: **A** ice edge eddy, **B** ice edge jet, **C** Vortex Pair.

2.1.2 Newly formed ice

Newly formed ice includes several types of ice which are formed during a few days, such as frazil ice, grease ice and pancake ice. *Frazil ice* is the initial stage in sea ice formation, followed by *grease ice*, a thin layer of soupy mixture of sea water and unconsolidated frazil crystals, as shown in Figure 2.2 a. Under calm conditions the grease ice quickly freezes to form a thin elastic crust of continuous ice cover, called *nilas*, with thickness between 1-10 cm. Under pressure nilas can easily bend or give rise to finger rafting, a phenomenon where one finger-shaped sheet of ice is pushed on top of another. Grease ice and nilas dampen the short surface waves which normally appear as bright signatures in the SAR images. Grease ice and nilas appear as dark areas in the SAR image because the backscatter of the SAR microwaves from these surfaces is very low.

If freezing occurs in the presence of a wave field, grease ice is transformed into *pancakes* within a few hours. Pancakes are circular plates of semi-consolidated frazil ice (Figure 2.2 b), which can grow from 0.3 m to 3 m in diameter during a few days. Pancakes acquire a characteristic elevated rim of compressed ice due to the continuous collisions with adjacent floes. These rims cause very high backscatter in the SAR images. Eventually, the pancakes freeze together to form continuous sheets of ice, also called consolidated ice.

SAR imagery can readily distinguish between grease ice or nilas, which have very low backscatter, from pancake ice which has very high backscatter. The dampening effect of grease ice on the short surface waves is clearly illustrated in Figure 2.2. The shortest surface waves (capillary waves) are immediately filtered out as the wave field propagates into grease ice. Johannessen et al., (1988 a, 1994 a) suggested and showed that grease ice is an important mechanism to reduce the ambient noise, which will be discussed in chapter 9.

2.1.3 Firstyear and multiyear ice

Most of the ice in zone 2, 3 and 4 is firstyear ice or a mixture of firstyear and multiyear ice. The firstyear ice has been formed locally during the winter season and can attain an average thickness of 1 - 2 m as a result of freezing and deformation (ridging and rafting). Multiyear ice, with average thickness of 3 - 4 m, is transported to the MIZ from the interior of the Arctic. The multiyear floe size is generally much larger than for firstyear ice. In convergence zones ridges are formed which may be more than 5 m above sea level and corresponding ice keels can extend several tens of meters below sea level. SAR imagery has good capability to distinguish between multiyear and firstyear ice due to differences in salinity which has strong impact on the reflection of microwaves: multiyear ice with surface salinity less than 1 ‰ gives significantly higher backscatter than firstyear ice with salinity of 6 - 7 ‰. During summer conditions SAR imagery cannot distinguish between multiyear and firstyear ice because both ice types are normally covered by wet snow or melt ponds. The Fram Strait has more multiyear ice in the MIZ than the Barents Sea where firstyear ice is the dominant ice type (Sandven and Johannessen, 1993). The thickness and roughness of the bottom surface of this ice has important effect on the acoustic propagation.

a)

b)

Figure 2.2. Photographs of grease ice (a)and pancake ice (b).

2.1.4 Icebergs

In the Barents Sea icebergs originating from glaciers in Franz Joseph Land and eastern Svalbard often occur in the MIZ between Hopen and Bjørnøya (Vinje, 1985; Kloster and Spring, 1993). The size of icebergs found in the MIZ is typically 100 - 200 m in horizontal scale and 30 - 50 m in vertical extent. The size depends on the generation mechanism (Løset and Carstens, 1993). Larger icebergs are produced if the glacier becomes a floating ice shelf in deep water before calving. If the glacier front is grounded the calving results in smaller icebergs (called bergy bits). The currents in the Barents Sea transport the icebergs in a south-westerly direction to the shallow bank between Hopen and Bjørnøya, where they are grounded if the draft is larger than the bottom depth.

Figure 2.3 shows the interaction between grounded icebergs and the sea ice motion driven by a strong tidal current superimposed on a mean southwesterly current (Johannessen et al., 1992 c). This interaction can be seen as tracks cut into the moving sea ice cover by the stationary icebergs. Such tracks are also generated by drifting icebergs due to the differential motion between sea ice and icebergs. This is an important mechanism for cutting large ice floes in to smaller floes in the southwestern part of the Barents Sea. The combined effect of iceberg cutting and wave penetration causes the small size of ice floes frequently observed in the MIZ of Barents Sea, especially in the winter. Johannessen et al., (1990, 1994 a) hypothesized that iceberg cutting of the sea ice cover, in combination with swell, could be an important mechanism for ambient noise generation in this region, which is discussed in chapter 6 and 8.

When drifting icebergs enter the MIZ and open water they are exposed to the surface wave field, especially swell, which eventually breaks up icebergs into smaller pieces. Measurements of surface strain and vertical heave of a tabular iceberg in responses to swell were made in Kong Oscars fjord, East Greenland in September 1978 (Goodman et al., 1980). Their results showed that the tabular iceberg (large tabular icebergs are also called ice islands) flexed and heaved at periods above 16 s. This corresponds to the longest components of the surface wave field. Smaller tabular icebergs in the Barents Sea observed visually during SIZEX 92 were bending and heaving as swell was passing the iceberg. This process was documented by in situ observations to generate strong ambient noise as the surrounding ice was interacting with the icebergs.

2.2 Dynamical ocean processes

2.2.1 Ocean currents and water mass distribution

The water mass structure of the Arctic Ocean and adjacent seas is characterized by relatively cold and less saline waters in the surface layer which are determined by seasonal variability of the ice cover (melting and freezing) and outflow of fresh water from rivers. Warmer and more saline waters are found at intermediate depths originating from inflow of Atlantic water. The deep water masses, which occupy most of the water column, are quite homogeneous with variability in temperature of order 0.1°C and in salinity of order 0.02 ‰. The temperature structure in the upper few hundred meters defines a very strong vertical gradient in the sound speed profiles at a

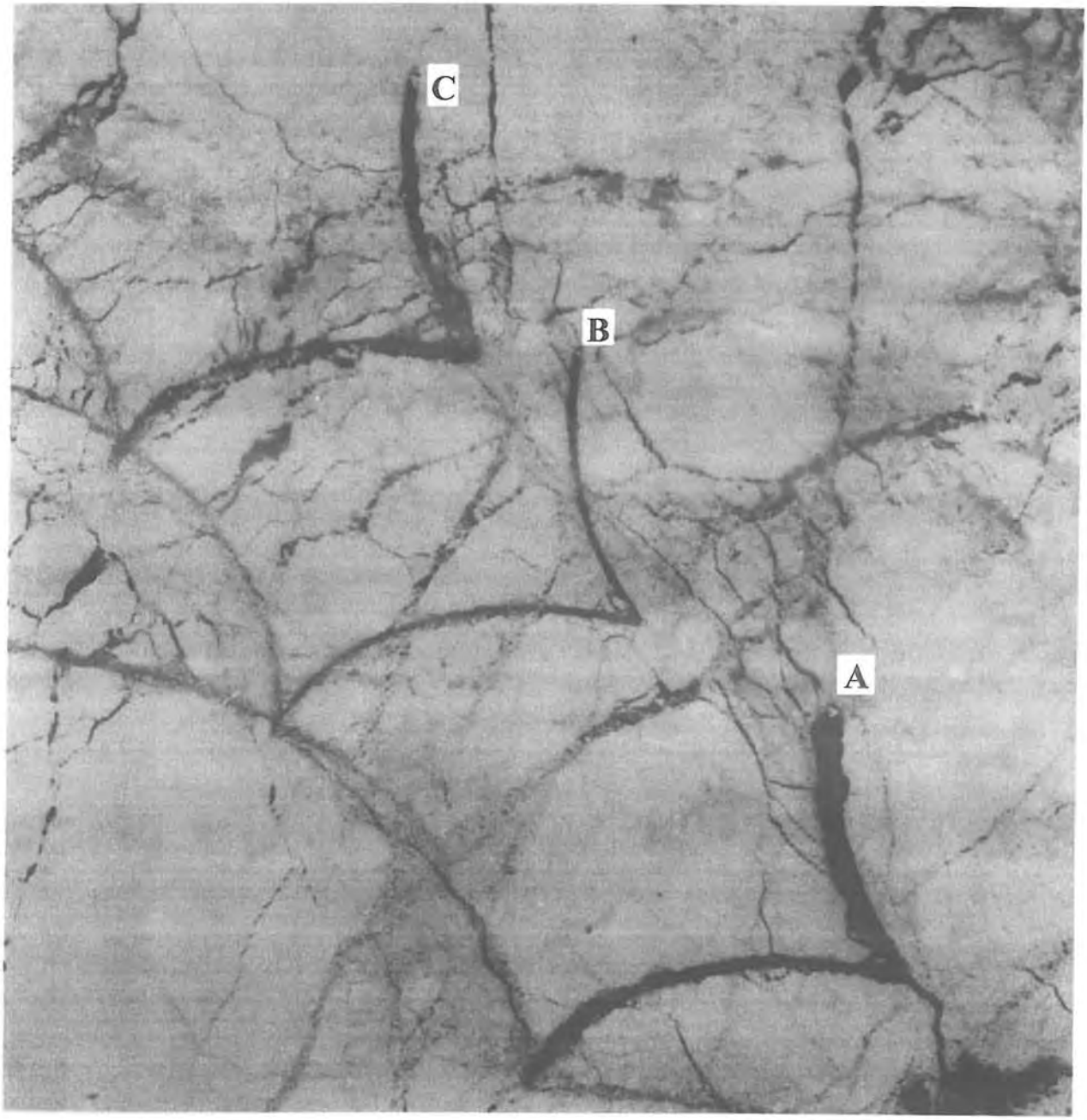

Figure 2.3. SPOT image from the Barents Sea ice cover with curved tracks generated by grounded icebergs. Fresh tracks appear dark due to open water. Three icebergs (A-C) are observed at the end of the fresh tracks. As the tracks become older (more than a day) they are filled with smaller, broken floes which appear more grayish. The image is obtained on April 11 1988 and is centred on Spitsbergenbanken between Hopen and Bjørnøya (75° 45'N 23°E). The image is SPOT panchromatic with 10 m pixel size and covers an area of 20 by 20 km.

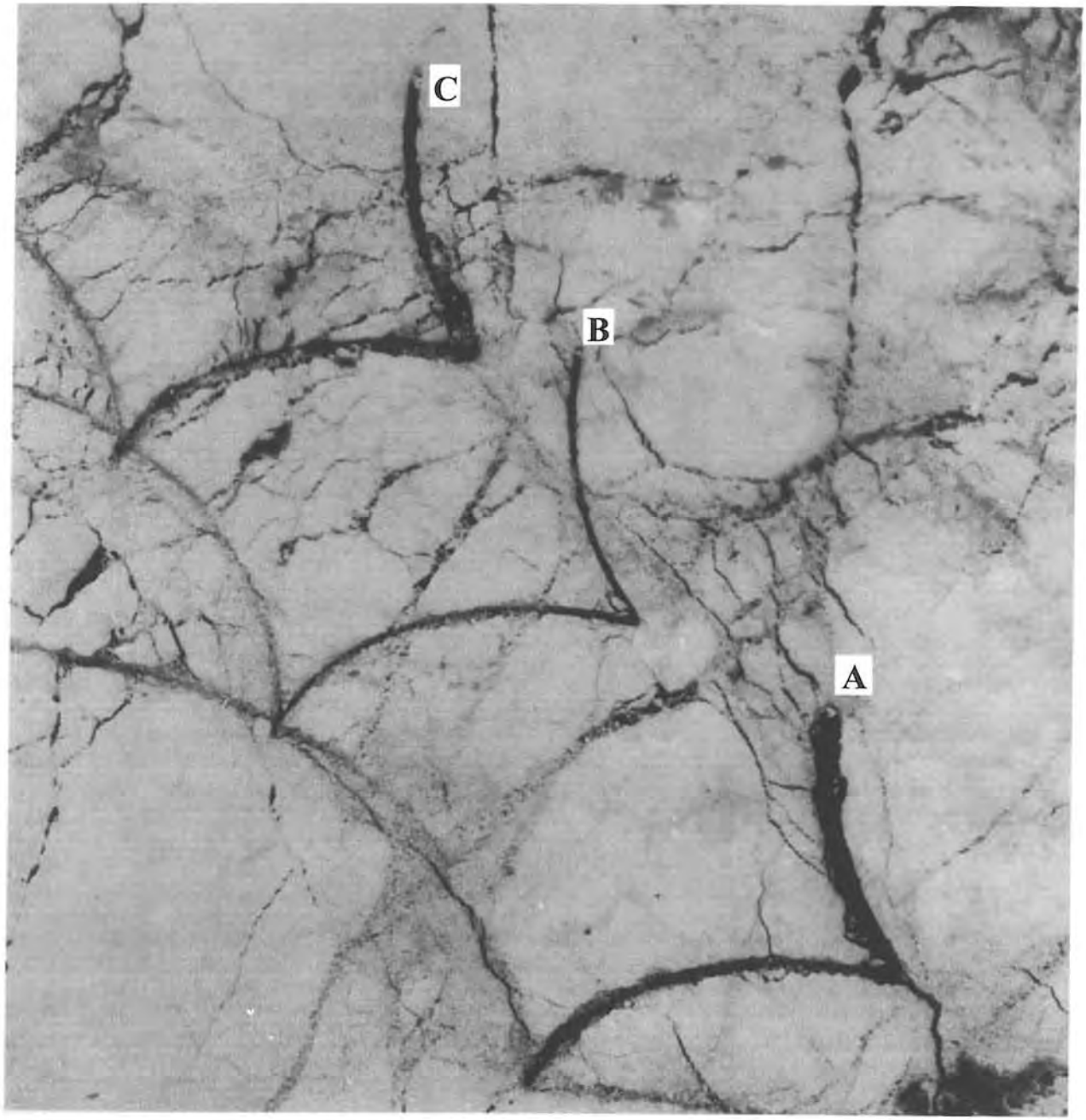

Figure 2.3. SPOT image from the Barents Sea ice cover with curved tracks generated by grounded icebergs. Fresh tracks appear dark due to open water. Three icebergs (A-C) are observed at the end of the fresh tracks. As the tracks become older (more than a day) they are filled with smaller, broken floes which appear more grayish. The image is obtained on April 11 1988 and is centred on Spitsbergenbanken between Hopen and Bjørnøya (75° 45'N 23°E). The image is SPOT panchromatic with 10 m pixel size and covers an area of 20 by 20 km.

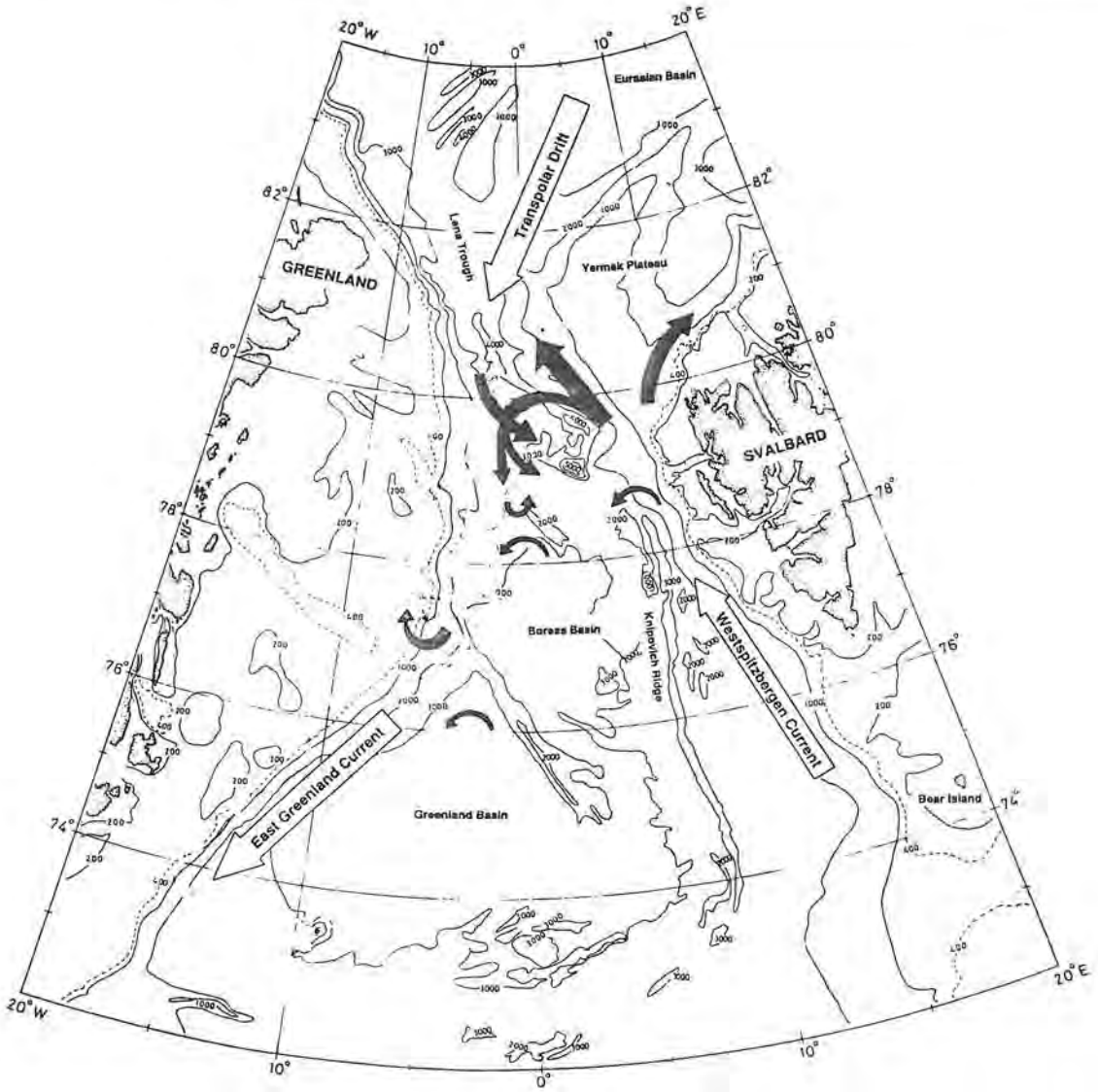

Figure 2.4. Bathymetric chart of the Greenland Sea and the Fram Strait. The large arrows indicate main ocean currents, the small arrows indicate some of the eddy areas (Sandven and Johannessen, 1990).

depth between 80 and 150 m; this gradient defines the lower boundary of the characteristic surface duct in the Arctic ocean.

Oceanographical sections in the interior Arctic show water structures with small horizontal gradients and small temporal variations (Anderson, et al. 1994), in contrast to the strong gradients found in the MIZ (Johannessen et al., 1983). The Fram Strait is the main area for exchange of water masses, heat flux and sea ice between the Arctic Ocean and the Greenland Sea and Norwegian Sea (Sandven and Johannessen, 1990). About 240 km of the 600 km wide Fram Strait at 79° N is more than 2000 m deep (Figure 2.4, Sandven and Johannessen, 1990). The maximum sill depth between the Greenland Sea and the Arctic Ocean is 2600 m (Coachman and Aagaard, 1994), allowing deep water masses to be exchanged through the Fram Strait. A 300 km wide continental shelf of less than 400 m depth covers the Greenland side of the strait. On the Svalbard side the shelf is less than 100 km wide. The width of the Fram Strait allows inflow of warm water to the Arctic Ocean and outflow of cold water and ice to

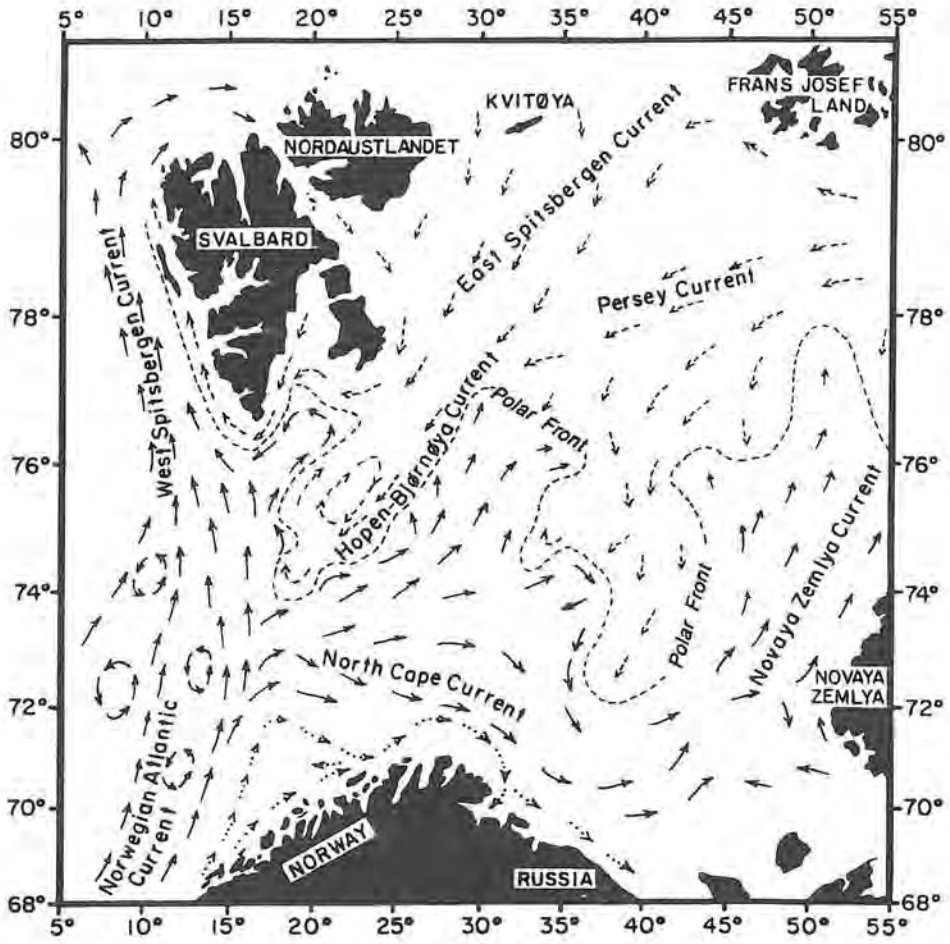

Figure 2.5. Circulation of surface waters in the Barents Sea showing main warm currents (Atlantic water: solid arrows), Cold currents (Arctic water: dashed arrows), Norwegian and Murmansk Coastal current (dotted arrows) and location of the oceanic polar front (dashed line). From Pfirman et al., 1994.

be separated horizontally, with the warm water advected northwards on the Svalbard side.

The current system is dominated by the shallow southward flowing cold and low salinity East Greenland Current (EGC) which exports ice and polar water out of the Arctic Ocean, and the northward flowing warm and saline Atlantic water in the West Spitsbergen Current (WSC). The WSC is a continuation of the Norwegian North Atlantic current which branches northwards (WSC) and eastwards (North Cape Current) off the northern cost of Norway (Figure 2.5, Pfirman et al., 1994). These currents bring relatively warm coastal and Atlantic water into the Barents Sea, keeping a large part of it ice-free during the winter. The polar front separates the warm Atlantic water from the cold Arctic water (Johannessen and Foster, 1978). The Arctic water is close to the freezing point and dominates the upper part of the water column north of the polar front. There are three currents transporting this cold water and sea ice into different parts of the northern Barents Sea: the Persey Current, the East Spitzbergen Current and the Hopen Bjørnøya Current. Because the Barents Sea is

shallow (200 - 500 m) with many banks and trough, the bathymetry plays an important role to guide currents and water mass exchange. (Figure 2.5, Pfirman et al., 1994).

2.2.2 Mesoscale features and processes

The currents in the Fram Strait and Barents Sea are characterized by high mesoscale variability which has strong influence on the ice configuration as well as on acoustic sound propagation. The MIZ is generally associated with ocean fronts observed as horizontal gradients in salinity, temperature and density. The fronts separate lighter, colder and less saline water beneath the ice cover from heavier, warmer and more saline water outside the MIZ. Mesoscale features along the ice edge region represent an important mechanism to exchange and mix water masses across the fronts.

Many of the mesoscale eddies propagate through the Fram Strait as part of the general circulation in the area. There are also stationary eddies locked to topographic features such as the Molloy Deep (Figure 2.4). Previous investigations indicate that jet currents (narrow, intense currents in the surface layer) along the ice edge can occur under favorable wind conditions (Johannessen et al., 1983). Barotropic and baroclinic instability along the fronts in the MIZ as well as topographic trapping are suggested to be important generating mechanisms for eddies (Johannessen, O. M. et al. 1987; Johannessen, J. A. et al. 1987). Remote sensing observations have shown that meanders in these jets can spin off eddies which may grow into vortex pairs which are more or less asymmetric and propagate into open ocean normal to the ice edge (Johannessen et al., 1994). Mesoscale eddies, vortex pairs and ice tongues have characteristic horizontal scales from 10 to 50 km, as shown in Figure 2.1, and life time from a few days to a few weeks (Johannessen, O. M., et al. 1987; Johannessen, J. A. et al., 1987). The Fram Strait and Greenland Sea eddies are often cyclonic with orbital speeds up to 40 cm/s. The velocity field in eddies and vortex pairs is characterized by strong horizontal shear observed in the ice floe pattern and by drifting buoys. This process is hypothesized to generate "hotspots" in ambient noise, to be discussed in chapter 6.

Mesoscale eddies and meanders in the ice edge region have strong impact on sea ice motion and configuration of the ice edge. Meanders in the ice edge are often the first stage in the development of an eddy or an ice tongue. When the eddies are fully developed filaments of ice are advected into open water forming ice tongues or curved filaments of ice (Figure 2.6). Many of the cyclonic eddies tend to accumulate ice in the eddy center because of convergence in the surface currents (Johannessen, J. A. et al., 1987).

2.2.3 Tidal currents

It has been known from the time of Nansen that tidal currents, forming elliptical trajectories, produce periodic convergence and divergence in the ice pack. The tidal current oscillations in the Arctic Ocean influence the ice distribution and generate periodic leads in the ice cover. Tidal currents consist of many constituents where the most important in the Fram Strait and Barents Sea are the semidiurnal M_2 and S_2 and diurnal K_1 and O_1 constituents. The diurnal components can be trapped due to non-uniform bottom topography as found at the shelf break where the tidal current can be enhanced. Johannessen et al. (1992) have used Gjevik's tidal current model (Gjevik et

Figure 2.6. Photograph of a 20-40 km ice edge eddy present on 30 June, 1984, Greenland Sea. (Johannessen, O. M. et al, 1987)

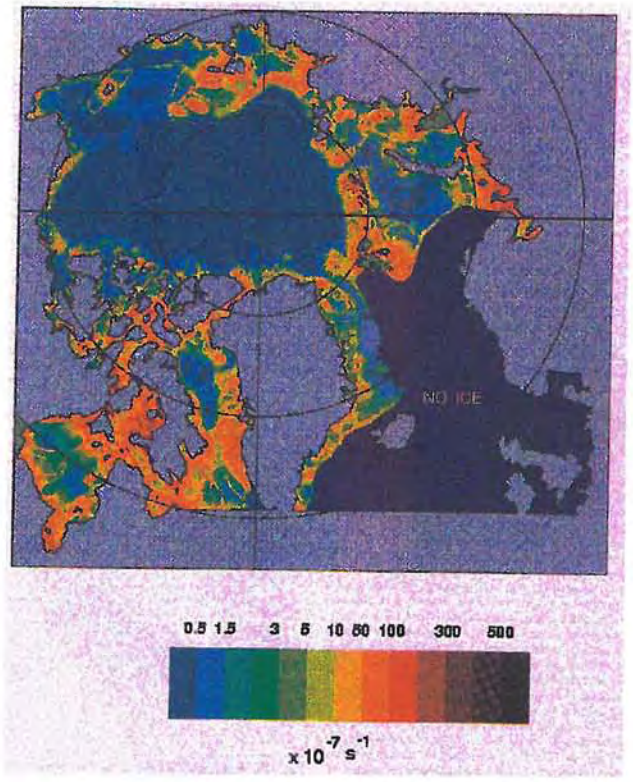

Figure 2.7. Distribution of maximal shear of ice velocity in the Arctic ocean caused by four tidal components : M2, S2, K1, O1 (From Kowalik and Proshutinsky, 1994).

al., 1990) with two diurnal and two semidiurnal components to estimate tidal ice motion. A high cross correlation is found between tidal current derived from Gjevik's model and the ice motion measured by Argos drifters. These results confirm that the ice floe motion is strongly determined by the tidal motion (Johannessen et al 1992a). The ice-tide interaction affects not only the ice distribution but also changes amplitude and phase of the tidal current significantly in shallow water under shore-fast ice (Kowalik and Proshutinsky, 1994).

Kowalik and Proshutinsky (1994) have modeled the dynamical interactions in the ice-water system using a space grid of about 14 km, which is of higher resolution than the Gjevik model used by Johannessen et al. (1992a). Numerical experiments show that the ice cover in the Arctic ocean is of minor importance for the tidal wave propagation, and the model was unable to reproduce the phase lag and amplitude change in very shallow water under shore-fast ice (Kowalick and Proshutinsky, 1994). Ice motion due to tides usually generates elliptical trajectories superimposed on a translatory motion, observed in satellite images (Figure 2.3). Grounded icebergs are seen to cut up the moving ice field driven by wind and current forcing (Johannessen et al., 1992a). Maximum tidal current speeds, which range from 50 to 130 cm/s, are found on the continental shelf of Svalbard, especially on the Spitzbergen Bank in the Barents Sea. Figure 2.7 shows the maximum shear of ice velocity due to the $M_2+S_2+K_1+O_1$ components calculated by Kowalick and Proshutinsky, (1994). A considerable velocity shear, between 50 - 100 x 10^{-7} s^{-1} is found in all ice covered regions on the shelves surrounding the Arctic Ocean, including the area south of Svalbard. A high shear (above 10^{-6}) favours the generation of leads and regions of high internal ice stress. The interaction between tidal current and the ice cover causes strong periodic fluctuations in low frequency ambient noise, where maximum ambient noise coincide with maximum tidal velocity (Johannessen, et. al. 1992; Bourke and Parsons 1993).

2.2.4 Surface waves

Swell interaction with the ice cover is the most important mechanism to break up large ice floes into smaller size, typically 20 - 50 m, in the marginal ice zone. The ice cover acts as a low pass filter, removing the shortest periods near the ice edge and gradually attenuating longer waves as they travel into the ice pack. Studies in the Greenland Sea shows that the attenuation is exponential, with an attenuation rate which increase as the square of frequency (Wadhams, 1973, 1987, 1994).

The SAR image in Fig 2.8 shows a fairly homogenous and regular wave field propagating into the ice pack from the open ocean. SAR images of the MIZ can map wavelength and wave propagation direction (Shuchman et al., 1994). Wave propagation models can provide dispersion relations both for open water and ice covered regions (Fox and Squire, 1991, 1994). The ice conditions vary from open water and grease ice to very compact and broken up FY or MY ice causing changes in material properties and thereby the constitutive laws and corresponding dispersion relations. There is no general constitutive law covering all ice conditions found in the MIZ, and correspondingly the dispersion relation changes within a MIZ.

Flexible ice sheet models are used in regions with high concentration of ice (Fox and Squire, 1991, 1994). In frazil ice and pancake ice Wadhams and Holt (1991) successfully used a massloading model, which is a flexible ice sheet model with no rigidity (Squire, 1993b). In the diffuse ice edge a scattering model including solitary floe theory can be used (Wadhams, 1986; Meyland and Squire, 1994). Surface waves have by several investigators been shown to be the major noise generator in the MIZ (Makris and Dyer, 1991, Johannessen et al, 1992). As mentioned before swell propagation is a dominant ambient noise generating mechanism.

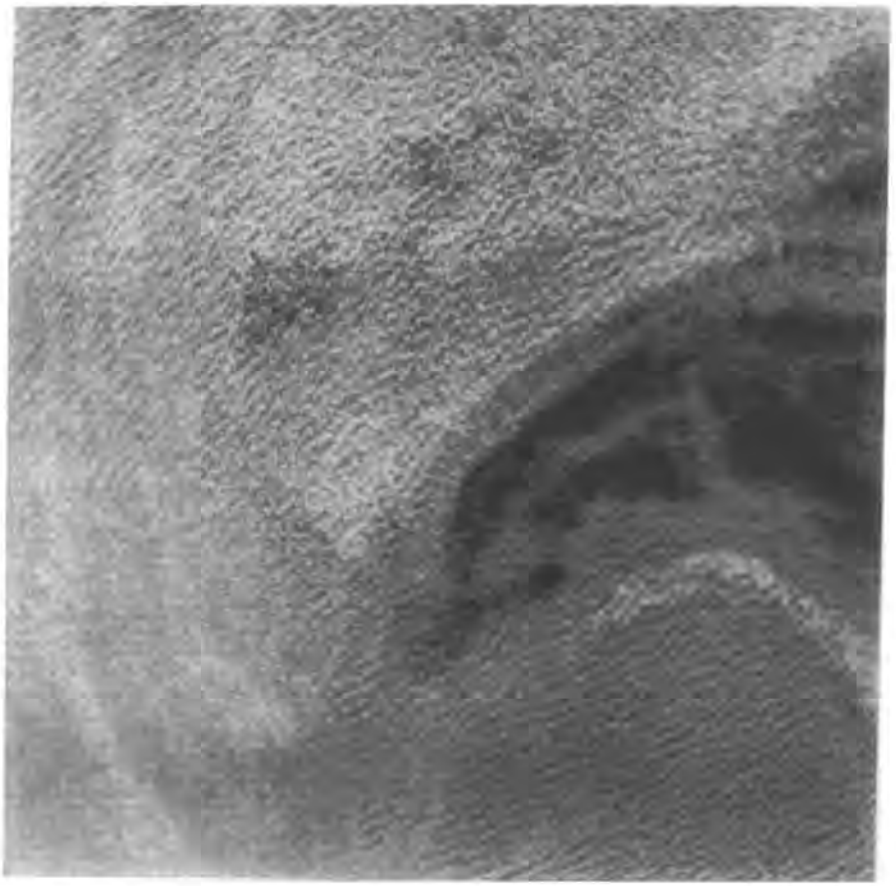

Figure 2.8 High resolution SAR image of the MIZ covering 8 by 8 km of the ice edge eddy **A** in Figure 2.1. The wavelength of the swell is about 250 m long and propagation direction is to the northeast into the ice pack (towards the upper left corner)

2.2.5 Internal Waves

High-frequency internal waves can occur anywhere in the ocean where there is vertical stratification and generating mechanisms. Studies in ice covered regions show that internal waves can be generated by several mechanisms such as current interaction with seamounts, ice keels moving relative to the underlying water masses, and interaction with eddies and current shear (Sandven and Johannessen, 1987). Internal waves can be manifested by SAR observations at the surface and underwater arrays of temperature

Flexible ice sheet models are used in regions with high concentration of ice (Fox and Squire, 1991, 1994). In frazil ice and pancake ice Wadhams and Holt (1991) successfully used a massloading model, which is a flexible ice sheet model with no rigidity (Squire, 1993b). In the diffuse ice edge a scattering model including solitary floe theory can be used (Wadhams, 1986; Meyland and Squire, 1994). Surface waves have by several investigators been shown to be the major noise generator in the MIZ (Makris and Dyer, 1991, Johannessen et al, 1992). As mentioned before swell propagation is a dominant ambient noise generating mechanism.

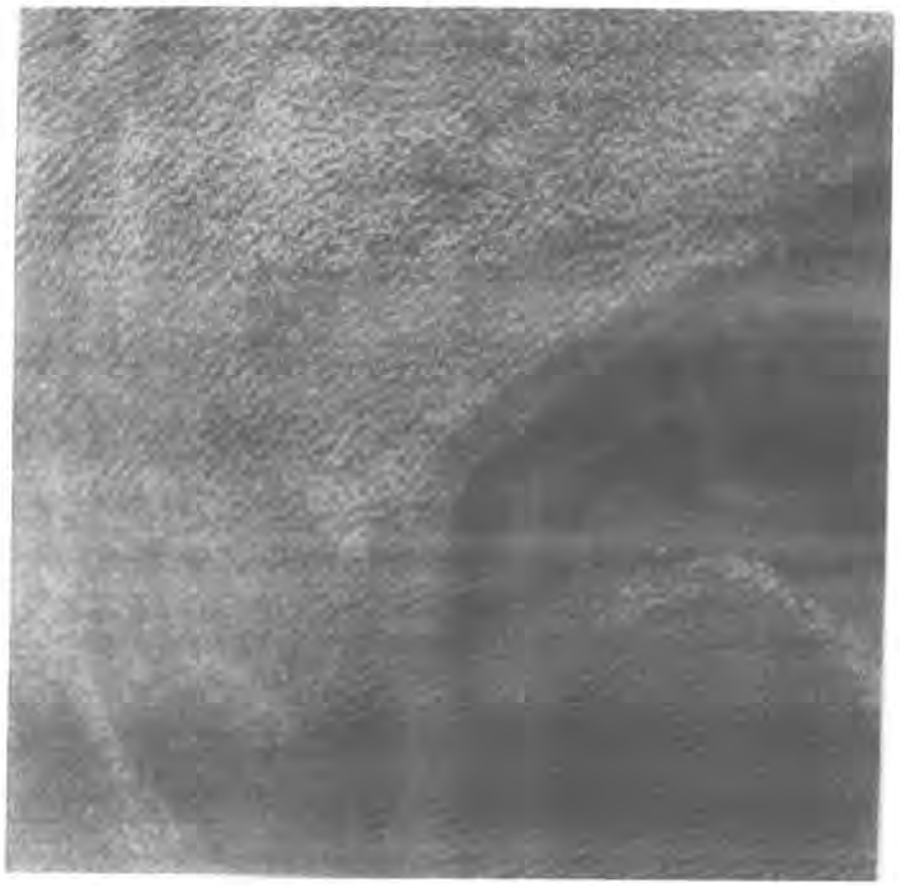

Figure 2.8 High resolution SAR image of the MIZ covering 8 by 8 km of the ice edge eddy A in Figure 2.1. The wavelength of the swell is about 250 m long and propagation direction is to the northeast into the ice pack (towards the upper left corner)

2.2.5 Internal Waves

High-frequency internal waves can occur anywhere in the ocean where there is vertical stratification and generating mechanisms. Studies in ice covered regions show that internal waves can be generated by several mechanisms such as current interaction with seamounts, ice keels moving relative to the underlying water masses, and interaction with eddies and current shear (Sandven and Johannessen, 1987). Internal waves can be manifested by SAR observations at the surface and underwater arrays of temperature

profiles. Investigations of internal waves in the Fram Strait MIZ show that density and corresponding temperature surfaces in the pycnocline can oscillate vertically with amplitudes up to 5 m and a frequency of typical 3 - 4 cycles per hour, which is near the buoyancy frequency for internal waves. These oscillations will have impact on the sound velocity profiles and the acoustic propagation conditions (Dyer et al., 1987, Lynch et al., 1996) as well as on low frequency ambient noise (Makris and Dyer, 1991).

transport equations gives the amplitude for each ray. The complex pressure field is found by summing up the contributions of each ray passing through a point (eigenrays). Several ray trace models have been developed using different numerical algorithms to solve the ray equations and different methods to correct for the anomalies obtained by the traditional ray trace model. Ray theory has reduced validity in the following cases:

- in shadow zones where the pressure is found to be zero,
- near and within caustics,
- if the acoustic wavelength is larger or of comparable size to any of the length scales of the problem on hand, and
- at interfaces not correcting for beam displacement.

The most important advantages of the ray trace theory are :

- simple physical interpretation,
- efficient numerical codes,
- the ability to model in range dependent environments, and
- the ability to model in three dimensions

Generalized ray trace, which includes correction of beam displacement, has been used to study the effect of ice cover on travel times (Jin et al., 1993).

The most popular models for range dependent problems in ocean acoustics solve a parabolic equation by discretisizing the area and using a finite difference scheme or a marching solution technique. The development of the parabolic equations is based on the assumption of outgoing waves (one way propagation) which means that the interface interaction is not handled generally. Far field assumption ($k_0r>>1$) and angle restrictions are introduced by the paraxial approximation (wide angle parabolic equation). The angle restrictions have been improved by using other approximations. Another drawback is that the results have to go through a post processing to present physical interpretation capabilities. Elastic parabolic equations have been developed recently, but they still need to be verified (Goh, 1998).

3.2.2 Range independent seismo acoustic models.

Wave motion in a solid, described as a elastic media, is described completely by displacement vector which can be written as a sum of the gradient of a scalar potential and the curl of a vector potential (see Schmidt, 1988 for details).

$$\mathbf{u} = \left[u_1, u_2, u_3\right] = \nabla\Phi + \nabla \times \Psi \qquad 3.1$$

3. Acoustic propagation models for the marginal ice zone.

3.1 Introduction.

Ambient noise is a superposition of contributions from a large number of natural sources of acoustic energy. After the noise is generated it propagates according to the propagation conditions characterizing the region. Therefore, the ambient noise is strongly dependent on the propagation conditions. Increased knowledge of acoustic propagation will correspondingly increase the knowledge of ambient noise. As seen in Table 1.1 in Chapter 1 relatively little work have been done on acoustic modeling in the MIZ, and the work that has been done includes very strong simplifications of the physical environment (Mellberg et al., 1987, 1990, Buckingham, 1992). An appropriate acoustic model for the MIZ has to include the effect of elastic ice cover, elastic bottom and range dependence. Development of such a model is not covered in this thesis. The objective of this Chapter is to give a short and descriptive review of the actual models and a brief rationale for selecting the OASES model for use in the MIZ.

3.2 Acoustic propagation models

The open ocean is ususally considered as an acoustic wave guide limited by the sea floor and the sea surface, and the main problem is to model a rough free surface and a rough more or less solid sea floor with varying geo-acoustic conditions. Several advanced numerical models have been developed during recent years, see reviewed by Buckingham, (1991) and Jensen et al., (1994).

In the Arctic ocean the ice covered regions can also be considered as a waveguide limited by a solid rough surface and a solid rough bottom. The inclusion of the reflection and scattering from rough elastic surfaces complicates the modeling work significantly (e.q. Fricke, 1991, 1993; Schmidt, 1994; LePage and Schmidt, 1994). In the MIZ, the modeling is further complicated by strong horizontal gradients and temporal variations in both ice conditions, the oceanographic fields and the bottom conditions. Therefore, very few attempts has been made to model acoustic propagation in the MIZ. The modeling attempts includes strong simplifications of the physical conditions (e.q. Mellberg et al, 1987, 1991; Buckingham 1990, 1991) where the effect of ice mostly have been neglected. The effect of a discontinuous ice cover, which is normally found in the MIZ, has only been addressed by a few investigators (e.q. Dahl, 1989, Fricke 1991).

3.2.1 Ocean acoustic models.

Ray trace models have a long history in underwater acoustics and are still the most widely used technique in operational underwater acoustic. Much of the physical interpretation of more advanced numerical models are based on the concept of rays. A ray path is given as the solution of the eikonal equation, whereas the solution of the

Each of the potentials in the displacement representation can be shown to satisfy the wave equation (See any text book on elastic waves)

$$\nabla^2\Phi = \frac{1}{c_L^2}\frac{\partial^2\Phi}{\partial^2 t}, \text{ where } c_L^2 = \frac{\lambda + 2\mu}{\rho} \qquad 3.2$$

$$\nabla^2\Psi = \frac{1}{c_T^2}\frac{\partial^2\Psi}{\partial^2 t}, \text{ where } c_T^2 = \frac{\mu}{\rho} \qquad 3.3$$

λ, μ are the Lame´constants, and ρ is the material density

The first equation describes the longitudinal (pressure or volume) wave propagation, and the second one describes the transverse (shear) wave. These equations also cover the case of waves in a fluid. By solving the wave equations for the displacement potentials, and using constitutive equations the stress components can be found.

The potentials (sound field), assuming small amplitudes, from a point source of strength s(t) is a solution of the in-homogenous wave equation. If the source term s(t) is a pulse wave form, the solution can be by found by Fourier transforming the wave equation. The resulting Helmholtz equation is then transformed to the inhomogeneous depth separated wave equation by a Hankel transform. The solution of the depth separated wave equation, the depth separated Greens function, is written as

$$g(k,z) = \overbrace{\hat{g}(k,z)}^{\text{The field produced by the sources in absence of boundaries}} + \underbrace{A^-(k)g^-(k,z) + A^+(k)g^+(k,z)}_{\text{Linear combinatiotwo solutions to the homogeneous depth separated wave equation}} \qquad 3.4$$

where the arbitrary coefficients A^- and A^+ are determined from the boundary conditions. k is the horizontal wave number, while z is the depth component. When the unknown coefficients are found, the total field at the angular frequency (ω) is found at any range by carrying out the inverse Hankel transform. The time response is obtained by evaluating the inverse Fourier transform.

The basic property of the full wave field solution is to restrict the depth dependence of sound speed to cases where the depth separated wave equation can be solved analytically, limiting the numerical effort to determine the unknown coefficients from the boundary conditions and to evaluate the inverse integral transforms.

This concept is used in SAFARI and OASES models (Schmidt, 1988, 1997). The SAFARI model (Schmidt, 1988) and the OASES model (Schmidt, 1997) calculate the depth separated Green functions using direct global matrix approach, and a Fast Fourier Transform to obtain the inverse Hankel transform. In order to evaluate the

wavenumber integral the Hankel transform is approximated to a Fourier integral. This approximation is good a few wavelengths away from the source. Numerical errors are introduced by truncation of the wavenumber integration domain and by under-sampling of the integrand. The theory and numerical method is described in detail by Jensen et al. (1994) and Schmidt (1988).

The advantage of SAFARI and OASES is the inclusion of multi-layers which can be described both as a fluid and an elastic solid.

Scattering from rough surfaces was not originally included in the model theory. Elastic roughness conditions have recently been introduced in the models by transforming the boundary conditions given on an elastic rough surface into a mean horizontal surface through a matrix formulation of a perturbational approach (Kupermann and Schmidt, 1989; LePage and Schmidt, 1994).

3.2.3 Range dependent solutions including elastic ice cover.

Scattering due to surface roughness is a "statistical constant" range dependence included in the boundary conditions. Discontinuity in the boundary description such as the ice edge separating open water from ice is not covered by this theory. Diffraction/scattering models dealing with changes in formulation of boundary condition matrices and complicated boundary geometries involve partial differential equations with mixed boundary conditions and/or boundary conditions involving singularities which cannot be solved by elementary mathematical or numerical models.

An ice-edge diffraction problem has been studied by Dahl (1989) using the Wiener Hopf technique (Noble, 1958). The achievements of using this method was a better understanding of the physics behind scattering, but due to numerical difficulties it is not useful as a numerical approach. A direct numerical way to obtain a solution in a range dependent ocean environment is to discretezise the governing equations and using a finite element or a finite difference schemes to calculate the solutions. Fricke (1991,1993) developed and used a finite difference method to solve the heterogeneous elasto-dynamic equations in two dimensions in order to calculate the scattered field from the elemental scatterers. The model permits arbitrary roughness, unrestricted slope, displacement or radius of curvature. The model is well suited to study broadband sources and produces the solution in time domain. Generally, finite element or finite difference schemes are very time and space demanding solution methods because of dense sampling of a large area. Additional large calculation areas are needed due to the problem of false reflections from the numerical boundaries.

Another approach is to develop hybrid schemes involving a combination of wavenumber integration and boundary integral methods, (BEM) as described by Gerstoft and Schmidt (1991). BEM combines an integral representation of the wave field within a volume with a point representation of stresses and displacements on the boundary between the two domains. The need for a dens mesh is limited to the

boundary alone, eliminating the problem of discretely representing the wave field throughout the volume. In contrast to discrete methods, such as the finite element and finite difference approaches, the solution obtained with the hybrid scheme is efficient for short as well as long range reverberation. The total solution is decomposed in the temporal and spatial spectral components, which is important to the basic physical understanding of the factors affecting seismo-acoustic facet reverberation.

Recently, by using *spectral super element methods* it has been possible to model strong range dependence in both ocean waveguides (Goh and Schmidt, 1995), and in wave guides with seismo-acoustic boundaries (Goh and Schmidt, 1996). The spectral super element approach is an hybridization of the finite elements, boundary integrals and wavenumber integration to solve the Helmholtz equation in a range dependent environment. The environment is first divided into a series of range dependent sectors or super elements, separated by vertical boundaries or cuts. Within each sector the ocean environment is horizontally stratified and will allow for fluid-elastic stratification's. The field in each sector is now expressed as a superposition of the field produced in the stratified element in absence of the vertical boundaries $\mathbf{u}^*$, the field arising from the left boundary, $\mathbf{u}^-$, and the field arising from the right boundary, $\mathbf{u}^+$,

$$\mathbf{u}(x,z) = \mathbf{u}^*(x,z) + \mathbf{u}^-(x,z) + \mathbf{u}^+(x,z) \tag{3.4}$$

where $\mathbf{u}$ is taken to denote contributions from the displacement potentials. $\mathbf{u}^*$ is calculated by using the SAFARI/OASES model. The wave fields from the vertical boundaries are found by using a indirect boundary integral method, based on Greens theorem for the semi-infinite virtual element obtained by eliminating the other vertical boundary and letting the element continue to infinity. For fluid super elements the boundary conditions are the continuity of pressure and particle displacement, for elastic super elements the boundary conditions are the continuity of stresses and displacements.

While the spectral super element approach solves the coupled integral equation using a high-order panel-boundary-element formulation, an approximate approach is to solve reflections and transmission locally at a discrete number of depths, yielding a description of virtual panel sources (VISA), (Schmidt, 1997). This method has been used to provide a range dependent version of OASES. The results from this model correspond well to canonical benchmark results obtained by the spectral super element approach (Goh et al., 1997).

3.3 Model to be used in this thesis.

Based on the above review the most interesting model for use in the MIZ is the super element method approach. This model is a research model which is not available for the time being. The range dependent model, OASES, using VISA is less computing time demanding than the model using the spectral super element method. A benchmark study by Goh and Schmidt (1997) have shown that this model produces

results which agree well with the spectral super element method. The range dependent version of OASES will be used in AMOC (Johannessen et al. 1997). This model is a licensed model, which was not made available in time for this project..

The range independent version of OASES is a public domain model. This model is basically a expanded version of SAFARI. The model allows for arbitrary stratification's incorporating fluids with depth dependent sound speed profiles, linearly visco elastic solids, transversely isotropic solids and poro-elastic layers. All common source representations are handled, including plane waves, point and line explosive sources, line arrays, and a variety of plane or axis symmetric seismic moment sources. This model is used in Chapter 5 to do a preliminary study of the effect of ocean and ice parameters on acoustic propagation.

4. The Acoustic Experiments 1984-1992

During the years between 1984 and 1992 five MIZEX/SIZEX field experiments were carried out in the marginal ice zone of the Greenland sea and the Barents Sea. The overall objective of the acoustic studies was to investigate the effect of ice edge eddies on ambient noise and acoustic propagation. This chapter gives an overview of the acoustic experiments during the MIZEX (Marginal Ice Zone Experiment) and SIZEX (Seasonal Ice Zone Experiment) programmes with brief description of data collection and data processing.

4.1 Summary of the acoustic experiments

Ambient noise studies were carried out in the deep part of the Greenland Sea during the experiments in 1984, 1985, 1987 and 1989 (Johannessen et al., 1988 b; Johannessen et al., 1990; Focke, et al., 1993, Johannessen et al., 1993a). The Barents Sea were investigated in 1989 (Engelsen, 1989; Johannessen et al., 1992) and 1992 (Engelsen, 1993 a; Johannessen et al., 1993b). A propagation loss study was performed during SIZEX 92 using CW sources and SUS charges (Engelsen, 1993 b; Johannessen et al., 1993). The location of the experiment areas is shown in Figure 4.1.

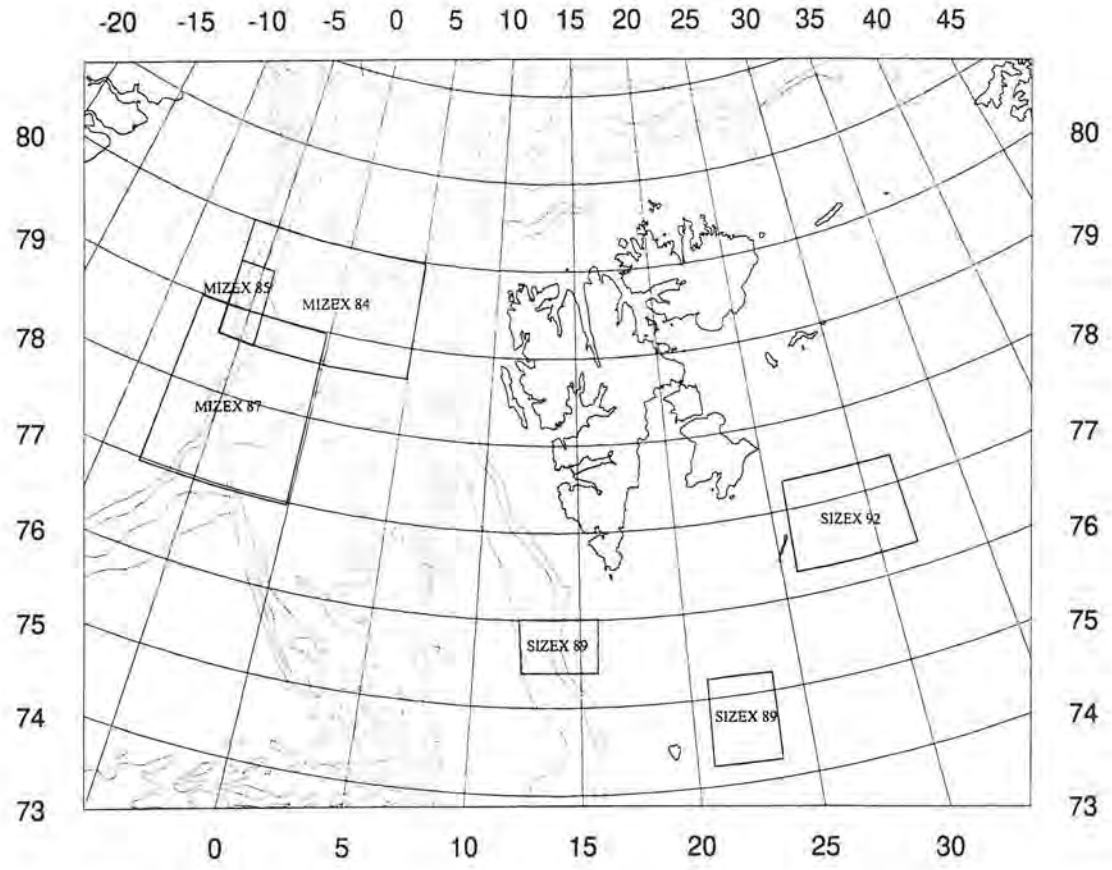

Figure 4.1 Location of the acoustic experiments during the MIZEX /SIZEX programmes.

All the campaigns, except MIZEX 85, were multi-disciplinary, international experiments, which employed various observational platforms such as ice strengthened ships, open ocean ships, drifting buoys, bottom-moored buoys, helicopters, aircraft, and satellites (Johannessen et al, 1992 c). In MIZEX 85 a dedicated acoustic experiment was carried out using a P3 aircraft to deploy sonobuoys and AXBT´s. Also satellite data were used in the 1985 experiment.

In all the experiments remote sensing of the ice played an important role both for location of the experiments and in the interpretation of the ambient noise characteristics. In 1992 the ERS-1 satellite provided for the first time high-resolution spaceborne SAR images of the experiment area in the Barents Sea.

4.2 Data collection and processing

During the five field experiments twelve flights were conducted by Norwegian P3 aircraft. The aircraft deployed sonobuoys and AXBT's both in open water and in areas of open leads within the ice pack. In addition, helicopters were used for deployments in areas of high ice concentration. A total number of 169 operating sonobuoys at 82 different locations were deployed during the flights. The sonobuoy deployment depth was 18 and 122 m in the Fram Strait experiments and only 18 m in the Barents Sea experiments. An overview of the buoy deployment for each experiment is given in Table 4.1. Only a part of the data (marked by shadows) has been used in the present study. An overview of data sets and data processing used in the thesis is given in Table 4.2

These acoustical data were collected by the 333 Squadron of the Royal Norwegian Air Force, using P3-B aircraft equipped with AN/ARR-72 receivers and 28-track analog, FM wideband group II tape recorders. Details of the data collection, calibration and processing have been described in the following data and technical reports. The MIZEX 84 and 85 data were processed by ARL in Texas and are reported in Johannessen et al. (1988b). The MIZEX 87 data are described in Johannessen et al. (1990), and the SIZEX 89 data are reported by Engelsen (1990). The SIZEX 92 data were initially processed at NDRE and reported by Engelsen (1993 a,b), and along with environmental conditions by Johannessen et al. (1993). Then the SIZEX 92 data were re-processed in order to study short term variations, using software developed at NERSC based on calibration algorithms used at NDRE (Engelsen 1993 b). Raw data from the MIZEX experiments are located at ARL, Austin Texas, while the SIZEX 89 and 92 data is located at NERSC. The SIZEX 92 data is also located at DRA.

4.2.1 MIZEX 84-87

Six ambient noise case studies in MIZEX 84/85 were carried in the Fram Strait. In MIZEX 87 one ambient noise experiment was carried out in the Fram Strait. All MIZEX data were calibrated and processed at Applied Research Laboratory, Austin, Texas. All the data for each recording sonobuoy in MIZEX 84, 85 and 87 are given by time averages at four selected frequencies 40, 100, 315 and 1000 Hz. All levels are given in dB re $1\mu Pa^2/Hz$, and the frequency domain was chosen from 12.5 up to 1000 Hz. The

calibration, averaging and processing of the data are described in detail in Johannessen et al, (1988) and Johannessen et al, (1990).

Table 4.1 The MIZEX and SIZEX acoustic ambient noise experiments. Shadowed data are used in the present study.

Experiment date	Area and center position	Number of sonobuoys /Number of AXBTs	Depth of acoustic buoys	Recording period (Z)
MIZEX 84	**Fram Strait**			
26 June	79° 03'N 00° 30'E	5/32	122	09:59 - 12:46
19 June	79° 36'N 03° 35'E	6/22	122	08:16 - 10:20
11 June	81° 30'N 01° 45'E	6/22	122	11:22 - 13:25
MIZEX 85	**Fram Strait**			
30 April	78° 24'N 01° 25'E	21/29	18, 122,305	11:15 - 19:07
25 April	78° 12'N 04° 30'E	15/8	18, 122,305	11:45 - 19:07
24 April	79° 14'N 01° 25'E	16/13	18, 305	11:00 - 14:35
MIZEX 87	**Fram Strait**			
2 April	78° 00'N 04° 00'W	21/0	18/122	10:00 - 17:00
SIZEX 89	**Barents Sea**			
February 27	75° 45'N 14° 00'E	24/7	18	11:30 - 16:00
February 18	74° 30'N 23° 00'E	18/4	18	14:00 - 17:45
February/ March		2 (RBS)/0		
SIZEX 92	**Barents Sea**			
March 9	77° 00'N 28° 30'E	26/2	18	12:49 - 15:15
March 6	77° 00'N 30° 30'E	11/5	18	11:00 - 16:00
March 1-2	76° 29.6'N 26° 00.2'E	1 (DATOS)	(Bottom mounted) 83 m	17:00 March 1- 20:00 March 2
March 6-9	77° 17'N 30° 14.5'E	6 (Ice array)	18,38	13:00 March 6- 01:23 March 9

Table 4.2 Summarized data processing and data used in the study.

Data sets used in the thesis	Averaged levels at at selected frequencies	Time series at selected frequencies	Frequency spectra	Sonogram	Data reports
MIZEX 85 30 April	x				Johannessen et al 1988 b
MIZEX 87 2 April	x	x	x		Johannessen et al 1990
SIZEX 89 February 27	x	x	x		Engelsen, 1990
SIZEX 92 March 9, March 6 March 1-2 (DATOS)	x	x	x	x	Engelsen, 1993b; Johannessen et al., 1993; Turner, 1993

The data from 1987 are presented by time series at selected frequencies and frequency spectra presented by 10, 50 and 90 percentiles as shown in Figure 4.2 (Johannessen et al, 1990). Averaged values at each sonobuoy location for comparison to earlier experiments were calculated based on the times series (NOTE: the levels are converted to Pa^2 before averaging, and then converted back to dB) (Johannessen et al, 1990).

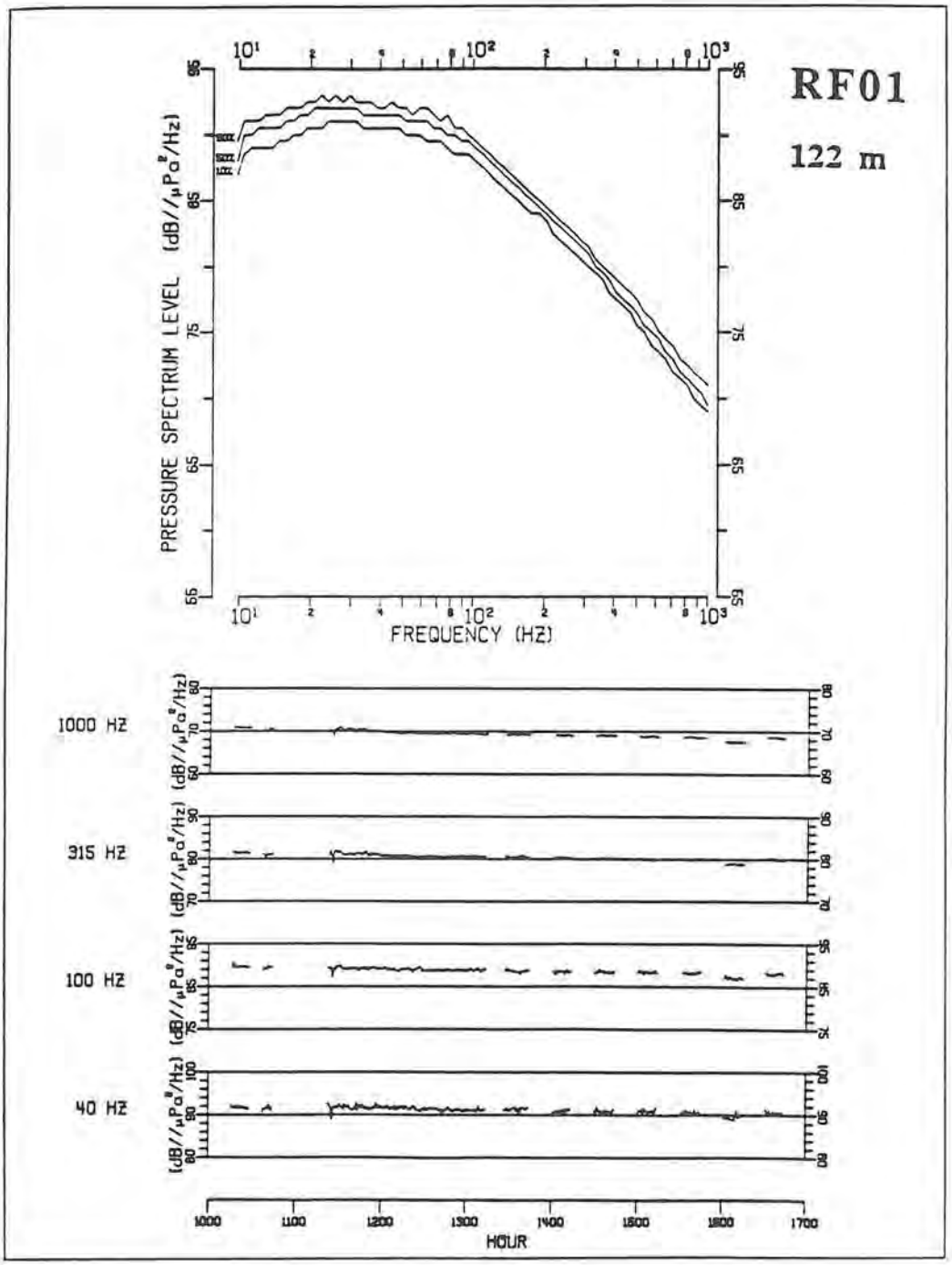

Figure 4.2 Upper graph: frequency spectra averaged over the whole recording period represented by 10, 50 and 90 percentiles. Lower graphs: time series of one minute averaged noise levels at selected frequencies. Data are from receiving buoy RF01 in the Fram Strait on April 2 1987.

4.2.2 SIZEX 89 and 92.

During SIZEX 89 and SIZEX 92 several acoustic experiments were performed at three different locations in the Barents Sea (Figure 4.1 and Table 4.1). Acoustic data were obtained from sonobuoys, bottom mounted acoustic buoys and acoustic arrays deployed on ice floes.

During the two campaigns four case studies were performed focusing on effects of eddies, swell, tides, icebergs and other ice types on ambient noise in shallow waters. Sonobuoys were deployed from P3-aircraft and helicopters in arrays based on ice information from SAR data. The acoustical data were processed at NDRE and made available as raw data on tape and in data reports (Engelsen, 1990; Engelsen, 1993 a, b). All processed data are represented as dB re 1 $\mu Pa/\sqrt{Hz}$, which is equivalent to values given in dB re 1 $\mu Pa^2/(Hz)$. The frequency bandwidth was from 12.5 Hz up to 5 kHz.

The acoustic data from four case studies were represented by frequency spectra averaged over 3 minutes (512 individual frequency spectra) at selected times when the data was of a good quality (Figure 4.3). Time series at selected frequency were generated based on the results from the frequency spectra. Averaged levels at selected frequency and selected times were plotted on ice maps generated from remote sensing data (Engelsen, 1993, Johannessen et al, 1993). The analysis of these data is presented in chapter 6.

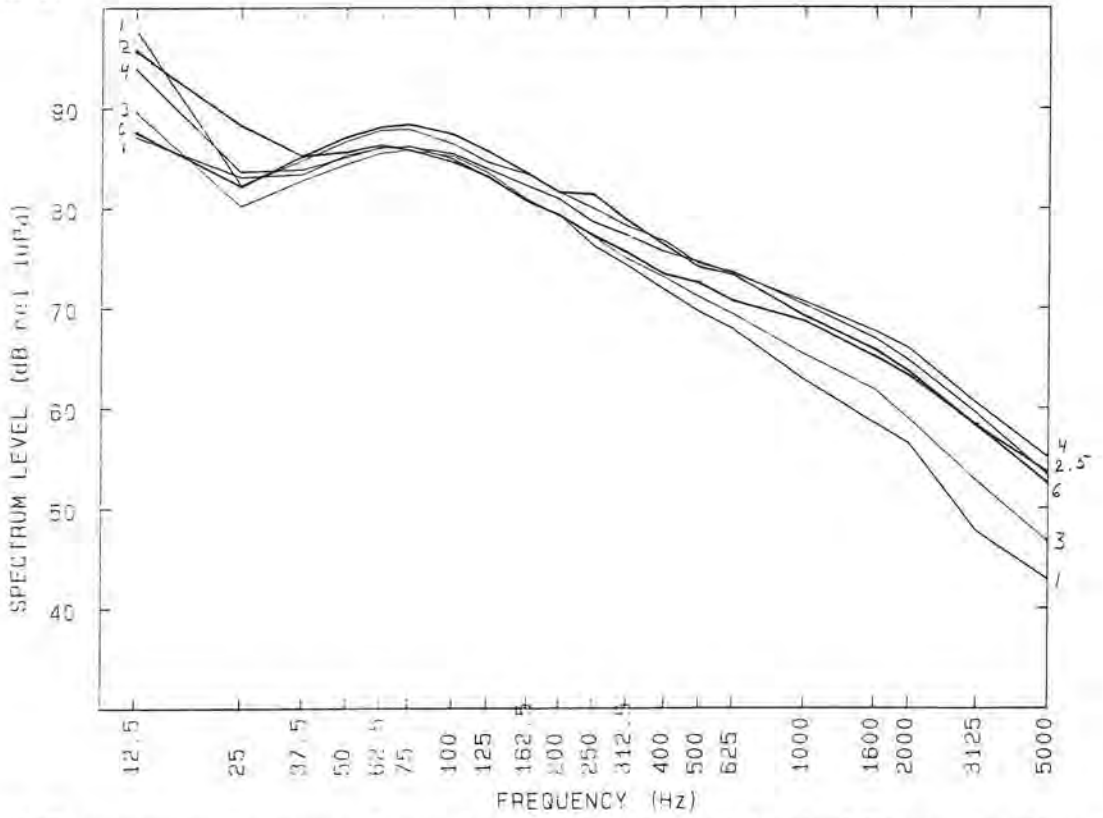

Figure 4.3. Frequency spectra averaged over 3 minutes from buoy 19 for six different periods on March 9 1992. Each averaged spectrum is derived from 512 individual frequency spectra.

A software system for data calibration, and processing is developed at NERSC which makes it possible to do more detailed and flexible analysis of the SIZEX 92 data. The system is used to make time series of 4 second averaged frequency spectra for 5 minutes recording intervals, called sonograms. The sonograms show the time variation in ambient noise at all frequencies in a 2-D contour plot. An example of a sonogram starting at 14:00 Z on March 6 1992 is shown in Figure 4.4. The system can also be used to produce averaged frequency spectra and plots of deviation from the averaged frequency spectra. Details of the processing algorithm is presented in the appendix.

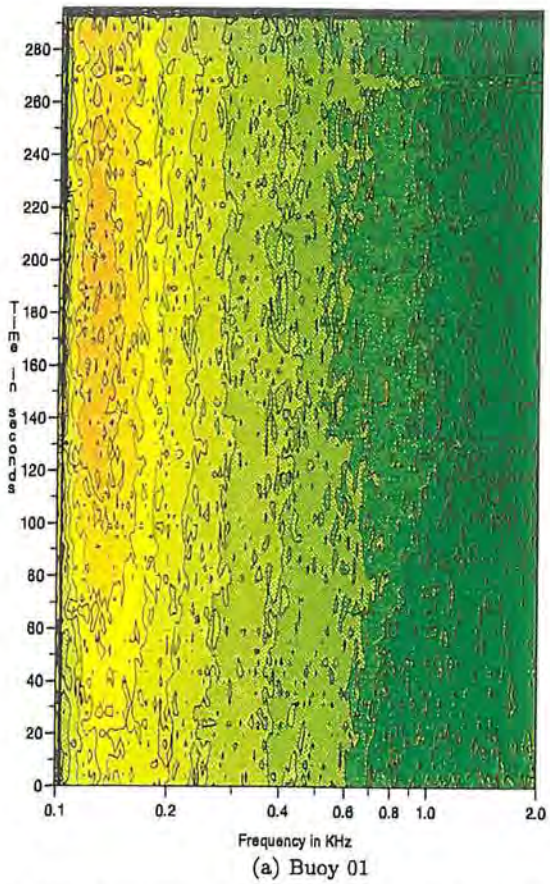

(a) Buoy 01

Figure 4.4 Sonogram obtained from buoy 01 between 14:00 and 14:05 on March 6 1992. The vertical axis shows the time variability.

4.3 Bottom mounted acoustic buoys

Five bottom mounted acoustic recording stations were deployed in the SIZEX 89 and 92 experiments of which four were successfully recovered. The data was calibrated and processed in cooperation with NDRE. During SIZEX 89 three buoys with a bandwidth 10-630 Hz were deployed at two locations (two in February and one in June). The buoys provided data for about three weeks. Details of processing and results are presented by Engelsen (1993) and in a joint NERSC-NDRE report (Johannessen, et al., 1993).

In SIZEX 92 two buoys with a bandwidth of 3-20000 Hz were deployed for long-term recording. The recording was set to 4 minutes every hour for 23 days. Only one buoy

was recovered and the buoy recorded successfully for only 28 hours. Frequency spectra, with bandwidth 12.5-5000 Hz, were estimated for the 28 hour period with an averaging interval of 2 minutes every hour. Times series of 2 minutes averages at selected frequencies is also estimated. Additional statistics were computed by Engelsen, (1993b). Sonograms at selected times were generated at NERSC similar to Figure 4.4.

4.4 Selection and organization of ambient noise data

Due to the large amount of data and the variability in data presentation by the participating institutions subsets of data were selected for further analysis in the thesis. The selection of data was primarily based on availability of uniformly processed data and on availability of environmental data.

4.4.1 Summary of ambient noise studies

The presentation of the ambient noise study results is as follows. In Chapter 6, averaged levels from April 30, 1985; April 2, 1987; February 27, 1989; and March 9, 1992 are presented in a study focusing on hotspots due to ice edge eddies and icebergs. In chapter 7 frequency spectra are used to study the effect of sound propagation on broadband ambient noise. Chapter 8 is focusing on short term variations in ambient noise, especially due to swell, using data from March, 9 1992. DATOS buoy data are used to study the effect of grease ice on ambient noise in Chapter 9.

4.4.2 Use of environmental data

Environmental parameters such as wind velocity, ice velocity, wave height and wave period are summarized in Table 4.3 for each experiment used in the thesis. CTD and AXBT data were obtained in every experiment to provide information on sound speed profile, water masses and eddy circulation.

Table 4.3. Summary of environmental conditions for each experiment used in the thesis

Environmental parameters	MIZEX 85	MIZEX 87	SIZEX 89	SIZEX 92	
Date	30.04.85	02.04.87	27.02.89	06.03.92	09.03.92
Bottom depth (m)	2000 - 3000	2000 - 3000	200 - 1000	200 - 300	
Wind (m/s)	3 - 5	5 - 9	2 - 3	2 - 4	2 - 10
Wind dir(deg)	0 - 50 Parallel to ice edge	60 Parallel to ice edge	30 - 40 Off ice	30 - 40 Off ice	180 - 270 On ice
Significant wave height (m)	< 0.5	0.7 - 1.5 (*)	0.13	Weak	1-2 m
Dominant wave period (s)	3	12.1 - 13.5 (*)	13.6	no	13
Air temperature	-10	-20	-15	-2 ,-9	-1,-14
Ice edge features	Eddies	Eddy, jet, vortex pair	Shear zones	Weak swell	Swell, Icebergs

(*) Wave measurements inside the compact ice edge

Analysis of ice information obtained from remote sensing data (SAR), in situ observations, aerial photos are presented together with the acoustical data in chapters 5 - 10 .

4.5 The Acoustic Propagation Loss Study in SIZEX 92

As part of SIZEX 92 a dedicated propagation loss experiment was done in a 100 km section across the ice edge northeast of Hopen on March 6 1992. The experiment was performed using SUS Mk 82 charges with explosion depth at 18 m. Twenty SUS charges were dropped from a P3 aircraft, but only 11 detonated successfully and could be used in the propagation loss study. Source levels for the Mk 82 charges detonated at a nominal depth of 18 m. The sonobuoys used in the experiment was modified AN/SSQ 41B with a sensitivity reduction of 40 dB. In cases of overloading and low signal to noise levels the results are discarded from the analysis. Propagation loss between each detonated charge and the four receiving sonobuoys has been computed in 1/3 octave frequency bands from 12.5 Hz to 3150 Hz and then normalized to 1 Hz. Details of the data recording, calibration and processing algorithms are given in a data report (Engelsen, 1993a). Analysis of data is presented in Chapter 5.

5. Acoustic propagation experiment and numerical simulations.

5.1 Introduction.

Ambient noise depend on sound propagation conditions. Therefore the specific objective of this chapter is to

Investigate broad band sound propagation in shallow water MIZ.

In the first part of this chapter broad band propagation loss data from the Barents Sea during SIZEX 92 will be analyzed and related to environmental conditions. The calculated losses are compared to standard geometrical loss models and to a propagation loss experiment in the interior Arctic reported by Diachoke (1976). The frequency domain considered ranges from 10 Hz up to 5000 Hz.

Based on oceanographic data obtained at the same time and in the same region as the acoustic experiment a simple range independent physical model is constructed. The physical model includes six homogenous layer; vacuum, ice, two water layers and two bottom layers. This environmental model is used as input to the multi-layered range independent acoustic propagation model OASES (version 2.1) (Schmidt, 1997). As a first step to study the sensitivity of changing ice and ocean parameters on acoustic propagation, the OASES model have been run for different ice thickness and surface duct depths. The model output used here is reflection losses as function of grazing angle and frequency, transmission loss as a function of range and depth at selected frequencies, and transmission loss as a function of frequency and range. Scattering from the ice cover or sea floor is not included in the numerical study.

5.2 The acoustic transmission loss experiment.

The experiment area is shown in Figure 5.1, where the location of ordinary and desensitized sonobuoys, detonation positions of the SUS charges, CTD section and AXBTs are plotted. In addition a SAR scene covering 100X 100 km^2 obtained on March 5, 1992 is superimposed on the map, showing the ice edge, and ice types. SUS charges number **2, 3** and **4** are located within the compact ice cover whereas number **5, 6, 7,** and **8** are deployed along the ice edge. The rest of the charges were deployed along a north-south line out to a distance of 56 km from the ice edge. The listening desensitized sonobuoys were number **D-24** and **D-22** in open ocean, **D-5** (just outside the ice edge), and **D-21** in compact ice. The experiment includes propagation paths in different ice-ocean regimes, 1) paths totally within the interior compact ice region, 2) paths from the interior ice pack to the diffuse ice edge zone, 3) paths from the interior ice pack to the open ocean and finally 4) paths completely in open ocean. These four paths make it possible to compare the effect of ice cover, ice edge and the open ocean on the propagation loss.

5.2.1 The environmental description of the experiment area.

The experiment was located in an area where the water depth increases from 200 m in the ice edge region in north to 300 m at the distance of 100 km south of the ice edge. The depth contours are shown in Figure 5.1. The bottom conditions are generally characterized as bed rock with 50 % coverage of sandy gravely mud (Elverhøi and Solheim, 1983, Solheim and Kristoffersen, 1984).

Based on the ice conditions obtained from the SAR image the experiment area can be divided into a open ocean part, south of 77° 03´ N, diffuse ice edge zone south of 77° 11´ N and a compact ice zone of small floes, between 77° 11´ N and 77° 35´ N. An interior zone with consolidated ice with large floes is found North of the compact ice zone. The diffuse ice edge zone outside the main ice edge consists of new frozen ice, grease ice formed during the previous night and pancake ice which can be a few days old. The 30 - 40 km wide compact ice edge zone inside the main ice edge consists of broken up first year ice floes with a diameter of 10-100 m (Johannessen et al., 1993b, Sandven et al., 1993b). The ice thickness measurements showed that the individual level ice floes could be typically 2 m thick while the real thickness could be more than 4 m in rafted areas, i.e. one floe is located on top of another. The interior ice zone is characterized by leads, multiyear ice floes and consolidated first-year ice. The leads have usually a dark signature in SAR images due to the low back-scatter from smooth new frozen ice which is typical in the winter time. If the leads are ice free they appear bright in the SAR images under influence of wind, which generates small surface wave and thereby increases the backscatter returns. A blow up of the SAR image of 5 of March is shown in Figure 5.2 for the region where **BT 7** was dropped and Håkon U. Sverdrup P R/V was located on March 6. The SAR image shows a relatively homogeneous signature of around 280 m long surface waves penetrating into the ice from the open ocean. The day after the SAR image was obtained, calm winds of 2-4 m/s from north was observed indicating a low sea state. Aerial photos from 6 March showed a smooth sea surface with no breaking of waves but with a significant long-wave pattern.

Speed of sound fields calculated from CTD sections obtained on 5-6 March are shown in Figure 5.3 a. According to the CTD section and open ocean AXBT´s deployed 6 March a strong 50-100m deep surface duct is present outside ice edge with weak horizontal gradients. The **BT 7** dropped in open sea close to the main ice edge shows a surface duct depth of 25 m, while another AXBT (**BT 4**) located approximately 40 km into the ice pack has a duct depth of 100 m, Figure 5.3 b. Other experiments, for example in MIZEX 87, have shown generally stable surface ducts within the ice pack suggesting that the shallow duct found close to the ice edge can be associated with an ice edge front.

5.2.2 Acoustic propagation analysis

The propagation study is based on the experiment on 6 March 1992 where sound emitted from 11 SUS charges was recorded by 4 desensitized sonobuoys, Figure 5.1. The data analysis is concentrated to two of these buoys: **D-5** located near the ice edge and **D-21** located about 45 km into the ice pack. The propagation loss have been plotted as

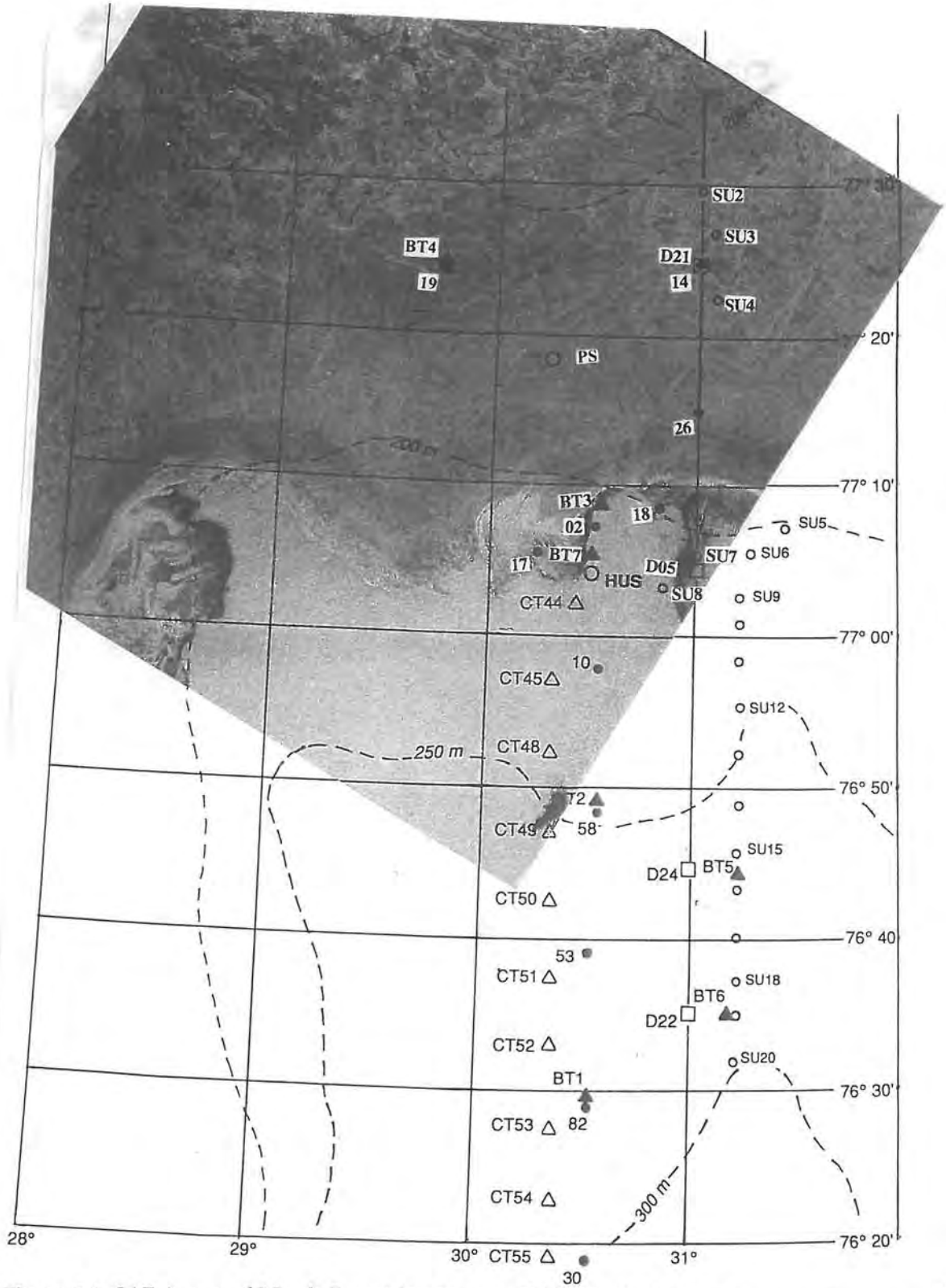

Figure 5.1. SAR image of March 5 covering an area of 100 by 100 km. Locations of ... ships, and other devices are indicated:

- ordinary sonobuoys
  desensitized sonobuoys
Δ CTD Stations by Håkon Mosby R/V
° Location of Håkon U. Sverdrup R/V and Polarsyssel R/V March 6.

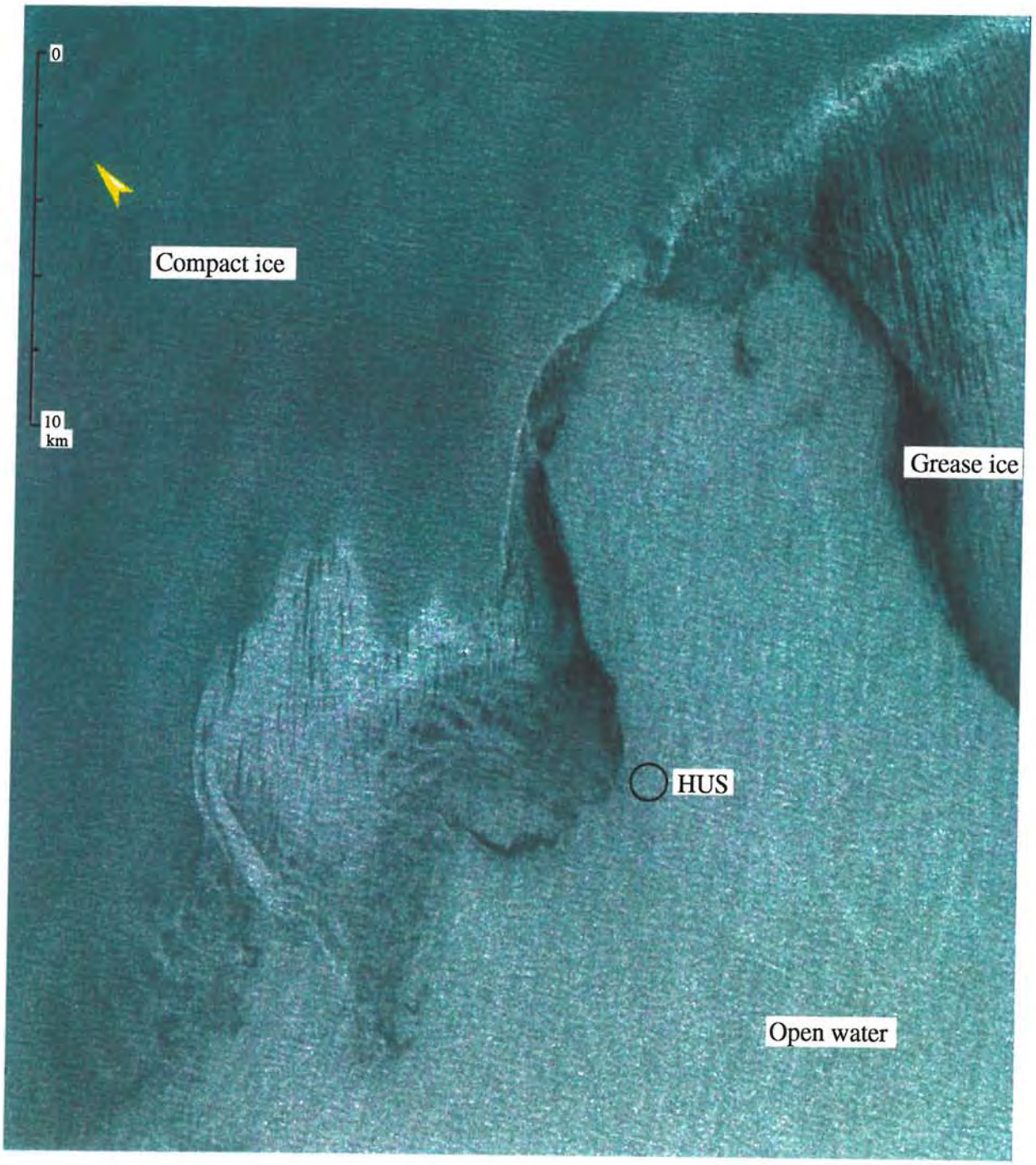

Figure 5.2. Blow up SAR image in Figure 5.1 in the region around the position of Håkon U. Sverdrup R/V.

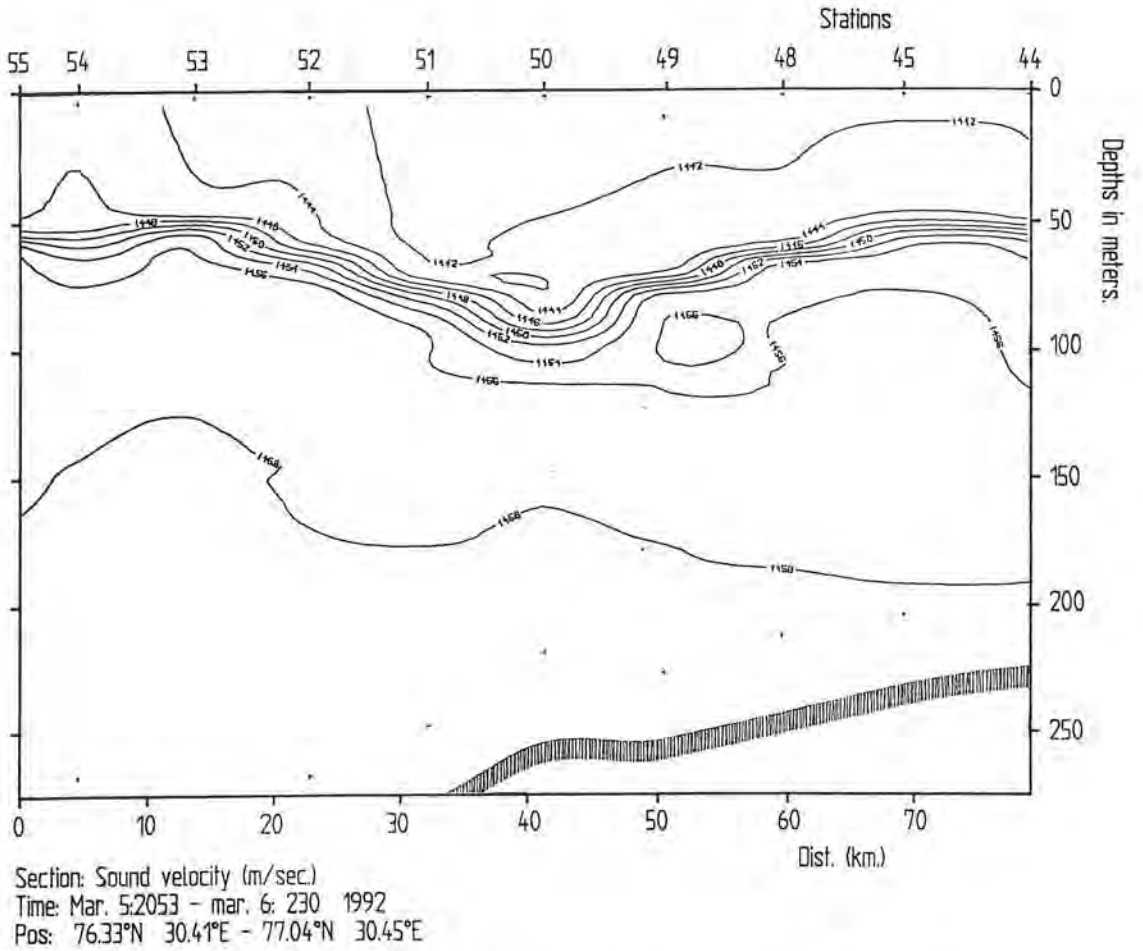

Figure 5.3. a) CTD section obtained by Håkon Mosby normal to the ice edge on March 5-6.

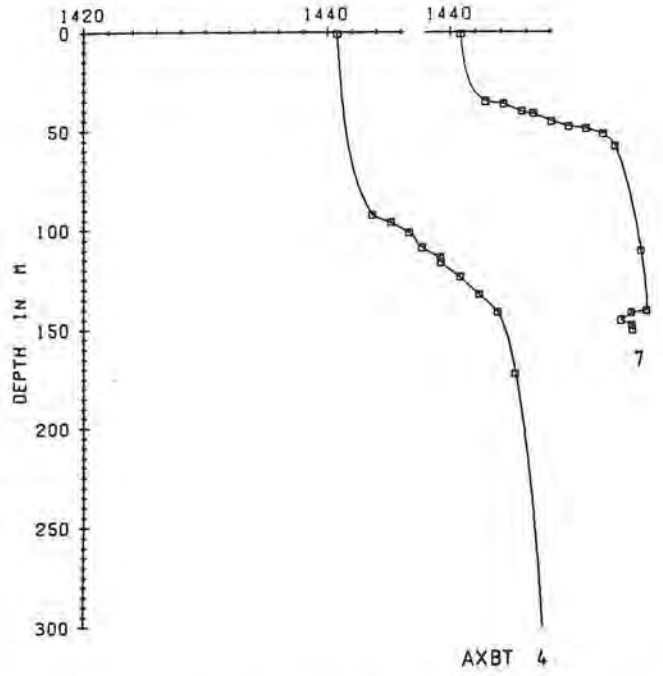

Figure 5.3. b) AXBT, March 6. BT 7 obtained close to the ice edge and BT 4 obtained 40 km into the ice pack.

function of range at five selected frequencies and as a function of frequency at different ranges. The losses are given in dB relative to source levels for SUS Mk 82 at 18m detonation depth (Engelsen, 1993a) normalized to 1 Hz frequency bands.

5.2.2.1 Propagation loss at selected frequencies.

In Figure 5.4 and 5.5 the propagation loss between the array of SUS charges and each receiving sonobuoy has been plotted as a function of range for five selected frequencies 31.5, 100, 315, 1000, and 3150 Hz. The receiving sonobuoy is located at zero range, and the distances to the SUS charges are given in km. The transmission loss is compared to geometrical spreading given as

$$I(R)=-kLog_{10}(R)=-kLog\ R \qquad 5.1$$

where k=20 for spherical spreading in free space and k=10 for cylindrical spreading loss in a acoustic waveguide. Range R is in meters.

The observations at sonobuoy **D-5** (Figure 5.4), which is located 12 km from the ice edge in open ocean, can be described as follows: At 31.5 Hz the short range propagation follows a spreading law close to 16 Log (R) curve, while at longer ranges above 35 km,

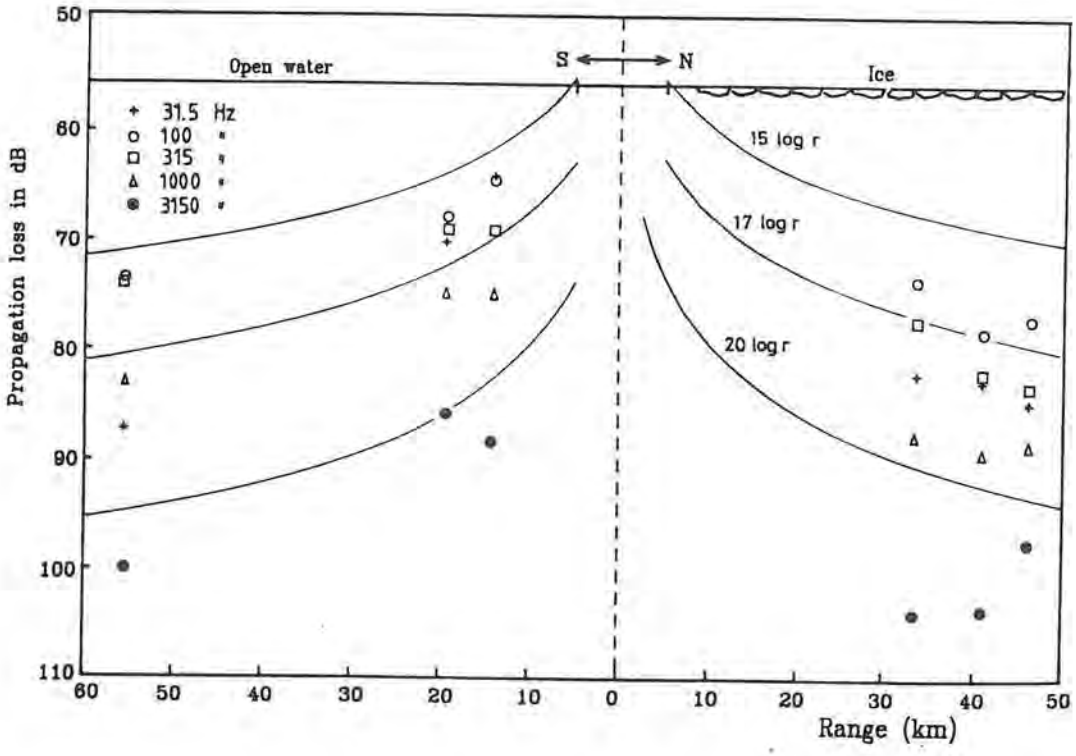

Figure 5.4 Propagation losses measured at buoy **D-5** have been plotted as a function of range for five selected frequencies 31.5, 100, 315, 1000, and 3150 Hz. The receiving sonobuoy is located at zero range, and the distances to the SUS charges are given in km. Spreading law curves for 15, 17 and 20 times Log (R) is included for comparison.

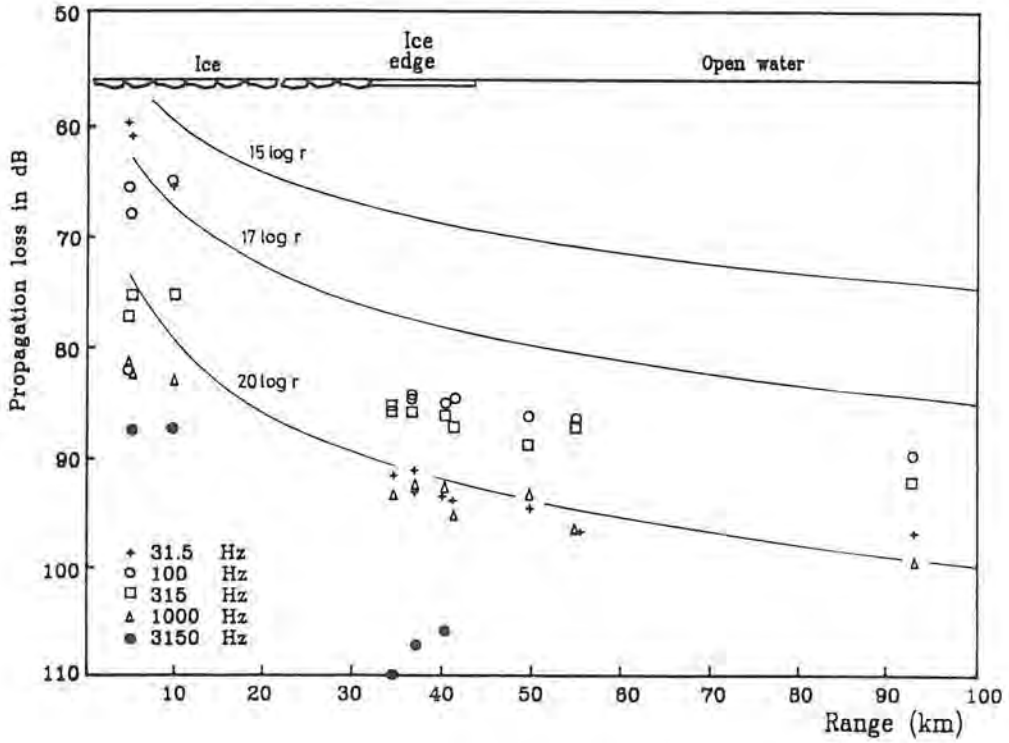

Figure 5.5 Propagation losses measured at buoy **D-21** have been plotted as a function of range for five selected frequencies 31.5, 100, 315, 1000, and 3150 Hz. The receiving sonobuoy is located at zero range, and the distances to the SUS charges are given in km. Spreading loss curves for 15, 17 and 20 times to the range is included for comparison.

the transmission loss increases to follow a 18 Log (R) curve. This is seen both for open water path and for the partly ice covered path (Figure 5.4). For 100 Hz and 315 Hz the propagation loss corresponds to a spreading law of 16 to 17 Log (R) when the propagation path is in open water. If the propagation path is partly or completely under the ice the propagation loss is slightly stronger, corresponding to a spreading law of 16 to 18 Log (R). At 1000 Hz the transmission loss curve is between 17 to 18 Log (R) in open water and just above 20 Log (R) within the ice. At 3150 Hz, the propagation loss follows a curve just below 20 Log (R) outside the ice edge, while it is well below the 20 Log (R) curve within the ice pack.

In Figure 5.5 the listening sonobuoy (**D-21**) is located 45 km into the ice pack from the ice edge, implying that the acoustic propagation is partly under ice and partly in open ocean. At short ranges (less than 20 km) the smallest propagation loss is at 31.5 Hz following a curve close to 17 Log (R). The transmission loss increases gradually with frequency to be below the 20 Log (R) curve at 1000 Hz and 3150 Hz. At long ranges the smallest losses is seen at the mid frequencies (100 and 315 Hz), which follows a curve close to 18 Log (R). At 31.5 Hz the transmission loss increases, compared to the short ranges, to follow a 20 Log (R) curve for ranges greater than 35 km. At 1000 Hz the transmission loss follows 20 Log (R) curve, while at 3125 the transmission loss measured is well below the 20 Log (R) curve.

The main result of the observations is that the presence of ice increases the transmission loss at all the selected frequencies, except at 31.5 Hz. On the other hand the 31.5 Hz has significant stronger transmission loss in the far field than in the near field independent of ice or no ice. This is interpreted to be a filtering of low frequency sound at long ranges caused by bottom interaction. Above 315 Hz, the attenuation increases with frequency in all regions, but strongest in the ice covered regions indicating a filtering of the higher frequencies due to the ice cover. Observations shows that the presence of relatively shallow water and presence of ice favors the long range propagation at 100 and 315 Hz.

5.2.2.2 Optimum frequencies

Propagation losses has been plotted in Figure 5.6 and 5.7 as a function of frequency for each shot as recorded **D-5** and **D-21**, respectively. The plots includes indication of shot no for each curve. Table 5.1 gives the distance between shot and receiving buoy, and a brief description of the surface conditions along the path.

Table 5.1. Distance between shot and receiving buoy. In addition a general description of ice condition along the path is given.

Shot number	Ice condition at SUS drop position	Receiver D-5 Distance[km]/Type	Receiver D-21/ Distance/Type
2	SUS within compact ice	46.3 /ice	9.8 /ice
3	SUS within compact ice	40.8/ice	4.6 /ice
4	SUS within compact ice	33.4/ice	5.0 /ice
5	SUS close to ice edge		34.6 /ice
6	SUS close to ice edge		37.0 /ice
7	SUS close to ice edge		37.0 /ice
8	SUS close to ice edge		40.4 /ice
9	SUS in open water		41.3 /ice & open water
11	SUS in open water	14.3 /open water	49.8 / ice & open water
12	SUS in open water	19.5 /open water	55.2 / ice & open water
19	SUS in open water	55.9/open water	93.0/ ice & open water

These curves gives information about optimum frequencies for different ranges, and ice conditions in a shallow water region; showing a clear minimum in propagation loss in the frequency range 80 to 400 Hz in for the longest propagation paths either they are in open water or in ice. Larger losses are observed at frequencies below 80 Hz and the losses increases strongly with frequencies above 400 Hz. Only at a very short range the optimum frequency is shifted down to the region below 100 Hz as shown by the SUS charges no **11** and **12** at **D-5** and **2**, **3**, and **4** at **D-21**. In other words the optimum frequency is below 100 Hz at short distances (less than 20 km) and between 100 and 400 Hz at longer distances (more than 20 km). This show that the strongest effect on optimum frequency is the distance to travel either it is in open water or in ice covered regions.

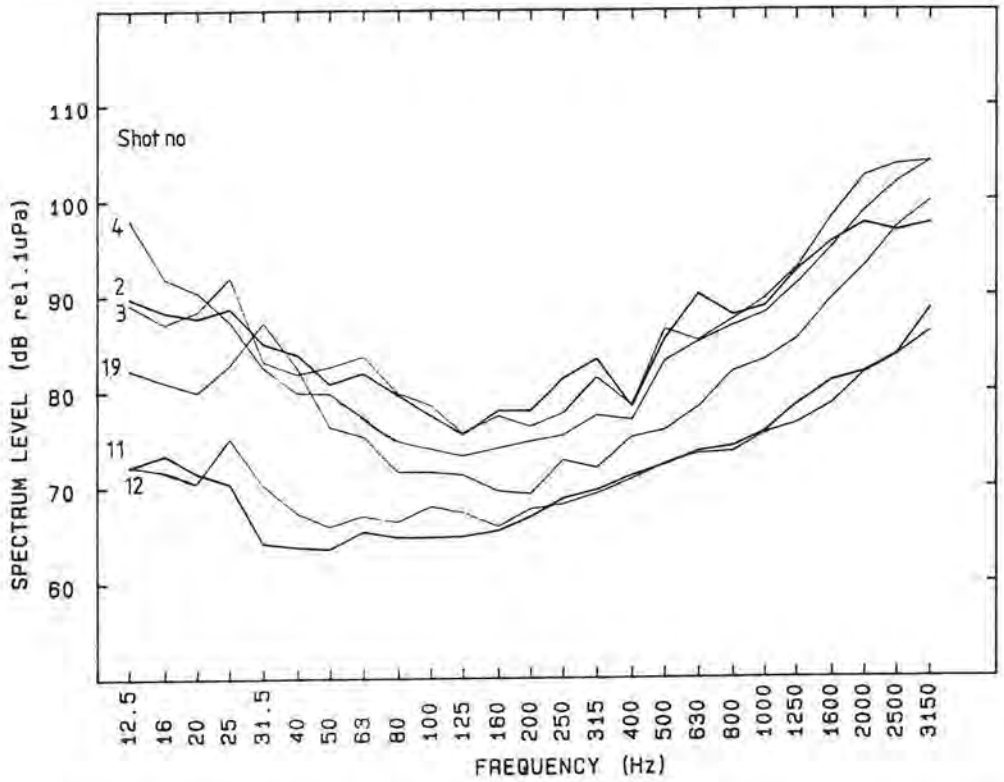

Figure 5.6 Propagation losses measured at buoy **D-5** plotted as a function frequency for each shot. Curves corresponding to shot number 2,3,4 have a propagation range between 33 and 46 km. Shot number 19 have propagated 56 km, and 11 and 12 have propagated less than 20 km.

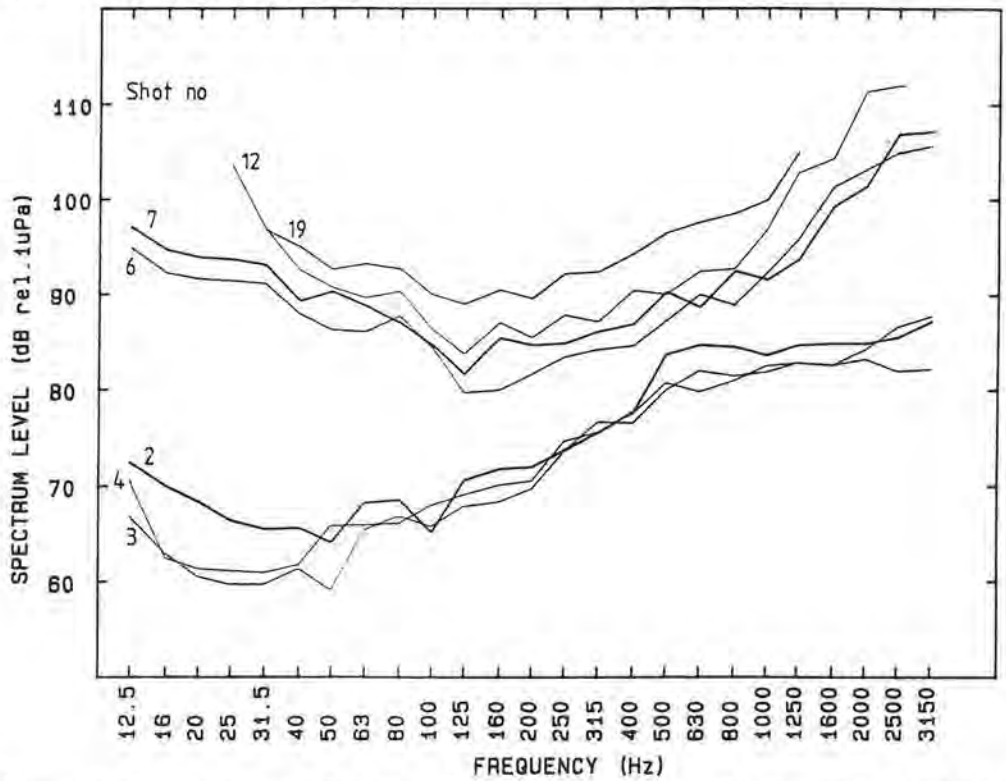

Figure 5.7 Propagation losses measured at buoy **D-21** plotted as a function frequency for each shot. Curves corresponding to shot number 2,3,4 have a propagation range less than 10 km. Shot number 5,6,7,8,9,11 have a range between 35 and 55 km. Shot number 19 have propagated 93 km.

The effect of ice and no ice is observed in Figure 5.6. Shot **19** have a 55.6 km long path in open water to reach **D-5** , while shot **2-4** have path length between 33-46 km generally under compact ice. Despite the longer path to travel the shot **19** is around 2-5 dB less attenuated at all frequencies than the paths within the ice pack. This shows that the filtering effect of the ice cover is present at all frequencies.

The long range propagation loss and the short range propagation loss measured at **D-21** have a very different frequency dependency. At short ranges the attenuation increases as $f^{1.7}$ between 50 and 500 Hz, above 500 Hz the attenuation reaches a maximum and is almost constant with increasing frequency. For long ranges the attenuation is reduced as $f^{-1.5}$ up to 125 Hz. Between 125 and 600 Hz the attenuation is increasing as $f^{1.1}$. At 600 Hz the slope increases and the attenuation increases as $f^{5.7}$. The main difference except from the difference in range is that the short range is propagating in one type of ice regimes, while the longer range section travels through ice free regions and through regions with increasing ice thickness. The kinks in frequency dependence is not observed at **D-5**.

5.2.3 Discussion of Results.

Both source and receivers in the above experiment is positioned within the 50-100 m deep surface channel which is present both within the ice pack and outside the ice edge. Therefore it is expected that the attenuation at low frequencies are caused by leakage out of the duct and bottom interaction. Sound at higher frequencies is trapped within the surface duct and therefore assumed to be more sensitive to changes in the surface conditions either through scattering or reflection losses.

5.2.3.1 Optimal propagation frequency

Previous investigations have shown that the optimum frequency for deep water regions of the Arctic is around 20-40 Hz, whereas for propagation in shallow water (60 m) in the Barents sea it is reported an optimum frequency at around 200-400 Hz (Jensen, et al. 1994 pp. 31). Our study shows that for the intermediate water depths (200-300m) the optimal frequencies is found to be between 80-400 Hz within the surface duct. The increase in water depth have extended the optimum frequency domain to lower frequencies compared to the shallow water, which indicate significant bottom interaction at frequencies below 80 Hz in intermediate water depths. In the SIZEX 92 data a strong increase in losses with frequency is observed above 400 Hz in intermediate waters, this is also observed in shallow water (Jensen et al, 1994). This corresponds to a high frequency filtering due to reflection and scattering losses from the ice cover or rough sea surface.

5.2.3.2 Comparison of MIZ results to observation in the interior Arctic.

The transmission loss (TL) can be separated into two parts

TL=TL(geometric)+ TL(losses)

The first part includes geometrical effects like reflections and leakage from surface ducts, while the other includes absorption, scattering and other non geometrical effects. Commonly the transmission loss data are corrected for cylindrical spreading loss expressed by (10 Log (R)), where R is the distance from the source, when estimating the attenuation coefficient.

This was done by Diachoke (1976) in a experiment similar to SIZEX 92 performed in the interior of the Arctic. As in our experiment the concept of SUS charges, hydrophones and recording aircraft where used. Furthermore, the processing and presentation of the transmission loss data is apparently identical to ours. The main differences between the two experiments are the environmental conditions in the interior Arctic versus the MIZ, and the longer paths, up to 300 km, investigated by Diachoke. The attenuation coefficient above cylindrical spreading, calculated by Diachoke was between 0.1 and 0.3 dB/km for frequencies between 100 Hz up to 1000 Hz. The result at 100 Hz obtained by Diachoke compares well to numerical calculations of losses due to scattering at 100 Hz performed by Fricke (1991,1993). This indicates that cylindrical spreading models the geometrical losses fairly good for the interior Arctic.

The results presented in Table 5.2 are derived from the SIZEX 92 data by subtracting 10 Log (R)(expressed in m) from the transmission loss data and divided by the range in R (expressed in km). The attenuation expressed in dB/km range from 0.43 to 1.19 are more than twice the attenuation found by Diachoke, (1976). According to Table 5.2 the losses are largest for sound transmitted from SUS 8 detonated at the ice edge propagating 40 km into the ice pack. By increasing the portion of open water along the transmission path the loss/km is reduced significantly at all frequencies. A similar observation is made by receiver **D-5**. This again show that the attenuation of sound increases when ice is present.

Table 5.2. Attenuation expressed in dB/km where cylindrical geometrical losses is removed from the measured transmission loss. **D5,2** is loss measured at buoy **D-5** shot no **2**. **D5, 19** is loss measured at buoy **D-5** shot no **19**. **D21, 19** is loss measured at buoy **D-21** shot no **19**. **D21, 8** is loss measured at buoy **D-21** shot no **8**

Frequency, Hz	D5,2 46.3 km Ice/water	D5,19 55.9 km Open water	D21,19 93.0 km water/ice	D21,8 40.4 km ice
31.5	0.828	0.7124	0.5077	1.187
100	0.666	0.4333	0.4346	0.9687
315	0.791	0.4505	0.4604	1.0009
1000	0.910	0.6408	0.5410	1.172
3150	1.098	0.7871	--------	1.632

Figure 5.4 and 5.5 clearly show that the cylindrical spreading (10 Log (R)) underestimates the transmission loss observed in the MIZ during SIZEX 92. The use of cylindrical spreading is equivalent to the assumption of propagation in an ideal wave guide. The environment in the MIZ is very different from an ideal wave guide. In order to calculate the attenuation coefficient in dB loss/km, whiteout including

In order to compare the results to Diachoke's numbers for the interior Arctic only sections covered mostly by ice are considered, i.e. section **D5,2** and **D21,8**. The best fit attenuation coefficients range from 0.003 to 0.089 in the frequency domain from 100 Hz to 1000 Hz. These coefficients (Table 5.3) are significantly smaller than the attenuation coefficients obtained in the interior Arctic region. This suggest that the ice cover in the MIZ introduces less loss/km due to scattering than the interior ice cover in the range from 100 up to 1000 Hz. This again indicates the effect of generally smoother ice conditions in MIZ than in the interior Arctic.

On the other hand the large correction coefficients in Table 5.3.b corresponds to larger geometrical losses than cylindrical losses. This leads to the hypothesis that the large transmission losses observed in the MIZ during SIZEX 92 is generally caused by reflection losses due to the bottom interactions at low frequencies and due to interaction with the ice cover at the higher frequencies.

The attenuation coefficients generated from transmission loss data section **D5,2** and **D21,8** below 100 Hz are compared to the model simulations done by Fricke (1993) and the empirical model described by Pritchard (1990) in Figure 5.8. The frequency dependence of our data corresponds generally good to slopes in the data curve and numerical simulations of attenuation due to scattering from ice edges and fluid keel. The numerical values obtained by **D5,2** compares best to the other experiments, while the **D21,8** have a larger attenuation. This indicate that the scattering effect of the ice in the MIZ is similar or higher to the scattering effect in the Arctic below 100 Hz.

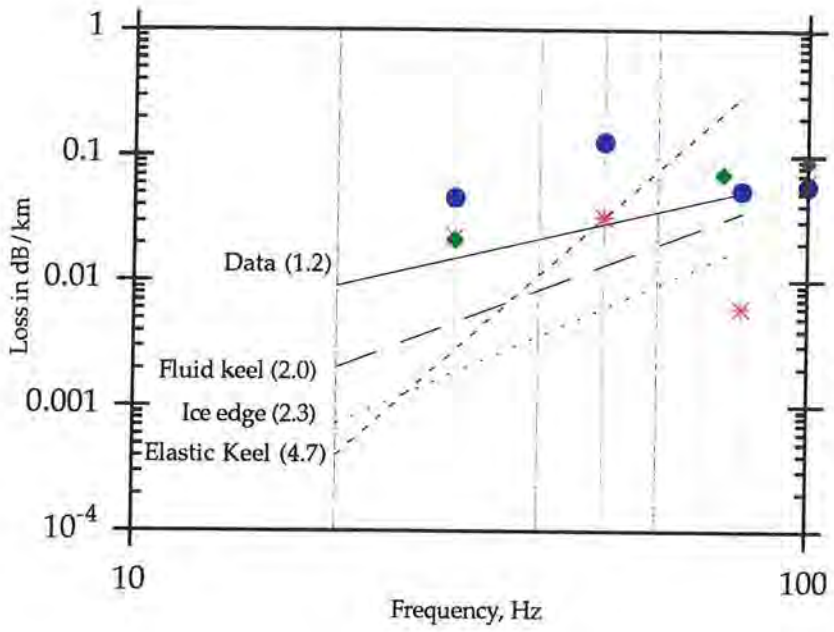

Figure 5.8. Black lines (dotted and dashed) corresponds to model simulations by Fricke, 1993. Black full line corresponds to data obtained by Mellen (see Fricke, 1993). The green marks corresponds to estimates using transmission loss formulas (Pritchard, 1990) for three meter thick ice. Red is data generated by the **D5,2**, blue is generated from **D21,8**. These tracks are generally covered by ice.

geometrical effects, requires a model which takes into account the range dependent reflection coefficients for surface and bottom boundaries, as well as horizontal stratification and variations in range for the water layer.

Another approach is first to find the kLog (R) best fit curve to the measured transmission loss data in Figure 5.4 and 5.5 . Then the attenuation coefficient is found by subtracting the best fit curve from the transmission loss data and thereafter divide by range in kilometers. The attenuation coefficients found by using this approach are presented in Table 5.3 a, and the k factors used in the calculations are shown in Table 5.3 b.

Table 5.3. a)Transmission loss corrected for best fit geometrical losses.

Frequency, Hz	D5,2 46.3 km Ice/water	D5,19 55.9 km Open water	D21,19 93.0 km water/ice	D21,8 40.4 km ice
31.5	0.022	0.033	0	0.046
50	0.032	0.008	0.035	0.126
80	0.006	0.009	0.245	0.052
100	0.062	0.009	0.007	0.057
315	0.086	0.016	0.033	0.089
1000	0.003	0.046	0.007	0.030
3150	1.191	0.089	--------	0.492

Table 5.3. b) Coefficient k for best fit geometrical losses, given by kLog (R).

Frequency, Hz	D5,2 46.3 km Ice/water	D5,19 55.9 km Open water	D21,19 93.0 km water/ice	D21,8 40.4 km ice
31.5	18	18	20	20
50	17	16	18	18
80	17	15	18	18
100	16	15	18	18
315	17	15	18	18
1000	19	17	20	20
3150	19	20	--------	20

The highest coefficients are generally found for the highest frequencies O(1), while the smallest coefficients, O(0.001), are generally found at the lower frequencies for paths where compact ice covers less than half of the path. The attenuation coefficient in Table 5.3 a have the lowest values for the open ocean path (**D5,19**) and it increases as the ice coverage increases to be highest for **D21,8** which is a path totally covered by ice. This seems reasonable. Small attenuation coefficients indicates that most of the losses is caused by the geometrical effects. Large attenuation coefficients indicate that either is the propagation model underestimating the geometrical effects or large losses are introduced by the environment.

trapped within the duct and repeatable interacting with the ice cover. At long distances, after several bounces, the sound has been exposed to several reflection losses and scattering losses. In this study the scattering effect is eliminated by using smooth surfaces, and only the characteristics of specular reflection is included. The reflection loss is defined as

RL=-20 Log $|R_c|$, where R_c is the complex plane wave reflection coefficient.

The reflection loss have been calculated as a function of grazing angle (angle relative to the horizontal) and frequency for 3m, 2m, 1m and 0.5 m ice thickness. The results are plotted in Figure 5.9, where the white color corresponds to close to total reflection. The reflection loss function with respect to grazing angle depends strongly on the frequency. Furthermore, the plots reveals a strong sensitivity in the reflection coefficient function with respect to frequency to changes in ice thickness. Thinner ice moves the hole reflection loss pattern towards higher frequencies whiteout any other changes. Below a given frequency ($f_{r,c}$ in Table 5.5), increasing with decreasing ice thickness, the reflection is total at all angles, while above this frequency the losses are introduced at a relatively narrow angle interval close to critical angle of compressional waves. The reflection loss is due to the transmission of acoustic energy into compressional shear wave in the ice cover. Then in a frequency band (f,F in Table 5.5), dependent on ice thickness, the reflection loss increases rapidly for a very broad range of angles down to a minimum grazing angle between 10^0-20^0. This corresponds to transmission of acoustic energy into elastic shear waves in the ice cover. The frequency domain is switched towards higher frequencies as the ice thickness is reduced. Above the upper limit of this frequency domain the reflection loss function is more or less constant with respect to frequency. Total reflection occurs at all frequencies for grazing angles less than 10^0 in all cases. Therefore the reflection coefficient indicates a filtering of rays steeper than a given angle.

Table 5.5. The effect of increase in ice thickness on reflection losses based on Figure 5.9. Surface duct 50 m.

Ice thickness	$f_{r,c}$ [Hz]	f [Hz]	F [Hz]
3.0 m ice	60	160	400
2.0 m ice	80	250	660
1.0 m ice	200	460	1320
0.5 m ice	398	891	2818

5.3.2 Transmission loss.

In this section the transmission loss for single frequencies are plotted as a function of depth and range. The same material parameters as above (Table 5.4) are used during the simulations. First four selected frequencies are studied for 2 m ice overlaying a 50 m deep surface duct. Next the depth of the surface duct is varied and finally the effect of changing ice thickness is investigated.

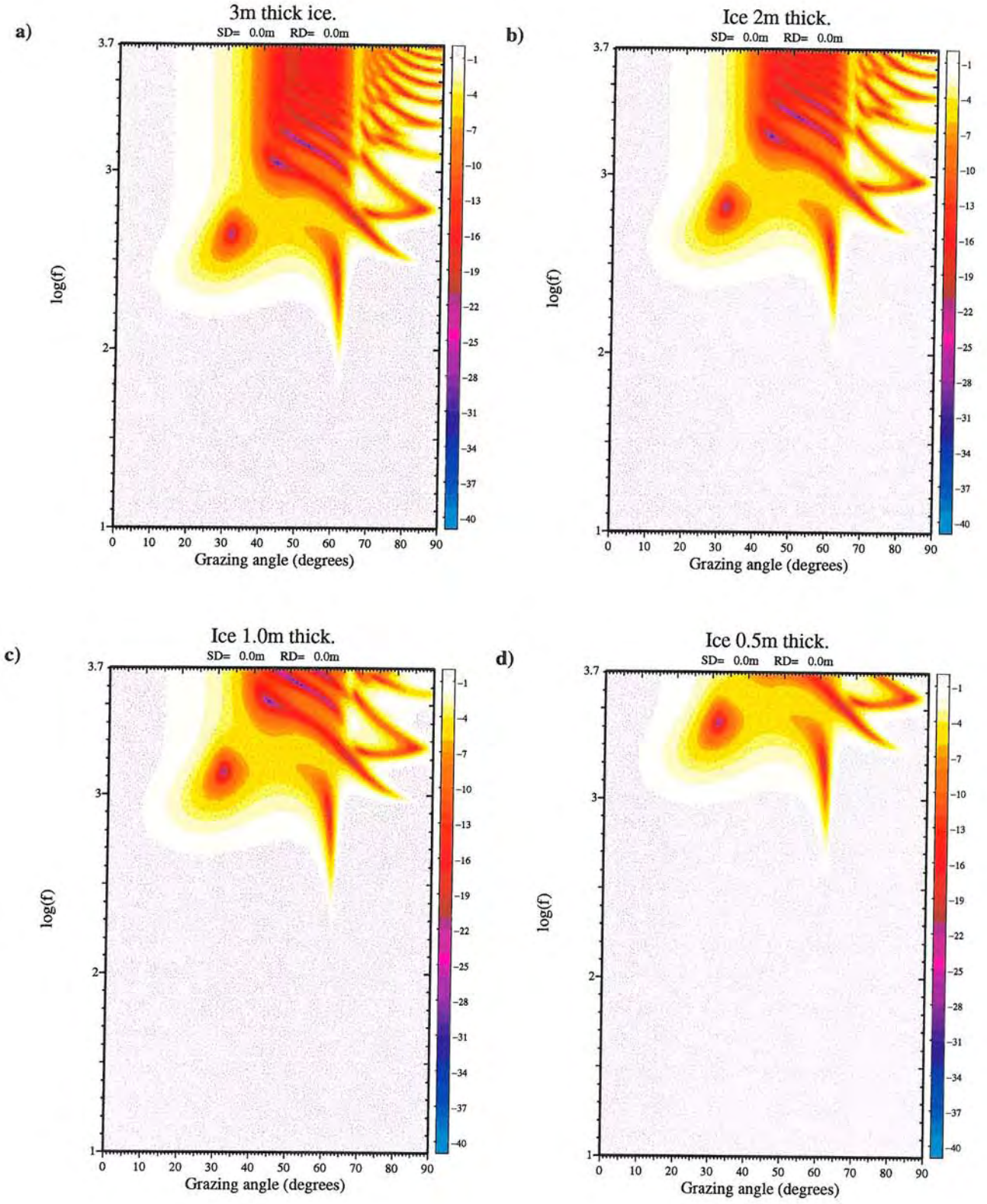

Figure 5.9. Reflection loss calculated by using OASES model for varying ice thickness a) 3m, b) 2m, c) 1m, d) 0.5 m. Material parameters are given in Table 5.4.

5.3.2.1 Transmission loss at selected frequencies.

In Figure 5.10 the frequency is varied for an environment including 2m ice and 50 m

At 100 Hz, the wavelength is 14.4 m within the surface duct, trapping of sound in the surface duct is significant, at the same time as leakage out of the duct and bottom interaction is still significant. The trapped sound within the surface duct interacts strongly with the ice cover, which according to the reflection loss calculations causes small losses in a narrow interval of angles. This corresponds to a combined filtering process dominated by bottom interaction, but also influenced by the interaction with the ice cover. At 315 Hz, wavelength 4.6 m, the bottom interaction is limited to the first 20 km, and the compressional wave in the bottom layer dies out within 10-20 km range. The sound is now very trapped in the surface duct, and the reflection loss has become significant at this frequency. Therefore, the loss within the surface channel is larger than at 100 Hz. Interference pattern due to reflection from the ice cover becomes apparent at this frequency. This is because the sound arrive the acoustic farfield at a shorter range where rays steeper than 10^0 are considerably filtered both by leakage and by reflection losses. By increasing the frequency further, up to 800 Hz, the propagation in the surface duct is characterized by clear convergence and shadow zones from 20 km range. The transmission loss in the surface duct is considerably larger than at the lower frequencies due to the increased reflection loss pr bounce. The sensitivity to surface duct depth.

Keeping the frequency at 800 Hz the effect of increasing the surface duct from 25 m to 50 m and 100 m is studied (Figure 5.11).The ice thickness is kept equal to 2 m, and thereby no changes in the reflection coefficient is made. The rays of steep angels leaks out of the surface duct, whereas the rays with less steep angles are trapped within the surface duct suffering reflection loss. The sound intensity within the duct is reduced at ranges less than 30-40 km as the surface duct depth increases. This is because the same amount of energy (same number of rays) is put in to the channel causing largest intensity in the shallow channel. At distances larger than about 50 km the intensity reduces faster in the shallow duct than in a deeper duct. As the duct depth reduces the number of bounces pr km increases and causing increase in the loss pr km. This effect becomes significant after a number of interactions, and therefore the increase of dampening within the channel becomes apparent at some distance from the source in the transmission loss plots.

5.3.2.2 The sensitivity to ice thickness .

In Figure 5.12 the ice thickness is reduced from 2 m to 0.5 m at 315 Hz keeping the surface duct equal to 50 m. Such a reduction in ice thickness reduces the reflection loss considerable, at 315 Hz (Figure 5.9); from significant losses to total reflection. The effect of the decreased ice thickness is a decrease in transmission loss with range at all depths,

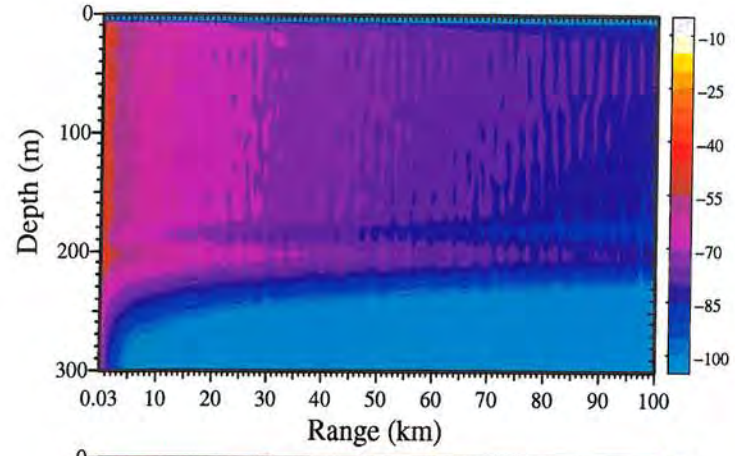

Frequency: 40 Hz

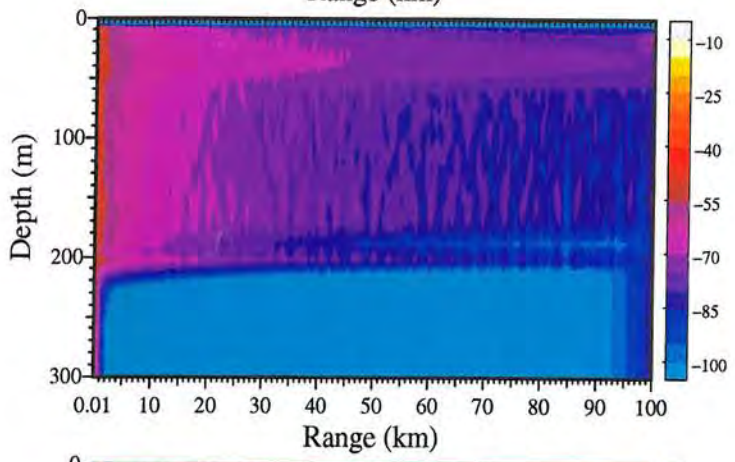

Frequency: 100 Hz

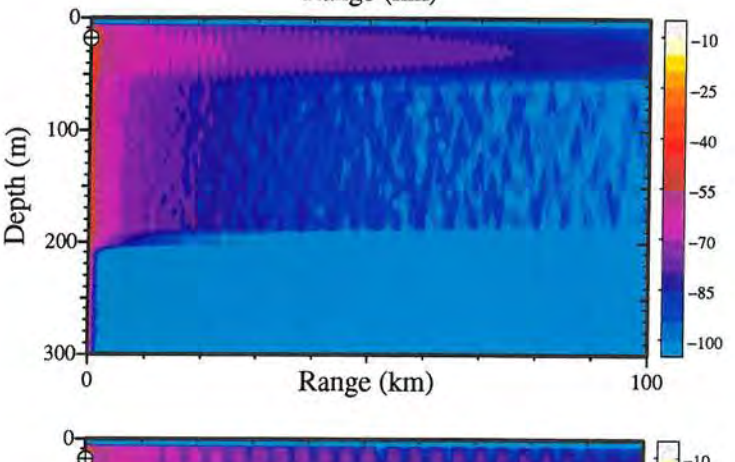

Frequency: 315 Hz

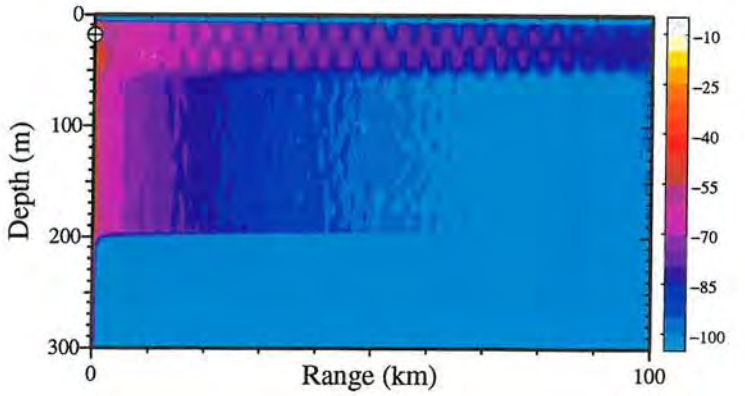

Frequency: 800 Hz

Figure 5.10 Transmission loss plotted as a function of depth and range for selected frequencies 40, 100, 315 and 800 Hz. Ice thickness is 2 m and surface duct is 50m. Material constants are given in Table 5.4.

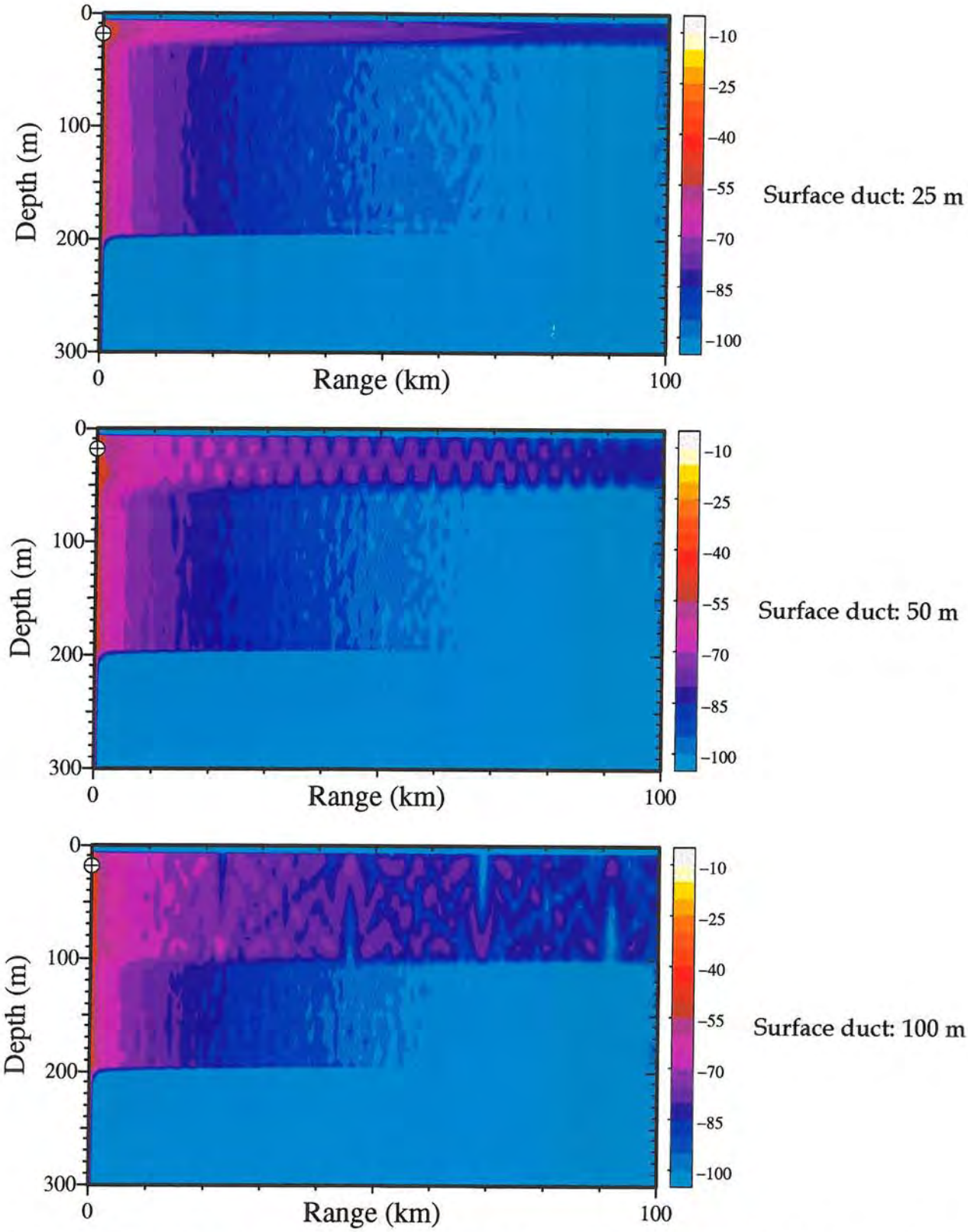

Figure 5.11 Transmission loss at 800 Hz plotted as a function of depth and range for different surface duct depths a) 25m; b) 50 m and c) 100 m. The ice is 2m thick. Material constants are given in Table 5.4.

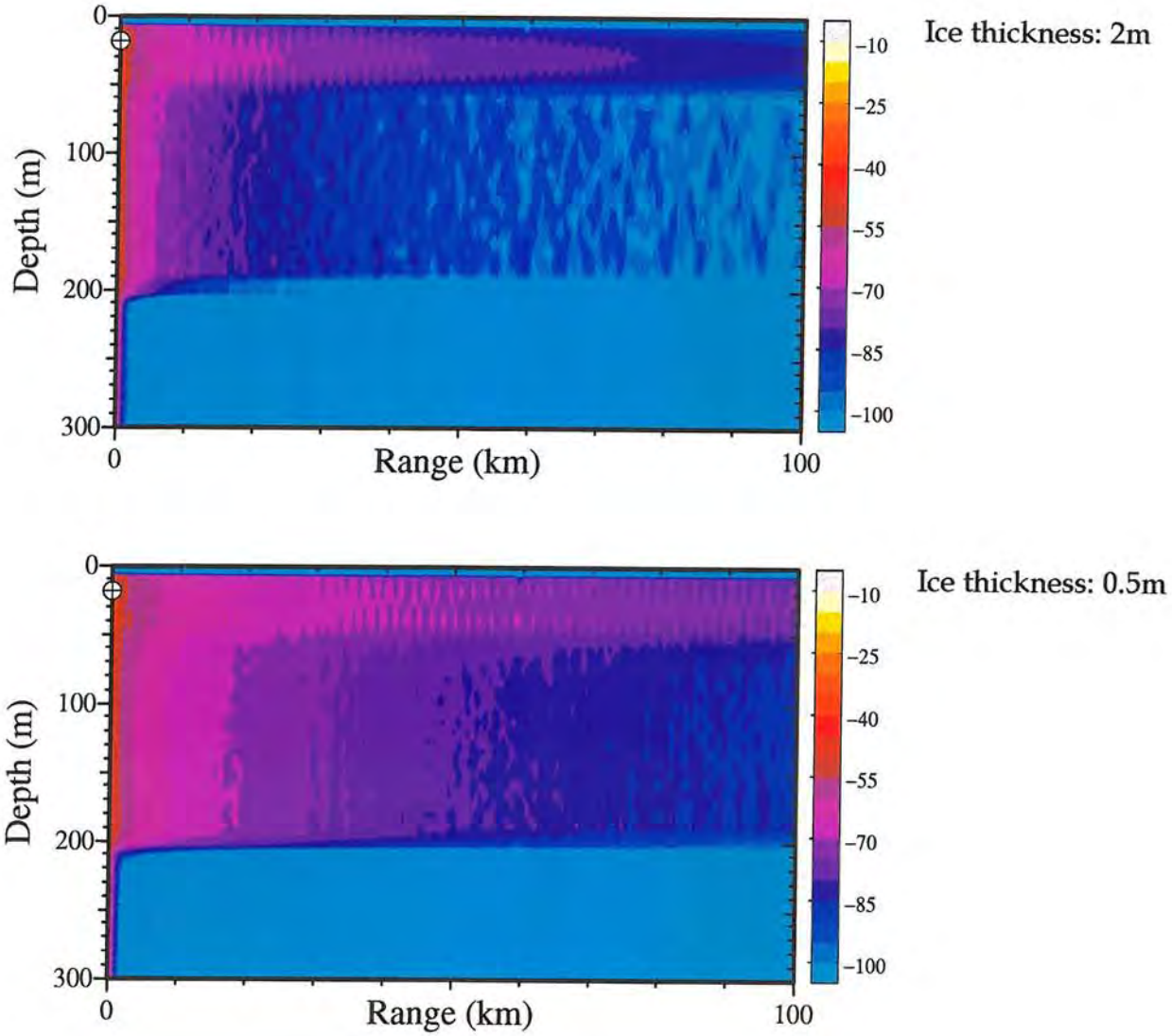

Figure 5.12 Transmission loss at 315 Hz plotted as a function of depth and range for different ice thickness a) 2 m and b) 0.5 m. Surface duct depth is 50 m. Material constants are given in Table 5.4.

both within the surface duct and below it. This is in accordance with reduced reflection loss at this frequency when reducing the ice thickness. The effect of the reduced reflection loss is reduced by increased leakage into deeper water depths where the sound suffer from losses due to interaction with the bottom. This clearly indicates the complicated competitions between the different filter processes.

5.3.3 Optimum frequency domain.

Optimal frequency can be studied by plotting the transmission loss as a function of frequency and range for selected source and receiver depths. First source and receivers are located at 18 m depth in order to study the effect of varying ice thickness and surface duct depth for receivers within the surface duct. Next step is to move the receivers below the surface duct. The material constants are given in Table 5.4.

5.3.3.1 Optimum frequency within a surface duct.

First the effect of variable surface duct depth is considered. A two meter thick ice cover is first overlaying a 100 meter deep surface duct and then a 50 m deep surface duct, Figure 5.13. The optimum frequency domain is a function of range and a clear narrowing effect with range is seen in all plots. The optimal frequency domain is in both cases limited by 40 Hz and 125 Hz at 75 km. The main effect of decreasing the depth of the surface duct is that the optimal frequency domain becomes more enhanced at the higher frequencies. This corresponds to the increased dampening at higher frequencies due to the increased number of bounces by reducing the surface duct depth.Next step was to reduce the ice thickness to 0.5 m, and thereby changing the reflection coefficient according to Figure 5.9, while the surface duct is constant, 50 m. In the case of 0.5 m ice the optimal frequency gradually narrows to 125-398 Hz at 75 km. By comparing this to the case of 2 m ice and 50 m deep surface duct it is clearly seen that the optimal frequency domain is switched towards higher frequencies as the ice thickness is reduced. This is because reflection loss is introduced at a much higher frequency corresponding to the upper limit of the optimum frequency at around 400 Hz. From this it is concluded that the effect of ice thickness (or reflection loss) have a stronger impact on the optimum frequency within the surface duct than the duct depth.

5.3.3.2 Optimum frequency below a surface duct.

As observed in the transmission plots the effect of trapping sound within the surface duct becomes very effective with increasing frequencies. Regarding to positions below the surface duct this corresponds to a low pass filtering process. In this study the sensitivity of surface duct depths on the optimum frequency below the surface duct is investigated, by considering receivers, at 60 m and surface duct depths at 50, 25 m. As expected the low pass filtering process due to the surface duct is very clear in both cases, see Figure 5.14 a,b. The optimum frequency is moved to frequencies below 100 Hz. Changes in duct depths causes small modifications at frequencies above 100 Hz. This is because more energy at higher frequencies leaks out of the surface channel and interacts with the bottom, when the duct depth is reduced.

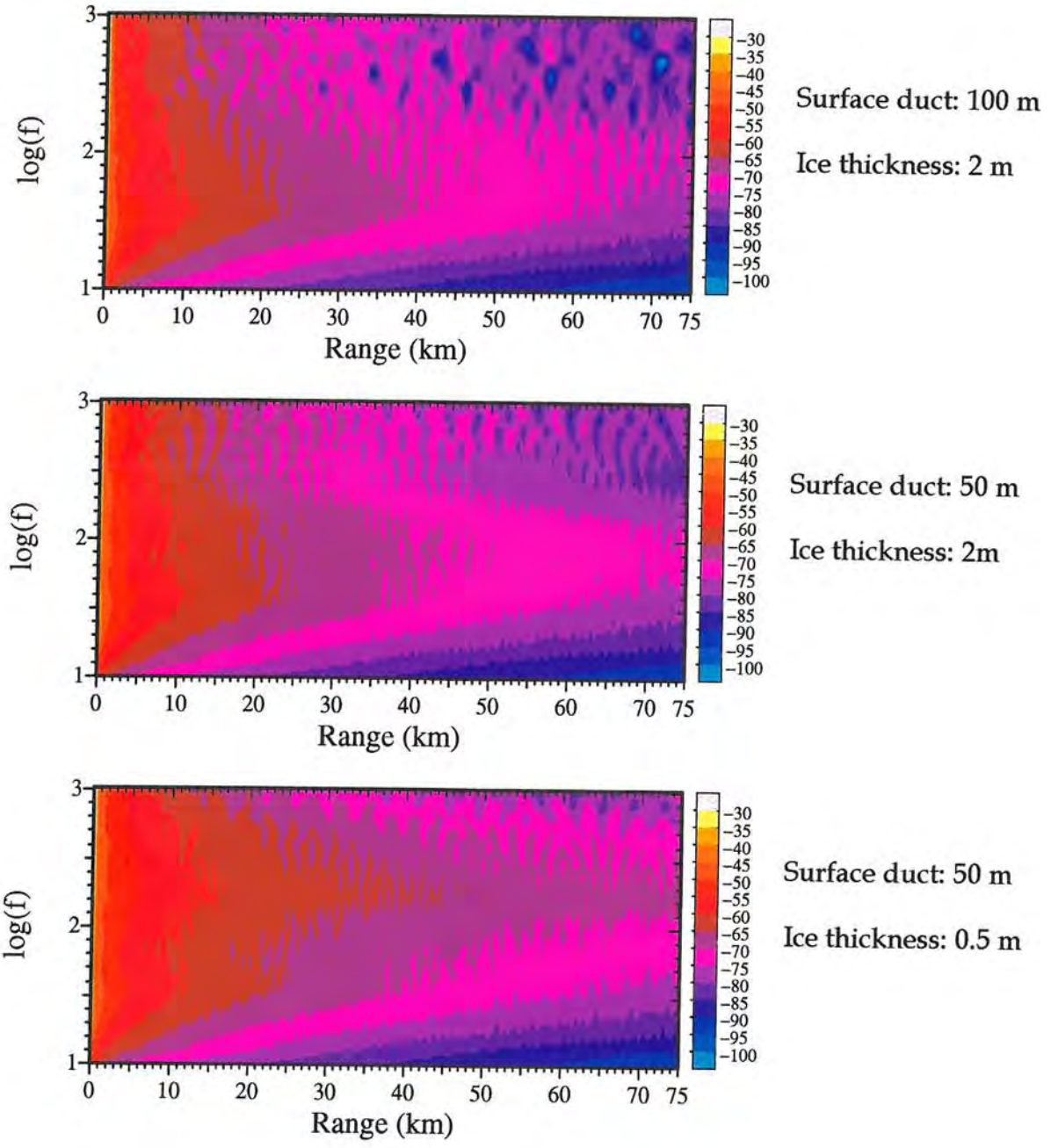

Figure 5.13 Transmission loss as a function of frequency and range for different surface duct depths and ice thickness a) 100 m surface duct, 2m thick ice and b) 50 m surface duct, 2 m thick ice, c) 50 m surface duct, 0.5 m thick ice. Receiver within the duct. Material constants are given in Table 5.4.

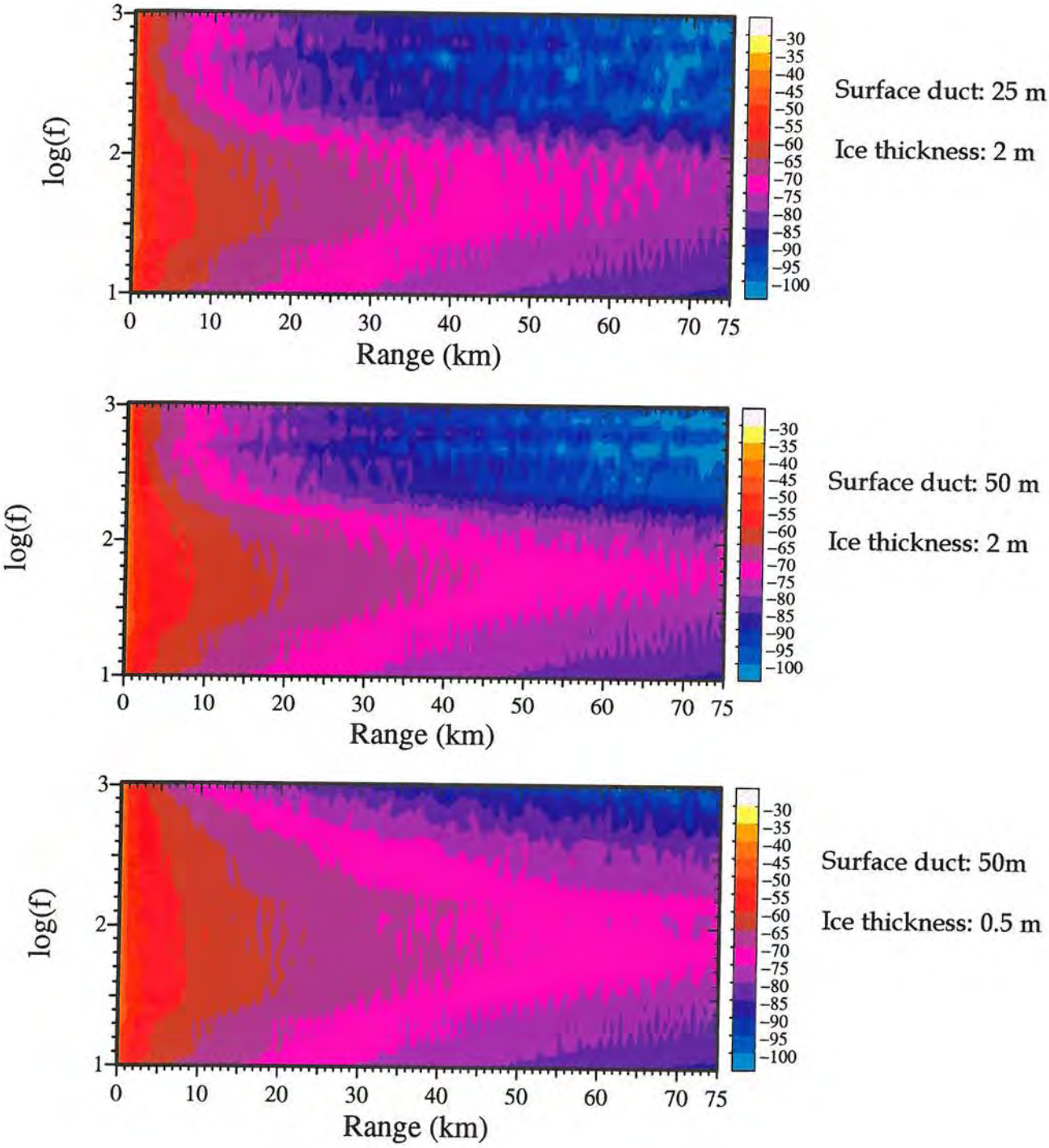

Figure 5.14 Transmission loss as a function of frequency and range for different surface duct depths and ice thickness a) 25 m surface duct, 2m thick ice and b) 50 m surface duct, 2 m thick ice, c) 50 m surface duct, 0.5 m thick ice. Receiver outside the duct. Material constants are given in Table 5.4.

In Figure 5.14 c the ice thickness is reduced to 0.5 m, the surface duct the same as in Figure 5.14 b. This causes significant changes at frequencies above the optimum frequency domain, but also within the optimum frequency domain. By reducing the ice thickness the reflection loss at the ice water boundary is significantly reduced for all the frequencies considered. The reduction of reflection loss clearly causes more acoustic energy at a higher frequency to leak out of the surface duct where it is attenuated by bottom interaction.

5.4 Summary of results.

While the transmission loss in the Arctic follows the law of cylindrical spreading (Diachoke, 1976), the losses in the Barents Sea MIZ follows a spreading law close to or stronger than spherical spreading. The large transmission losses is generally due to geometrical losses, including reflection losses, while the scattering from the ice cover seems to be less or equal to the scattering form ice depending on frequency. Scattering above 100 Hz seems to be less than in the interior Arctic, while below 100 Hz the scattering is similar to (or higher than) the scattering in the interior Arctic. Due to uncertainty in the calculation of attenuation due to scattering the numerical simulations should be used to calculate the geometrical losses to verify these results in future work.

Propagation effects as observed in the numerical simulations are summarized in Table 5.6. Sound at frequencies below a cut off frequency (domain) leaks out of the channel and interacts with the bottom and surface, causing reflection loss due to two boundaries. Higher frequency sound is trapped within the surface duct, and repeatable exposed to a angular and frequency dependent reflection coefficient at the water ice boundary. This corresponds to first a high pass filtering and then a filtering of higher frequencies due to the interaction with the ice cover. The combined effect is a band pass filter or a optimum frequency domain in the mid frequency domain (125-400 Hz). A reduction of the surface duct increases the number of interaction with the ice cover, but not enough to change optimal frequency bandwidth significantly. A reduction of the ice thickness moves the reflection losses towards higher frequencies, and correspondingly the optimum frequency domain is narrowed and switched towards higher frequencies.

Underneath the surface duct the optimum frequency domain is below 100 Hz. Filtering of sound at frequencies above 100 Hz is caused by the surface duct but intensity of leakage from the surface duct to the underlying waterlayer is regulated by the ice thickness. The simulations indicates that the duct depth seems to be less important for positioning the optimum frequency domain than the ice thickness. The bottom interaction is important for the frequencies that leaks out of the duct, so it is important to do similar simulations for the bottom as for the ice cover in the coming studies.

According to the above results the acoustic field below the surface duct is dominated by the propagating low frequency sound and by the more locally generated sound at frequencies above 150 Hz. While within the surface duct the acoustic field is

dominated by the trapped sound at frequencies above cut-off domain, and by the local field at the lower frequencies.

Table 5.6. Summarized propagation effects in a ice covered ocean with strong surface duct and not to deep water.

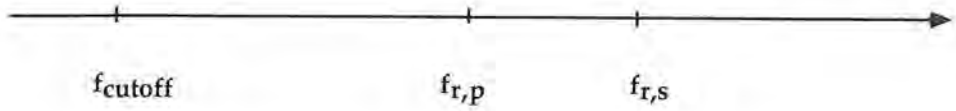

$f<f_{cutoff}$	Sound leaks out of the surface duct and significant bottom interaction occurs at shallow and intermediate water depths. The cutoff frequency increases as the duct depth reduces.
$f > f_{cutoff}$	The sound is trapped in the surface duct, and influenced by the interaction with the ice cover. The number of interactions with the ice cover increases as the duct depth reduces, this will increase the attenuation.
$f_{cutoff}<f<f_{r,p}$	The transmission loss is dominated by scattering from the ice cover or rough sea surface. The reflection coefficient is one (or close to one) and causes no transmission loss.
$f_{r,\,p} <f<f_{r,\,s}$	P waves starts to be refracted into elastic p waves in the ice cover this corresponds to an reflection coefficient less than one for angles above critical grazing angle for p waves. The reflection coefficient causes an steadily increase in attenuation for frequencies above this frequency.
$f_{s,p} <f< F$	Reflection loss due to energy conversion to elastic shear waves are introduced for a very broad range of angles, and the reflection loss increases very rapidly above this frequency and up to a frequency F from where the Reflection loss as a function of grazing angle is constant with increasing frequency.

5.5 Concluding remarks.

In this study both experimental measurements and numerical simulations have been used to investigate how the ice cover, surface ducts and bottom influences the sound propagation in the MIZ. This work represents a preliminary and simple study. The physical complexity will be increased gradually in a forthcoming modeling work, under AMOC project (Johannessen et al., 1997).

The effect of changing shear wave speeds and shear wave attenuation in ice will be considered in detail in forthcoming work. Temperature, density, porosity and salinity profiles are used in theoretical models to calculate compressional and shear wave speeds (Laible and Rajan, 1996). Furthermore, temperature measurements of sea ice from the Barents sea indicates that the multi year ice is colder (-11 C) and less saline than the first year ice (-5 C) (Sandven et al, 1993). This corresponds to different shear velocity in MY and FY ice. First of all the elastic properties of the ice cover are

important for the reflection loss and has to be considered. Thereafter the transmission loss will be considered.

Next step will be to modify the sound speed profile in the water layer to be more similar to the data obtained in the MIZ. Scattering from the ice cover and sea floor has to be included. Finally the rang dependence in all layers will be included.

Furthermore, time domain solutions using explosive sources or beams will be studied in order to study the sensitivity in acoustic travel times varying environmental parameters.

Despite the simple approach, the study have produced important results, which can be used in further studies of propagation in ice covered regions and in the interpretation of ambient noise observations. One of the important consequences of the results above is the conflict between the optimum transmission frequency and the optimum frequency for retrieving information about the ice cover. If an experiment is designed to propagate over long distances at a relatively low frequency, lets say 19.7 Hz, as used in the TransArctic Experiment (Mikhalevsky, 1994), then the reflection from a smooth ice cover is total and there will be no information about the ice thickness or internal properties of the ice cover. The attenuation due to the ice will be dominated by scattering from rough surface. So this type of experiments will give information about the averaged temperature through the travel times, while the ice information will be limited. Concepts to measure ice parameters need other types of sources including more than one frequency.

6. Study of hotspots by averaged levels at selected frequencies

6.1 Introduction to studies of ambient noise hotspots

This study has two specific objectives:

- Investigate the hypothesis that ambient noise hotspots along the ice edge are due to ice edge eddies
- Investigate the hypothesis that icebergs interacting with the ice field represents strong noise generators

6.1.1 Ice edge eddies

Ice-ocean eddies, which occur frequently in the ice edge zone (Johannessen et al. 1983) were postulated by Yang et al (1987) to create maxima in the ambient noise field, denoted hotspots. This hypothesis arose from their observations of ambient noise hotspots along the ice edge that had the same scale distributions as eddies in the ice edge zone. However, no synoptic oceanographic or satellite data were available in the study by Yang et al., (1987) to validate the presence of eddies in the vicinity of their measurements.

In the present study our aim is to investigate the hypothesis of Yang et al (1987). In our study ice edge eddies were localized visually and by use of real time SAR, and sonobuoys were positioned within these eddies in optimal locations (Johannessen et al, 1988 a, b; Johannessen et al, 1992 b). Averaged ambient noise levels at selected frequencies, described in chapter 4 and Appendix, are used to study spatial variations in ambient noise within regions of ice edge eddies. Three case studies are selected for analysis of ambient noise hotspots:

- MIZEX 85: April 30, 1985, in the Fram Strait
- MIZEX 87: April 2, 1987, in the Fram Strait
- SIZEX 92: February 27, 1989, in the western part of the Barents Sea.

6.1.2 Icebergs

Furthermore, visual and audible observations close to grounded and drifting icebergs have shown high levels of noise as the sea ice cover is cut up in smaller floes by icebergs. Therefore, grounded and drifting icebergs have been postulated to be strong sources of ambient noise in the Barents Sea (Johannessen et al , 1990). In order to also test this hypothesis a fourth case study is included from March 9 1992 when 24 sonobuoys were deployed in the Barents Sea just east of Hopen where several icebergs were observed. Two of the sonobuoys were deployed in open water wakes behind the drifting icebergs, created due to the difference in drift velocity between sea ice and icebergs

The location of the study areas is shown in Figure 4.1 and a summary of the environmental conditions for all the cases are shown in Table 4.3. In each case the averaged levels are plotted against the least distance from buoy to ice edge. The ice edge is defined as the main ice edge.

6.2 MIZEX 85: April 30, 1985

6.2.1 Environmental conditions

On 30 April 1985 an ambient noise experiment was conducted in the Fram Strait at approximately 78° 24' N, 1° 25' E (Figure 4.1) where the water depth is between 2000 m and 3000 m (Johannessen et al 1988b). In order to resolve the horizontal structure of the ambient noise in an area of ice edge eddies, 21 sonobuoys were deployed in an area with two cyclonic ice edge eddies identified by in situ observations from the aircraft and by satellite imagery (Figure 6.1 a). Seven buoys were deployed at 18 m, twelve at 122 m and 2 at 305 m. Only the 12 buoys at 122 m are analyzed in this study. One smaller eddy ("A"), with a diameter of 20 km (Figure 6.1 b) was located inside the ice edge, and a larger eddy ("B") was located at the ice edge.

Based on observations from NOAA AVHRR satellite images, aerial photographs, and visual observations from the aircraft, the area can be divided into open sea, diffuse ice edge, compact ice zone, and interior ice pack. Despite tongues of FY floes extending out into the open ocean, the ice edge was generally compact. The south-southwesterly orientation of the ice edge follows the direction of the East Greenland Current. The ocean depth in the experiment area is more than 1400 m and most of the sonobuoys were located in depths greater than 2500 m. The ice edge follows the 2700 m contour that marks the beginning of the rise of the of the Greenland continental shelf. The position of eddy "B" and the nearby ice edge correlates well with a NW/SE ridge that rises to 1400 m depth below positions "h" and "n", indicating topographic generation of eddies. The position and size of the eddies is clearly shown in the horizontal temperature distribution obtained from the AXBT launched from the aircraft (Figure 6.2.a). The vertical temperature section through eddy "A" (Figure 6.2.b) shows a dome-like structure at the ice edge and a temperature front at the ice edge.

The wind was 3 - 5 m/s and directed parallel to the ice edge. The wave field outside the ice edge was dominated by short waves with period of 3 - 4 s, with significant wave height predicted to be less than 0.5 m using wave model results from the Norwegian Meteorological Institute (Johannessen et al, 1988 b). During such calm conditions, ice interactions are mainly caused by ocean currents and particularly by ice edge eddy circulation. In the absence of strong winds, eddies with on-ice velocity components create an overall compact ice edge, while off-ice velocity components create diffuse streamers of ice into the open ocean. The ice convergence due to the rotational motion of these eddies was clearly observable in the centre of eddy "A" in the aerial photographs (Figure 6.1 b).

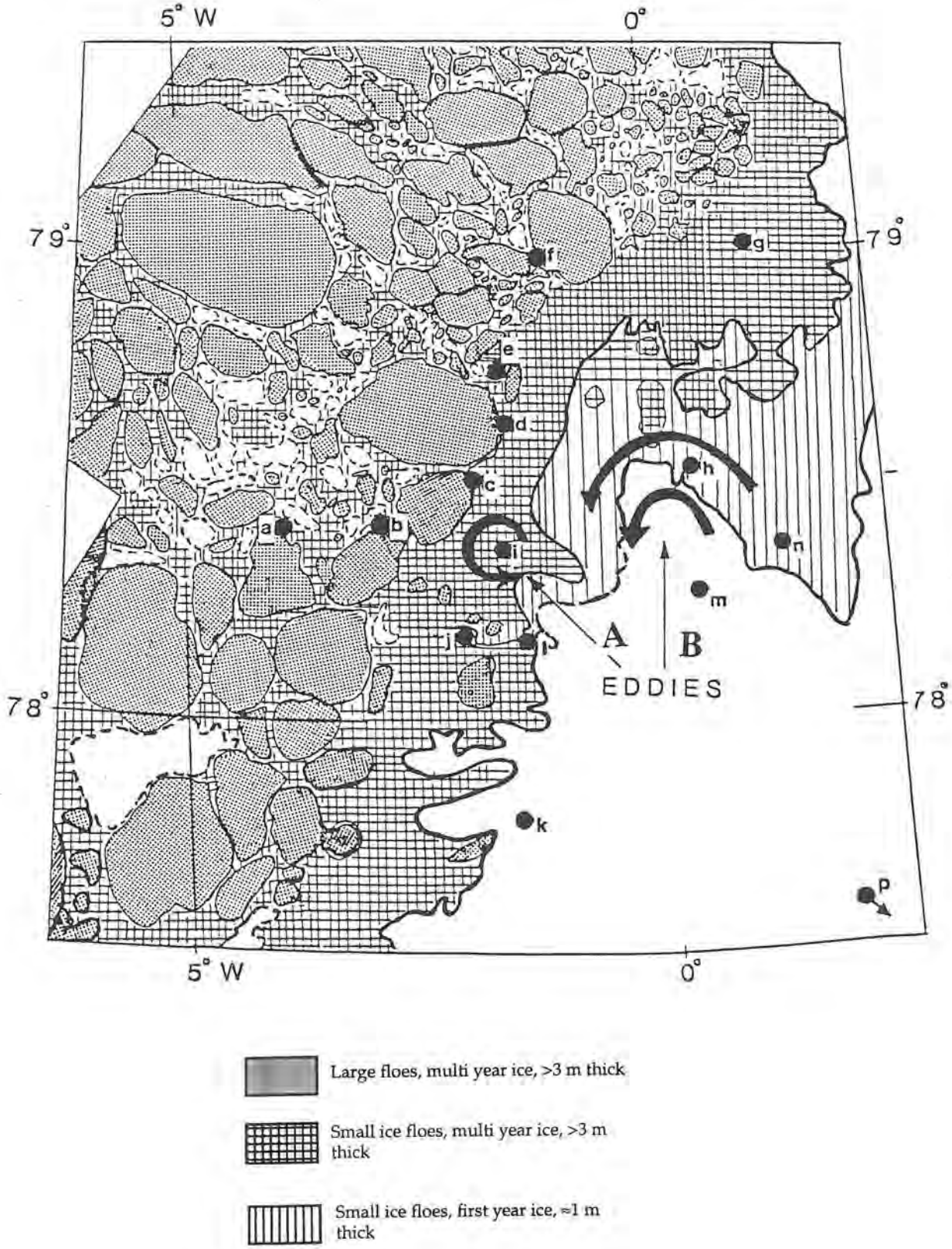

Figure 6.1 (a) Schematic ice map of the ice edge produced from NOAA AVHRR satellite image on April 30, 1985 with the sonobuoy positions marked as bold dots (a to p). Eddy "A" is within the ice and eddy "B" is on the ice edge.

Figure 6.1 (b) Aerial photograph of eddy "A". The distance across the image from left to right is 20 km.

6.2.2 Acoustic observations

6.2.2.1 Examination of the horizontal variation of ambient noise levels

The ambient noise levels at 122 m depth vary considerably at all the four investigated frequencies in the study area. Figure 6.3 shows the variation of ambient noise as a function of least distance from the ice edge. At 40 Hz and 100 Hz there is no clear peak in noise at the ice edge. Across the ice edge, the 40 Hz level is fairly constant, but 15 - 20 km into the ice pack the horizontal variability increases to 8 dB. The maximum level at 40 Hz was observed in the northern part of the experiment area where buoys **f** and **g** were deployed. Buoy **f** was located between large ice floes and showed a level of 88 dB, while buoy **g** which was located between small multi-year floes showed a level of 89 dB. . The variability is 8 dB at 40 Hz, 5 dB at 100 Hz, 7 dB at 315 Hz and 9 dB at 1000 Hz.

At 100 Hz the ambient noise level is fairly constant over the entire experimental region, except for a maximum of 2 dB, 35 km into the ice pack, at the border between the compact ice zone and the interior ice pack. The lowest level at 100 Hz (79 dB) was observed 64 km into the ice pack at buoy **f**.

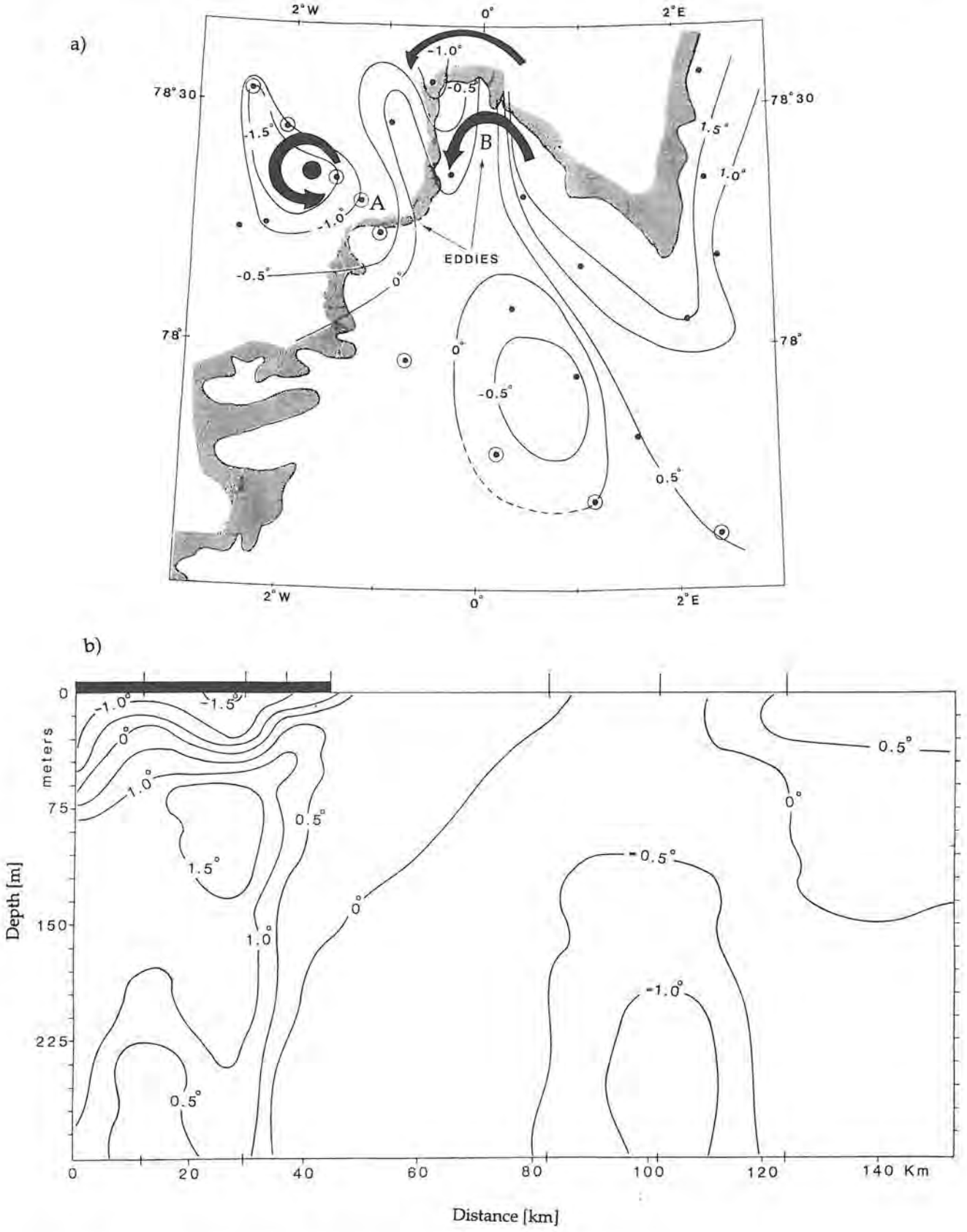

Figure 6.2 (a) Map of ice edge in the experiment area 30 April 1985 with horizontal contours of temperature (° C) at 5m depth. The dots represents location of the AXBTs; the circled dots are the buoys used in the vertical temperature section shown below . **(b)** Vertical section of temperature (° C) along a NW to SE transect though eddy "A". The vertical ticks at the top of the figure indicate the position of the AXBTs used to estimate the temperature structure.

At 315 Hz and 1000 Hz, a peak in the noise level is observed in the ice edge eddy region. The peak extends up to 20 km into the ice pack. The general trend at 315 and 1000 Hz is a reduction in noise level as the distance from the ice edge increases, the reduction being 7 dB at 315 Hz and 9 dB at 1000 Hz over a distance of 50 km into the pack ice. Two buoys located in the transition zone **e** and **c** do not follow this trend, showing almost as high levels as in the eddy region. In Figure 6.3 it is also observed that the ambient noise levels at 315 Hz and 1000 Hz are more rapidly reduced towards open ocean than towards the interior of the ice pack. This suggests that the ambient noise level is determined by a combined effect of very low wave activity outside the ice edge and increased noise generation due to the ice edge eddies located within the ice edge.

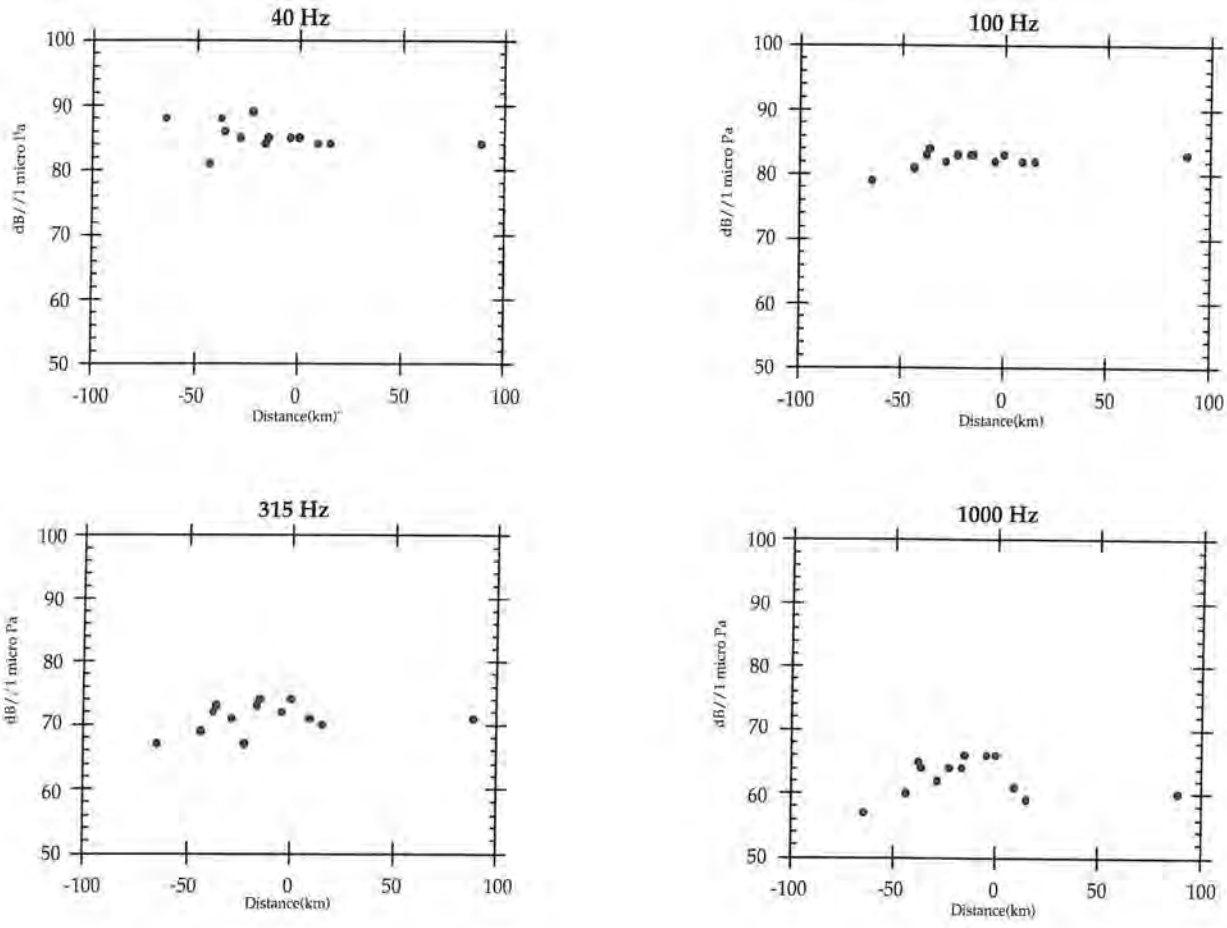

Figure 6.3 Plot of averaged ambient noise level observed on April 30, 1985 at 122 m depth as a function of least distance from the ice edge.

6.2.2.2 Ambient noise in the eddy region.

In the ice edge zone, where eddies "A" and "B" are located a 4-7 dB variation was observed at 315 and 1000 Hz, whereas only 2-3 dB variation was observed at the two lower frequencies. At 315 Hz, buoys **i**, **j**, **l** and **c**, in eddy "A", have levels of 73-74 dB, which are 5 dB above the mean level of the other buoys in the compact ice zone. At 1000 Hz there is a maximum of 66 dB near the center of the large eddy "B" (buoy **h**) and at the southern periphery of the small eddy (buoys **j** and **l**), which are 2.5 dB above the mean background noise of 63.5 dB (excluding buoys **j** and **l**). No maximum was observed at buoy **i** at 1000 Hz, although it was deployed near the center of the small eddy.

In the experiment on April 30, 1985, which was a calm day, maximum ambient noise levels were found inside the ice edge, in the eddies "A" and "B", at 315 and 1000 Hz. This case study verify that hotspots in ambient noise are related to ice edge eddies during calm wave and wind conditions.

6.3 MIZEX87: April 2, 1987

6.3.1 Environmental Conditions

The ambient noise experiment in MIZEX 87 was integrated with acquisition of 12 consecutive days of airborne Synthetic Aperture Radar (SAR) images of the study area. The SAR images, which had a high-resolution of 15 m, were transmitted to the ship in real time and proved to be a powerful tool in planning and implementation of the acoustic field experiment (Figure 6.4). Successive images enabled observation of several mesoscale processes, such as eddies, jets, and vortex pairs along the ice edge (Johannessen et al 1994 b).

Ocean currents and ice drift were monitored by several drifting ARGOS buoys with strings of current meters suspended from floes inside the main ice edge. The array of buoys drifted southwards, showing that the velocity field is dominated by the East Greenland Current flowing southwards at typical speed of 0.30 - 0.50 ms^{-1}. The maximum velocity of the current was observed along the continental shelf break, which coincided with the location of the main ice edge during MIZEX 87. Further into the ice pack and out in open water, the southward current was weaker, typically 0.10 - 0.20 ms^{-1}. The maximum shear deformation of the ice field was estimated to be 1.5×10^{-4} s^{-1}, which is very high and comparable with the Coriolis parameter.

Several mesoscale features such as eddies, jets, and vortex pairs were observed to be superimposed on the main current (Johannessen et al. 1994b). The SAR image from April 2 shows a cyclonic ice edge eddy developing at 78° N, with eddy center located in the compact ice edge zone close to sonobuoy no 18 (**RF 18**) indicated in Figure 6.4. South of the cyclonic eddy, an ice tongue, which had advected out from the ice edge 2 - 3 days earlier, is seen extending 30 km out into open water. The wind direction was northerly, with a component normal to the tongue, resulting in a compact ice edge

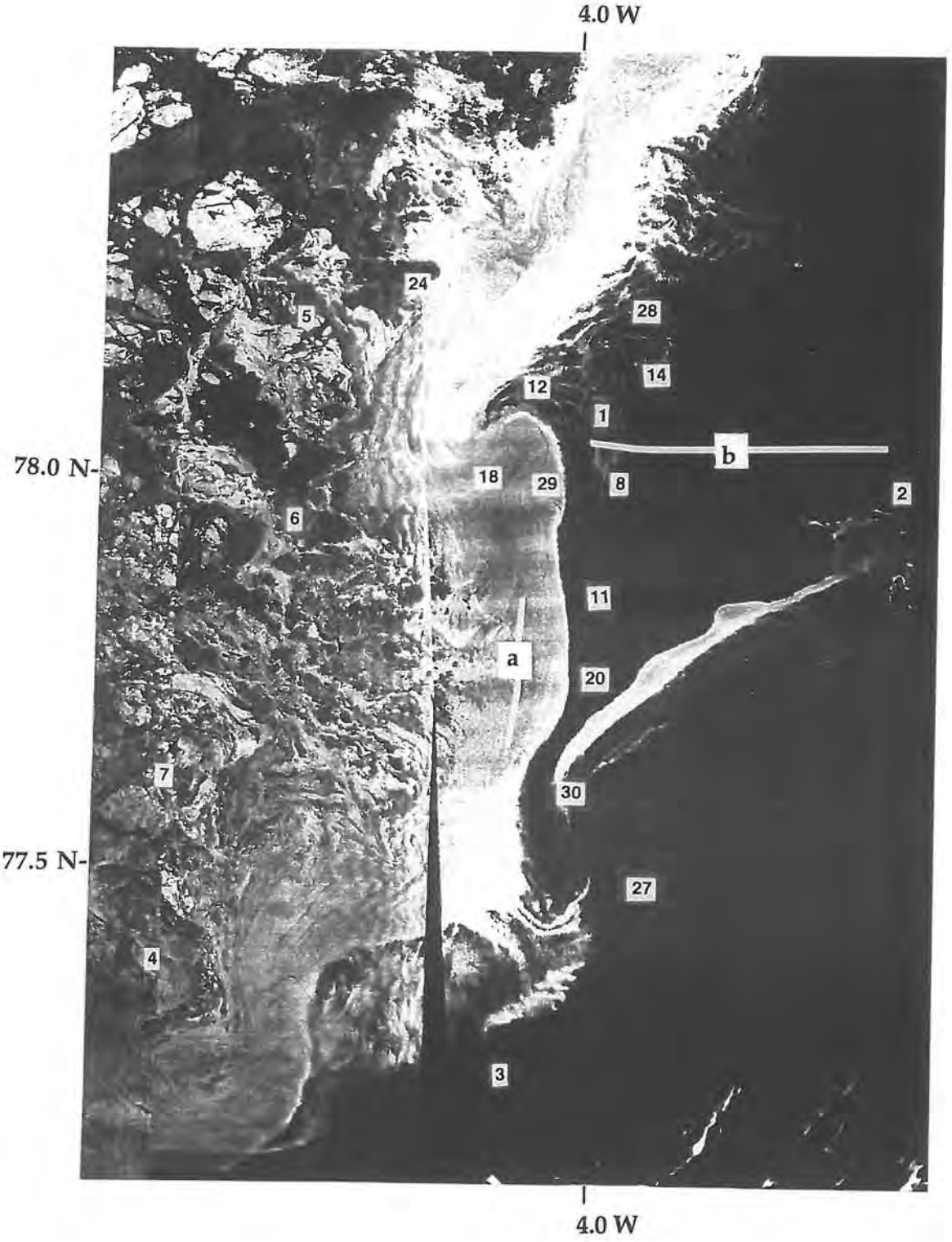

Figure 6.4. SAR mosaic from April 2, 1987, with sonobuoy positions superimposed. The numbers are the sonobuoy ID numbers. Ice and water can easily be distinguished in SAR images because water has generally a lower back scatter (dark areas) compared with ice (bright areas). Lines **a** and **b** denote CTD sections obtained by R/V Polarcircle and R/V Håkon Mosby, respectively on this day.

north of the jet (**RF 20**). Further south, another jet with a developing vortex pair is observed near **RF 27** and **RF 3**. The SAR image also shows that the compact ice zone is a 10 -20 km wide belt inside the main ice edge where the ice concentration is generally high (80 - 95%). Aerial photographs taken from a helicopter on the same day showed that the compact ice zone consisted of broken-up floes with typical size of 10 - 50 m, ridges and slush ice. The broken-up floes consisted mainly of MY ice which is transported southwards from the Arctic Ocean. The eddy area was characterized by scattered MY floes and patches of thin ice to the north and east, while the southern part of the eddy, including the eddy center, is located inside the main ice edge with a high concentration of multi-year floes (Figure 6.4).

The wind speed observed by R/V Håkon Mosby, located some 30 miles outside the ice edge, decreased from 9 m/s to 5 m/s at about 12:00 Z on April 2, at the same time as the wind direction shifted from northeast to north. On R/V Polarcircle, located inside the ice edge, the wind was observed to blow steadily from north at about 7 m/s without any change in direction. From the SAR image, it was found that the dominant wavelength of the swell is about 200 m and the principal propagation direction is north-westerly. The significant wave height 6 km into the ice pack varied between 0.7 and 1.5 m, and the dominant wave period varied from 12.1 s to 13.5 s.

6.3.2 Acoustic Observations

6.3.2.1 Averaged ambient noise levels normal to the ice edge

The location of the sonobuoys deployed on April 2 1987 is superimposed on the SAR image shown in Figure 6.4. The averaged ambient noise levels are plotted as a function of least distance from the ice edge (Figure 6.5), showing strong variability (7 - 10 dB) at all frequencies along the ice edge. The predominant feature is the general higher levels observed at all frequencies outside the ice edge compared to inside the ice edge. Also the variability is higher outside the ice edge at all frequencies except at 1000 Hz.

At 40 and 100 Hz the levels in the compact ice zone is generally 4 - 6 dB higher than in the interior of the ice pack. At 315 Hz and 1000 Hz this difference is larger; the lowest levels in the interior ice pack are 8 dB and 13 dB lower than recordings made in the center of the eddy located in the compact ice edge zone 11 km from the main ice edge. The noise level is reduced by 4 dB at both 315 Hz and 1000 Hz moving 8 km eastwards to a position 2 km from the ice edge. This clearly demonstrates the effect of the ice edge eddy on ambient noise, compared to the effect of swell.

6.3.2.2 In the eddy region

In order to study the horizontal variability within the cyclonic eddy at 78° N seven sonobuoys (**RF-18, RF-29, RF-28, RF-14, RF-12, RF-8, RF-1**) were located in the eddy area (Figure 6.4). A horizontal variation of 4 dB at 40 Hz increasing with frequency to 8 dB at 1000 Hz is observed within the 40 X 40 km eddy region. This represents fairly large gradients The maximum at 40 Hz and 100 Hz was located in the outer part of the diffuse ice zone (**RF-1** and **RF-8**) in an area of low ice concentration and in patches of thin ice.

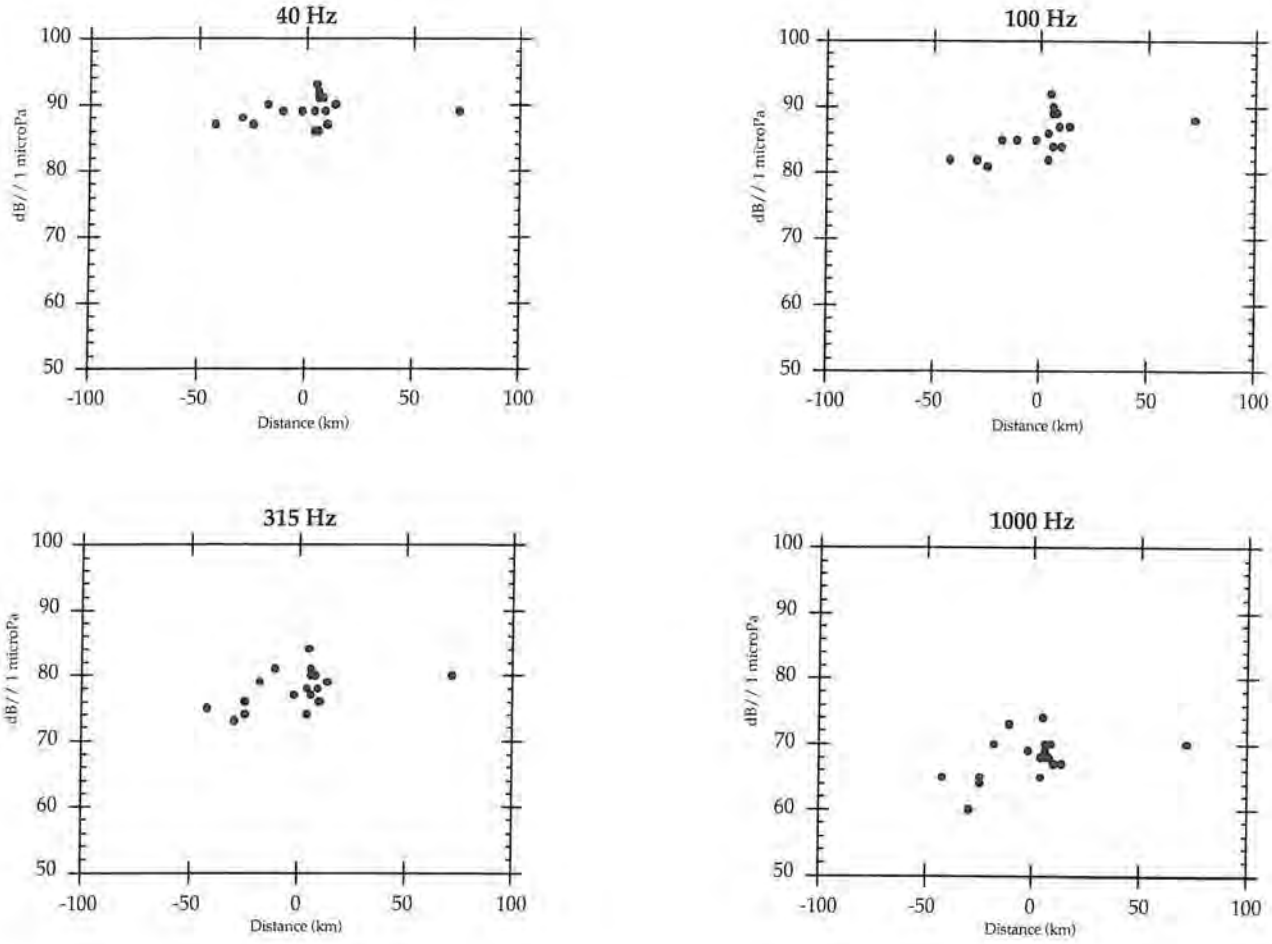

Figure 6.5. Plot of averaged ambient noise level at 122 m depth, obtained on April 2, 1987, according to least distance from the ice edge.

At 315 Hz there are three local maxima: one near the eddy center and two outside the main ice edge. At 1000 Hz the level observed near the eddy center represented a 3 - 4 dB maximum compared with the other buoys deployed within the eddy. Although **RF-29** is located within the same type of ice and is nearer to the ice edge, implying that the swell is less attenuated, the ambient noise level was 4 dB lower at 315 Hz and 1000 Hz than near the eddy center. This indicates that the increase in ambient noise near the eddy center is a local phenomenon caused by increase of internal ice stress due to shear zones and convergence zones, driven by the combined interactions of the eddy current, the main southward directed current, and wind forcing on the ice floes. The effect of swell interaction with the ice cover on ambient noise levels may be enhanced due to the increased internal ice stress close to the eddy center.

At all frequencies a 2 - 4 dB minimum was found in the eddy area at buoy **RF-12**, which was located to the north of the eddy center, where bright bands and very dark areas in between are seen in the SAR image (Figure 6.4). The bands of ice consist of first year ice and pancake ice, whereas the dark areas are grease ice. During cooling, a very thin visco-elastic film of ice, grease ice, can be formed over large areas of the MIZ. This thin layer of ice has been observed to dampen out the shorter surface waves, which in turn reduces the ambient noise level (Johannessen et al 1988 a; Johannessen et al 1994 a).

6.3.2.3 Averaged ambient noise levels along the ice edge

In order to investigate the eddy hotspot effect eleven sonobuoys were deployed outside of and parallel to the main ice edge (Figure 6.4). The ambient noise measurements along the main ice edge show a small peak in the eddy field (**RF-8** and **RF-1**) at all selected frequencies.

Although the northern buoys are influenced by swell and eddies, the observed noise levels increase southwards to a maximum level at **RF 20,** located just north of the ice jet/tongue. Buoy **RF-20** measured the highest level at all frequencies during the experiment. The hotspot was most pronounced at 1000 Hz with an averaged level of 74 dB which is 5.5 dB above the mean averaged level of all the other buoys along the ice edge at this frequency. Of all the other buoys in the experiment only **RF-18**, located near the eddy centre at 78° N, showed levels above 70 dB at 1000 Hz, namely 73 dB. The northerly winds creating the very compact northern edge of the ice tongue may explain the maximum in noise level observed at **RF-20** at all frequencies. No other places did the wind have a component towards the ice edge on the study area. South of the ice tongue the wind fetch was interrupted because of a 3 - 5 km wide band of dense ice in the ice tongue. The tongue therefore acted as an lowpass filter for the wind-generated waves propagating from the north. The minimum noise levels south of the jet may be caused by this reduced wave activity and the diffuse ice conditions in this area. At the southernmost buoy (**RF-3**) the level was higher, probably due to the influence of another ice tongue generated by a vortex pair.

A time series of the ambient noise levels at **RF-20** are presented in Figure 6.6, showing a significant increase of 2 - 4 dB at all frequencies between 12:30 and 14:10 UTC. In this period the wind observed from R/V Polarcircle, located inside the ice edge, was fairly constant. However, in open sea the wind speed observed from R/V Håkon Mosby was reduced from 8.5 m/s to 5 m/s around noon. Under these circumstances a noise reduction is expected immediately after the wind speed reduction, and it is therefore concluded that the wind speed does not directly influence the noise level in this case.

The wind direction observed from R/V Håkon Mosby, however, shows a gradually veering from northeast to north which coincided with the increase in noise level. The change in wind direction corresponds to an increase in the wind component directed perpendicular to the ice tongue increasing the packing of ice at the northern edge of the tongue. This is an important mechanism to build up the internal ice stress (Overland, 1988).

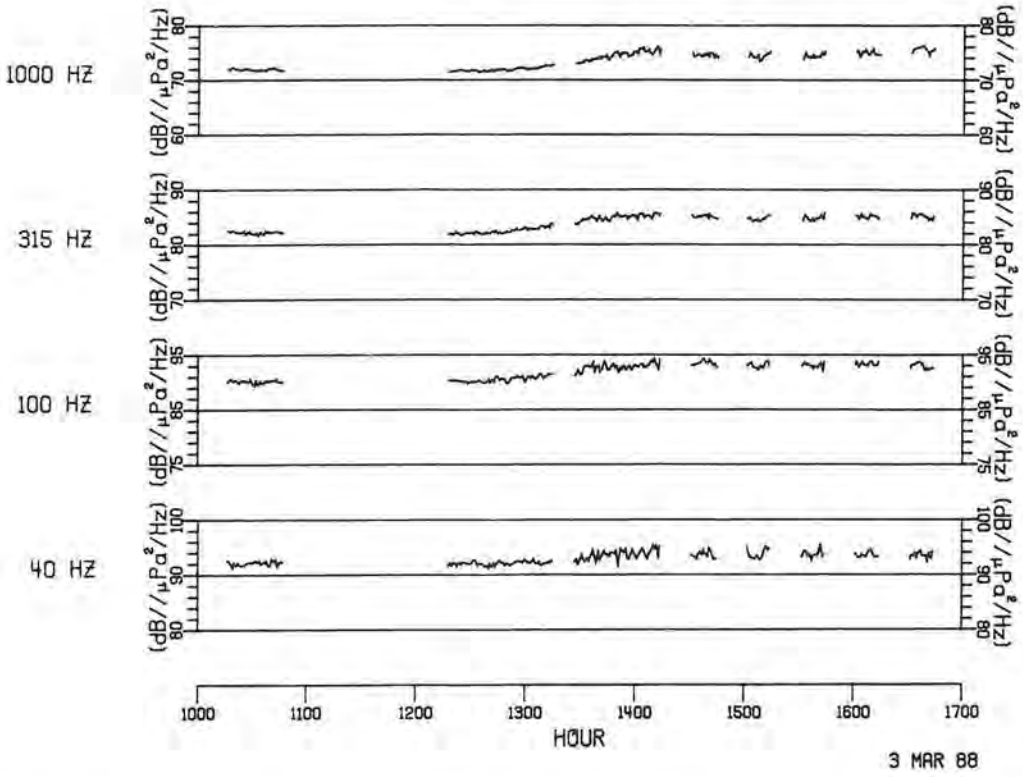

Figure 6.6. Time series of ambient noise at 40, 100 315 and 1000 Hz observed at **RF 20**, April 2, 1987.

RF-2, which was located in thin ice at the head of the ice tongue where a vortex pair is located, had a similar and larger increase at 100 Hz, 315 Hz and 1000 Hz, but it recorded no observable increase at 40 Hz. A comparison of time series between **RF-20** and **RF-2** at 1000 Hz shows a time delay of 30 minutes at **RF-2**. It appears that the response to the change in wind direction is stronger, but "slower" in thin ice (**RF-2**) than at the compact edge near the ice tongue (**RF-20**). The time delay at **RF-2** may indicate that some time is needed to form ice concentrations high enough to increase the interaction between ice floes. The change in the wind direction does not change the fetch significantly for any of the other sonobuoys, and there are no records of any increase or reduction in noise level for any of the other sonobuoys along the ice edge.

From the analysis above it is concluded that the ice edge eddy at 78 N showed a significant and local hotspot close to the eddy center located inside of the compact ice edge. The most pronounced hotspot, however, was observed in open water near the ice tongue with on-ice wind direction. This last observation modifies the hypothesis made by Yang et al., 1987. Hotspots along the ice edge can also be generated by on-ice wind component and corresponding wave action on the ice edge.

6.4 SIZEX89: February 27, 1989

6.4.1 Environmental conditions

The ambient noise experiment on February 27 1989 was dedicated to eddy studies in a 50 x 60 km shallow area north-west of Bjørnøya in the Barents Sea. In the eddy area, which was identified using a SAR image from the previous day, sonobuoys were deployed by a P-3 aircraft and a helicopter. The sonobuoy locations are superimposed on the SAR image of February 27 (Figure 6.7 a). The spacing between the buoys was approximately 8 km, and the sonobuoy depth was 18 m.

The experiment area was located partly in deep water (west of 14° E) and partly on the shelf between Svalbard and Bjørnøya (Figure 4.1) with water depth below 500 m. Along the shelf break relatively warm water is transported northwards by the Westspitsbergen current. On the shelf the current field is influenced by bathymetric features and interaction with currents from northeast, the East Spitsbergen Current. A current map for the Barents Sea is shown in Figure 2.5 (Pfirman et al, 1994).

Several ice deformation zones were visually observed during the field experiment and can be identified in the SAR image as small eddies and vortex pairs which were present in the experimental area (Figure 6.7 a, b and c). A north-easterly light breeze (2-3 ms^{-1}) was blowing from the ice towards open water, resulting in a diffuse ice edge. A swell field propagating in a north-easterly direction, opposite to the wind direction, was observed by examination of the full resolution version of SAR image from February 27.

Wave data collected by wave buoys deployed on ice floes showed a 0.16 m significant wave height when the SAR image was obtained. The wave buoy was located 5 km east of sonobuoy **C-23**, approximately 8 km inside the ice edge (Figure 6.7 a). The swell, as well as several ice floe collisions, were observed visually in this region during the wave buoy deployment.

The SAR image (Figure 6.7 a) can be used to divide the experiment area into a diffuse ice edge zone and a compact ice zone. The ice concentration increases gradually from the diffuse ice edge zone towards the compact ice zone. The ice conditions in the diffuse ice edge zone varied from almost open water around buoy **C-17**, **C-10** and **C-31**, to an ice concentration of 50-60 % around **C-19** and **C-20**. The other buoys were located further into the diffuse ice edge zone where the ice concentration was generally higher than 60 %. The ice in the diffuse ice edge region was mainly FY ice of thickness 1 - 2 m and some young ice. The compact ice zone located inside the diffuse ice edge zone was a fairly broad region of high concentration of small FY ice. The floe size generally increased from 5 - 10 m in the outer part of the compact ice edge zone to 10 - 50 m in areas further into the ice pack. In the compact ice edge zone the ice concentration was above 80%. Some areas within the compact ice zone had a lower ice concentration due to open leads, while others had a very high ice concentration (90 - 100 %). Between 30 km and 50 km into the icepack, larger ice floes (up to several km) interspersed with thin ice, indicating that the wave conditions had been calm for several days.

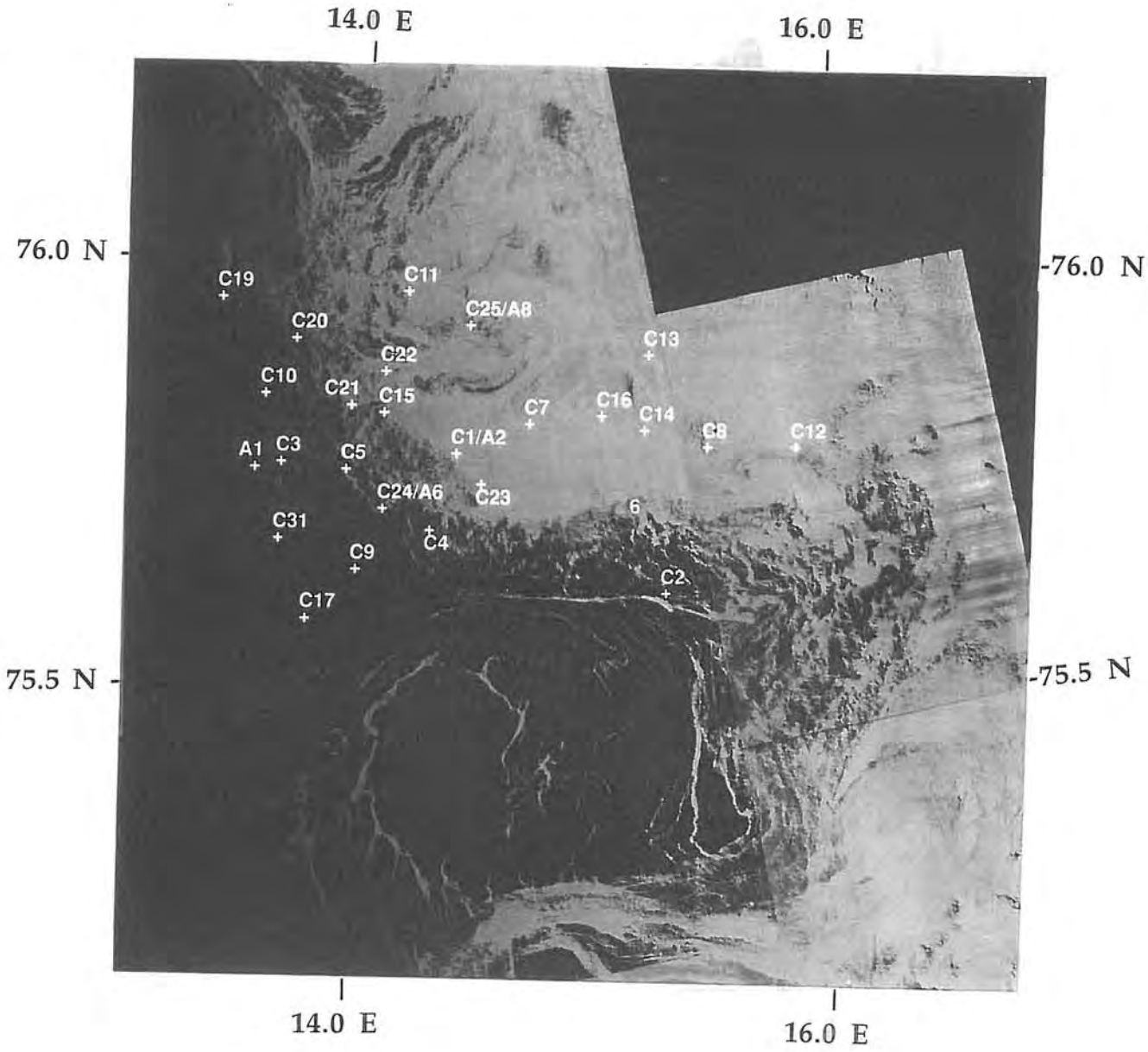

Figure 6.7 (a) SAR image of February 27, 1989, with the sonobuoy (C) and AXBT (A) positions marked by numbers.

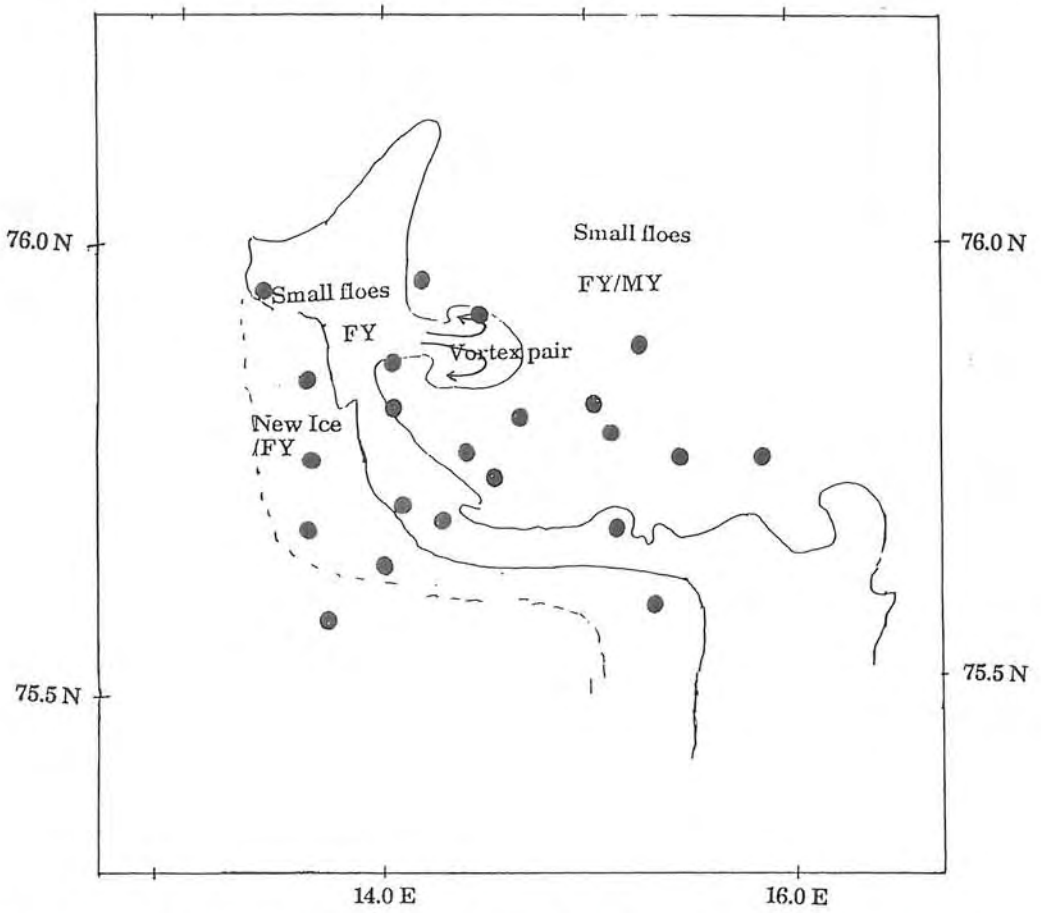

Figure 6.7 (b) Interpretation of the SAR image in the area of sonobuoy deployment, showing the location of the vortex pair near C25.

Figure 6.7 (c) Aerial photograph of the vortex pair shown in (b).

6.4.2 Acoustic Observations

The ambient noise levels from the February 27 experiment are plotted as function of the least distance from the ice edge in Figure 6.8.

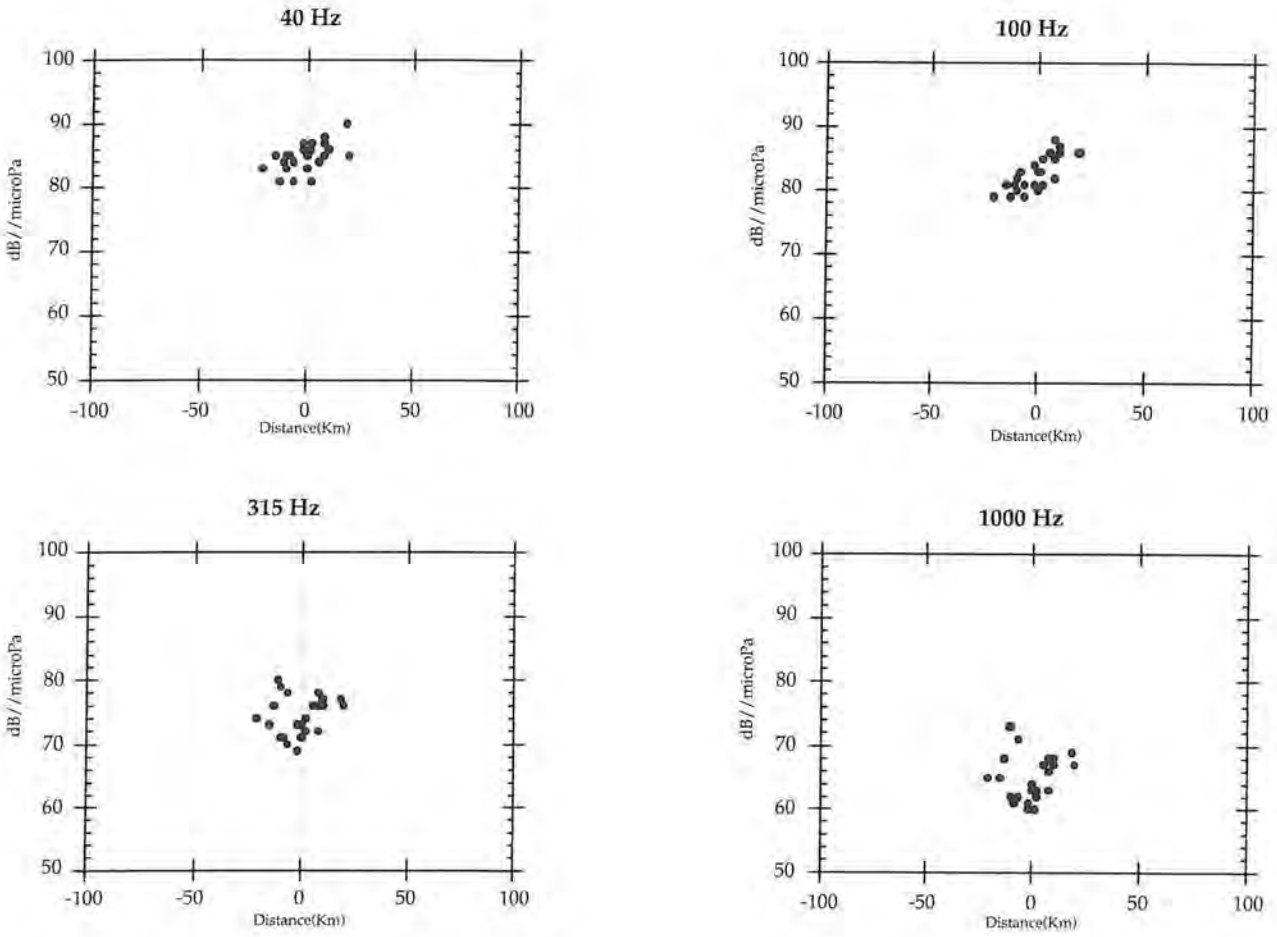

Figure 6.8. Plot of ambient noise levels at 18 m depth according to least distance from the ice edge on February 27, 1989. Negative distance is inside the ice edge, positive distance is outside the ice edge.

By comparing Figure 6.8 with Figure 6.3 and 6.5, much stronger horizontal gradients are observed in this data set than in any of the two previous data sets. The total variability within the 50 by 60 km experiment region is about 10 dB at all frequenies.

The ambient noise level is generally reduced by 4 - 6 dB from 20 km outside the main ice edge to about 20 km inside the compact ice pack. Inside the ice edge the variability in noise level becomes more complex: the first cluster of data points are the measurements in the outer part of the compact ice zone (**C-01, C-22, C-23, C-11, C-25, C-07**). The second cluster of data points consists of measurements all performed in the inner part of the compact ice zone (**C-12, C-14, C-8, C-16, C-13**) (not necessarily far from the ice edge). This cluster indicates strong horizontal gradients in ambient noise in the

inner compact ice zone where convergence zones was observed visually during the experiment. The high levels at 315 Hz and 1000 Hz in the inner part of the compact ice zone reflect the action of strong shear in a region of high ice concentration.

In an ice covered region with convergence zones due to small current features such as vortex pairs and complex general circulation the horizontal variation in averaged ambient noise is larger than for the 1985 and 1987 experiments.

6.5 SIZEX92: March 9, 1992

The experiment on March 9, 1992 was dedicated to test the hypothesis of ambient noise hotspots generated by interaction between icebergs and sea ice in a shallow area. The ambient noise measurements were obtained in the MIZ east of Hopen (Figure 4.1) in a regular grid planned by use of the ERS-1 SAR image on the previous day (March 8). The SAR image with sonobuoy locations is shown in Figure 6.9. The experiment area had no ice edge eddies, but contained several icebergs and all main ice types (grease ice, pancake ice, firstyear ice, multiyear ice) as well as different floe size and ice concentrations. The effect of grease ice on ambient noise was specially investigated and is described in chapter 9.

Five lines of sonobuoys, oriented in east-west direction, were deployed between 76.5° and 77.5° N in an area of about 100 by 100 km which was covered by the ERS-1 SAR image. A shallow depth setting (18 m) was used for all sonobuoys. During the acoustic experiment meteorological and oceanographic data were collected from three research vessels: R/V H. U. Sverdrup, R/V Polarsyssel and R/V Håkon Mosby. Wave and swell conditions were measured from Polarsyssel using wave buoys deployed on ice floes.

The ERS-1 SAR image shows the ice edge and several types of ice which are characteristic for Barents Sea in winter: grease ice, pancake ice, broken-up firstyear ice, consolidated firstyear ice, multiyear ice and refrozen leads. In situ ice thickness measurements showed that the individual firstyear floes could be typically 2 m thick, while the real ice thickness could be more than 4 m in areas of ridging and rafting. The compact ice zone is characterized by a relatively homogeneous signature in the SAR image with a pattern of surface waves penetrating into the ice. Inside the compact ice zone, leads, multiyear floes, and consolidated first year ice are observed.

6.5.1 Environmental Conditions

6.5.1.1 Wave conditions

On March 9, the sea state was estimated to be 1 - 2 m outside the ice edge. Locally generated short waves were observed *in situ* on top of the swell which propagated into

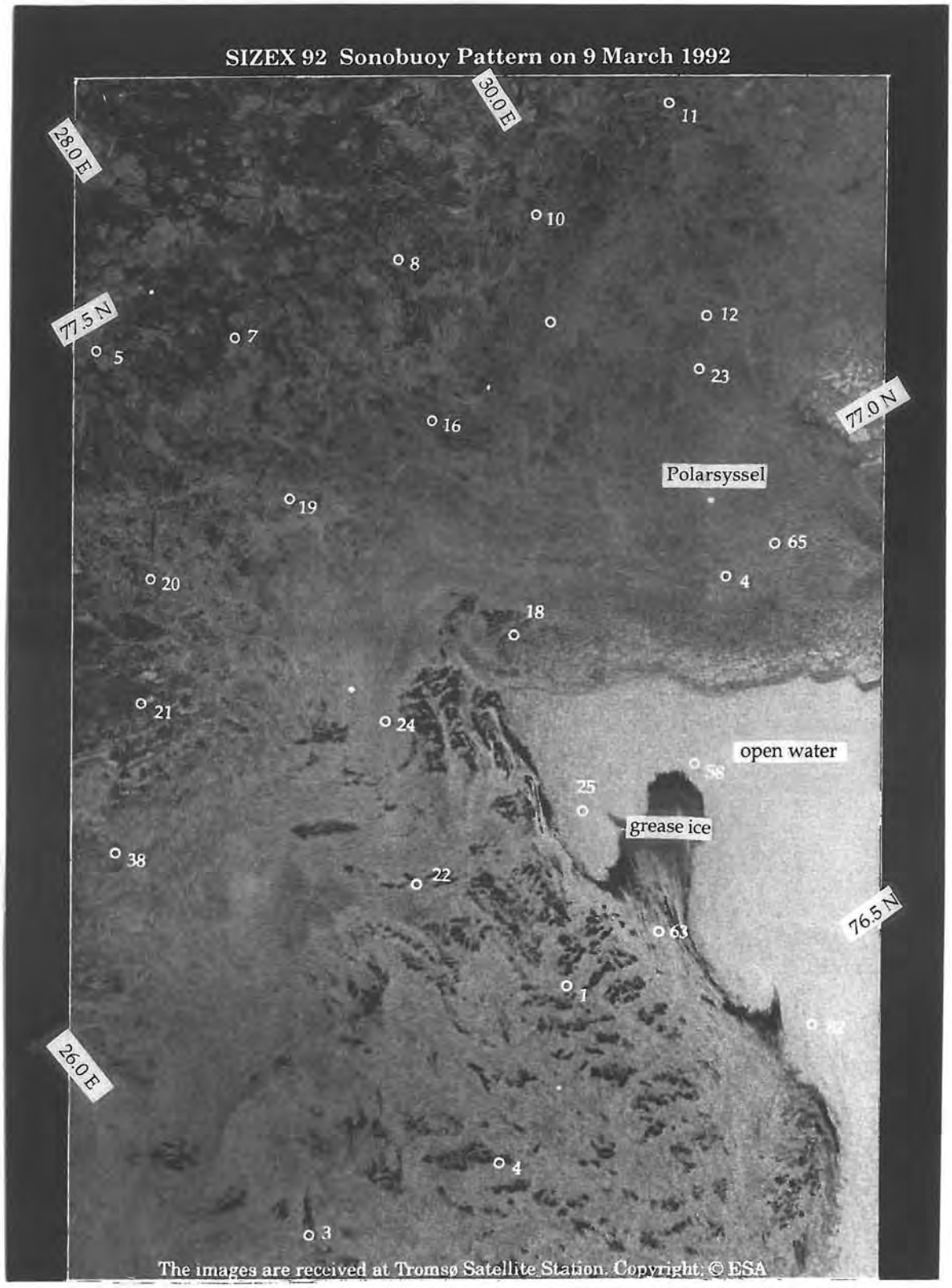

Figure 6.9 ERS-1 SAR image of March 8, 1992, covering 100 by 200 km of the MIZ in the Barents Sea east of Hopen. The sonobuoy deployment pattern of March 9 is superimposed on the image. Buoy no. 12 and 23 were deployed in the open water wakes of icebergs. Buoy 21 was deployed near an iceberg. Two buoys have the same number (4) and are denoted "4S" (southern buoy) and "4N" (northern buoy) in the text.

the ice. The short waves had a northerly direction and a wavelength of about 20 m. The amplitude was estimated to be approximately 1 m in the south (between buoy 3 and 4) and 2 m in the north (near buoy **18**). Inside the ice edge, the wind was blowing at 2 - 10 m/s from southerly directions, the ice edge was moving northwards and the swell was significant with a main period of about 13 s estimated from in situ observation onboard R/V Polarsyssel.

6.5.1.2 Ice conditions.

Ice information on March 9 was obtained from the SAR image and helicopter surveys on the previous day and from visual observations and photographs that were taken each time a sonobuoy was deployed in the northern part of the area (Figure 6.10).

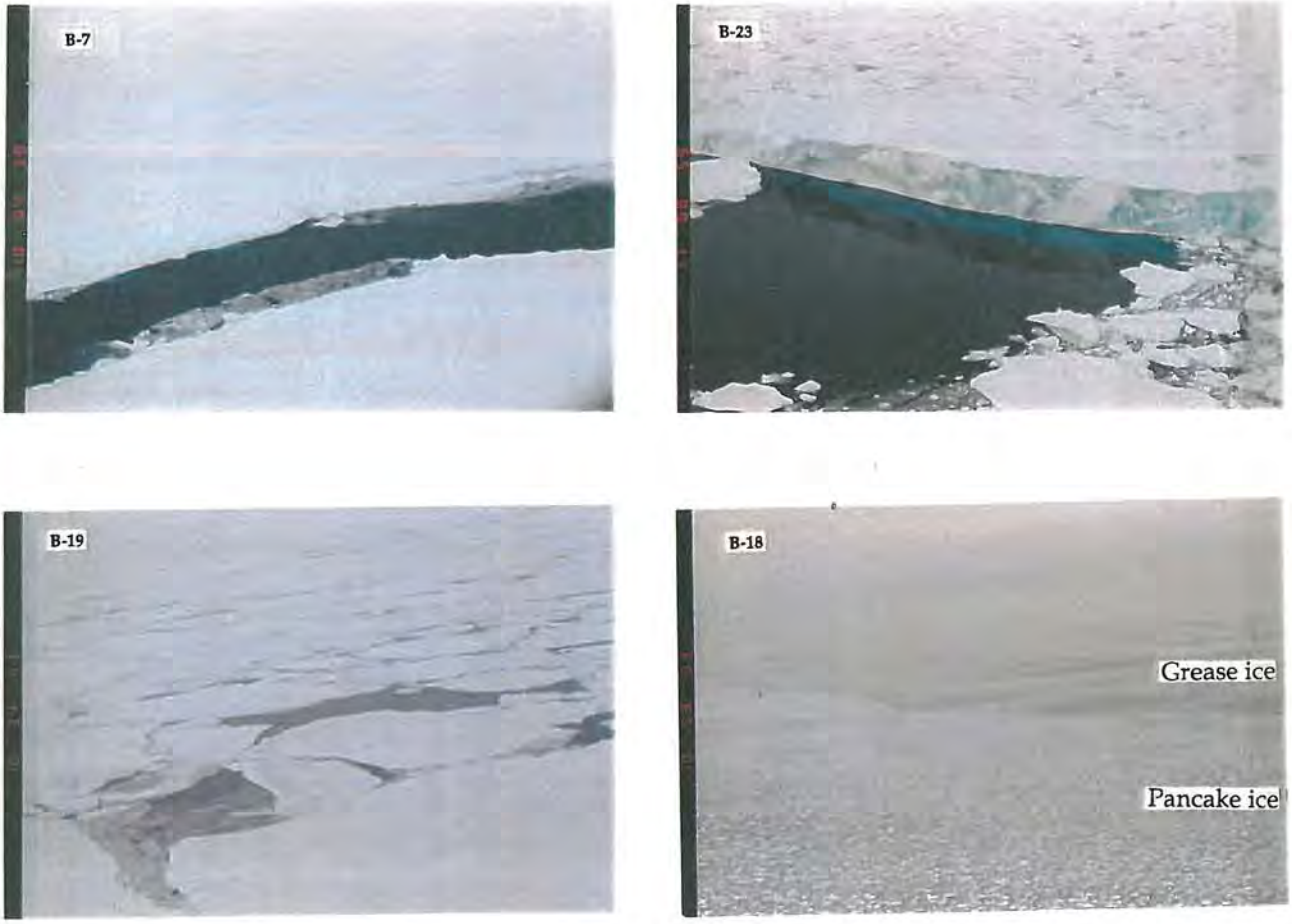

Figure 6.10 Photographs showing ice conditions at four sonobuoy locations on March 9, 1992.

Due to low visibility (fog and low stratus clouds) no photographs were taken in the southern part of the experiment area. The ice conditions in north and south are quite different; in the northern part the floe size is 100 m or more, concentration is more than 95 %, and there are many leads between the floes with open water or new ice. The leads are generally oriented in a north-south direction. Buoys no. **5**, **7**, **8**, **9** and **11** were deployed in open and refrozen narrow leads. Some smaller pressure ridges (< 1 m) were observed. In the northernmost area, which was not covered by sonobuoys, the ice field was more consolidated with a mixture of multiyear and first year ice. Between buoy **5** and **7** the ice is very fractured. Near buoy **21** the ice was broken up and closely spaced, small cracks were seen. Several icebergs were observed which had typical horizontal scale of 100 m.

Icebergs in this area are not grounded and were observed to drift, but with different velocity compared to the sea ice which generated a lead of open water in the wake of the icebergs. Icebergs were observed near buoy **21**, **23** and **12**. Both **23** and **12** were deployed in a wakes behind two different icebergs.

In the area near the ice edge (at about 77.0° N) the floe size is typically to 5 - 20 m. Most of the ice floes are 1 - 2 m thick firstyear ice. Near open water pancake and grease ice are found. The southern part of the area (between 76.5°N and 77.0° N) is dominated by a mixture of grease ice, pancake ice and patches of open water.

6.5.1.3 Observation of Animals in the experiment area

Animals (whales, seals and polar bears) were observed visually from the aircraft in most of the experiment area. The highest concentration of animals was in the ice edge zone and especially around buoy **18** where hundreds of whales were observed from the P3 aircraft. Whales were also observed near buoy **20**. Seals and polar bears were seen between buoy **5** and **7**. Ambient noise data for further analysis were selected from periods with low impact of animal sound.

6.5.2 Acoustic observations

Horizontal maps of ambient noise at four frequencies are shown in Figure 6.11. The data consist of 3 minute averaged ambient noise levels at 40, 100, 315, 1000 Hz from all sonobuoys taken at 1400 Z. It is clearly seen that the lowest levels at all frequencies are found in the southern part of the area where mainly grease ice, pancake and open water is present. The highest gradients in this region are found at 40 Hz. The levels at 40 Hz vary between 59 - 80 dB, while the levels at 1000 Hz vary between 57 - 63 dB. At 40 Hz the lowest level is observed at buoy **4S** which was deployed in an area with mixed ice conditions (pancake ice and open water). The lowest level at 1000 Hz is found at buoy **63** which was deployed in an are dominated by grease ice.

In the area of compact 2 m thick ice north of the ice edge the level is higher than for thin ice and open water. The local variability is larger; at 40 Hz the levels varies between 72 - 96, while the levels are between 56 - 76 dB at 1000 Hz.

The highest levels at all frequencies are found in the area of most broken up and compacted ice, located around the position of R/V Polarsyssel (Figure 6.11).

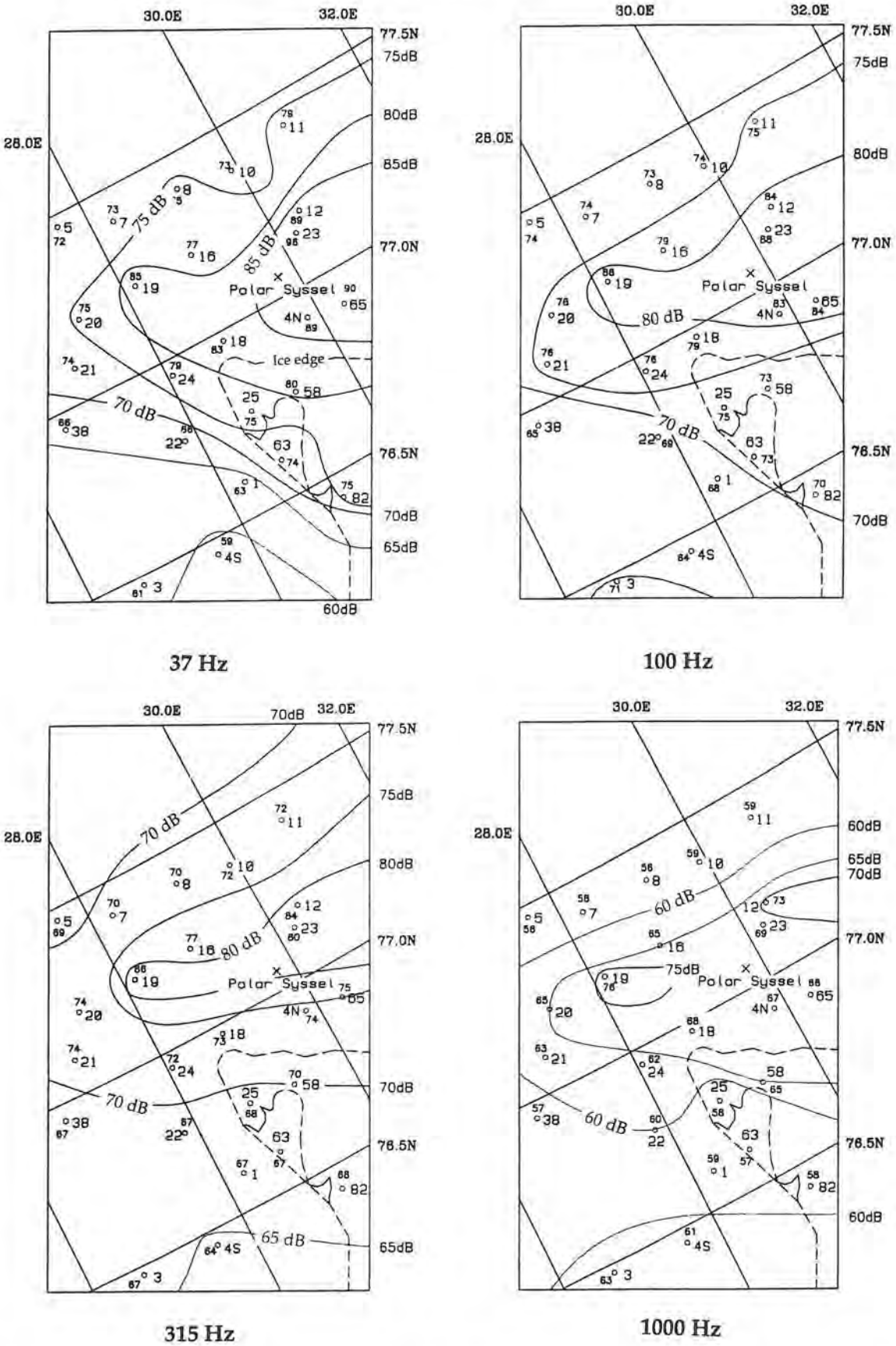

Figure 6.11. Maps of averaged ambient noise level at 40, 100, 312 and 1000 Hz, obtained at 14:00 Z on March 9, 1992. The small fonts indicate the noise level in dB, while the large fonts show the buoy numbers. The full lines are isolines for noise levels at 5 dB interval and the dashed line is the ice edge.

Clear hotspots are found within this region at three buoys: no **19**, which has a clear maximum at 1000 Hz (76 dB), no **12**, and no **23**, which both have maximum at 40 Hz. Buoy **19** is located in lead with new ice, and there is no obvious reason which can explain this hotspot. Buoy **23** and **12** are located in wakes behind drifting icebergs, and the maximum noise level can be attributed to interaction between swell and the icebergs.

6.6 Summary and comparison of results

Due to the different geographical locations of the experiments, different environmental conditions, and different hydrophone depths only a qualitative comparison of the four cases can be done.

6.6.1 The effect of swell

None of the experiments were carried out in real rough conditions. The 1987 experiment had the most pronounced wind and wave conditions of the four case studies, with 5 - 9 ms^{-1} wind and 0.7 - 1.5 m significant wave height. In 1985 the wave field outside the ice edge was dominated by short waves with period of 3-4 s and less than 0.50 m significant wave height. In 1987 and 1989 the wave field was dominated by long waves (swell) with period of about 13 s and significant wave height less than 2 m (summarized in Table 4.3).

The ambient noise was higher in 1987 than in 1985 and 1989 both outside the ice edge and within the compact ice. Along the ice edge the ambient noise was 8 - 10 dB higher at all frequencies in 1987 than in 1985, which is comparable to the variation in ambient noise levels observed along the ice edge in 1987. This reflects how the response of ice floes to ocean waves are influenced by varying ice edge composition, diffuse and compact ice edges, and ice edge configuration relative to the wind field and wave field.

The smallest influence on mean ambient noise caused by wind and waves is found to be in the compact ice zone and interior ice pack at 100 Hz.

For all frequencies, except 100 Hz, the mean ambient noise levels in the compact ice zone on days without swell were between 4.8 dB and 7.3 dB below the mean level on the rough day in 1987. The noisy conditions in the compact ice zone are due to the response of the coupling of long ocean surface waves to the compact ice cover. A significantly higher mean ambient noise level in the interior ice pack was observed in 1987 compared to 1985. This noise is most likely generated in the adjacent compact ice zone due to the strong interaction with swell and the ice cover. Some noise is also generated in the transition zone between the compact ice zone and the interior ice zone due to break up of larger ice floes by the swell. Possible sources in the interior ice pack are due to ridging and thermal cracking, these are more local and much more sporadic in time than the swell-generated noise in the compact ice zone. During periods of no swell, less noise is generated in the compact ice zone and therefore broad-band local sources will dominate the noise field in the interior and cause relatively large horizontal variations in ambient noise as observed in the interior ice pack in 1985.

Table 6.1. Comparison of local maxima found in averaged ambient noise level at 315 Hz and 1000 Hz with the mean ambient noise value for the corresponding zone where the maximum occurs. The maxima may be classified into following two generating mechanisms: A Ice edge/ wind; B Deformation zone/ Current shear. Distance from ice edge is given in km, with positive values into the ice.

a) 315 Hz

Year	Buoy ID	Zone	Mean level	Hotspot	Difference between hotspot and mean level	Distance from ice edge	Generating mechanism
1985	c	Compact ice (interior icepack)	70.7 (69.1)	73	2.3 (3.9)	35.0	B
1985	i	Compact ice	70.7	73	2.3	16.7	B
1985	j	Compact ice	70.7	74	3.3	17.3	B
1985	l	Compact ice	70.7	74	3.3	1.0	B
1987	RF-18	Compact ice	78.0	81	3.0	10.0	B
1987	RF-20	Open ocean	78.0	84	6.0	0.0	A
1989	C8	Compact ice	72.3	80	7.7	16.3	B
1989	C14	Compact ice	72.3	79	6.7	12	B

b) 1000 Hz

Year	Buoy ID	Zone	Mean level	Hotspot	Difference between hotspot and mean level	Distance from ice edge	Generating mechanism
1985	j	Compact ice	63.5	66	2.5	17.3	B
1985	h	Compact ice	63.5	66	2.5	2.7	B
1985	l	Compact ice	63.5	66	2.5	1.0	B
1987	RF-18	Compact ice	69.5	73	3.5	10.0	B
1987	RF-20	Open ocean	68.0	74	5.5	0.0	A
1989	C8	Compact ice	63.4	73	9.6	16.3	B
1989	C14	Compact ice	63.4	73	9.6	12.0	B

6.6.2 Eddy-related hotspots

The most significant hotspots at 315 Hz and 1000 Hz in each region from 1985, 1987 and 1989 are presented in Table 6.1. It can be concluded from this table that the observed hotspots are located in compact ice with one exception. In the Greenland Sea experiments (1985 and 1987) eddy-related maxima of 2.0 - 3.5 dB above the mean level are located in deformation zones near the eddy centre or at the periphery of the eddy. The presence of swell superimposed on the eddy current in 1987 seems to enhance the maximum level at 1000 Hz close to the eddy center (RF-18), when compared with calmer conditions in 1985. In 1987, a significant hotspot which was 5.5 dB above the mean level was found close to the edge of an ice tongue with on-ice winds. This was the highest noise level observed for all frequencies in the eddy areas.

In the Barents Sea in 1989, the most significant hotspots at 315 and 1000 Hz were related to deformation zones in the inner part of the compact ice zone. These hotspots

were 6.4 to 9.0 dB above the mean level in the compact ice zone (Table 6.1). The strong horizontal gradients in ambient noise observed in 1989 can be attributed to the shallower receiver depth, different sound propagation conditions, stronger gradients in currents and ice conditions and also due to a denser sampling of the eddy region.

6.6.3 Hotspots related to icebergs

Maximum levels during the SIZEX 92 experiment was found in the wakes behind drifting icebergs surrounded by high concentration of 2 m thick firstyear ice. The wakes of open water are generated because there is a difference in drift velocity between sea ice and the icebergs. Drifting icebergs have been observed to cut up larger floes of sea ice, furthermore it has been observed that swell affects both the surrounding ice field and icebergs.

6.7 Concluding remarks

Swell has, in several previous papers (Diachok, 1974, Makris 1991), been postulated to be the most important sound generator within the ice pack in the MIZ. In this study the comparison of four different experiments shows that swell propagation into ice pack increases the mean ambient noise in the compact ice edge zone at all frequencies, by as much as 7.3 dB at 315 Hz. These effects are of the same order as the reduction of ambient noise in the interior ice pack compared to levels obtained outside the ice edge due to the increased floe size and reduced wave activity. In fact, our data indicate that heavy swell in the compact ice zone has a slight influence on the ambient noise level in the interior ice pack at the selected frequencies, except at 100 Hz were no influence is observed.

Based on the results from the four experiments, it is concluded that there exist at least three types of ambient noise maximum levels for high frequency noise (315 - 1000 Hz):

- The first type is found in regions of high ice concentration and large shear in ice velocity. Such zones are frequently found within ice edge eddies and vortex pairs, both as dense bands of ice in the diffuse ice edge zone, and in the compact ice zone.

- The second type are hotspots along the ice edge that occur due to the local variations in ice edge configuration; they depend strongly on the wind and wave direction relative to the ice edge. These hotspots may also be related to the ice edge eddies through their impact on the ice edge configuration.

- The third type of hotspots is found in the Barents Sea where icebergs interact with the sea ice. The relative difference in ice drift between sea ice and icebergs is an important mechanism to break up sea ice into smaller floes, which is a dominant sound generating mechanism.

The first type is related to high ice concentration and corresponding high internal ice stress found in eddies and in compact ice edges. Strong horizontal ice velocity gradients in eddies can generate local maxima in internal ice stress which generate high levels of ambient noise. Gradients in the water masses caused by eddies and

fronts generate anomalies in sound propagation conditions, as shown in the models by Mellberg et al (1987, 1990). It can therefore be concluded that large gradients in ambient noise in eddies is a combined effect of high concentration of sources in limited regions of high ice concentration and propagation anomalies caused by the eddy current.

The results of this study suggest that a detailed characterization of the ice edge, including determination of its direction relative to the wind and dominating short wave fields, is important input data in ambient noise prediction algorithms. Furthermore, this study shows the necessity of identifying and localizing oceanographical mesoscale processes for the identification of regions of high ambient noise level in the frequency band 300 Hz to 1000 Hz. Several authors have suggested that the ice edge may be looked upon as a line source. Buckingham (1990) suggested to treat the ice edge as a ribbon source due to a significant sound generation within the compact ice edge driven mainly by the interaction between swell and the ice cover. According to the large variability of ambient noise levels observed along the ice edge we suggest that the line or ribbon source concept has to be given an amplification function which has several input parameters such as ice edge configuration and composition, directional wave field and current field (including ice edge eddies).

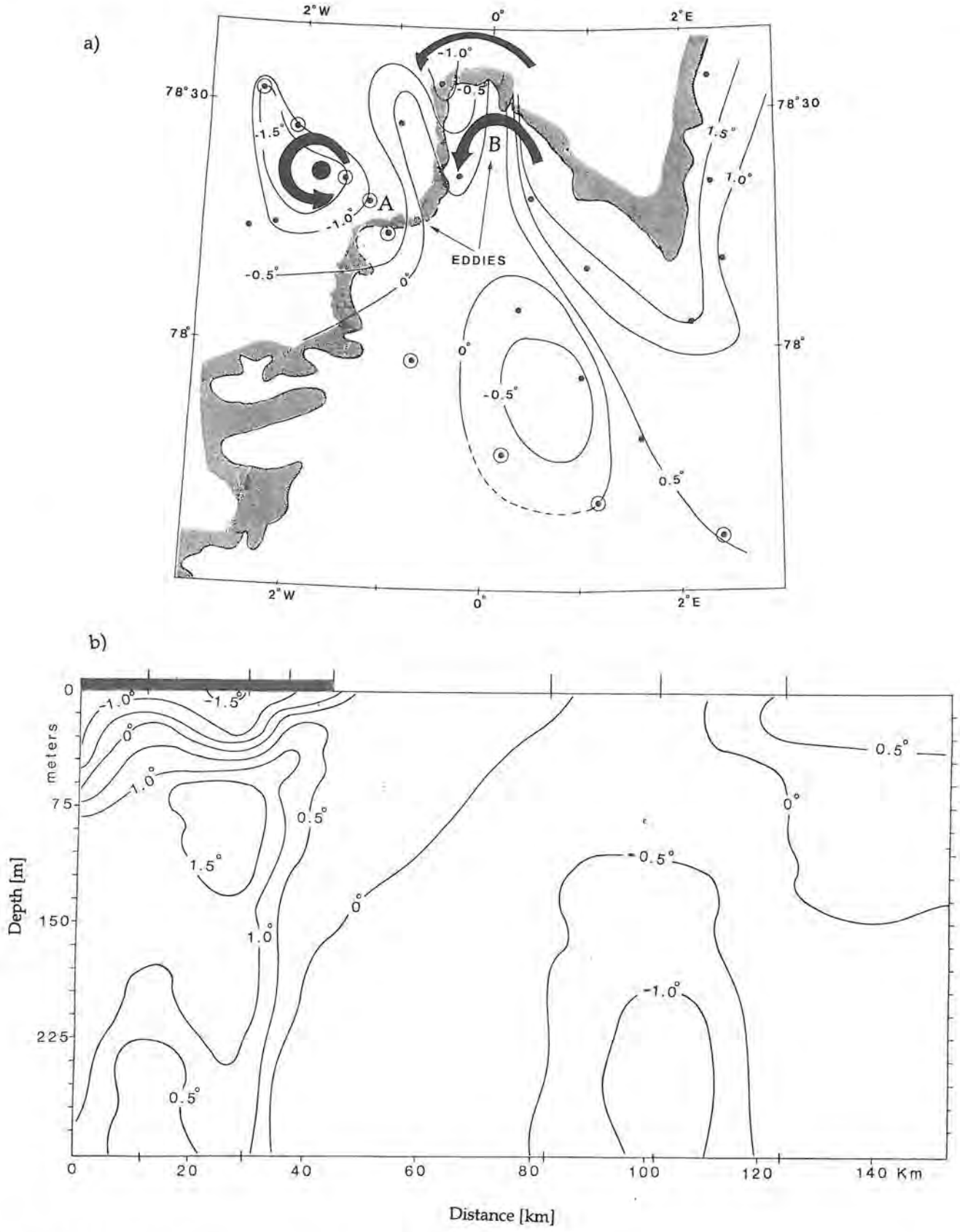

Figure 6.2 (a) Map of ice edge in the experiment area 30 April 1985 with horizontal contours of temperature (° C) at 5m depth. The dots represents location of the AXBTs; the circled dots are the buoys used in the vertical temperature section shown below . **(b)** Vertical section of temperature (° C) along a NW to SE transect though eddy "A". The vertical ticks at the top of the figure indicate the position of the AXBTs used to estimate the temperature structure.

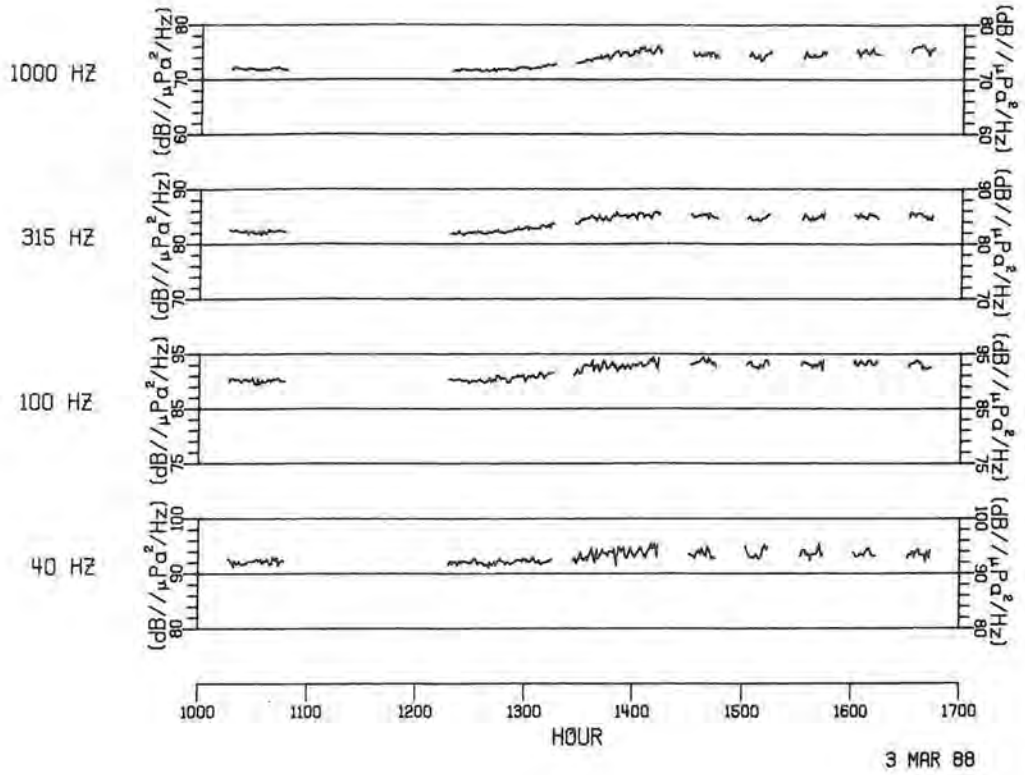

Figure 6.6. Time series of ambient noise at 40, 100 315 and 1000 Hz observed at **RF 20**, April 2, 1987.

RF-2, which was located in thin ice at the head of the ice tongue where a vortex pair is located, had a similar and larger increase at 100 Hz, 315 Hz and 1000 Hz, but it recorded no observable increase at 40 Hz. A comparison of time series between **RF-20** and **RF-2** at 1000 Hz shows a time delay of 30 minutes at **RF-2**. It appears that the response to the change in wind direction is stronger, but "slower" in thin ice (**RF-2**) than at the compact edge near the ice tongue (**RF-20**). The time delay at **RF-2** may indicate that some time is needed to form ice concentrations high enough to increase the interaction between ice floes. The change in the wind direction does not change the fetch significantly for any of the other sonobuoys, and there are no records of any increase or reduction in noise level for any of the other sonobuoys along the ice edge.

From the analysis above it is concluded that the ice edge eddy at 78 N showed a significant and local hotspot close to the eddy center located inside of the compact ice edge. The most pronounced hotspot, however, was observed in open water near the ice tongue with on-ice wind direction. This last observation modifies the hypothesis made by Yang et al., 1987. Hotspots along the ice edge can also be generated by on-ice wind component and corresponding wave action on the ice edge.

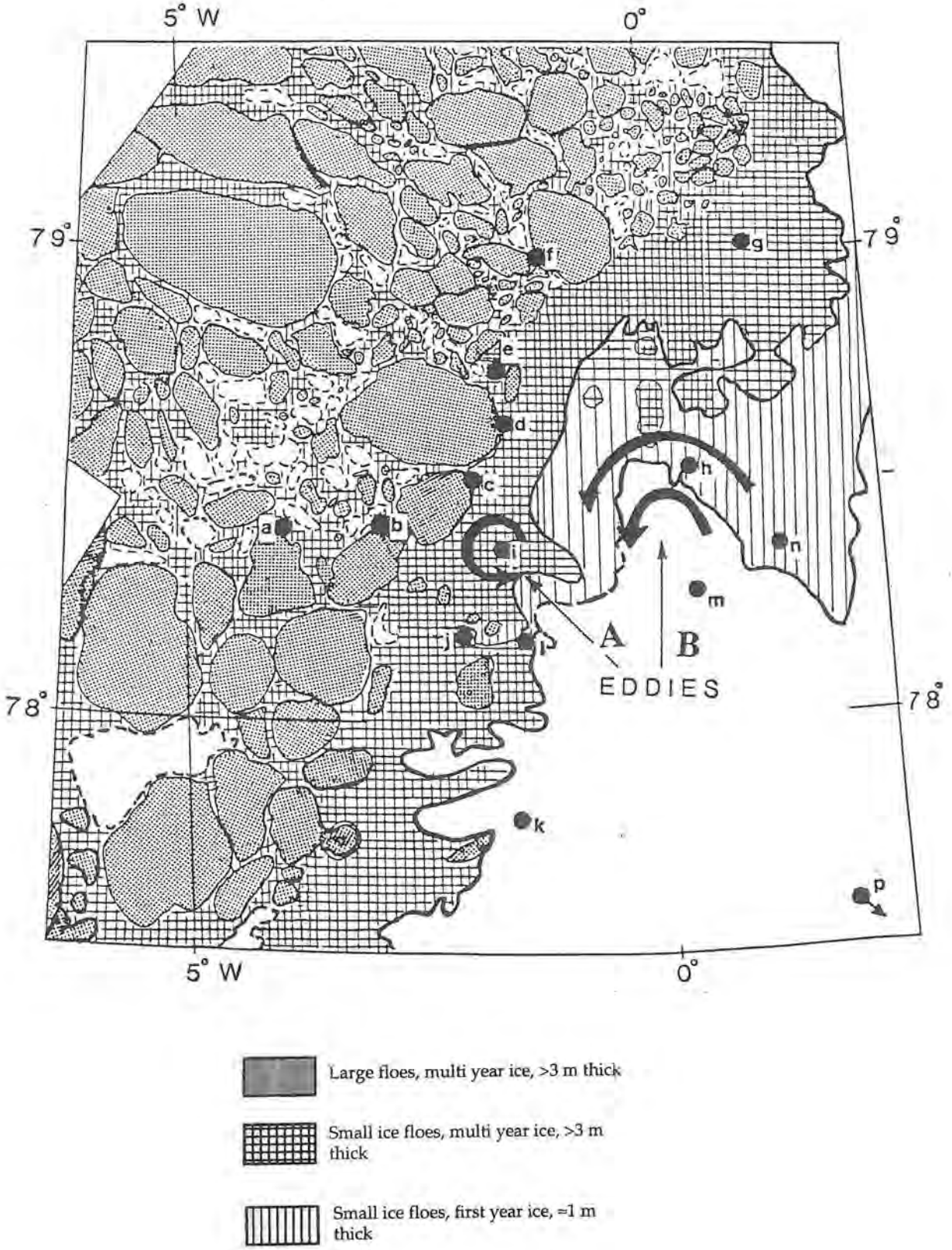

Figure 6.1 (a) Schematic ice map of the ice edge produced from NOAA AVHRR satellite image on April 30, 1985 with the sonobuoy positions marked as bold dots (a to p). Eddy "A" is within the ice and eddy "B" is on the ice edge.

the ice. The short waves had a northerly direction and a wavelength of about 20 m. The amplitude was estimated to be approximately 1 m in the south (between buoy 3 and 4) and 2 m in the north (near buoy **18**). Inside the ice edge, the wind was blowing at 2 - 10 m/s from southerly directions, the ice edge was moving northwards and the swell was significant with a main period of about 13 s estimated from in situ observation onboard R/V Polarsyssel.

6.5.1.2 Ice conditions.

Ice information on March 9 was obtained from the SAR image and helicopter surveys on the previous day and from visual observations and photographs that were taken each time a sonobuoy was deployed in the northern part of the area (Figure 6.10).

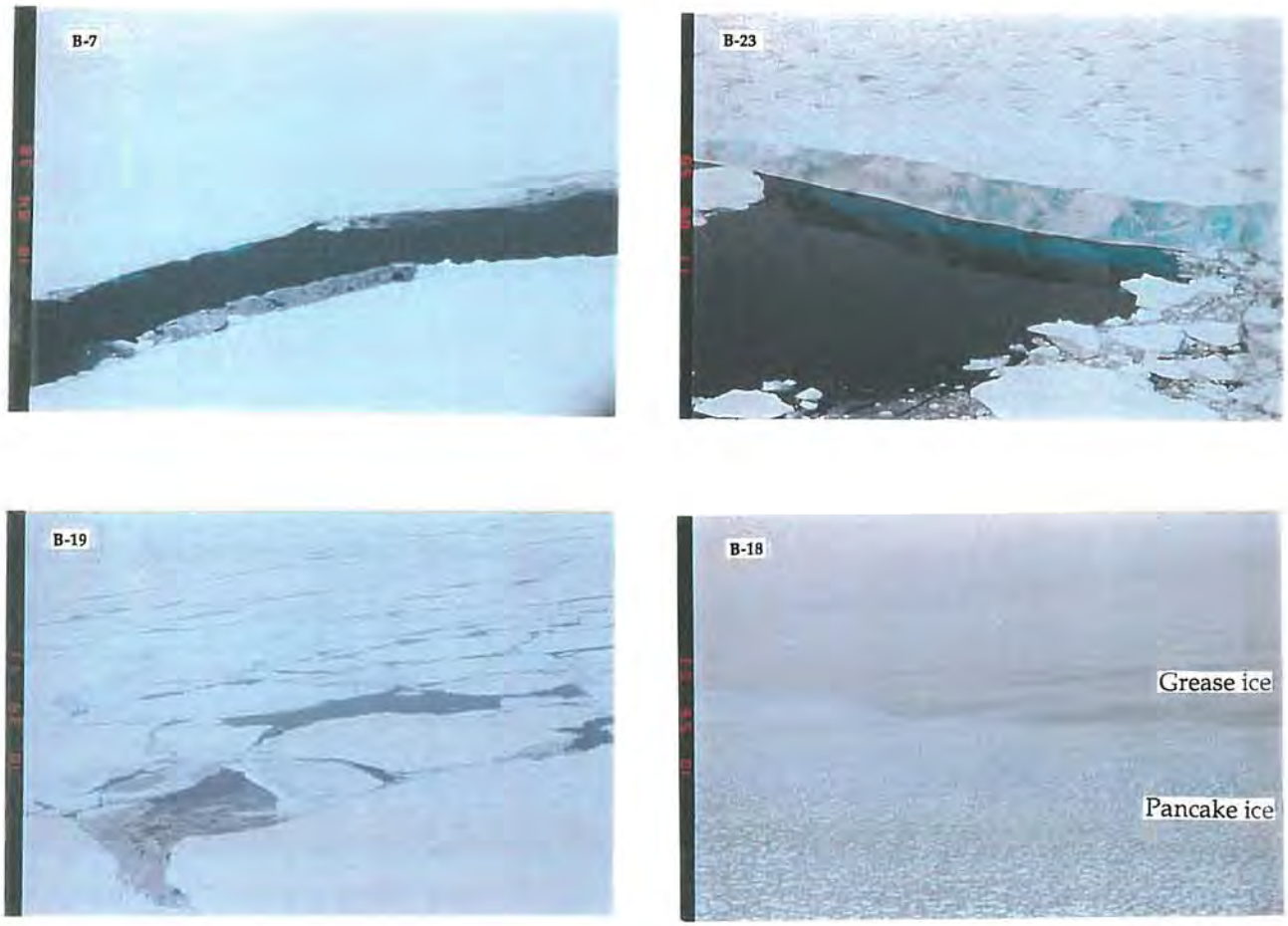

Figure 6.10 Photographs showing ice conditions at four sonobuoy locations on March 9, 1992.

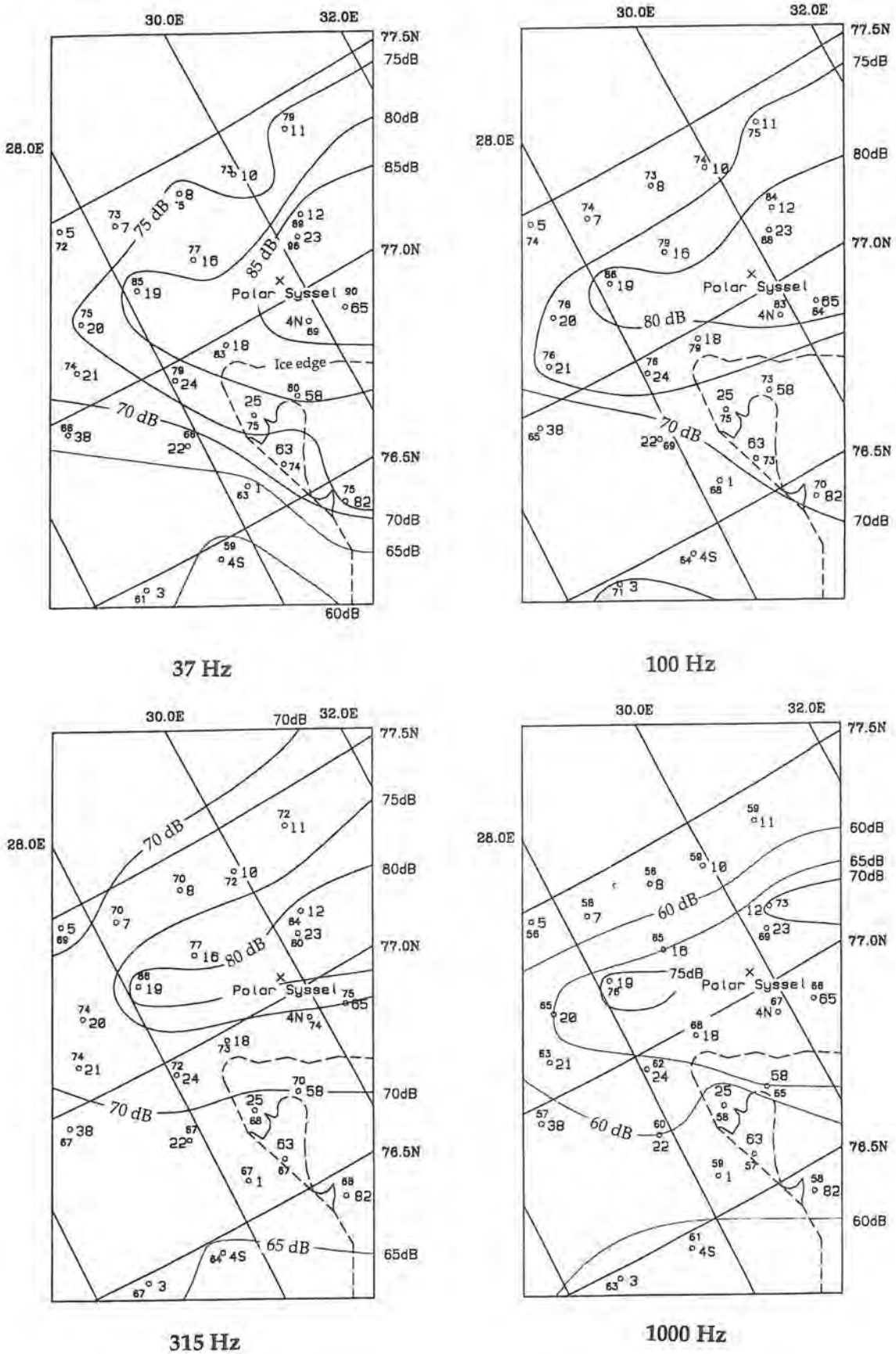

Figure 6.11. Maps of averaged ambient noise level at 40, 100, 312 and 1000 Hz, obtained at 14:00 Z on March 9, 1992. The small fonts indicate the noise level in dB, while the large fonts show the buoy numbers. The full lines are isolines for noise levels at 5 dB interval and the dashed line is the ice edge.

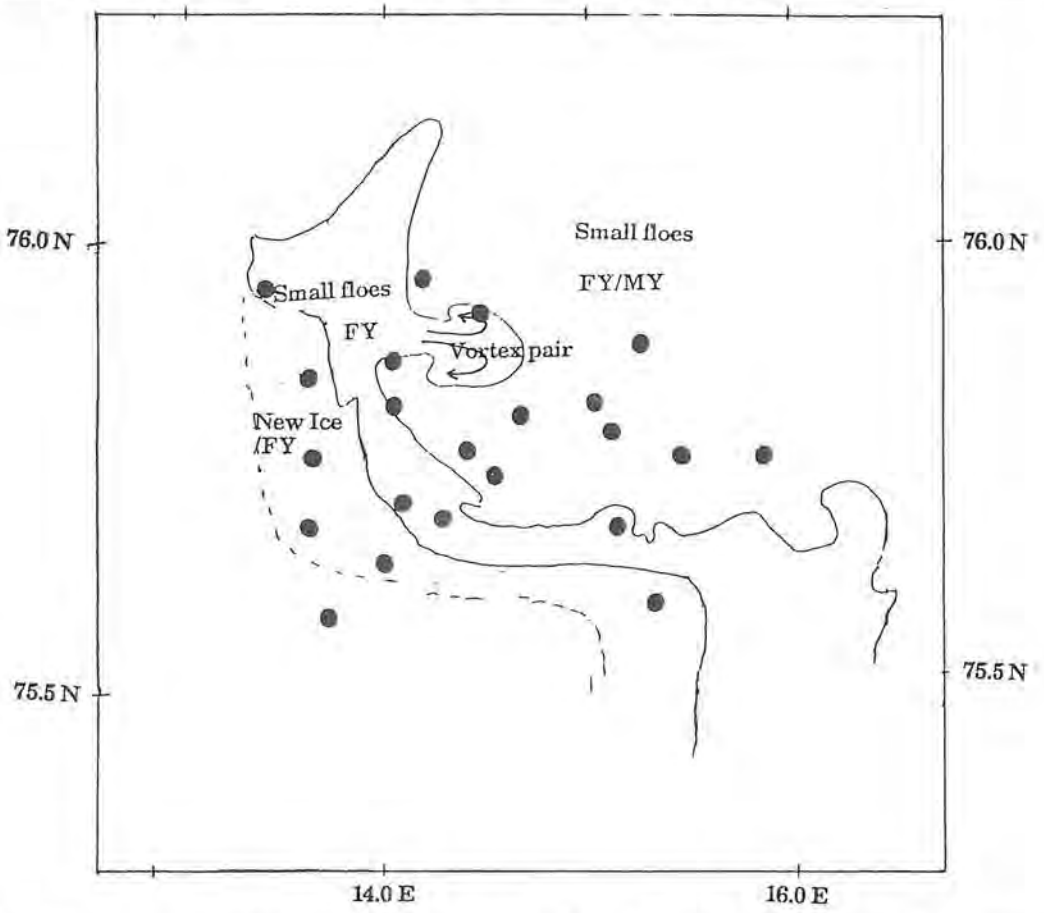

Figure 6.7 (b) Interpretation of the SAR image in the area of sonobuoy deployment, showing the location of the vortex pair near C25.

Figure 6.7 (c) Aerial photograph of the vortex pair shown in (b).

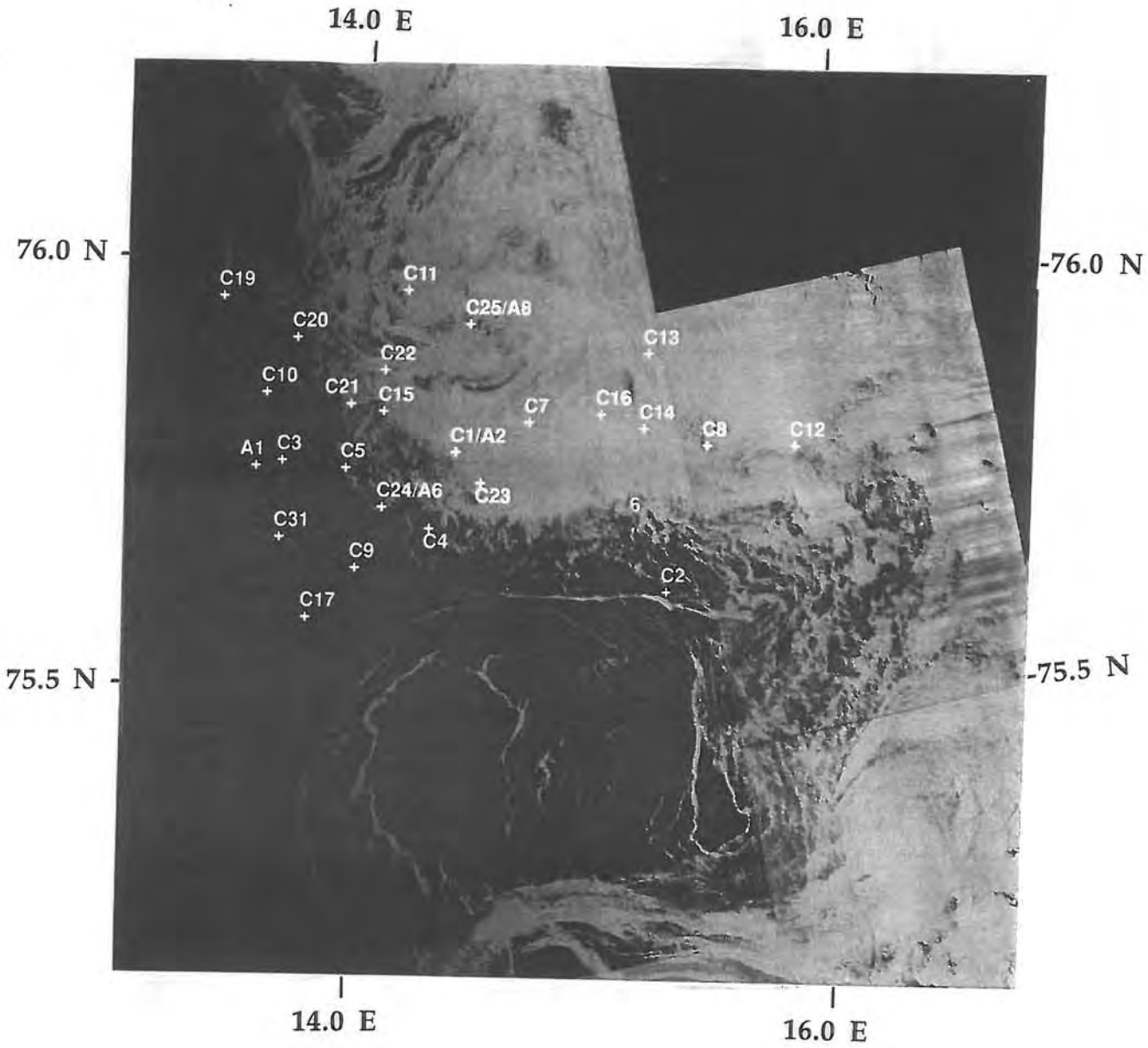

Figure 6.7 (a) SAR image of February 27, 1989, with the sonobuoy (C) and AXBT (A) positions marked by numbers.

Figure 6.1 (b) Aerial photograph of eddy "A". The distance across the image from left to right is 20 km.

6.2.2 Acoustic observations

6.2.2.1 Examination of the horizontal variation of ambient noise levels

The ambient noise levels at 122 m depth vary considerably at all the four investigated frequencies in the study area. Figure 6.3 shows the variation of ambient noise as a function of least distance from the ice edge. At 40 Hz and 100 Hz there is no clear peak in noise at the ice edge. Across the ice edge, the 40 Hz level is fairly constant, but 15 - 20 km into the ice pack the horizontal variability increases to 8 dB. The maximum level at 40 Hz was observed in the northern part of the experiment area where buoys **f** and **g** were deployed. Buoy **f** was located between large ice floes and showed a level of 88 dB, while buoy **g** which was located between small multi-year floes showed a level of 89 dB. . The variability is 8 dB at 40 Hz, 5 dB at 100 Hz, 7 dB at 315 Hz and 9 dB at 1000 Hz.

At 100 Hz the ambient noise level is fairly constant over the entire experimental region, except for a maximum of 2 dB, 35 km into the ice pack, at the border between the compact ice zone and the interior ice pack. The lowest level at 100 Hz (79 dB) was observed 64 km into the ice pack at buoy **f**.

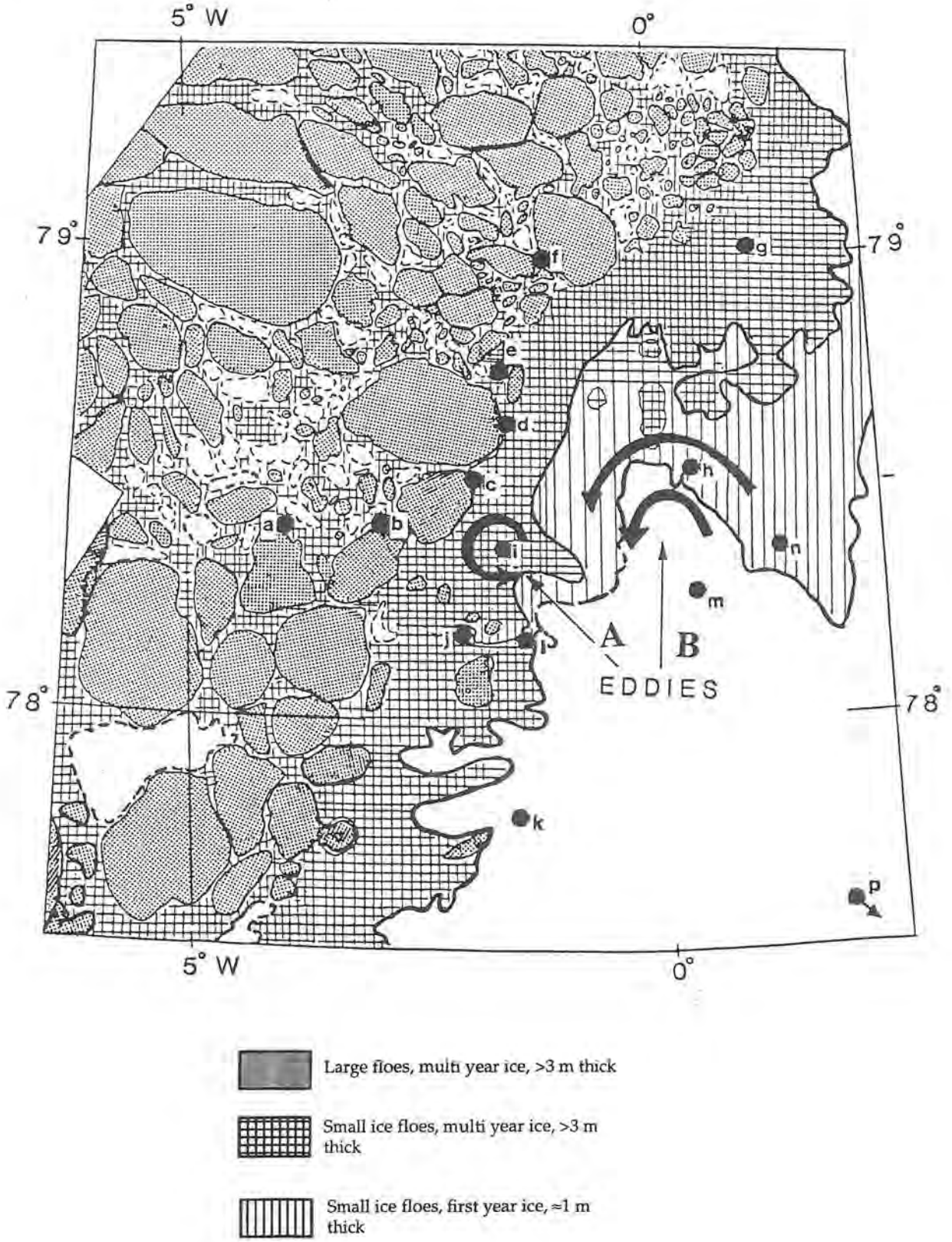

Figure 6.1 (a) Schematic ice map of the ice edge produced from NOAA AVHRR satellite image on April 30, 1985 with the sonobuoy positions marked as bold dots (a to p). Eddy "A" is within the ice and eddy "B" is on the ice edge.

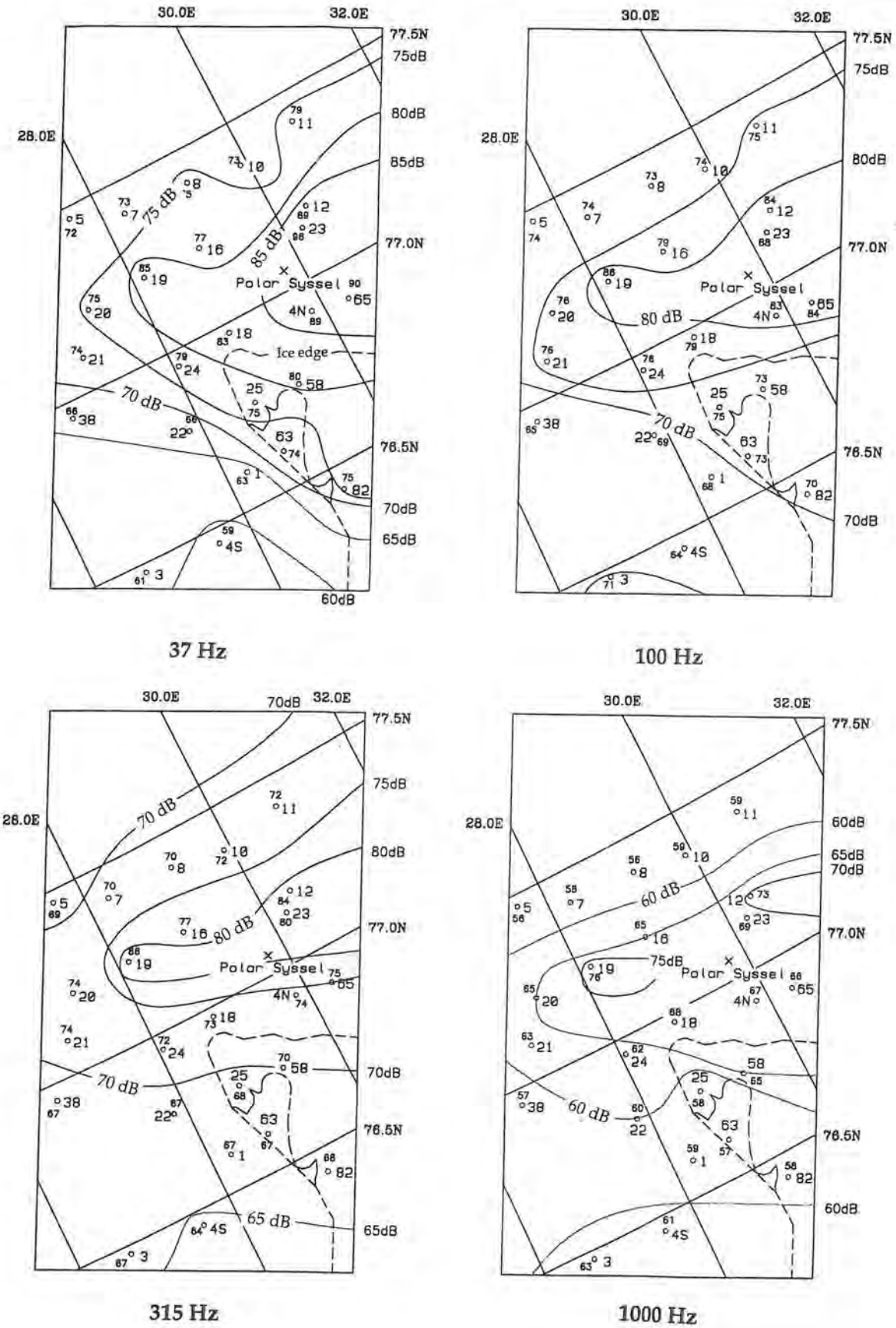

Figure 6.11. Maps of averaged ambient noise level at 40, 100, 312 and 1000 Hz, obtained at 14:00 Z on March 9, 1992. The small fonts indicate the noise level in dB, while the large fonts show the buoy numbers. The full lines are isolines for noise levels at 5 dB interval and the dashed line is the ice edge.

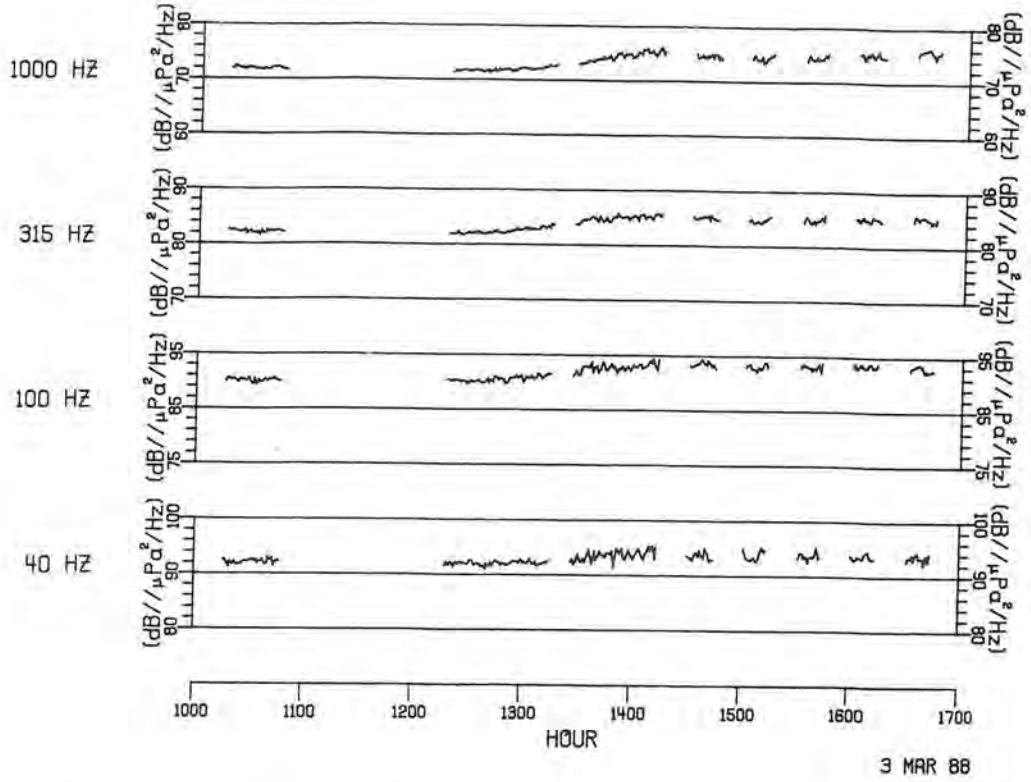

Figure 6.6. Time series of ambient noise at 40, 100 315 and 1000 Hz observed at **RF 20**, April 2, 1987.

RF-2, which was located in thin ice at the head of the ice tongue where a vortex pair is located, had a similar and larger increase at 100 Hz, 315 Hz and 1000 Hz, but it recorded no observable increase at 40 Hz. A comparison of time series between **RF-20** and **RF-2** at 1000 Hz shows a time delay of 30 minutes at **RF-2**. It appears that the response to the change in wind direction is stronger, but "slower" in thin ice (**RF-2**) than at the compact edge near the ice tongue (**RF-20**). The time delay at **RF-2** may indicate that some time is needed to form ice concentrations high enough to increase the interaction between ice floes. The change in the wind direction does not change the fetch significantly for any of the other sonobuoys, and there are no records of any increase or reduction in noise level for any of the other sonobuoys along the ice edge.

From the analysis above it is concluded that the ice edge eddy at 78 N showed a significant and local hotspot close to the eddy center located inside of the compact ice edge. The most pronounced hotspot, however, was observed in open water near the ice tongue with on-ice wind direction. This last observation modifies the hypothesis made by Yang et al., 1987. Hotspots along the ice edge can also be generated by on-ice wind component and corresponding wave action on the ice edge.

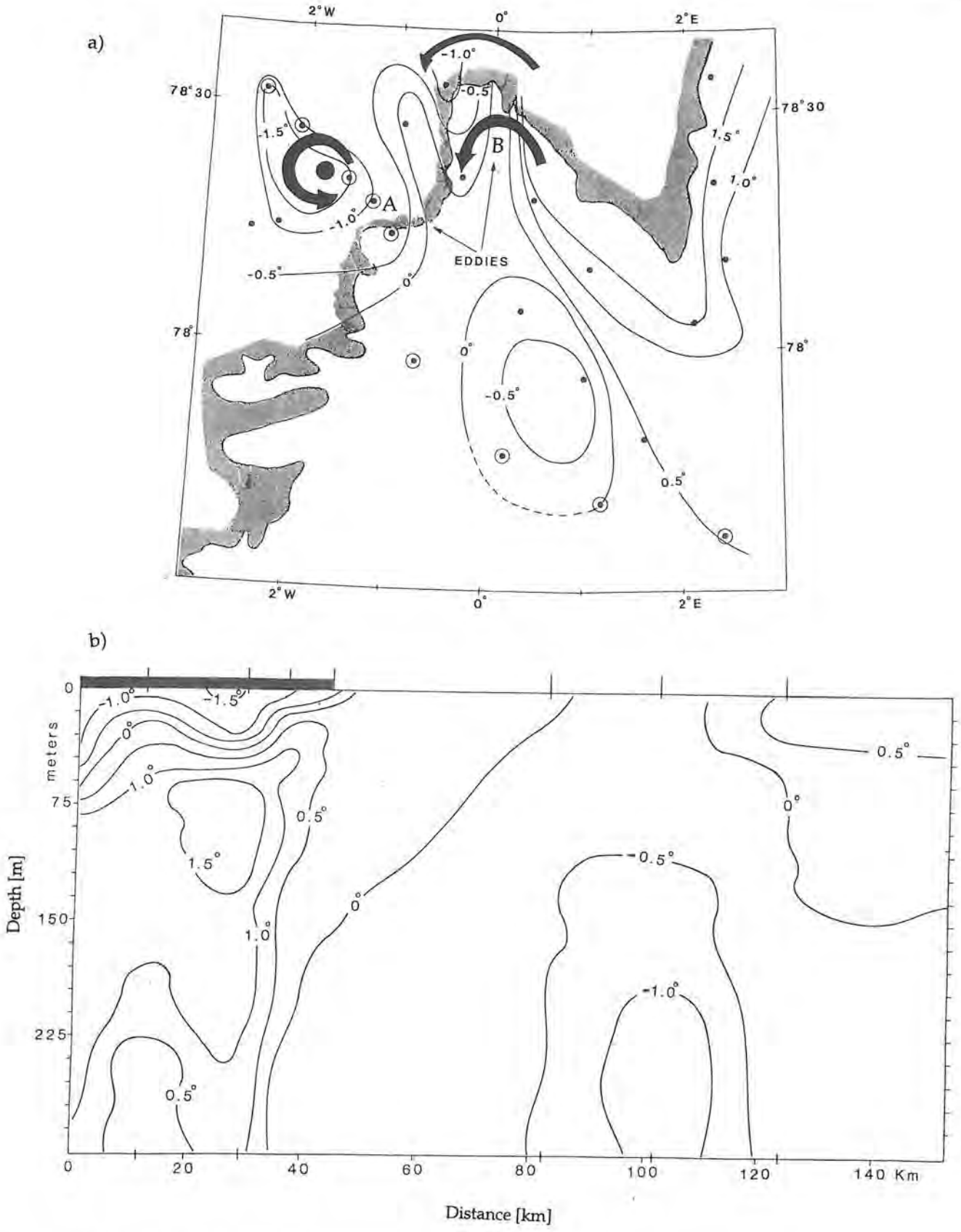

Figure 6.2 (a) Map of ice edge in the experiment area 30 April 1985 with horizontal contours of temperature (° C) at 5m depth. The dots represents location of the AXBTs; the circled dots are the buoys used in the vertical temperature section shown below . **(b)** Vertical section of temperature (° C) along a NW to SE transect though eddy "A". The vertical ticks at the top of the figure indicate the position of the AXBTs used to estimate the temperature structure.

the ice. The short waves had a northerly direction and a wavelength of about 20 m. The amplitude was estimated to be approximately 1 m in the south (between buoy 3 and 4) and 2 m in the north (near buoy **18**). Inside the ice edge, the wind was blowing at 2 - 10 m/s from southerly directions, the ice edge was moving northwards and the swell was significant with a main period of about 13 s estimated from in situ observation onboard R/V Polarsyssel.

6.5.1.2 Ice conditions.

Ice information on March 9 was obtained from the SAR image and helicopter surveys on the previous day and from visual observations and photographs that were taken each time a sonobuoy was deployed in the northern part of the area (Figure 6.10).

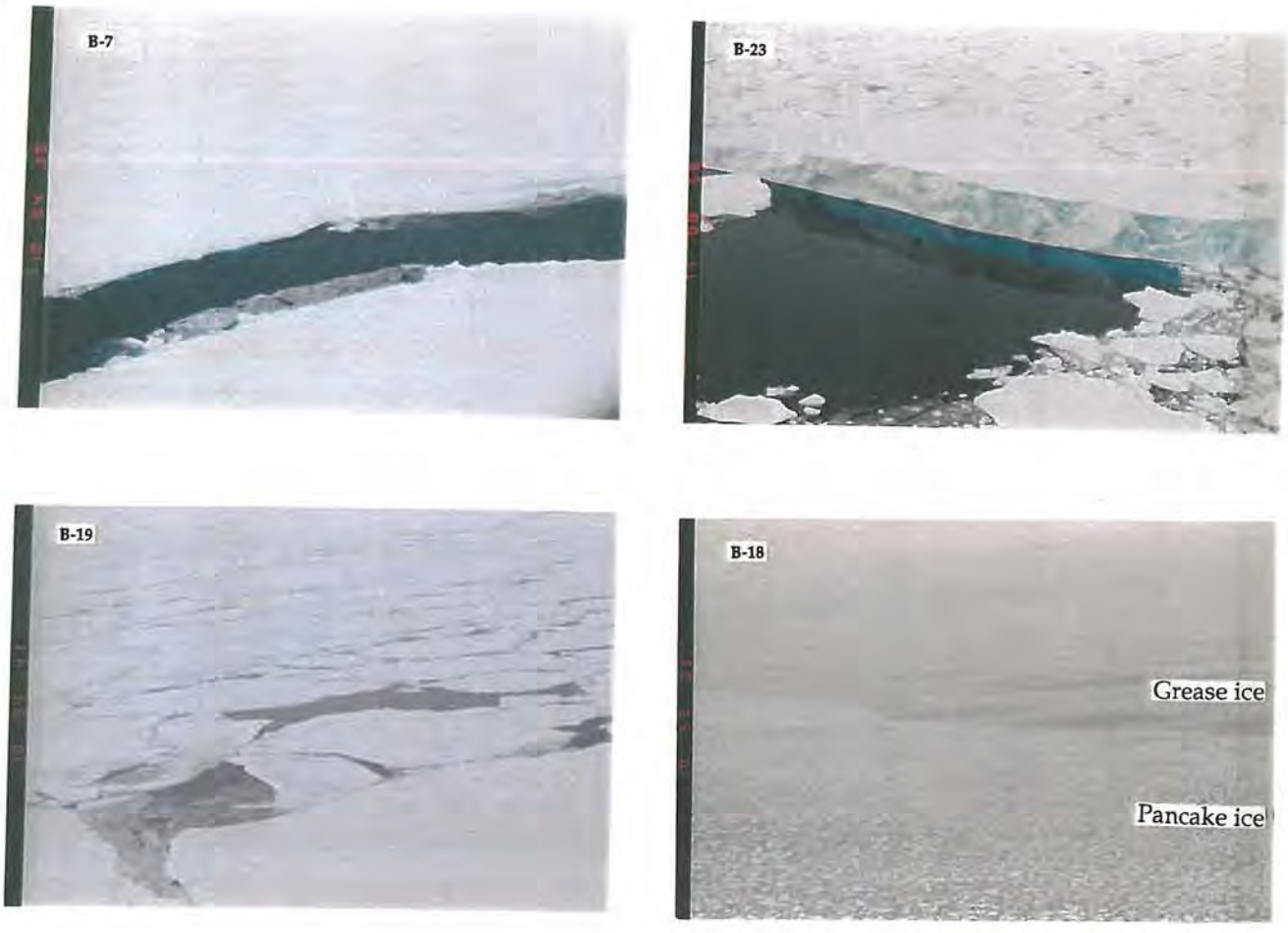

Figure 6.10 Photographs showing ice conditions at four sonobuoy locations on March 9, 1992.

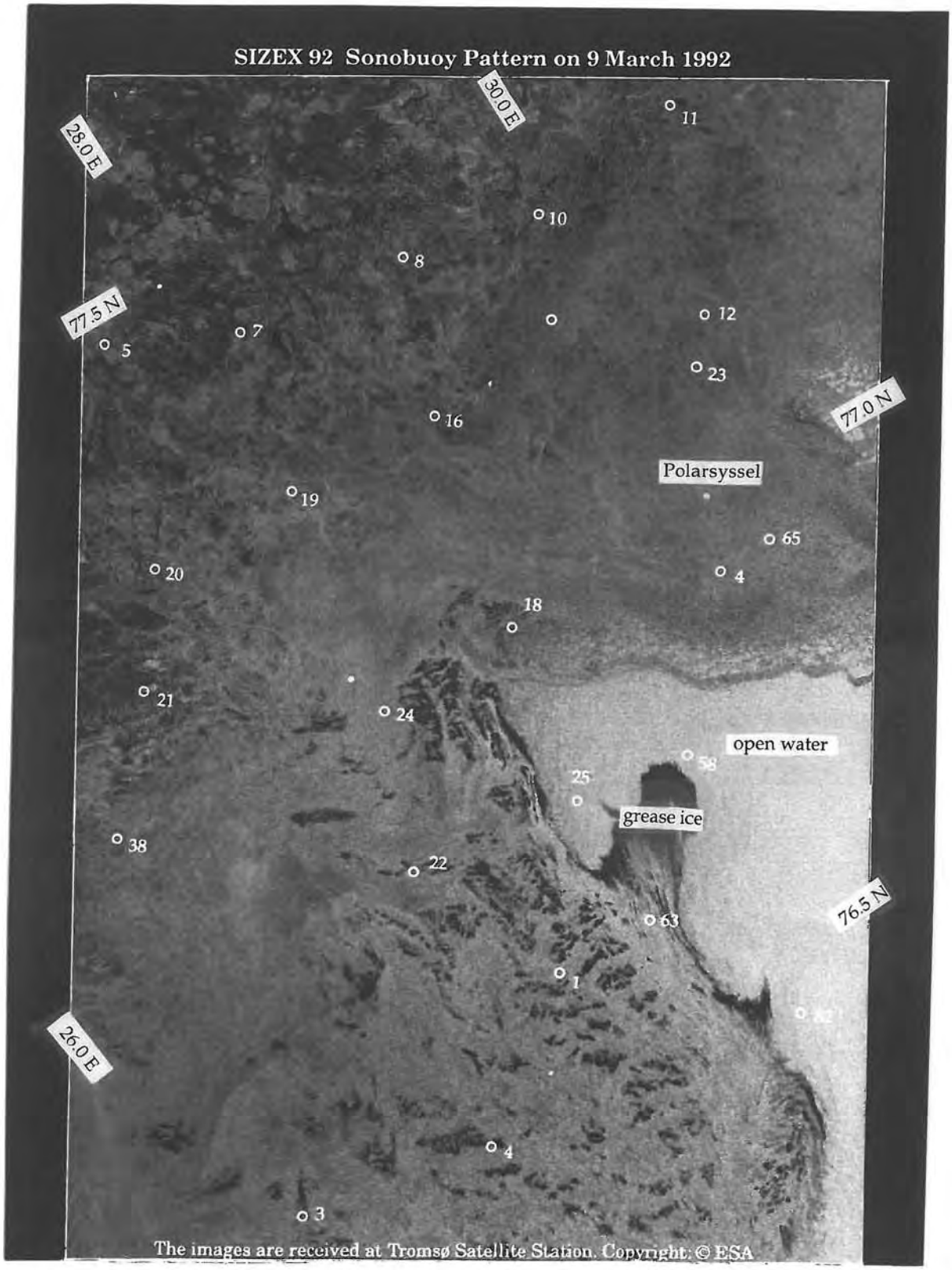

Figure 6.9 ERS-1 SAR image of March 8, 1992, covering 100 by 200 km of the MIZ in the Barents Sea east of Hopen. The sonobuoy deployment pattern of March 9 is superimposed on the image. Buoy no. 12 and 23 were deployed in the open water wakes of icebergs. Buoy 21 was deployed near an iceberg. Two buoys have the same number (4) and are denoted "4S" (southern buoy) and "4N" (northern buoy) in the text.

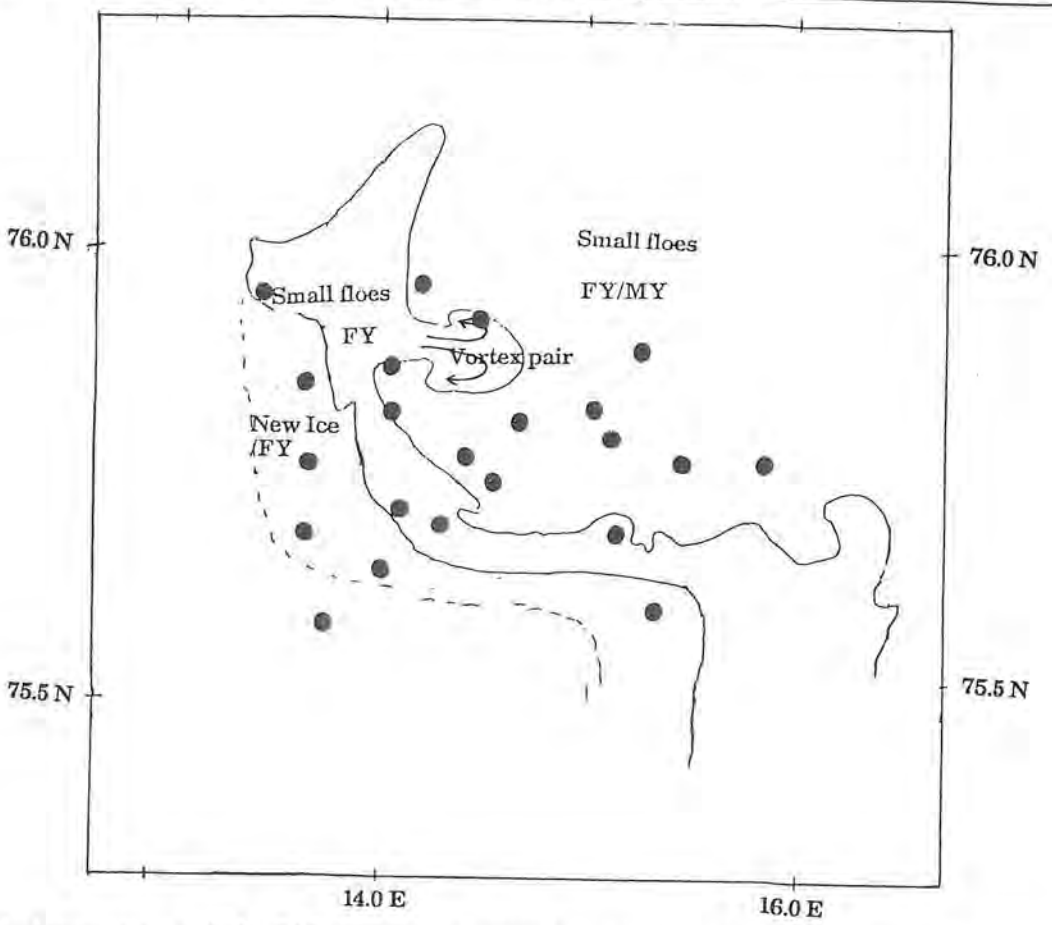

Figure 6.7 (b) Interpretation of the SAR image in the area of sonobuoy deployment, showing the location of the vortex pair near C25.

Figure 6.7 (c) Aerial photograph of the vortex pair shown in (b).

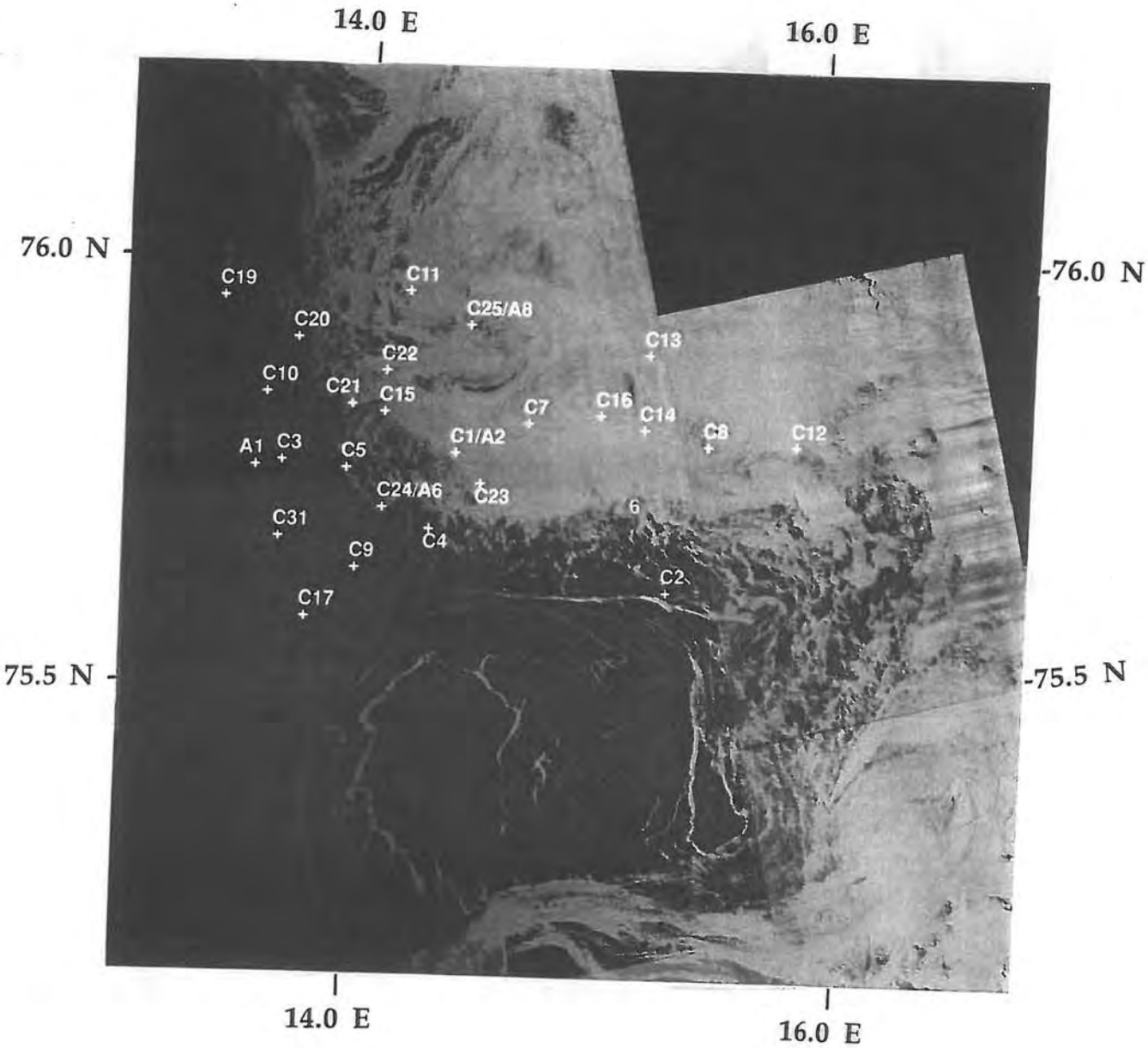

Figure 6.7 (a) SAR image of February 27, 1989, with the sonobuoy (C) and AXBT (A) positions marked by numbers.

Figure 6.4. SAR mosaic from April 2, 1987, with sonobuoy positions superimposed. The numbers are the sonobuoy ID numbers. Ice and water can easily be distinguished in SAR images because water has generally a lower back scatter (dark areas) compared with ice (bright areas). Lines **a** and **b** denote CTD sections obtained by R/V Polarcircle and R/V Håkon Mosby, respectively on this day.

7. Study of Ambient Noise Frequency spectra.

7.1 Introduction.

Ambient noise depend on sound propagation conditions, and the objective of this study is to

Investigate the effect of sound propagation conditions on broad band ambient noise.

Diachoke and Winikur (1974) concludes after a brief argumentation that "Reflection and scattering losses at the interfaces affect transmission loss and, consequently, the shapes of the ambient noise versus frequency curves". After this study very little attention have been made to the effect of propagation loss on MIZ ambient noise characteristics. As far as we can see only one work by Buckingham (1993) have focused on how the propagation conditions shapes the MIZ ambient noise frequency spectrum. According to Buckingham (1993), a typical frequency spectrum for the MIZ have a minimum below 20 Hz, an exponential decay above 50 Hz, with one kink in the decay close to 400 Hz. These observations are based on frequency spectra obtained at six locations in the Greenland Sea MIZ. The hydrophone depth setting was 160 m. Furthermore, Buckingham (1990, 1991), developed a complete and exact solution for the sound field from a point source in a semi infinite ocean with an inverse square sound speed profile and used this to calculate the ambient noise power spectrum (Buckingham , 1993 b). However, the model does not account for the effect of the ice cover and the strong horizontal gradients in sound speed profiles.

In this chapter the ambient noise frequency spectrum characteristics are characterized and related to environmental conditions. Special attention is made to ice conditions, which effect both the noise generation and sound propagation; and ocean stratification, which have a strong effect on sound propagation (See Chapter 5). In Chapter 5 sound propagation in the MIZ was studied with special attention to changes in transmission loss with frequency caused by ice and ocean parameters. Results from this study is used for interpretation.

Our study includes a large number (46) of ambient noise frequency spectra from different locations in the Greenland Sea and the Barents sea. Data included are

- MIZEX 87. April 2, 1987, located in the Fram Strait. Sonobuoys at 18 locations.
- SIZEX 89. February 27, 1989, in the Barents sea. Sonobuoys at 24 locations.
- SIZEX 92. March 6, 1992 in the Eastern Barents Sea. Sonobuoys at 4 locations.

The ambient noise spectra are described by a maximum lobe and a exponential decay with frequency, f^{-n}. The spectral slope, n, is given by

$$n = -\left[P_{dB}(f_1) - P_{dB}(f_2)\right] / 10 \cdot Log_{10}\left(f_1 / f_2\right) \qquad 7.1$$

where f_b is the break frequency, $f_b = f_1 < f_2$.

In MIZEX 87 the spectral slope has been calculated using the best fit line to the 50% percentile. Whereas in SIZEX 89-92 the slopes are calculated using the best fit lines to the averaged frequency spectra obtained at a selected time between 14:00 and 15:00.

7.2 April 2, 1987. MIZEX 87.

7.2.1 Environmental conditions

The sonobuoy positions are plotted in the SAR image (Figure 6.4), obtained simultaneously with the ambient noise recordings. A detailed interpretation of this image is performed in Chapter 2 and Chapter 6.

The sound speed contour plots in Figure 7.1 are generated from two Conductivity, Temperature and Density (CTD) sections obtained on April 2, 1987. One section is obtained inside the ice pack and one is obtained normal to the main ice edge across the diffuse ice edge and out in open ocean (Figure 7.1 a). The section within the ice pack show that a 80-90 m deep surface duct is present with the speed of sound equal to 1441 m/s (Figure 7.1 b). From 80 m the speed of sound increases gradually from 1441 m/s to 1458 m/s at 150 m. The CTD section taken outside and normal to the compact ice edge shows a 30-50 m deep surface layer, of cold polar water extending 40 km outside the ice edge, where the channel becomes shallower and strong horizontal gradients occur. The meandering of the polar front is in this case due to a jet that is observed as a 20 km long tongue of ice normal to the ice edge in Figure 7.1 a. The position of the ice tongue does not correspond to the location of the jet according to the CTD section. By considering the daily SAR images obtained during the MIZEX experiment it is observed that the tongue has been advected southwards with the East Greenland current.

In this experiment all hydrophones are deployed at 122.0 m below the sea surface. Within the ice pack, the receiver is positioned at the bottom of the surface duct where the sound speed increases gradually. In regions with a shallow surface duct, as found just outside the main ice edge, the receivers are well below the surface duct.

7.2.2 Ambient noise frequency spectra.

Frequency spectra from the interior ice pack, the compact ice zone, and from various ice conditions along the ice edge are shown in Figure 7.2. The characteristics for each spectrum are listed in Table 7.1, and summarized in Table 7.2. All the spectra have a clear maximum lobe, but with a varying band width. Widest lobes, ranging between 30-100 Hz, are found outside the ice edge (Figure 7.2; **RF-27** and **RF-8**)). In the interior ice edge the width of the lobe is much more narrow, between 20-30 Hz (Figure 7.2; **RF-5**)).

a)

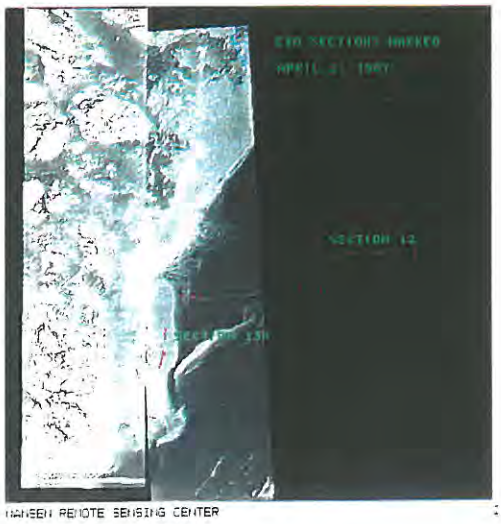

b)

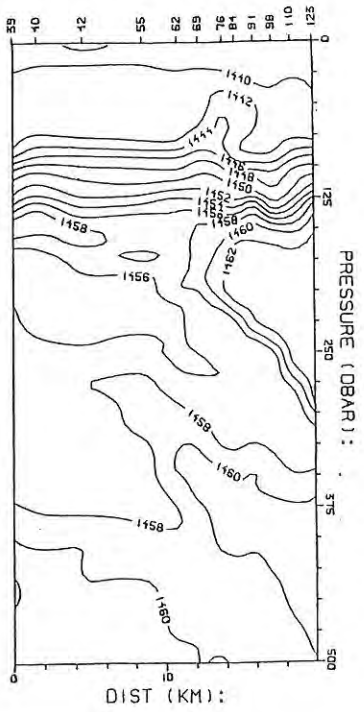

Two sound speed sections calculated
from CTD stations taken on 1-2 April.
a) Sections indicated in SAR mosaic.
b) Section 13 a. c) Section 12.

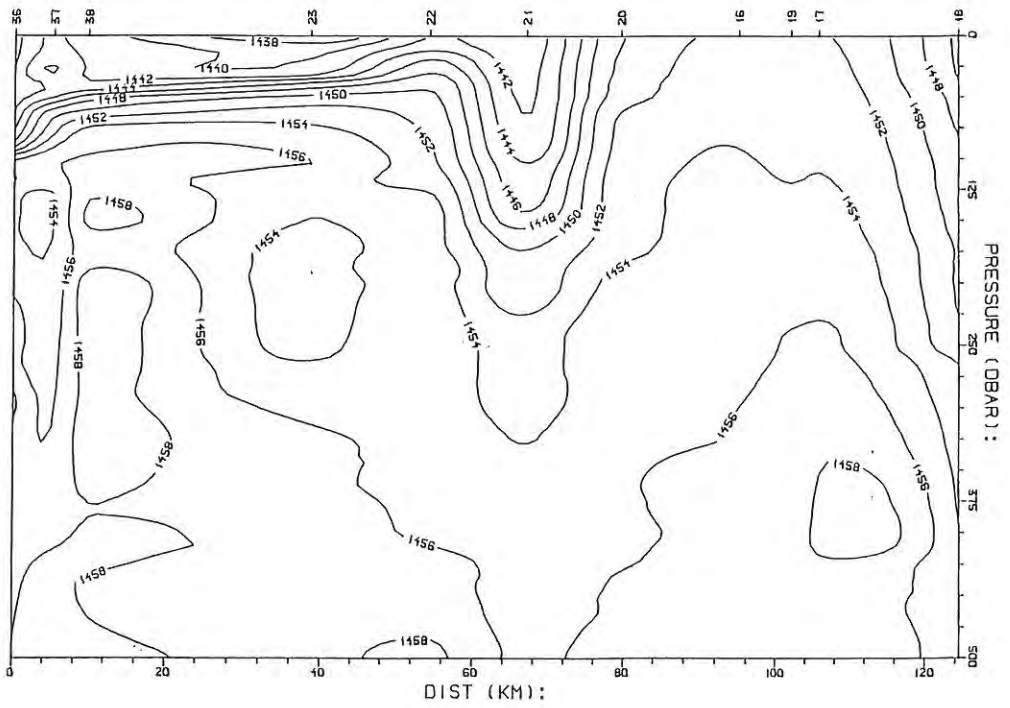

Figure 7.1. Sound speed sections derived from two CTD sections obtained 1-2 April 1987 during MIZEX 87. a) The localization of the sections are plotted in the SAR image b) Section inside the ice edge. c) Section outside and normal to the ice edge.

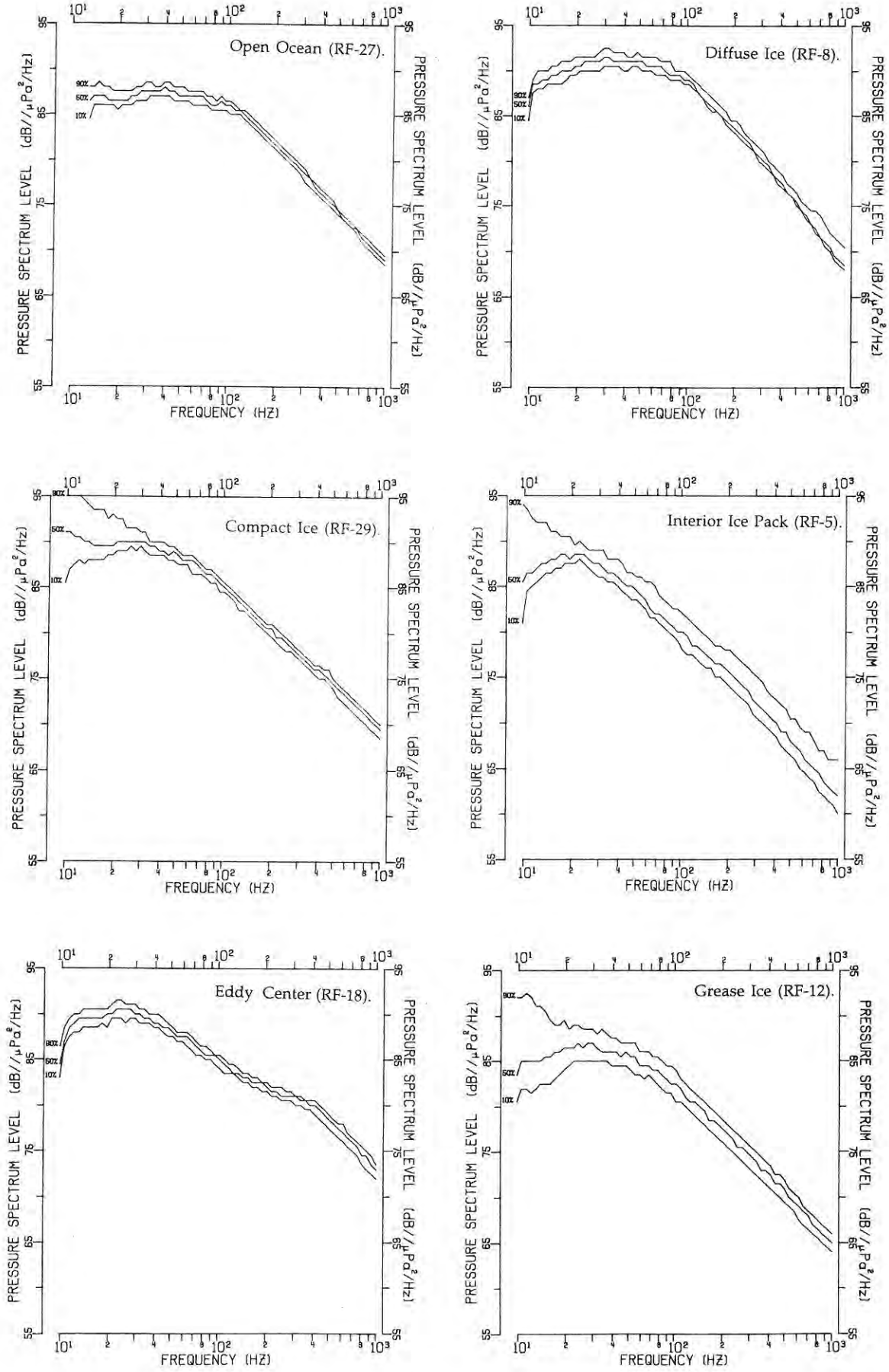

Figure 7.2 Ambient noise frequency spectra obtained April 2, 1987.

Table 7.1. Observations 2 April, 1987. Each buoy is listed along with the ice zone code, low frequency break point, and the spectral slope number and corresponding frequency domain. The data are ordered after number of kinks. Shadowed fields correspond to the locations with a low frequency break point less or equal to 40 Hz. Ice zones are defined as I: Open ocean; II: Diffuse ice; III: Compact ice and IV: Interior ice pack.

Buoy id	Ice Zone	Low frequency break point	Slope	Frequency domain.	Slope	Frequency domain.	Slope	Frequency domain.
No kink								
RF-29	III	20					1.3	(60,1000)
RF-12	II	20					1.9	(60,1000)
RF-30	II	30					1.63	(105,1000)
One kink								
RF-5	IV	20			1.5	(25,400)	2.2	(400,1000)
RF-6	IV	25			1.8	(30,400)	2.7	(400,1000)
RF-7	IV	<20			1.6	(30,400)	2.1	(400,1000)
RF-24	III/IV	20			1.3	(40,350)	1.8	(350,1000)
RF-28	II	25			1.6	(70,400)	2.2	(400,1000)
RF-14	II	no clear reduction			1.7	(90,390)	2.2	(390,1000)
RF-1	II	20			1.6	(100,290)	2.3	(290,1000)
RF-8	II	20			1.7	(90,390)	2.5	(290,1000)
RF-2	II	30			2.1	(100,390)	2.3	(390,1000)
RF-3	II	30			1.4	(100,400)	1.8	(290,1000)
RF-11	I	30			1.8	(90,350)	2.3	(350,1000)
RF-20	I	30			1.7	(100,500)	2.3	(500,1000)
RF-27	I	30			1.7	(105,250)	2.0	(250,1000)
Two kinks								
RF- 4	VI	<20	1.8	(30,100)	0.8	(100,300)	2.5	(300,1000)
RF-18	III	20	0.91	(30,100)	0.7	(100,390)	1.8	(390,1000)

Table 7.2. Summarized observations of the frequency spectrum in MIZEX 87.

Frequency domain	General Description	Specific description
$f<f_{min}$	The amplitude increases with frequency.	$f_{min}\approx$20 Hz within the ice pack $f_{min}\approx$30 Hz outside the ice edge
$f_{b,1}<f<f_{b,2}$	The amplitude starts to have a exponential decay at $f_{b,1}$, f^n	$n\approx1.7$ $f_{b,1}\approx$30-40 Hz within ice $f_{b,1}\approx$100 Hz outside the ice edge.
$f_{b,2}<f<$1000 Hz	The first kink in the frequency spectra slope is located at $f_{b,2}$	n=2.3. $f_{b,2}\approx$250Hz-400Hz.

Upward is the maximum lobe limited by the break point frequency from where the spectrum have an exponential decay with frequency, f^n. The exponential decay have a exponent varying (the spectral slope) from 1.3 up to 2.7 both within the ice pack and outside the ice edge. Exceptional small slopes, less than 1.0, are found at two buoys, **RF-18** and **RF-4.**

Above the break point frequency most of the frequency spectra have kinks due to a increase in the spectral slope, n. A kink is usually found between 250- 400 Hz where the slope number generally increases to 2.3. This corresponds to introduction of an additional attenuation.

Three buoys have no kinks above the break point frequency, while 13 out of 18 frequency spectra have one kink separating the exponential decay with frequency into two regimes. The first regime starts at the break point frequency and terminates at the kink where the slope number changes. The second regime starts at the kink and terminates at the upper frequency limit for the study. Two buoys have spectra with two kinks at frequencies less than 1000 Hz, **RF-18** (Figure 7.2) which is located in the center of the ice edge eddy and **RF-4** located in the interior ice pack but close to the transition zone north west of the vortex pair (Figure 6.4). The frequency spectrum obtained in the center of the eddy is different from all the other frequency spectra obtained in this experiment (Figure 7.2; RF-18. The shape of the frequency spectrum corresponds to a larger content of mid and high frequency noise above 300 Hz).

7.3 February 27. SIZEX 89.

7.3.1 Ice conditions and Ocean stratification,

The ice conditions in SIZEX 89 are a mixture of different types of new frozen ice, first year ice and some multi year ice. Generally, the ice cover is thinner than in MIZEX 87. Detailed description of the ice conditions in the experiment region is given in Chapter 6.4.

Eight AXBTs were dropped into locations within the ice pack and outside the main ice edge. The sound speed profiles show a shallowing of the surface duct from 75 m within the ice pack, to 50 m in the diffuse ice zone, and to a totally vanishing surface duct in the open ocean. The relatively warm water in the West Spitsbergen current is causing relatively high sound speeds in open water regions (1460-1467 m/s). The high sound speed (approximately 1470 m/s) is also seen below the surface duct in ice covered regions where the low temperatures gives a sound speed down to 1455 m/s in the diffuse ice zone, and down to 1445 m/s further into the ice pack.

All hydrophones are 18 m below the surface, and therefore the recordings are mainly from positions within the surface duct. This indicate that the noise will contain more high frequency components than in the MIZEX 87 case.

7.3.2 Acoustic Observations.

Frequency spectra were generated for each of the 24 buoys for up to seven selected times with records of good quality data (no man made or animal made noise included). The frequency band of interest was expanded up to 5 kHz. Figure 7.3 shows representative spectra at selected times obtained in the diffuse and compact ice edge zone. In order to study the spatial variations, similar to the study in MIZEX 87, we select to look at frequency spectra obtained between 14:00 and 15:00. The observed break point frequencies and calculated spectral slop numbers are listed in Table 7.3. The observations and calculations are based on the data report by Engelsen (1990). The main findings are summarized in Table 7.4.

7.3.2.1 Temporal variations.

The comparison of frequency spectra at different times from each buoy show that the noise level is fairly constant with time at frequencies below 200 Hz, except at **C-5**, **C-31** and **C-9** and at locations in the inner part of the compact ice pack. Buoy **C-5** has a rise of around 10 dB at all frequencies between 13:00-14:30 and is similar to **C-9** (Figure 7.3) and **C-31**. All these buoys was located in the southern part of the experiment field in open sea. The smallest variation at low frequencies is found at **C-4**, **C-6** and **C- 2.** These are also located in the southern part of the experiment field but in a region with more or less diffuse ice.

By considering frequencies above 200 Hz it is found that the noise level in all regions vary significantly with time. The temporal variation increases with frequencies above 200 Hz at all buoys. The spectra keeps the characteristic f^{-n} decay, but the numerical value of n vary significant with time, see Figure 7.3. The strongest increase in noise level with time is observed between 13:00-15:30 at all locations, except in the inner part of the compact ice zone.

The large variations in frequency spectra, at locations in the inner compact ice zone, show no monotonic increase with time.

7.3.2.2 The maximum lobe.

According to Table 7.3, in 10 out of 24 locations the maximum lobe ranges upwards from 50 Hz, and in three cases from 30 Hz. In the remaining (eleven) locations there was no lower limit of maximum lobe in the frequency domain of interest at the selected time (14:00-15:00 GMT). The break point frequency is found between 75 Hz and 100 Hz for all recordings made in open ocean (I), in diffuse ice (II) (**C-24** in Figure 7.3) and in the outer part of the compact ice region (III) (**C-23** in Figure 7.3).

Five spectra obtained at locations in the inner compact ice edge zone have a broader spectra than in the other regions, and a very wide maximum lobe (**C-14** in Figure 7.3). The lobe is not downward limited, while it is upward limited, by the break point frequency, between 800-1000 Hz. Similar spectra are found at buoys (**C-7** and **C-25**) located near the vortex pair in the compact ice zone.

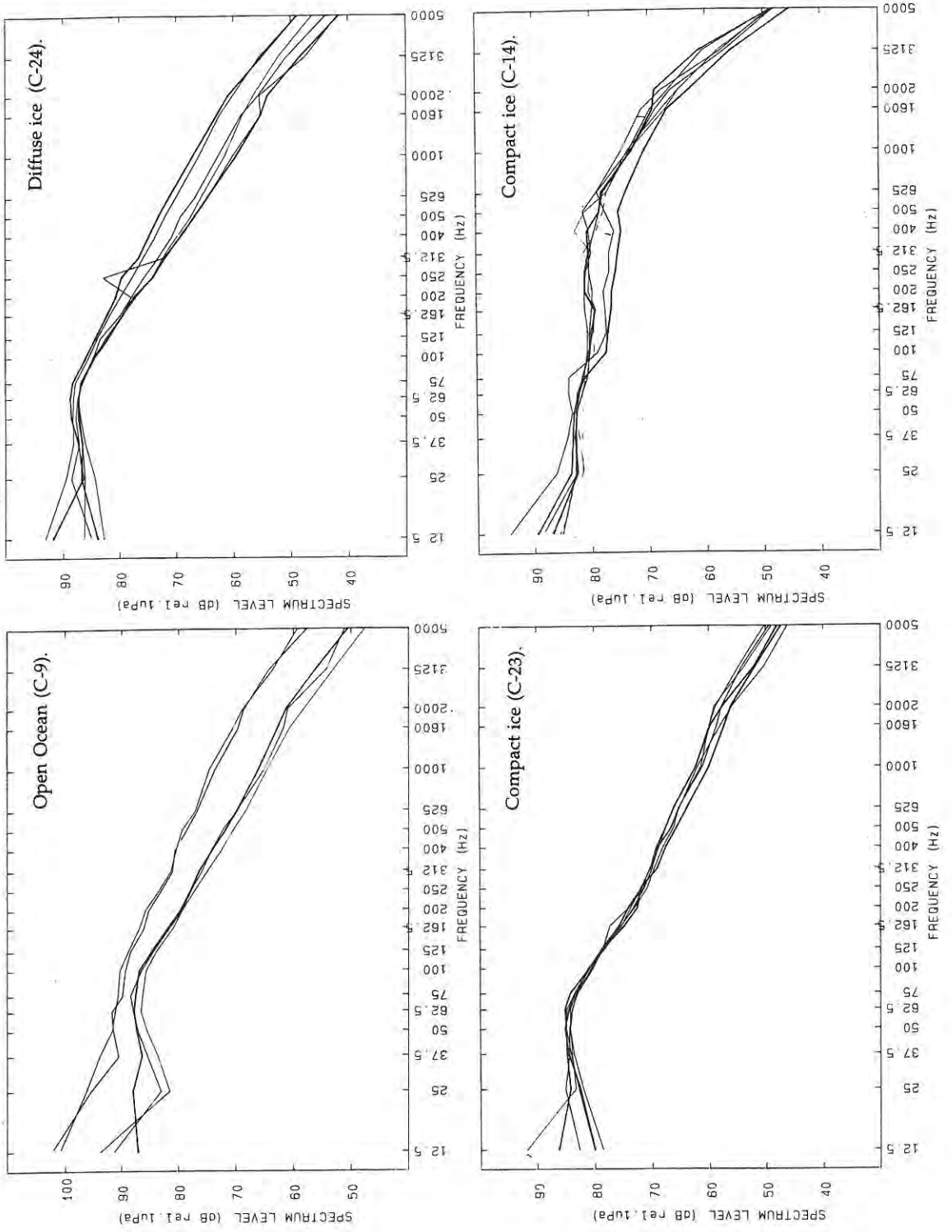

Figure 7.3. Frequency spectra obtained 27 February in the Barents Sea as part of SIZEX 89.

7.3.2.3 *Exponential decay with frequency.*

Spectra in all regions have a exponential frequency decay above the break point frequency. It is furthermore observed that the frequency spectrum may have up to three kinks in the frequency decay. Frequency spectra with no kinks are generally found in the inner part of the compact ice zone, and only one in the outer part. Twelve frequency spectra have one kink. These are mainly found in open ocean or diffuse ice, except **C-22** which is located in the compact ice region. Spectra obtained at five locations, within diffuse ice and compact ice, have two kinks. Only **C-6** shows three kinks. This spectrum has significant different slope numbers in the mid region and higher frequencies compared to what is found at other locations.

Table 7.3. Observations 27 February, 1989 at 14:05 (Z). Each buoy is listed along with the ice zone code, low frequency break point, and the spectral slope number and corresponding frequency domain. The data are ordered after number of break points. Shadowed fields corresponds to the locations with a low frequency break point less or equal to 40 Hz. Ice zones are defined as I: Open ocean; II: Diffuse ice; III: Compact ice and IV: Interior ice pack.

Buoy id	Ice Zone	Low frequency break point	Slope	Frequency domain	Slope	Frequency domain	Slope	Frequency domain
No kink.								
C12	III	none					2.55	1000-5000
C13	III	none					2.63	1600-5000
C7	III	none					3.14	2000-5000
C14	III	none					3.72	1000-5000
C8	III	none					3.75	1000-5000
C16	III	none					4.02	1000-5000
C25	III	50 1)					2.55	1000-5000
One kink								
C31	I	none			1.43	100-2000	1.96	2000-5000
C19	I	50			1.47	100-1600	2.55	1600-5000
C10	I	50			1.51	100-2000	2.69	2000-5000
C9	I	none			1.65	100-2000	2.39	2000-5000
C3	I	50			1.77	75-2000	2.69	2000-5000
C20	I	none			1.81	100-2000	3.17	2000-5000
C5	II	none			1.81	100-2000	4.12	2000-5000
C17	I	none			2.04	100-2000	2.74	2000-5000
C24	II	30			2.10	75-1600	2.99	1600-5000
C4	II	47.5			2.33	75-1600	3.11	1600-5000
C22	III	50 1)	1.87	75-312.5			2.29	312.5-5000
C2	II	47.5	1.90	75-312.5			2.53	312.5-5000
Two kinks.								
C15	II	40	1.70	75-400	1.74	400-1600	3.27	1600-5000
C23	III	30	2.09	75-200	1.64	200-2000	2.06	2000-5000
C6	II	30	2.14	75-200	0.87*	200-625	1.33	625-2000
C11	III	40.0	2.28	75-162.5	1.72	162-1600	3.01	1600-5000
C1	III	47.5	2.44	75-162.5	1.75	200-312.5	2.46	3125-5000

Table 7.4. Summarized observations of the frequency spectrum obtained in the SIZEX 89 case.

Frequency domain	General Description	Specific description
$f<f_{min}$	The amplitude increases with frequency below f_{min}.	no f_{min} within the compact ice pack $f_{min}\approx$30 or 50 Hz in the other zones
$f_{b,1}<f<f_{b,2}$	The amplitude starts to have a exponential decay at $f_{b,1}$, f^{-n}	$n\approx3.5$, $f_{b,1}$ =1000 Hz, III *) $n\approx2.2$, $f_{b,1}$ =75 Hz, II,III $n\approx1.5$, $f_{b,1}$ =100 Hz, I
$f_{b,2}<f<f_{b,3}$	The first kink in the frequency spectra slope is at $f_{b,2}$	$f_{b,2}$=5000 Hz *). $n\approx1.7$, $f_{b,2}$ =200 Hz, II,III $n\approx2.7$, $f_{b,2}$ =2000 Hz, I
$f_{b,3}<f<f_{b,4}$	The second kink in the frequency spectra slope is at $f_{b,3}$	$f_{b,3}$=5000 Hz I,II $n\geq2$, $f_{b,3}\geq1600$ Hz, II,III

*) Inner part of the compact ice region

Only 7 out of 24 locations have a kink below 1000 Hz, all of them are just outside or inside the main ice edge. Five of these have a clear reduction of the slope number at the kink found between 162.5 Hz up to 400 Hz. These observations are similar to the observations reported by Buckingham (1993). Two buoys have a kink frequency below 1000 Hz with a corresponding increase in the slope number, that is **C22** and **C2**. These are similar to the findings in MIZEX 87. Frequency spectra at 10 locations in the open ocean and diffuse ice zone and 7 locations in the compact ice zone, do not have a kink in the spectral slope below 1000 Hz. The positions in the inner part of the compact ice zone do not have an exponential decay at all at frequencies below 1000 Hz.

In the open ocean and diffuse ice the spectral slope is between 1.4 and 2.3 below 1000 Hz, and increases generally to above 2.5 above a kink located between 1600 and 2000 Hz. All together 13 spectra have a kink between 1600-2000 Hz. From the data presented by Buckingham (1993) we observe a very significant kink at around 1200 Hz. The MIZEX 87 data were not processed for frequencies above 1000 Hz and kinks above 1000 Hz could therefore not be studied for this case.

7.4 March 6. SIZEX 92.

In this case the open ocean noise field was dominated by noise from animals, and machine noise from a moving ship (Haakon U. Sverdrup R/V) outside the ice edge. Therefore only data from four locations within the ice pack are considered. The buoys included are **26, 19, 9,** see Figure 7.4. Buoy **14** is excluded from the analysis as the data are very different from data from the other locations, without any explanation. All the buoys are located within compact, broken up 1-3 m thick first year ice. The water depth is around 200 m. See Chapter 5 for detailed environmental description. Furthermore, the ocean stratification and propagation conditions are analyzed and discussed in detail in Chapter 5.

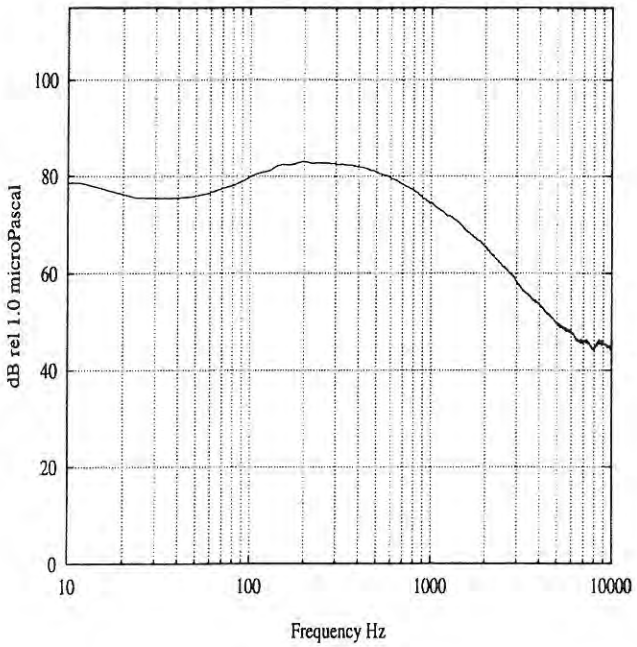

Buoy 09

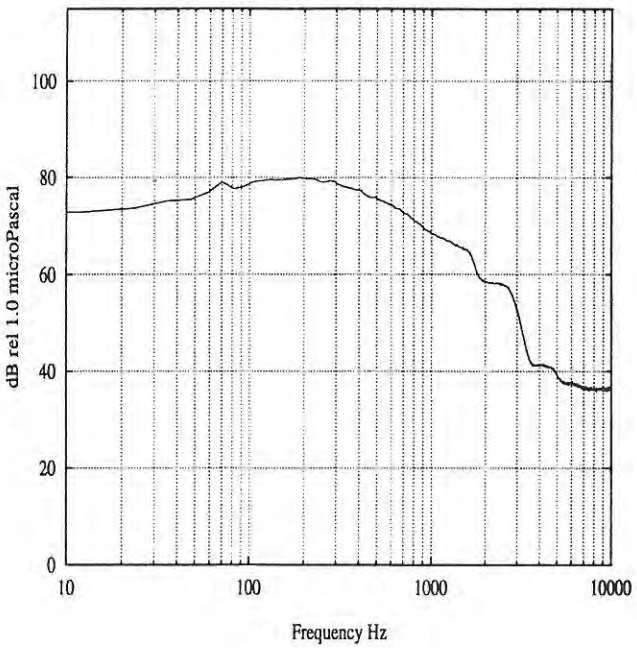

Buoy 14

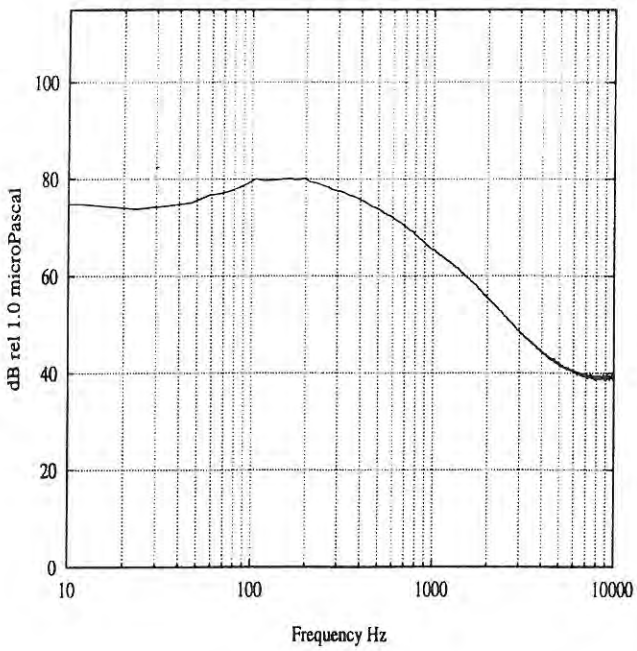

Buoy 19

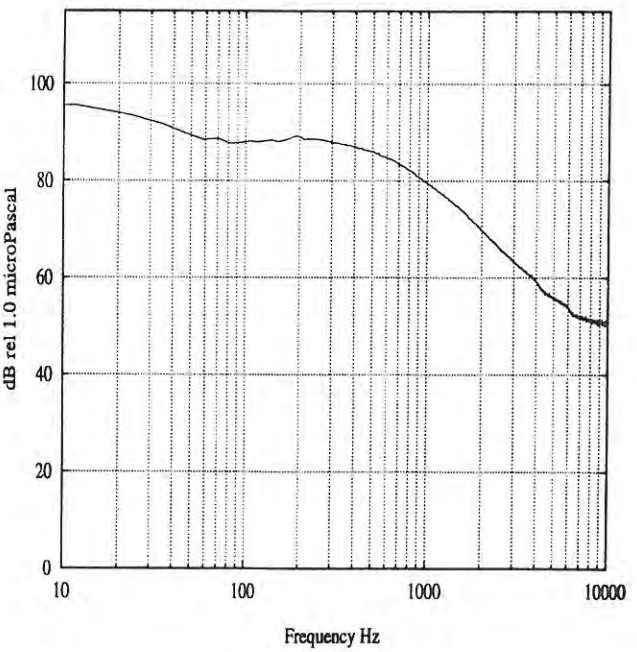

Buoy 26

Figure 7.4 Frequency spectrum obtained 6 March 1992 (SIZEX 92).

According to Figure 7.4, the ambient noise frequency spectra have a very broad maximum lobe from 100 Hz up to 400 Hz at **9** and 640 Hz at **26**. Above 640 Hz a exponential decay with frequency is observed at all locations. The exponents, n, are between 2.9 and 4.1 at frequencies above the break point frequency. A kink is observed at all locations between 1150 Hz (**19**) and 3000 Hz (**26**). The slopes become significantly steeper above the kink. The frequency spectrum should not be considered above 5 kHz due to limitations in the hydrophone sensitivity. A minimum centered around 20 Hz are most reasonable due to the bottom interaction.

The optimal frequency domain was observed to be from 100 Hz up to 400 Hz for the long range propagation paths in this region (Figure 5.7 and 5.8). This corresponds well to the measured maximum lobe of the ambient noise frequency spectrum.

Above the optimal frequency domain the transmission loss increases with frequency. This corresponds to increasing losses due to reflection and scattering with frequency. Reflection loss as a function of frequency was studied in Chapter 5, while the scattering function is not considered in the numerical simulations. A reasonable ice thickness for the experiment field is 2-3 m. In Chapter 5, Figure 5.9 numerical simulations show a significant increase in reflection loss at around 500 Hz for this ice thickness .

7.5 Comparison and Interpretation.

7.5.1 The maximum lobe

Makris and Dyer (1986) presented a composite ambient noise spectrum for observations from April 1982 at the Fram IV ice camp. The spectrum had a maximum lobe centered around 15 Hz. In our study the maximum lobe is found to be between 20-30 Hz within the ice pack in the Greenland Sea (MIZEX 87). These observations correspond well to the previously reported optimum frequency centered at 20 Hz for propagation in the ice covered Arctic (Jensen et al. 1994). At positions in the diffuse ice where the receivers are below the shallower surface duct, the maximum lobe is observed to be 30-100 Hz. This corresponds to broadening and slight switching towards higher frequencies. In the western Barents sea the receivers are well within the surface duct, and the maximum lobe is generally between 50-100 Hz (SIZEX 89). This is a slight switch towards higher frequencies compared to the Greenland Sea case. The wide maximum lobe, between 100-400 Hz, observed in the eastern Barents Sea (SIZEX 92) corresponds to the optimal frequency domain measured in the same area at the same day.

The observations above suggest a relation between optimum propagation frequency domain and the maximum lobe of the ambient noise frequency spectrum. In Chapter 5 it was shown by numerical simulations that the optimum frequency of propagation is very sensitive to the position of the receiver relative to the surface duct. Furthermore it was observed that the optimal frequency domain was influenced by changes in the reflection coefficient. Therefore we conclude that the maximum lobe of the ambient noise frequency spectrum is regulated by the position of the receiver relative to the surface duct and frequency dependent losses (filtering processes) due to the ice cover and sea floor. In Chapter 5 it was shown that the reflection losses are influenced by the ice thickness and material properties of the ice cover. This indicate that the ice

thickness may have a significant effect on the maximum lobe of the frequencies. Based on this discussion the observed differences in ambient noise spectra obtained in the Barents Sea compared to the Greenland Sea are proposed to be a combined effect of receiver position relative to the surface duct and different ice conditions.

Decreased water depth in the SIZEX 92 case, compared to the SIZEX 89, causes increased bottom interaction at frequency below 100 Hz, which moves the optimum frequency towards higher frequencies. Therefore, the very broad maximum lobe in SIZEX 92 is due to bottom interactions at the lower frequencies, and to the combined effect of filtering caused by reflection and scattering from the ice cover.

7.5.2 Exponential decay and kinks.

Above the maximum lobe all the frequency spectrum have a exponential decay with frequency, f^{-n}. The decay with frequency is generally exponential above the break point frequency with a negative power generally between 1.3 and 3.0. This is found both at positions within the ice pack and outside the ice edge in all experiment area. The observed decay corresponds to the inverse of the exponential increase of scattering with frequency due to ice (See Chapter 5; Fricke, 1993; Le Page and Schmidt., 1994).

Similar to the observations by Buckingham (1993), we observe a kink in the slope of the frequency spectrum at about 400 Hz in the Greenland Sea. In contrast to Buckingham, the slope observed in MIZEX 87 increases from 1.7 to 2.3, and up to two kinks can be see below 1000 Hz. These kinks are caused by additional losses, caused by the complicated and frequency dependent losses introduced by the repeated interaction with the ice- water boundary.

The ice cover is generally a mixture of old and new ice of variable thickness, and the frequency spectra will consist of sound which has been exposed to completely different reflection coefficients and scattering functions. The observation of several kinks in the exponential decay with frequency in ambient noise spectra can therefore be explained partly by the frequency dependency in the reflection coefficient and scattering, and by the presence of several ice regimes in the MIZ. By reconsidering the data used by Buckingham (1988) and (1993), more than one kink is found in these data too. One close to 400 Hz and one close to 2000 Hz is seen at all locations.

At some locations in the western Barents Sea, SIZEX 89 the kinks represent a decrease in decay with frequency. This is similar to the observations made by Buckingham in the Greenland Sea. The kinks are, according to Buckingham (1993), observed at a frequency where the local sources starts to dominate over the distant sources. Buckingham reports calm wave and wind conditions which is also the case in SIZEX 89. One reasonable explanation is fewer and less intensive sources during calm conditions. Under such circumstances the ambient noise field are dominated by the local sources, which have been less exposed to frequency dependent attenuation.

7.6 Concluding remarks.

The above analysis postulates a correspondence between broad band propagation effects and averaged ambient noise observations in the frequency band from 20 Hz up to 5 kHz. The specific findings of the study are:

1. The maximum lobe of the ambient noise frequency spectrum is related to the optimum frequency domain for acoustic propagation.

2. The kinks in the spectrum is located at frequencies where additional loss becomes significant or where the local field start to dominate over the distant field.

Ducting of acoustic energy above 100 Hz causing repeated interaction with the water-ice interface indicates that the break point frequency, slopes and kinks are related to ice parameters, such as ice thickness, elastic parameters (thereby to temperature and salinity profiles) and under ice roughness, through the reflection losses and surface scattering losses. This inspires one, to investigate the possibility to invert broad band ambient noise observations to sea and ice parameters in forthcoming work. The investigation will require a sensitivity study of ice parameters, such as ice roughness and ice thickness, and ocean stratification on ambient noise using existing acoustic propagation models and ambient noise models.

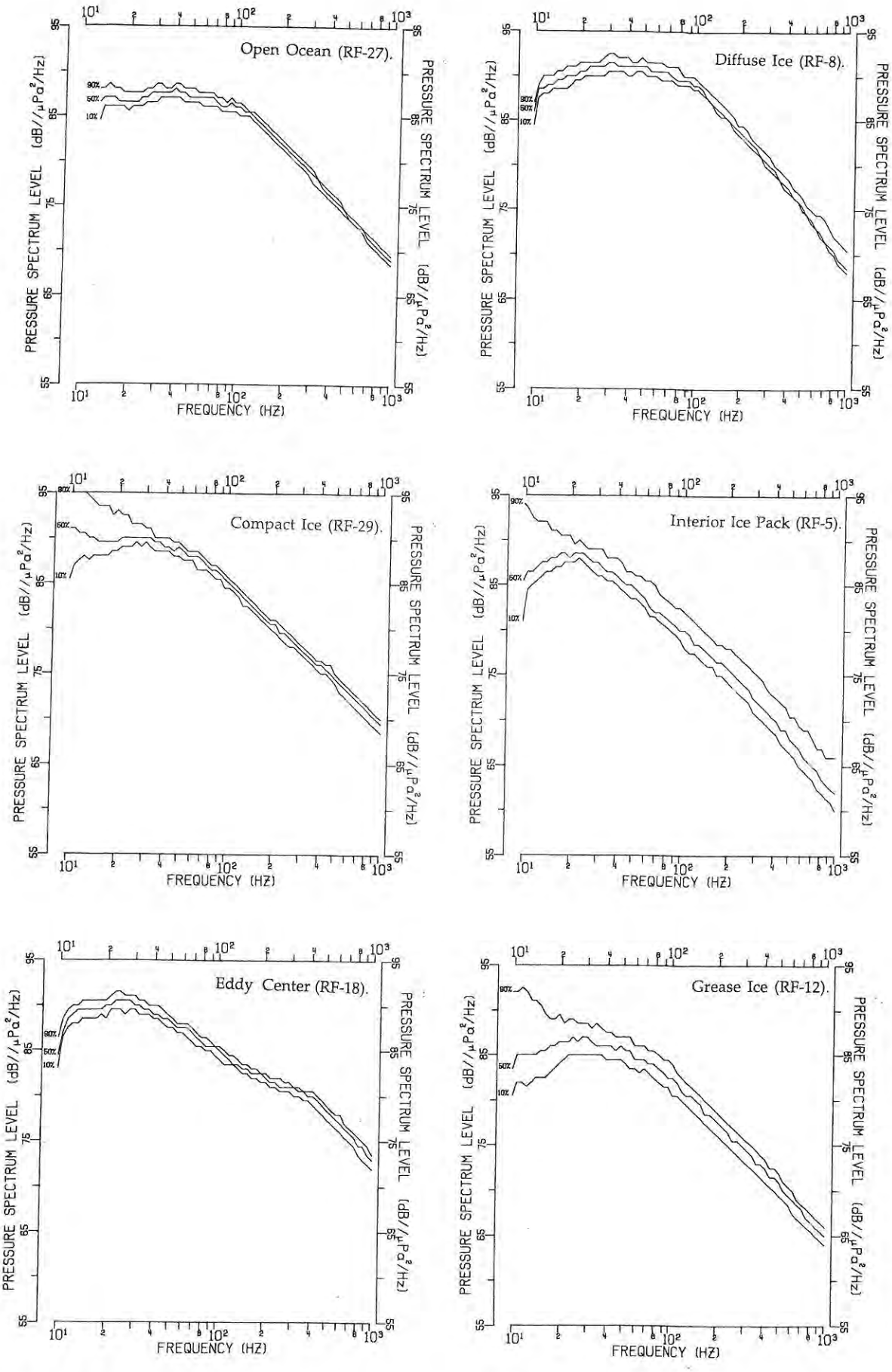

Figure 7.2 Ambient noise frequency spectra obtained April 2, 1987.

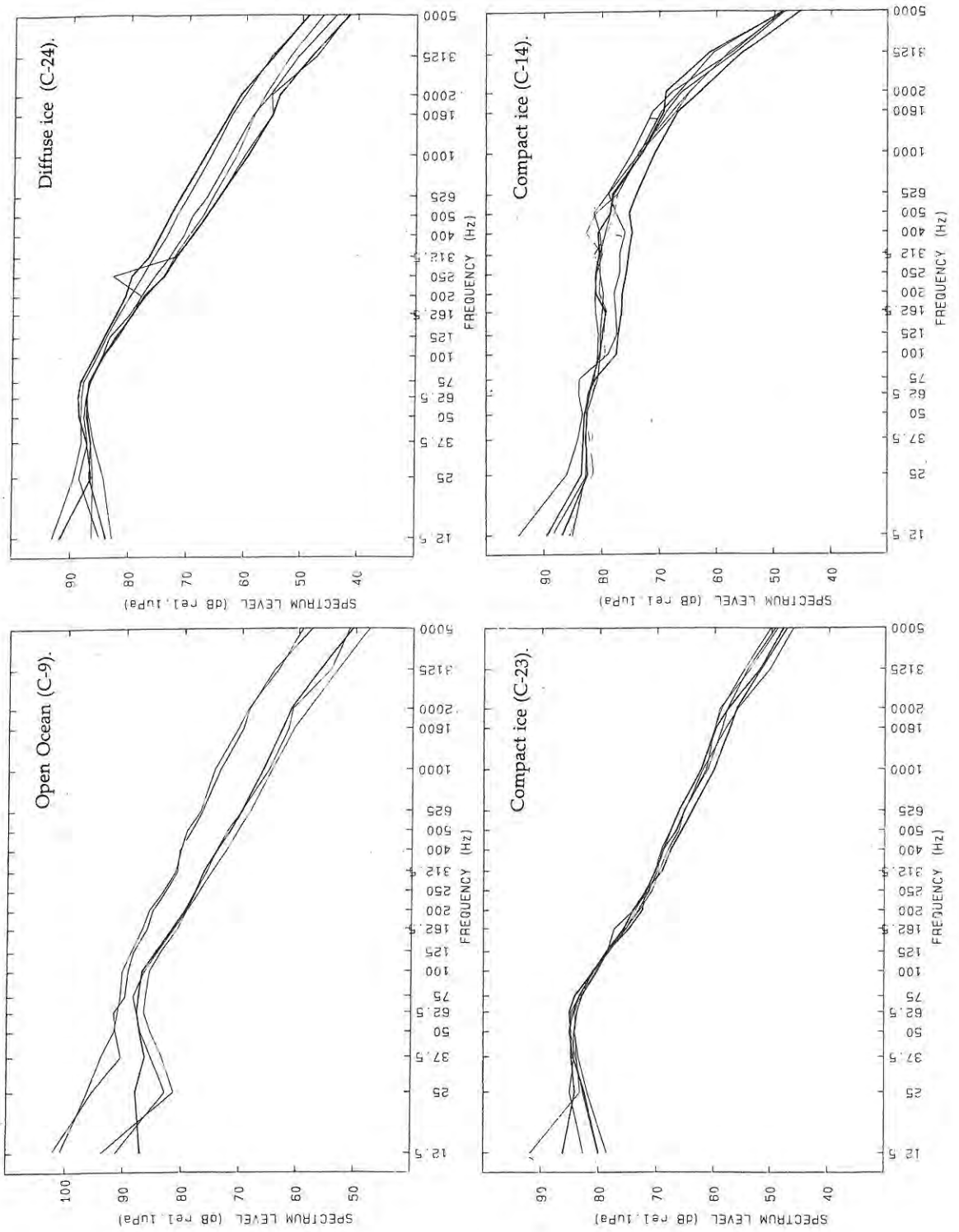

Figure 7.3. Frequency spectra obtained 27 February in the Barents Sea as part of SIZEX 89.

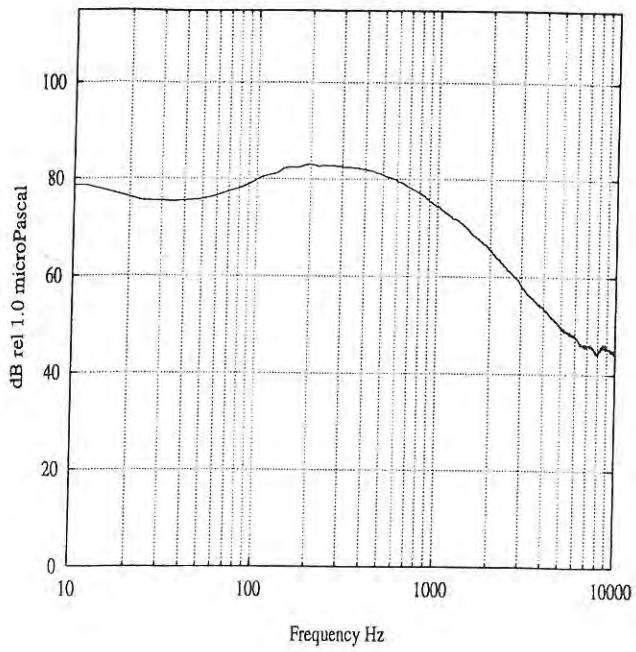

Buoy 09

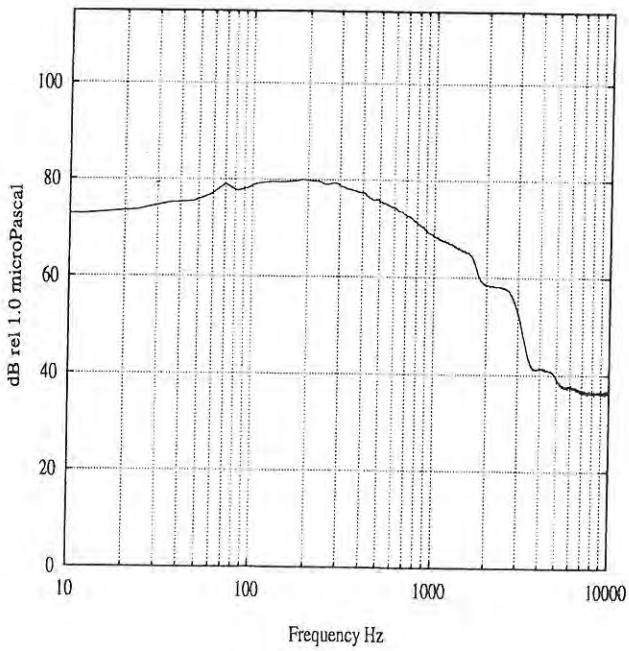

Buoy 14

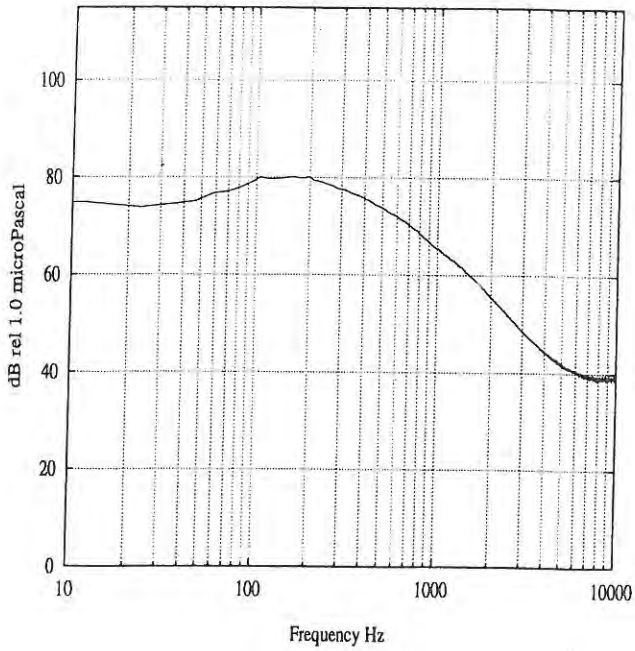

Buoy 19

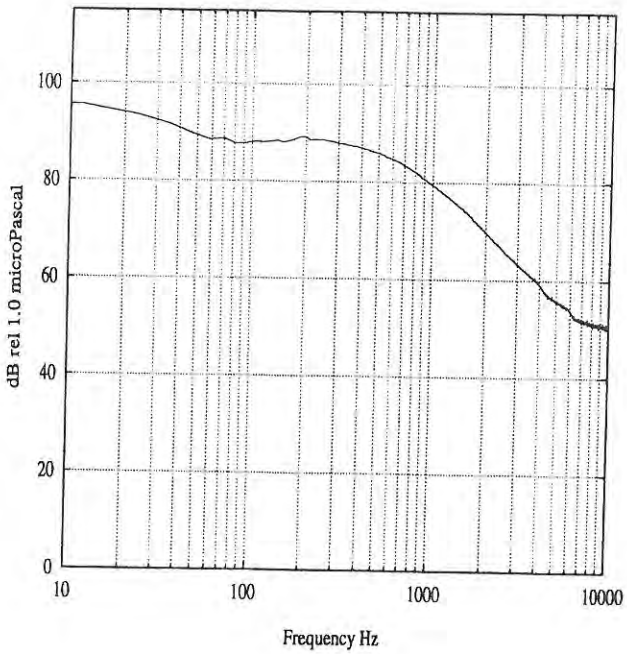

Buoy 26

Figure 7.4 Frequency spectrum obtained 6 March 1992 (SIZEX 92).

8. The signature of swell in ambient noise.

8.1 Introduction

The objective of this study is to

Investigate the effect of swell on ambient noise.

Short gravity waves with periods less than 7 s, are attenuated within a few hundred meters inside the ice edge while long waves, defined as swell, can penetrate up to 100 km into the ice pack impacting floe size distributions and the extent of the MIZ, see for example Wadhams, et al. (1973), Wadhams et al., (1987), Squire (1994). As swell propagates into the compact ice edge noise is generated by squeezing of brash ice between larger ice floes, cracking, shearing and flexure of the larger ice floes. Swell interaction with the ice cover was postulated by Diachoke and Winokur (1974) to be the major source of ambient noise in the MIZ. Later investigations in the MIZ (Makris and Dyer, 1991) have shown that swell and ice concentration correlates well with low frequency noise (25-50 Hz).

A total of 24 sonobuoys were deployed on March 9, 1992 northeast of Hopen in a pattern of five nearly parallel lines oriented east-west (Figure 6.9). The hydrophones were deployed at 18 m which was in the 50-100 m deep surface duct. Five minute long noise records from twenty "52-B" buoys are analyzed for frequencies from 100 Hz up to 5 kHz. Since swell have a typical periodicity of 10-20 s, we will consider short term variation down to a few seconds. The noise records are presented as sonograms consisting of integrated frequency spectra over 4 seconds which is an average of 48 individual spectra.

8.2 Ambient noise observations

A sonogram with a resolution of 0.3 s was obtained from acoustic recordings made by buoy **22** located close to the ice edge (Figure 8.1). The sonogram clearly shows a periodic signature of 4 s. Due to the long processing time and need of large storage capacity the averaging interval was increased to 4 s, corresponding to a reduction to 8-10 s in signature resolution. This makes it impossible to resolve the shorter waves present in the open ocean/grease ice regions but good enough to resolve the typical swell periods in ice covered regions. The sonogram obtained at buoy **5** in the interior ice pack region has clear periodic signature above 100 Hz with a period of 13.3 s, and a weak long term variation in signature of around 90 s (Figure 8.2).

Similar periodic signatures were observed in almost all sonograms obtained at locations within the ice pack. No periodic signatures were found in the sonograms obtained at locations outside the main ice edge. For each buoy Table 8.1 shows the ice zone, local ice conditions, distance from the main ice edge, along with estimated

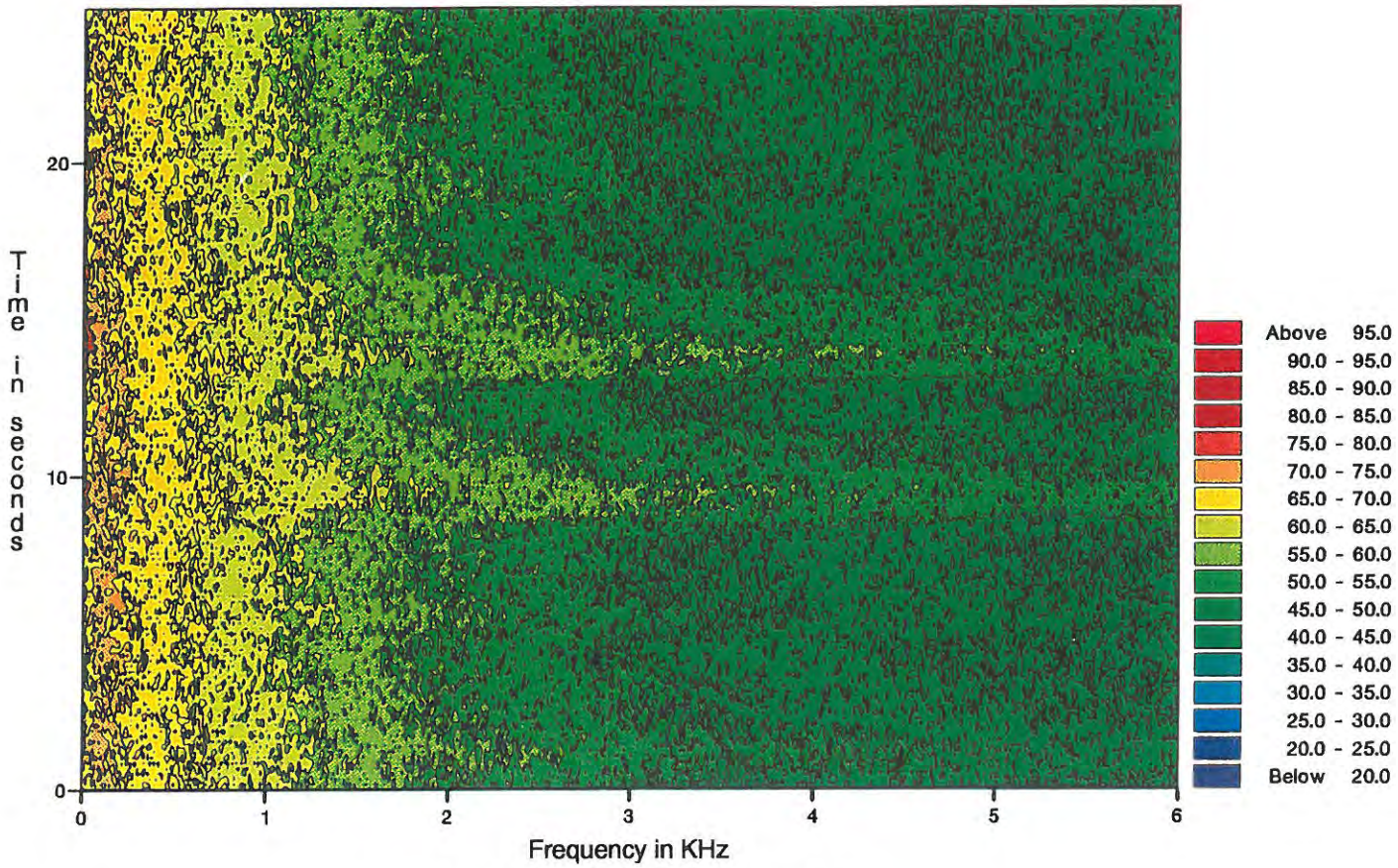

Figure 8.1. Sonogram obtained by using ambient noise data from buoy 22. Time resolution is 0.3 s.

periods and frequency domain of signatures in the sonograms. The buoys are listed according to the east-west lines.

8.2.1 Observations within the compact ice region

The northernmost east-west line, located in the interior ice pack, has periods between 13-19 s, and the mean period is 14.83 s. Near the ice edge the mean period is reduced to 9.6 s. Generally, the periodicity is present at frequencies above 400 Hz and in some locations down to 100 Hz as seen at buoy **5** and buoy **23** (Figure 8.2). The periodic signature is observed at all recordings within the ice pack, except at buoy **19**. The signature is too weak in **19** to provide an estimate of the wave period. Buoy **19** was reported in Chapter 6 to have very high levels compared to the surrounding buoys.

The strongest periodic signatures are observed at locations close to some icebergs (**21, 12** and **23**). The sonogram corresponding to **23** has clear periodic components both at higher and lower frequencies (Figure 8.2.c). Buoy 23 was deployed into a wake behind a tabular iceberg (Figure 6.10). Some of the records show an intensity modulation with the longer "period" at buoy **21, 23, 5,** and **22.**

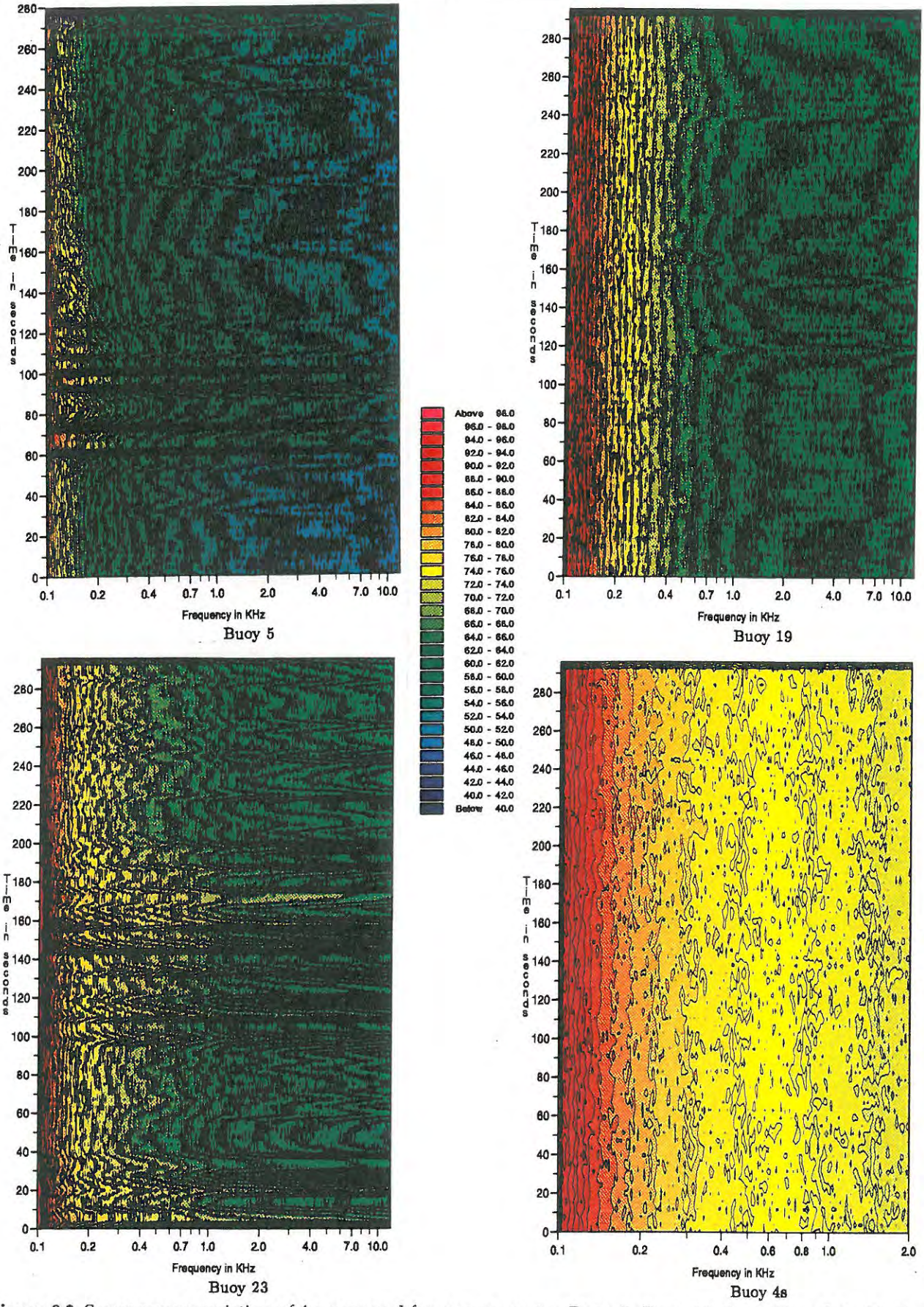

Figure 8.2. Sonograms consisting of 4 s averaged frequency spectra. Buoy 5, Buoy 19, Buoy 23 and 4s. Notice that the calibration of 4 s is not done correct, but this does not influence the periodic signature.

Table 8.1. Periodic signatures in ambient noise data from March 9, 1992. Observations are made by using sonograms consisting of 4 s averaged frequency spectra. I: Open ocean; II: Diffuse ice; III: Compact ice region; IV: The interior ice pack. Least distance to ice edge is estimated using the SAR image from the day before, and is given by positive numbers into the ice pack.

Buoy ID	Ice Zone	Local Ice conditions	Distance from ice edge. [km]	Swell signature	Frequency domain [kHz]	Estimated period [s]
5	IV	N/S lead, pressure activities, floe size 100 m	56	Clear, variable	0.1 -5.0	13.3; 93.3
7	IV	N/S lead, pressure activities, floe size 100 m	47	Weak, variable	0.4-5.0	13.75
8	IV	N/S lead, pressure activities, floe size 100 m	43	Clear	0.3-5.0	18.56
10	III/IV	Narrow lead, pressure activities, floe size 100 m	56	Clear	0.4-5.0	15.55
11	III/IV	Narrow lead, pressure activities, floe size 100 m	69	Clear, variable	0.4-5.0	13.33
20	III/IV	Large leads, new frozen ice	34	Clear, variable	0.1-5.0	13.33
19	III/IV	In large lead, with new ice	26	Weak	0.4-5.0	not resolved
16	III/IV	Ice is opening up, increasing number of cracks and leads	22	Clear, variable	0.5-5.0	12.9
12	III	Tabular ice berg	45	Very Clear	0.2-5.0	14.5
21	VI	Narrow lead Broken up 5-10 m ice floes, small cracks, ice berg close to the buoy	32	Clear , variable	0.2-5.0	11.66; 31.1
23	III	Tabular ice berg	39	Very Clear, variable	0.1-5.0	13.33 (11.25);150
24	III	Broken up 5-10 m ice floes	3	Very Clear, variable	0.2-5.0	12
18	II	Pancake ice, close to ice edge	0	Animal noise		not resolved
4n	III	In lead	11	Weak	1.0 -5.0	17.85
22	III	Broken up 5-10 m ice floes,	15	Very Clear, variable	0.2-5.0	9.2, 30.0
25	I	Ice edge, Broken up 5-10 m ice floes,	-4.0	Weak, variable	0.4-5.0	≈ 10
58	I	open water	11	None		
03	II/III	Broken up 5-10 m ice floes.	68	None		
4s	II	grease ice/pancake/FY/MY	38	No ne		
01	II	grease ice/pancake /FY/MY	17	None		

8.2.2 Observations within regions outside the main ice edge.

The three east-west lines in the more diffuse ice edge zone consist of 9 buoys. According to the SAR image in Figure 6.9 and visual observations, the ice condition in this region is a mixture of open water, grease ice, pancake ice and compact broken up first year ice. Data records from two buoys , **24** and **22** both located in compact ice close

to the ice edge, have a clear periodicity in signature. The other buoys, deployed in open water or thin ice, provide data records with a weak periodicity or none periodicity at all as observed by buoy 4s(Figure 8.2).

8.2.3 Results.

The mean period of 13.5 s estimated from all the sonograms corresponds well to estimated swell period of 13.0 s made by visual observations onboard Polarsyssel. The longer periods observed in the ambient noise data 30-90 s are not explained. According to Wadhams (personal communication) 30 s swell have been observed in the interior Arctic, but have not been measured in the MIZ before. On the other hand, there is no reason for this wave component not to be present in the MIZ.

Outside the ice edge no periodic signature was observed using 9 s signature resolution. This does not mean that there is no waves or swell outside the ice edge. In open sea the breaking of waves and other surface phenomena are the main sources of ambient noise, these processes are related to the shorter wind generated waves. Waves with periods less than 8-10 s are not resolved as periodic signatures by the sonograms used in this study. Ambient noise recordings can be used also outside the ice edge to study the surface processes caused by waves, but the time resolution in sonograms has to be increased considerably as in Figure 8.1. Noise generation due to long waves in open ocean and grease ice is completely different from noise generation caused by swell propagating into the compact ice zone. This noise generation mechanism is less understood and will be discussed in Chapter 9.

Table 8.1 gives the estimated mean period to be 9.5 s close to the ice edge increasing to 14.83 s for northernmost east-west line more than 40 km into the compact ice pack. This corresponds to the well known filtering process of the shorter waves, as the ice thickness/floe size increases. This illustrates the possibilities to use ambient noise observations to study the effect of ice on wave propagation.

The clearest and strongest signature of swell in ambient noise are recorded by buoys located in wakes behind ice bergs. In Chapter 6 it was shown that these buoys represented hotspots in averaged ambient noise. From this we can draw the conclusion that iceberg hotspots in this case is due to the swell interaction with the ice berg and the surrounding ice field.

Within the compact ice the periodic signatures in sonograms are generally limited to the frequency domain above 400 Hz. Most probably is the lower limit of periodic signature in the frequency domain related to the ice parameters. Another important descriptor of the sonogram is the intensity. Acoustic intensity is most reasonable related to the strength of the noise generating mechanisms which again is related to the mechanical behavior of the ice cove due to swell. These connections between acoustic energy and mechanical behavior of sea ice due to swell has to be addressed in another study. It is most likely that the wave dampening effects and sea ice mechanics can be studied by considering simultaneously ambient noise measurements, wave

buoy measurements, remote sensing data and numerical wave models. This is not done in this study.

An important conclusion of this study is that the wave period can be estimated the by means of simple ambient noise measurements and simple signal processing. This makes the ambient noise to be an important tool in studying the wave propagating into the ice pack. By increasing the total time of recording and processing the effect of internal waves and tidal waves can be studied (Nesse et al.,1992).

8.3 Connection between wave parameters and ice parameters.

The dispersion relation, which depends on the constitutive laws, gives the connection between wavenumber and wave period. The dispersion relation for open water, and thin elastic or visco elastic plate models are presented in this section following the work by Fox and Squire (1991, 1994). Thin plate dispersion depends on the plate thickness, elastic properties of the plate, gravity and water depth. This suggest a method to retrieve the ice thickness or elastic properties from the dispersion relation by using combination of wavelength information from SAR and wave period information from ambient noise measurements or conventional wave buoy measurements. This study represents a first approach to establish inversion of wave information from SAR and ambient noise to ice parameters.

8.3.1 The wave models.

A theoretical model describing surface wave propagating from open ocean into a compact ice cover have been established by Fox and Squire (1991), (1994). The approach used was to solve the problem analytically for each region, and then match the solutions numerically at the ice edge for discrete number of depths. In this sub-section the analytical solutions and corresponding dispersion relations are given separately for each region.

The physical restrictions are small wave amplitudes allowing for linear theory, and the use of the superposition principle. The ice cover is modeled as a thin plate, either elastic or visco-elastic. Incompressibility of water and lack of sources within the region are assumptions which imply that a non-viscous and irrotational flow can be described by velocity potential, $\Phi(x,y,z;t)$, which satisfies Laplace equation

$$\nabla_{xyz}\Phi = 0, \text{ where } \nabla^2_{xyz} = \frac{\partial^2}{\partial x^2} + \frac{\partial^2}{\partial y^2} + \frac{\partial^2}{\partial z^2}$$

The problem is formulated in the Cartesian coordinate system defined in Figure 8.3. By assuming a sinusoidal dependence in z and t the resulting velocity potential can be written as

$$\Phi(x,y,z,t) = \phi(x,y)e^{i\omega t}e^{ik_z z} \qquad 8.1a$$

where $\phi(x,y)$ satisfy

$$\left(\frac{\partial^2}{\partial x^2}+\frac{\partial^2}{\partial y^2}-k_z^2\right)\phi = 0 \text{ for } -\infty < x < \infty,\ 0 < y \leq H \qquad 8.1b$$

where H is the water depth. This is a diffusion type equation in two dimensions, sometimes refereed to as the modified Helmholtz equation.

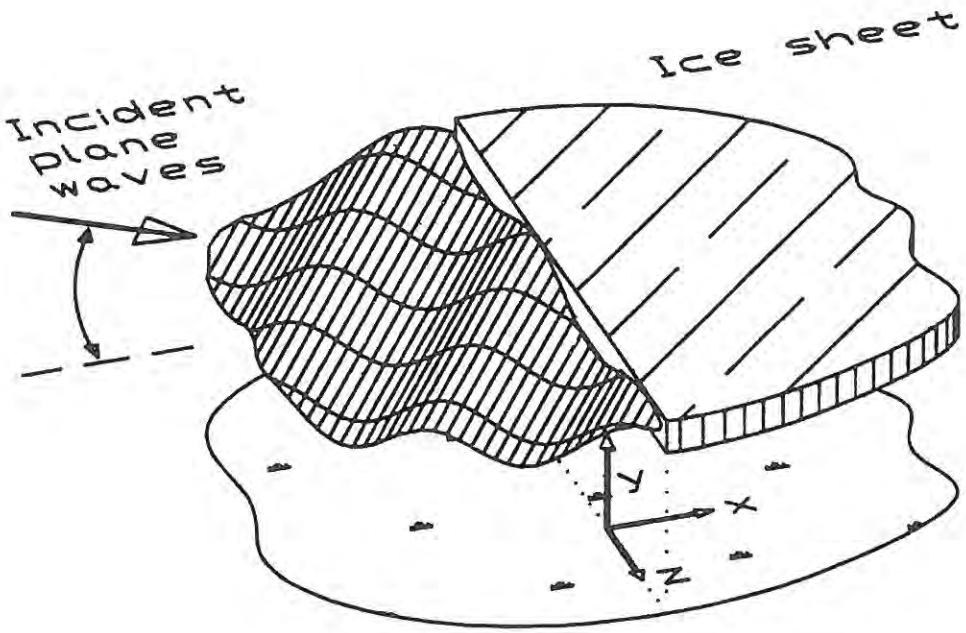

Figure 8.3 Plane ocean waves obliquely incident onto an MIZ. The coordinate system used in the model is located on the sea floor beneath the ice edge as shown. (After Fox and Squire (1994)).

By appropriate kinematic and dynamic bottom and surface conditions described by Fox and Squire, 1994 the solution is found separately for open ocean and ice-covered regions by representing the potential, ϕ, by modes

$$\phi(x,y) = e^{k_x x}e^{\pm ik_y y}, \text{ where } k_x^2 - k_y^2 - k_z^2 = 0$$

Use of bottom condition and open sea surface condition gives open water solution $(-\infty < x < 0)$

$$\phi_o = \underbrace{\left(Ie^{-ik_T' x} + \mathrm{Re}^{ik_T' x}\right)\cosh k_T y}_{\text{Travelling waves}} + \underbrace{\sum_{n=1}^{\infty} a_n e^{k_n' x}\cos k_n y}_{\text{Evanescent}} \qquad 8.2.a$$

where

$$k_T' = \sqrt{k_T^2 - k_z^2} \text{ and } k_n' = \sqrt{k_n^2 + k_z^2},\ k_z^2 \geq 0$$

and I, R, a_n are complex coefficients of the various modes. The solution in open water is the superposition of undampded incoming and reflected traveling waves and a infinite sum of evanescent waves. The wave numbers included in the solution have to satisfy the dispersion relation given as

$$k\tan(kH) = -\frac{\omega^2}{g} \qquad 8.2.b$$

Use of the elastic ice cover condition, in addition to the bottom condition, gives the solution in ice $(0 < x < \infty)$ as a superposition of a undampded traveling wave, (pure imaginary wavenumber), damped traveling modes (complex conjugated wavenumber denoted by an asterix) and a infinite sum of the evanescent modes (real wavenumber).

$$\phi_i = \underbrace{Te^{-i\kappa_T' x}\cosh\kappa_T y}_{\text{Undamped travelling mode}}$$

$$\underbrace{+b_+ e^{-\kappa_D' x}\cos\kappa_D y + b_- e^{-\kappa_D^* x}\cos\kappa_D^* y}_{\text{Damped travelling mode}} + \underbrace{\sum_{n=1}^{\infty} b_n e^{-\kappa_n' x}\cos\kappa_n y}_{\text{Evanescent modes}} \qquad 8.3.a$$

where $\kappa_T' = \sqrt{\kappa_T^2 - k_z^2}$, $\kappa_D' = \sqrt{\kappa_D^2 - k_z^2}$

and $\kappa_n' = \sqrt{\kappa_n^2 + k_z^2}$, $k_z^2 \geq 0$

and $\pm i\kappa_T$, $\pm\kappa_D$, $\pm\kappa_n$ are imaginary and complex roots of the dispersion relation

$$\kappa\tan\kappa H = -\frac{\rho\omega^2}{L\kappa^4 - m\omega^2 + \rho g} \qquad 8.3.b$$

where

$L = \dfrac{Eh^3}{12(1-\nu^2)}$, flexural rigidity

$m = \rho_i h$

E is effective average Young's modulus for ice, ν is Poissons ratio, and h is the ice thickness. T, b_+, b_- and $\{b_n\}$ are complex coefficients of the various modes.

A further refinement on the elastic model is introduced by inclusion of a viscous damping term, γ , in the thin plate boundary condition for the ice sheet (Squire, 1993 a). This is supposed to model the dampening of ice coupled waves. The visco elasticity gives superposition of damped principal traveling waves, a pair of damped traveling waves and a infinite sum of damped traveling waves.

$$\phi_i = \underbrace{Te^{-i\kappa_T x}\cosh\kappa_T y}_{\text{damped principal travelling waves}} + \underbrace{b_+ e^{-\kappa_+ x}\cos\kappa_+ y + b_- e^{-\kappa_- x}\cos\kappa_- y}_{\text{The pair of damped travelling waves}} + \underbrace{\sum_{n=1}^{\infty} b_n e^{-\kappa_n x}\cos\kappa_n y}_{\text{The infinite set of evanescent modes in elastic theory become damped-travelling modes when visco elastisity is introduced}} \qquad 8.4.a$$

The corresponding dispersion relation have only complex roots and is given as

$$\kappa \tan \kappa H = -\frac{\rho\omega^2}{L\kappa^4 - m\omega^2 + i\gamma + \rho g} \qquad 8.4.b$$

The full solution of the mixed boundary value problem is found by matching the potentials for each region across the ice edge, while ensuring the edge boundary conditions are satisfied (Fox and Squire, 1994). The edge conditions are derived from the requirement that no work is done by or to the edge of the sheet .

The z component of the wave number k_T in water and the z component of the wave number κ_T in ice are equal (Snells law). This is expressed as

$$k_T \sin\theta_o = \kappa_T \sin\theta_i \qquad 8.5$$

where the wave numbers are given by the dispersion relations. When $k_T < \kappa_T \rightarrow \sin\theta_i < \sin\theta_o \rightarrow \theta_i < \theta_o$ the wave bends away from the normal, while if $k_T > \kappa_T \rightarrow \sin\theta_i > \sin\theta_o \rightarrow \theta_i > \theta_o$ the wave bends towards the normal.

8.3.2 Ice thickness obtained from wave parameters.

Snells law, including wavenumbers satisfying the dispersion relation corresponding to thin elastic plate model, was used by Shuchman et al. (1994) in combination with wave observations from SAR to extract the ice thickness in the marginal ice zone. This concept needs the refraction of waves across the ice edge and corresponding wavelength as input from SAR.

Also in our study is the ice cover modeled as a thin elastic plate. The corresponding dispersion relation (Equation 8.3.b) depend on the ice thickness and the plate stiffness in addition to the densities, gravity and water depth. The dispersion relation can be reformulated to a cubic equation with respect to ice thickness

$$L'\kappa^4 h^3 - \rho_i \omega^2 h + \rho g + \frac{\rho\omega^2}{\kappa \tan(\kappa H)} = 0 \qquad 8.6$$

This equation can be used to calculate the ice thickness from given elastic parameters and densities, wave periods and wavelength. The difficulties in using the elastic (or visco-elastic) dispersion relations to retrieve the ice thickness are the unknown elastic properties of the MIZ. If the plate stiffness (or flexural rigidity), L=0, the model is equivalent to the mass loading model, which was used by Holt and Wadhams, 1991 to study wave propagation in thin ice. Fox and Squire (1991, 1994) used the engineer value given by Eq. 8.2, with E=6 GPa and, ν=0.3 for wave propagation in to shorefast ice. The plate stiffness in MIZ is unknown, but it is expected to be between these two values.

A simple demonstration can be made by assuming that the SAR measures a dominating wavelength of 350 m and the acoustic measurement gives a period of 13.3 s. Squires values E=6.0 GPa, ν=0.3, density in water is 1025 kg/m3, and density in ice = 922.5 kg/m^3 are used in the calculations, although they represents values for shorefast ice. The water depth in the region is set to be 200m. This gives a ice thickness of 3.95 m. In the MIZ of the Barents Sea the average thickness is between 2 and 3m. The over estimated value can be errors in the estimated wave length in SAR, which has a limited resolution, or in the plate stiffness which we know is smaller than the value used. By reducing the wavelength to 300 m the ice thickness is 2.3 m which is a very normal ice thickness in the MIZ. On the other hand keeping the wavelength constant (350 m), an increase in E causes the ice thickness to increase. Using half the value of Young's modulus (3G Pa) gives 5.1 m thick ice, and a considerable reduction of wavelength is needed. This illustrates that the ice thickness estimates are very sensitive to the elastic parameter (E) and the estimated wave length.

In MIZEX 87 simultaneously wave measurements was performed 6 km from ice edge into the ice pack and dominating wave period was found to be between 12.1 and 13.6 s, whereas dominating wavelength from SAR was estimated to be 225-250 m. Water depth was 500 m. By using the same values of the elastic parameters as Squire, the combination of wavelength 250 m and wave period 12.1 s gives an ice thickness of 1.86 m, which is reasonable for a location 6 km into the ice pack. On the other hand the other combination of wave -length and -periods gives open water conditions.

Contour plots of ice thickness versus wavelength and period have been generated by solving the cubic equation above for Squires parameter values and water depth equal to 200 m, Figure 8.3.a. The red color corresponds to ice thickness above 10 m, which is clearly unrealistic in the MIZ. Blue color corresponds to zero ice thickness where the wavelength and wave period are upward restricted by the deep water dispersion. This means that given a wavelength the period is upward limited by the open water

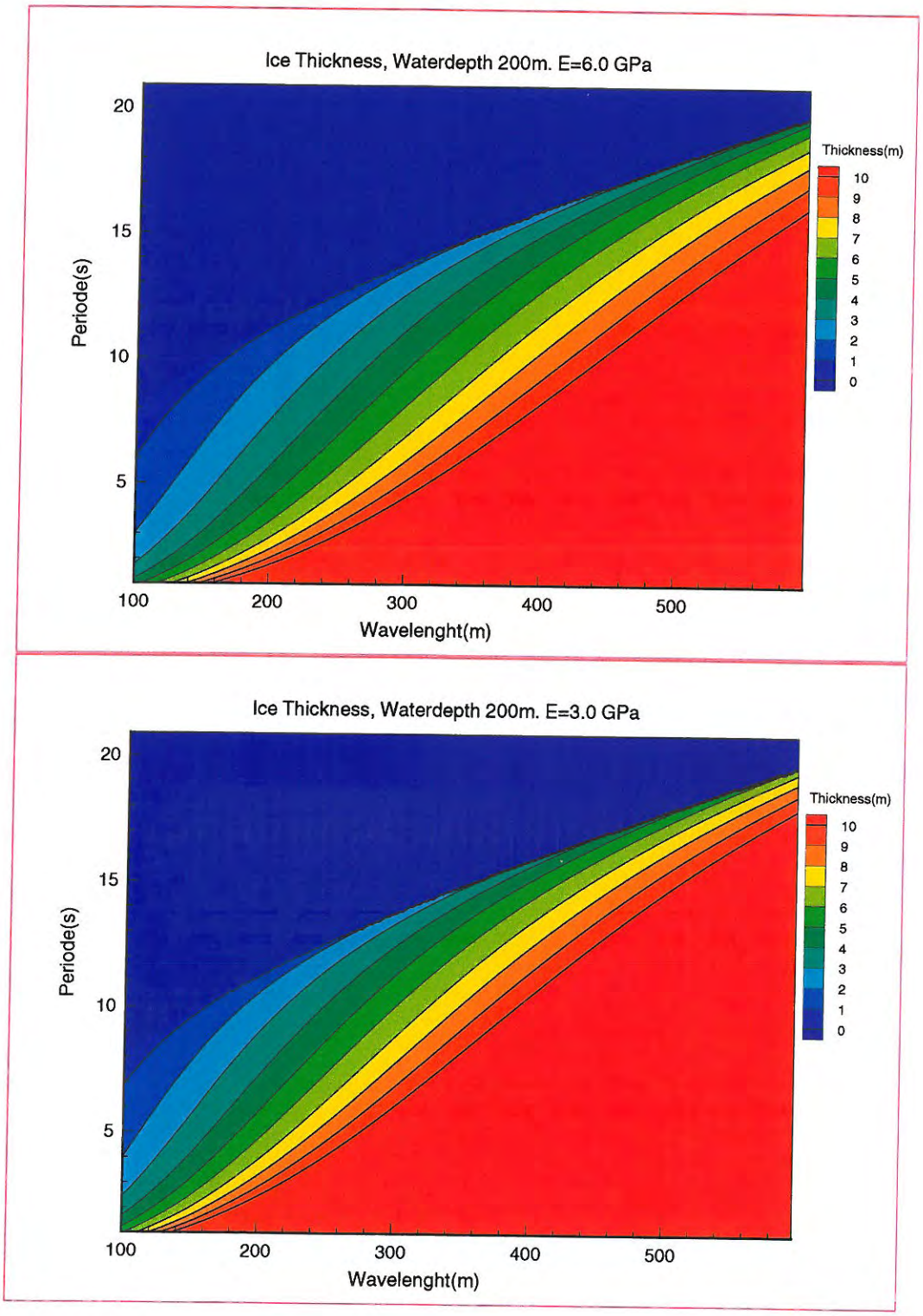

Figure 8.4. Contour plots of ice thickness versus wavelength and generated by solving the cubic equation, using v=0.3, density in water is 1025 kg/m3, and density in ice = 922.5 kg/m3. a) Water depth h=200 m, E=6.0 GPa b) Water depth =200 m, E=3.0 GPa.

dispersion relation and downward limited by unrealistic ice thickness. Between these extremes, the ice thickness is given by the wave period and wavelength. As the wavelength increases the period becomes less and less sensitive to changes in the ice thickness.

As pointed out above the ice thickness is very sensitive to the Young's modulus. In Figure 8.3.b the Young's modulus is reduced to 3.0 GPa. The contour plot shows that ice thickness typical for the MIZ (0-4 m) are not resolved for wavelengths above 200 m. By other words the waves above 200 m becomes less sensitive to the ice cover as the plate rigidity are reduced and will follow the open water relation. Other dispersion relations using other constitutive laws may give a better resolution for ice thickness close to zero. Contour plots with increasing water depth to 2000 m shows no influence in the ice contour plots. This indicate that the wave periods and wavelengths can be inverted to ice thickness without taking the water depth into account for depths considered here.

8.4 Conclusions.

This study have shown that ambient noise recordings made by omnidirectional hydrophones and simple post processing can be used to monitor the surface wave period. When the swell propagate into the ice pack noise is generated by squeezing of brash ice between larger ice floes, cracking and flexing of the larger ice floes. This is clearly observed as periodic signatures in sonograms, corresponding to broadening and narrowing of the frequency spectra, which readily gives the wave period. Therefore by deploying hydrophones at different locations in the MIZ the swell period can be monitored for a large area. In order to validate the quality of wave information from the acoustic observations synoptic wave and acoustic measurements should be made in future experiments.

A concept combining a wave model, SAR data and ambient noise recordings for retrieving the sea ice thickness in MIZ has been suggested. A preliminary sensitivity study shows limitations in estimating ice thickness close to 0 from wave parameters using the dispersion relation derived from the thin elastic plate approximation. Other dispersion relations, such as the visco-elastic relation given in equation 8.4.b, may reduce the strong gradient in ice thickness for wave periods and lengths close to the open water dispersion. This has to be considered in a future work. The method should also be compared to the concept based on Snell law as presented by Shuchman et al., 1994. Validation of the concept requires simultaneously measurements of ice thickness, wave period and wave length. Such an experiment would also provide a possibility to compare the different dispersion relations.

where $\phi(x,y)$ satisfy

$$\left(\frac{\partial^2}{\partial x^2}+\frac{\partial^2}{\partial y^2}-k_z^2\right)\phi = 0 \text{ for } -\infty < x < \infty,\ 0 < y \leq H \qquad 8.1b$$

where H is the water depth. This is a diffusion type equation in two dimensions, sometimes refereed to as the modified Helmholtz equation.

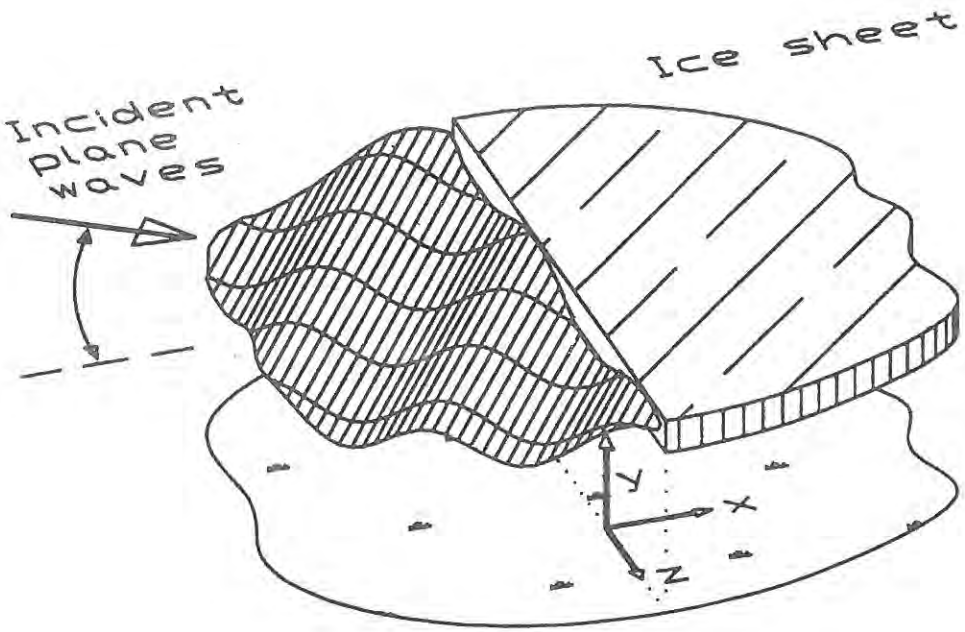

Figure 8.3 Plane ocean waves obliquely incident onto an MIZ. The coordinate system used in the model is located on the sea floor beneath the ice edge as shown. (After Fox and Squire (1994)).

By appropriate kinematic and dynamic bottom and surface conditions described by Fox and Squire, 1994 the solution is found separately for open ocean and ice-covered regions by representing the potential, ϕ, by modes

$\phi(x,y) = e^{k_x x}e^{\pm ik_y y}$, where $k_x^2 - k_y^2 - k_z^2 = 0$

Use of bottom condition and open sea surface condition gives open water solution $(-\infty < x < 0)$

9. The effect of grease ice formation on ambient noise.

9.1 Introduction

Short surface gravity waves are rapidly damped out in regions covered with grease ice and early stage pancake ice (Johannessen et al., 1986). Therefore it was hypothesized by Johannessen et al., (1988 a,b) that ambient noise levels are reduced in areas with grease ice compared to open ocean. Later studies have shown that the ambient noise level at 18 m depth, below a grease ice cover, was 8 dB lower than in open sea (Johannessen et al., 1994, Chapter 6). Similar to grease ice, the presence of monomolecular films (0.02 mm to 0.04 mm thick) reduces the number of breaking whitecaps and thereby the ambient noise below the surface (Rohr and Detsch, 1992). Attenuation's of up to 8 dB was observed at 9 m below the surface at frequencies above 1-2 kHz at wind speeds above 2 m/s.

During SIZEX 92 a reduction of up to 17 dB in high frequency ambient noise is observed as a grease ice cover develops at the sea surface above a receiver, positioned 2 m above the sea floor, in the ice edge zone east of Hopen (Engelsen, 1993).

The objective of this study is to

investigate why the grease ice causes a stronger dampening of the ambient noise close to the sea floor than when the receiver is closer to the surface.

9.2 Acoustic experiment.

As part of the acoustic experiment during SIZEX 92 two bottom moored DATOS buoys were deployed, by R/V Polarsyssel, east of Hopen in the eastern part of the Barents sea. Only the buoy located at 76:29.6 N 26:00:2 E south of Hopen, close to the ice edge, was recovered. The water depth was 85 m, and the hydrophone was 2 m above the bottom. The buoy was recovered in the summer and it appeared that the tape changing mechanism had failed to operate, and therefore only providing data for the period March 1 at 1700 GMT till March 2 at 20:00 GMT, giving total recording period of 28 hours. The data is presented as time series of averaged values at selected frequencies every hour for the 28 hours of recording. In order to study the frequency domain from 6.5 Hz up to 10 kHz the data from DATOS buoy averaged frequency spectrum is generated every hour and sonogram at selected times. Data processing is described by Engelsen, 1993 and in the appendix.

9.3 Environmental conditions.

The bottom conditions in the area east of Hopen are exposed bedrock with more than 50% coverage (Solheim and Kristoffersen, 1984). At the time of buoy deployment from R/V Håkon Mosby the area above the buoy was ice free and the sea was fully developed. The ice edge was north of the buoy location. Ice conditions after buoy deployment are retrieved from the

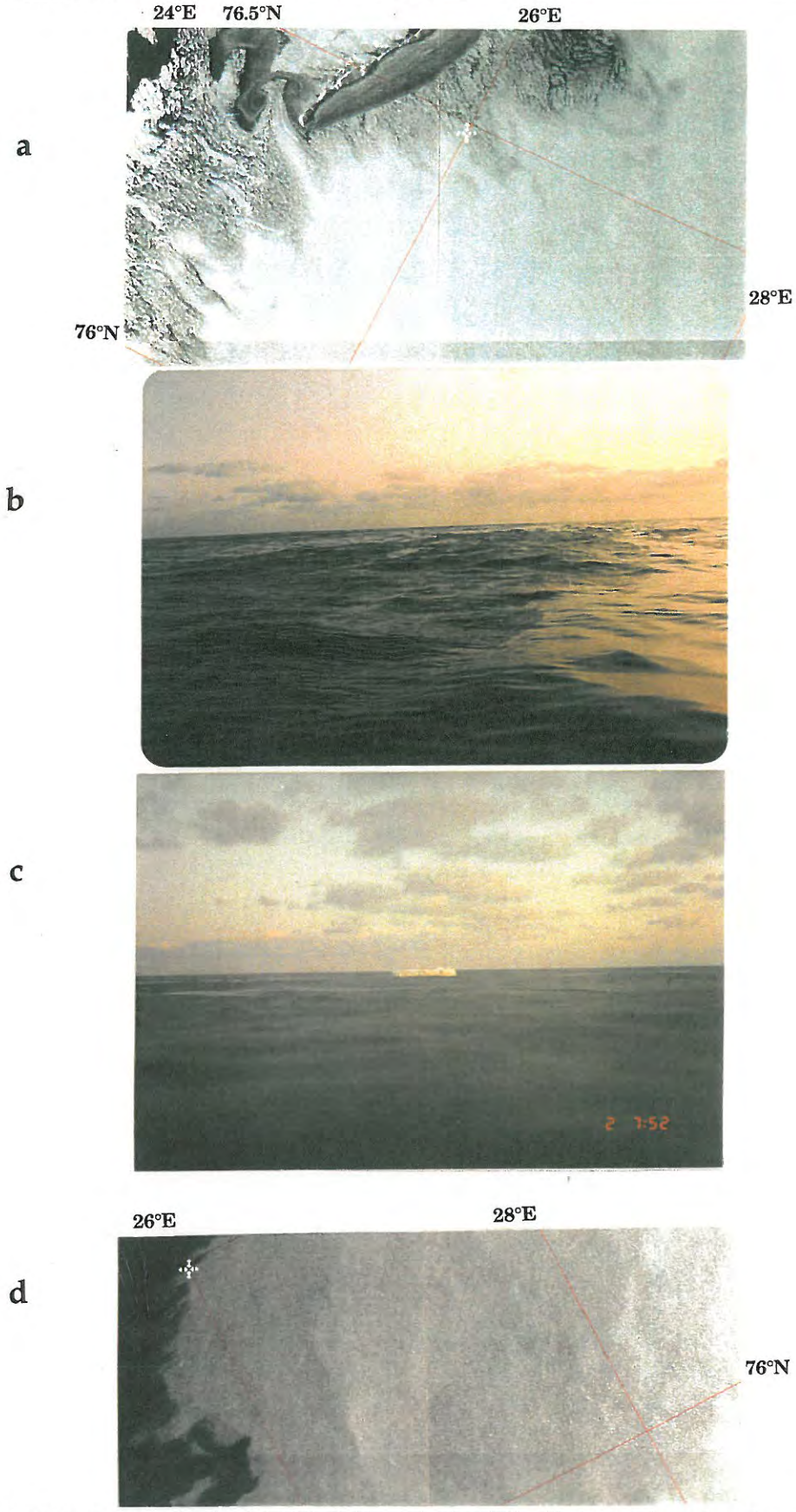

Figure 9.1 a) SAR image obtained 19:00 GMT 1 March 1992 . b) At the buoy location 7:15 GMT 1 March 1992. Mixed areas of grease ice and open water, the open water areas are covered with small capillary waves. c). This photo is taken further west showing a continuos cover of older grease ice and early pancake ice stage. d) SAR image obtained 10:30 GMT 2 March 1992.

- ERS-1 SAR images obtained 19:07 GMT, March 1 (Figure 9.1 a)
- photo taken at the buoy location 7:15 GMT, March 2 (Figure 9.1 b)
- photo taken north west of the buoy location 7:52 GMT, March 2 (Figure 9.1 c)
- and ERS-1 SAR images obtained 10:30 GMT March 2 (Figure 9.1 d).

The ERS-1 SAR image of 1 March 19:07 show a periodic pattern of bright and darker strips east of Hopen near the buoy location. The brighter strips, indicate the presence of wind rows and the darker strips are grease ice. The periodic system extends out from a continuos gray belt surrounding Hopen of older and thicker grease ice and early stage of pancake ice. A photo obtained from Håkon Mosby at 7:15 GMT March 2, show that the area above the buoy is characterized with new grease ice and open water in strips (Figure 9.1b). The portions of open water are clearly observed with locally generated capillary waves, whereas in the grease ice the short waves are smoothen out. Another photo taken at the same location at the same time but with another heading shows open water with a more complete and unfiltered wave field with a few whitecaps present. After crossing over the buoy position R/V Håkon Mosby moved towards Hopen. The next photo in Figure 9.1c show the thickening of the grease ice field as the ship moves north west towards Hopen. This indicate that the continuos belt of older grease ice and pancake ice develops towards the buoy location. In the thicker grease ice and early stage of pancake ice the wave field is further lowpass filtered resulting and there is no breaking waves. In the SAR image obtained 10:30 GMT 2 March it is observed that the area above the acoustic buoy is just to be covered by a continuos slick of grease ice or early stage of pancake ice. Based on the sequence of photographs and SAR images it is concluded that continuos coverage of thicker grease ice and pancake ice above the acoustic buoy develops between 7:15 GMT and 10:30 GMT.

Wind data obtained from the two moving ships outside the ice edge, R/V Håkon Mosby and R/V Polarsyssel, variation in wind speed and wind direction without any strong trends. By inspecting the ship track of Håkon Mosby and the position of Polarsyssel within the ice pack, it is found that the wind data from Polarsyssel are most representative from buoy deployment and the next 11 hours. After this Håkon Mosby become more representative as she moves in open water towards the buoy location. Taking wind speed and duration of wind into account the sea state is estimated to be 4 -5 during the 28 hours of acoustic recording. In open water sea state 4-5 imply more or less frequent wave breaking.

9.3.1 Acoustic observations.

Ship noise dominates and causes high acoustic levels at 17:00 GMT March 1 and between 7:00- 8:00 GMT, March 2, these data are excluded from further discussion.

9.3.1.1 Time series.

According to Figure 9.2 the low frequency noise components below 100 Hz varies different from the noise in the mid frequency domain 100-1000 Hz and high frequency domain 1-5.0 kHz.

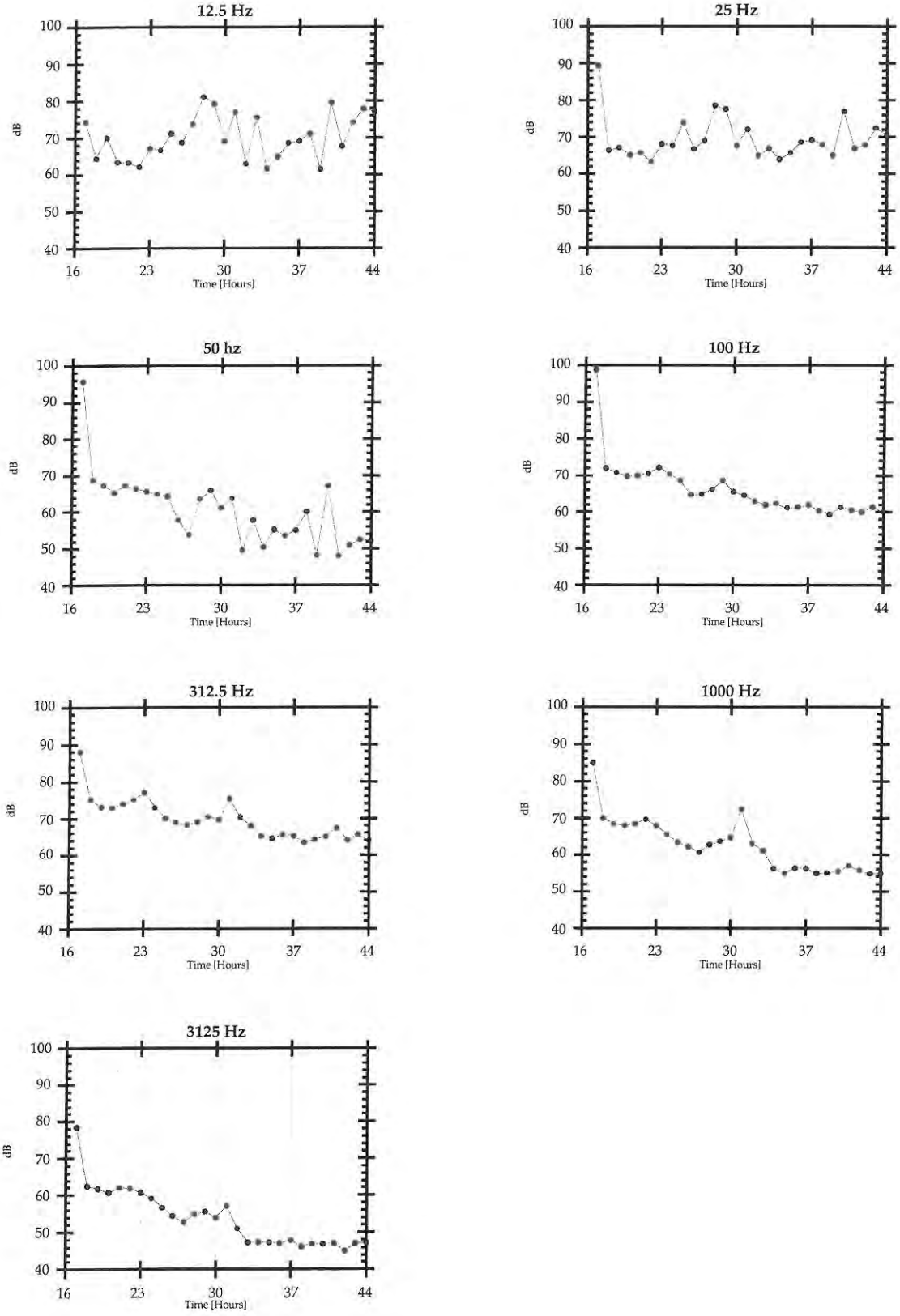

Figure 9.2. Ambient noise timeseries (17:00 GMT 1 March - 20:00 GMT 2 March) at selected frequencies.

Table 9.1. Ambient noise changes at selected frequencies. .

Time interval in GMT	Increase (+) /decrease (-) in ambient noise level at selected frequencies in dB				
	f=100	f=312.5	f=1000	f=3125	Sound characteristics
17:00-23:00	0	+2	0	-2	Strong sea noise
23:00-3:00	-7	-9	-7	-8	Reduced sea noise, bumping events
3:00-6:00	+1	+2	+4	+1	Sea noise and transients from animals
6:00-10:00	-3	-5	-9	-7	Reduced sea noise. Engine noise from HM between 7:00 and 8:00

At low frequencies there is a large variation in noise up to 20 dB at 12.5 Hz and 25 Hz. The variation has an hourly component and a 12 hour component. At 37 Hz the noise level is fairly constant, while the 50 Hz noise have unexplained large hourly variations.

The variation at the higher frequencies, above 100 Hz, are smoother. Five time intervals with reduction or increase in noise levels are observed in Figure 9.2, these are described in Table 9.1. The table show that there is two periods of significant noise reduction one during the night between 23:00-3:00, and one in the morning of March 2 between 6:00 and 10:00. After 11:00, March 2 only small temporal fluctuations of the order of 2-3 dB are observed at frequencies above 100 Hz.

9.3.1.2 Comparison with Wenz Curves.

Based on the wind data records from Håkon Mosby and Polarsyssel the sea state is given to be 4-5 during the 28 hours of acoustic recording. During the first 7 hours the ambient noise levels predicted by the Wenz curve for sea state 4, are significantly lower than the measured levels, which by Wenz curves corresponds to sea state 8. Between 23:00 and 3:00, March 2 the ambient noise levels is reduced. After the reduction the ambient noise level at the two highest frequencies corresponds to sea state 4. Low frequency ambient noise levels corresponds to a sea state above 4. This reflects a filtering of high frequency acoustic noise between 23:00-3:00. At 10:00 GMT the ambient noise levels are reduced to levels corresponding to sea state 2-3 at the highest frequencies and to sea state 4-5 at the mid frequencies.

9.4 Discussion.

The low frequency noise from the DATOS buoy have some indications that there is a diurnal component present, but since the time series is only 28 hours there is no

conclusive evidence of this. Explanation of the short term variations in this frequency domain have not been found.

The following discussion is on the ambient noise observations at frequencies above 100 Hz. Two periods of noise reduction have been identified in the analysis above. The first reduction of 8-10 dB, between 23:00 and 3:00, and the second reduction of 3-9 dB is between 6:00 and 10:00 (interrupted by engine noise from Håkon Mosby between 7:00 and 8:00).

9.4.1 Reduction prior to the grease ice formation.

The first period of reduction is not explained by reduced wave activity at the surface due to grease ice, since it has been shown that the grease ice cover develops between 7:15 and 10:30 March 2. Oceanographic measurements during SIZEX 92 show that prior to freezing processes a surface layer with cold water is formed (Sandven et al., 1998). The effect a surface duct and a thin layer of ice on acoustic propagation is investigated by numerical simulations using OASES using environmental parameters in Table 9.2. The water depth is 85 m, ice cover is 0.01 m and the surface duct is 40 m. The monochromatic and compressional point source is located 18 m below the ice cover. The receivers are positioned within the duct in Figure 9.3 a, while the receivers are positioned 2.0 m above the sea floor in Figure 9.3 b.

Table 9.2. Environmental parameters kept constant in the numerical simulations. The total water depth is kept to 200 m during all simulations.

		Parameter settings				
		CC	CS	AC	AS	RO
Layer no.	layer type	compressional speed	shear speed	compressional attenuation	shear attenuation	density
		[m/s];	[m/s];	dB/wavelength	dB/wavelength	[g/cm^3]
1	Vacuum	0	0	0	0	0
2	ice	3600	1800	1.0	2.5	0.92
3	water	1440	0	0	0	1.0
4	water	1460	0	0	0	1.0
5	bedrock 100 m thick	5000	3000	0.2	0.5	1.8
6	absorption layer (infinite)	5000	3000	1.0	2.0	1.8

The simulations show a high pass filtering of the acoustic energy within the surface duct, which corresponds to a trapping of sound from around 125 Hz and up within the duct. Only acoustic energy with steep enough grazing angle leaks out of the surface duct. Sound that leaks out of the surface duct will attenuate due to interaction with the bottom. Lower frequencies will propagate as if there was no surface duct.

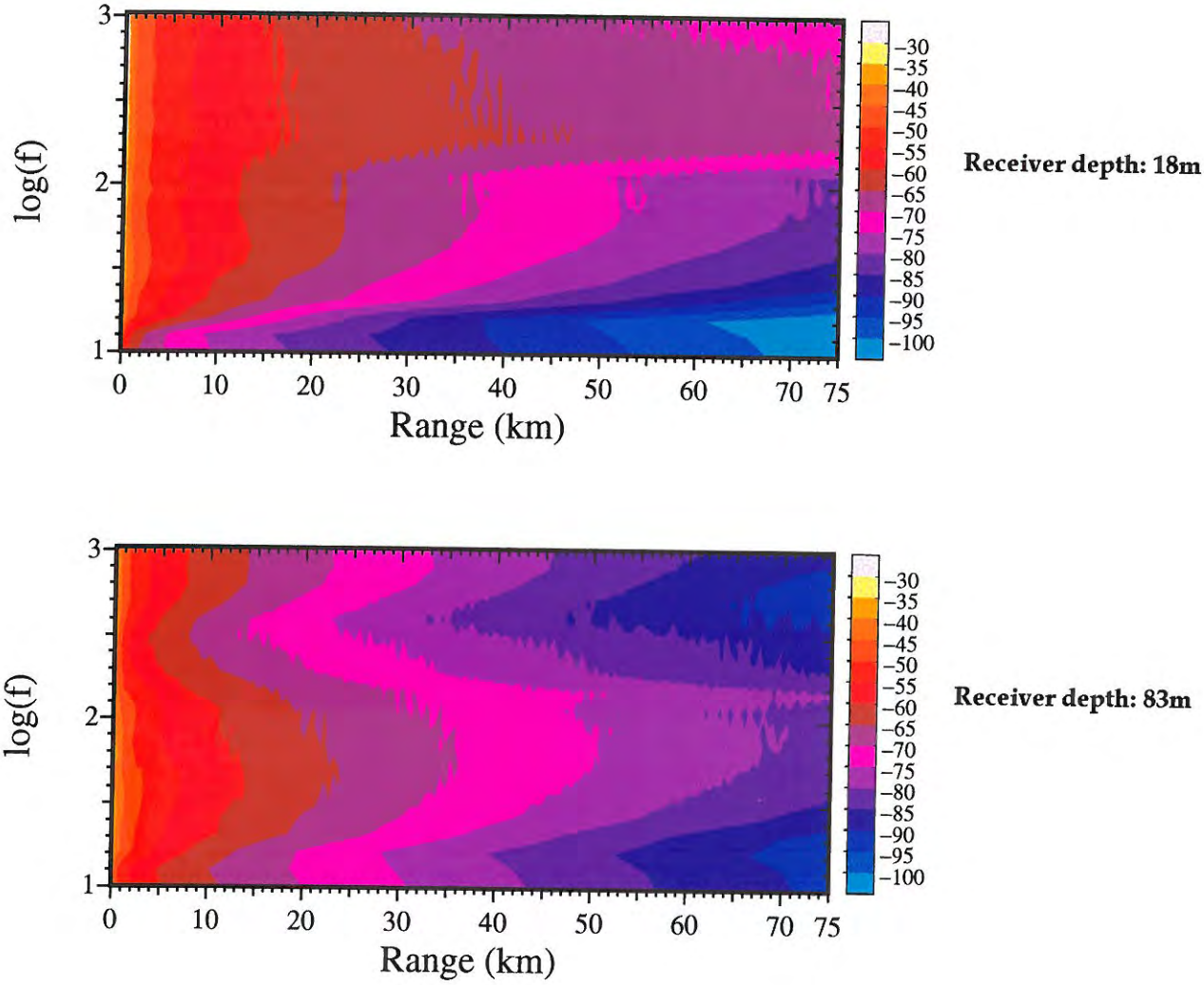

Figure 9.3. Tranmission loss as a function of frequency and range a) within the surface duct and b) close to the bottom. The source is positioned 18 m below a 1 cm thick cover with ice within a 40 m deep surface duct.

Losses due to interaction with the ice cover and seafloor is regulated according to the frequency dependent reflection coefficient and scattering function. Generally the losses increases with frequency.

According to the above a receiver positioned at 2.0 m above the seafloor records noise which have been low pass filtered. Furthermore, is the ambient noise field close to the sea floor dominated by locally generated noise at high frequencies, while at low frequency the noise field have contributions from both locally and distant sources. This explains the significant dampening observed in the ambient noise recordings at frequencies above 100 Hz, and why this dampening is not observed at lower frequencies

Furthermore, since the remaining ambient noise field is dominated by the local field at high frequencies, it will be more sensitive to local changes in ice and wave conditions. The sonogram obtained at 4:00 GMT show clear swell effects at high frequencies this coincide with a maximum in the time series at 4:00 and 5:00 at frequencies above 100 Hz, Figure 9.4 a.

9.4.2 Reduction of ambient noise due to grease ice.

The sonogram obtained at 10:00 GMT, Figure 9.4 a, shows a clear noise reduction at all frequencies, compared to 4:00 GMT, and only a very weak swell signature. This second reduction coincide with the progress of creation of grease ice and pancake ice, which occurs between 7:15 and 10:30 GMT. During sea state 4, the sea surface is characterized by relatively small waves and frequent whitecaps which indicate significant production of bubble. From Figure 9.1 the grease ice is clearly seen to reduce the number of whitecaps and the spilling ripples, this will accordingly reduce the sea state and thereby the ambient noise level. This confirms the hypothesis by Johannessen et al., 1988, that the wave dampening effect of grease ice reduces the ambient noise levels.

The effect of bubbles on ambient noise are twofold. Besides being one of the most important natural source of ambient noise, bubbles and bubble plumes have a strong impact on sound propagation(e.q. Leigthon, 1994). The presence of 0.01 % bubbles in water influences the speed of sound by tens of m/s. Bubble layers close to the surface can be around 2 m, and such layers have a lower sound speed and a much higher absorption than water layers below. The corresponding ducting of sound in such surface layer have been studied by Vagle and Farmer () and Buckingham(). The speed of sound in a bubbly fluid depends on the size and number of bubbles, and on the frequency of the sound. As this indicates, the bubble layer is a very complicated dispersive medium, which needs careful planning of numerical simulations. The bubble layer effect on propagation will not be studied in this thesis.

9.4.3 Speculations on the source of the residual ambient noise field.

The residual noise field is defined as the remaining acoustic field after the sources due to the spilling and breaking of surface waves has been eliminated by a complete cover of grease ice. The origin of the residual noise in regions covered with grease ice is not

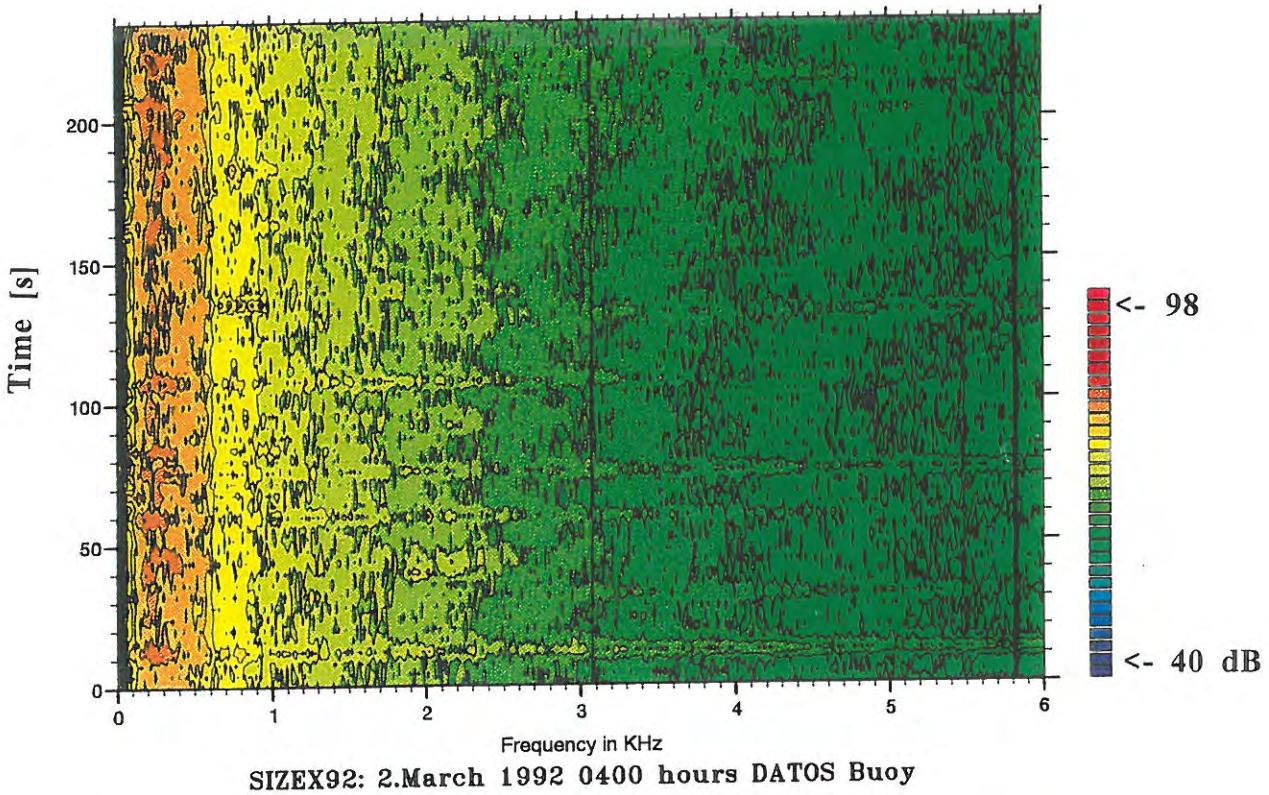

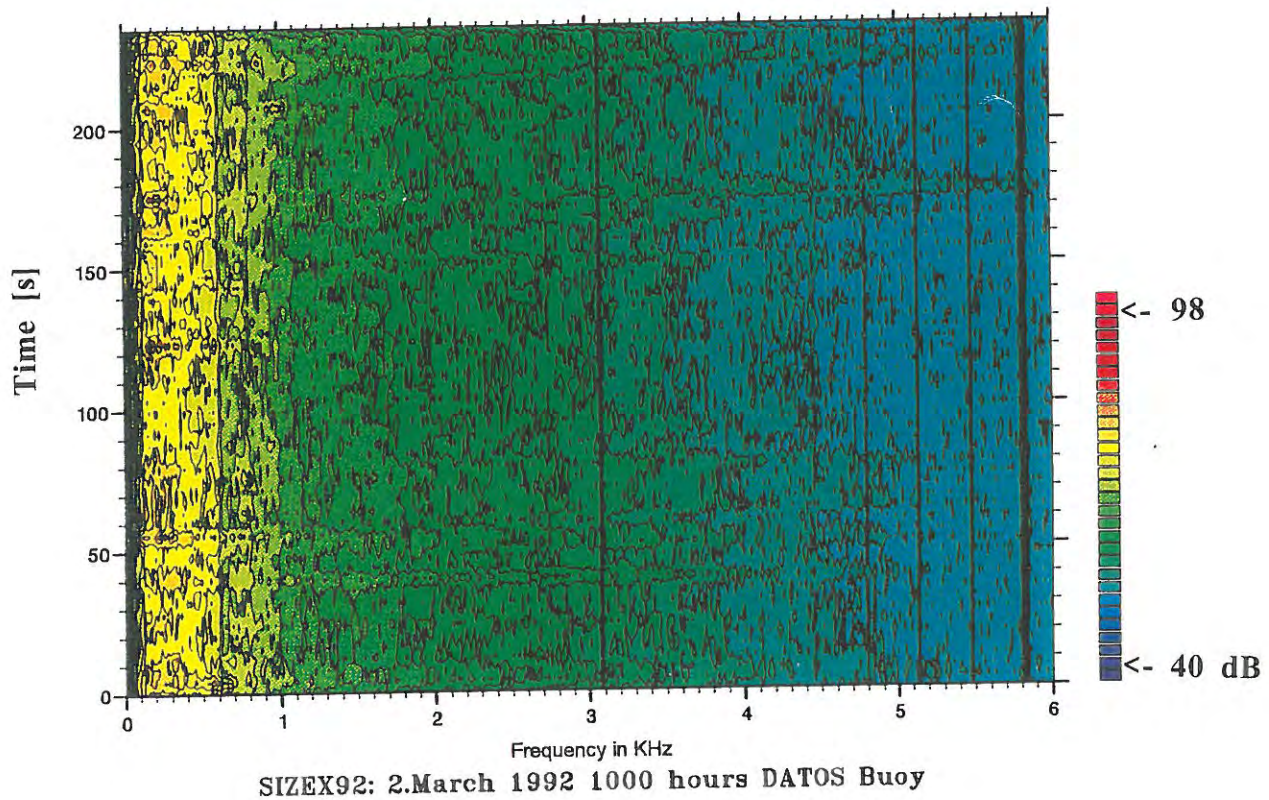

Figure 9.4. Sonogram obtained at 4:00 GMT and 10:00 GMT on 2 March 1992.

clear. Parts of the noise field is generated in the adjacent open ocean regions. Grease ice do not have significant dampening effect on the swell amplitude, from visual observations, but it will remove the bubble generating the surface processes. The sonogram at 10:00 GMT still have a weak signature of swell, indicating that the swell is causing local noise generating mechanisms. It has been shown in laboratories the gravity waves sets up internal current systems within the grease ice layer (Martin and Kauffmann, 1981). The grease ice and early stage pancake ice consist of small ice particles in which the wave motion or the wave induced current may cause several collisions between small particles.

The processes generating ambient noise at low sea states is less understood than the generation mechanisms at higher sea states (e.q. Rhor and Detsch (1992), Kerman et al., 1988, 1993). Non-linear surface wave interaction, or orbital wave motion, causing pressure fluctuations in the water has been proposed as the most possible low frequency sound generator (e.q. Cato, 1991). This corresponds well to our result that the ambient noise below 100 Hz, seems to be independent of the ice conditions which may be an indication of the above mentioned sound generation process. Another possible sound generation mechanism caused by swell may be increased water motion near the sea floor, which introduce increased upward spiraling of small particles which in turn may cause collisions with each other or with the hydrophone thereby generate high frequency sound.

9.5 Conclusion

The development of grease ice is preceded by a creation or enhancement of a surface duct which causes sound above around 100 Hz to be trapped close to the surface. This causes a dampening of acoustic ambient noise by 7-8 dB, at frequencies above 100 Hz close to the sea floor. As grease ice is formed and effectively dampens the shorter ocean surface waves the noise is reduced by 3-9 dB. The largest reduction of ambient noise is observed at the highest frequencies. The total dampening of ambient noise is up to 17 dB.

This study illustrates that the ambient noise characteristics are shaped partly by the noise generating processes and partly by propagation effects.

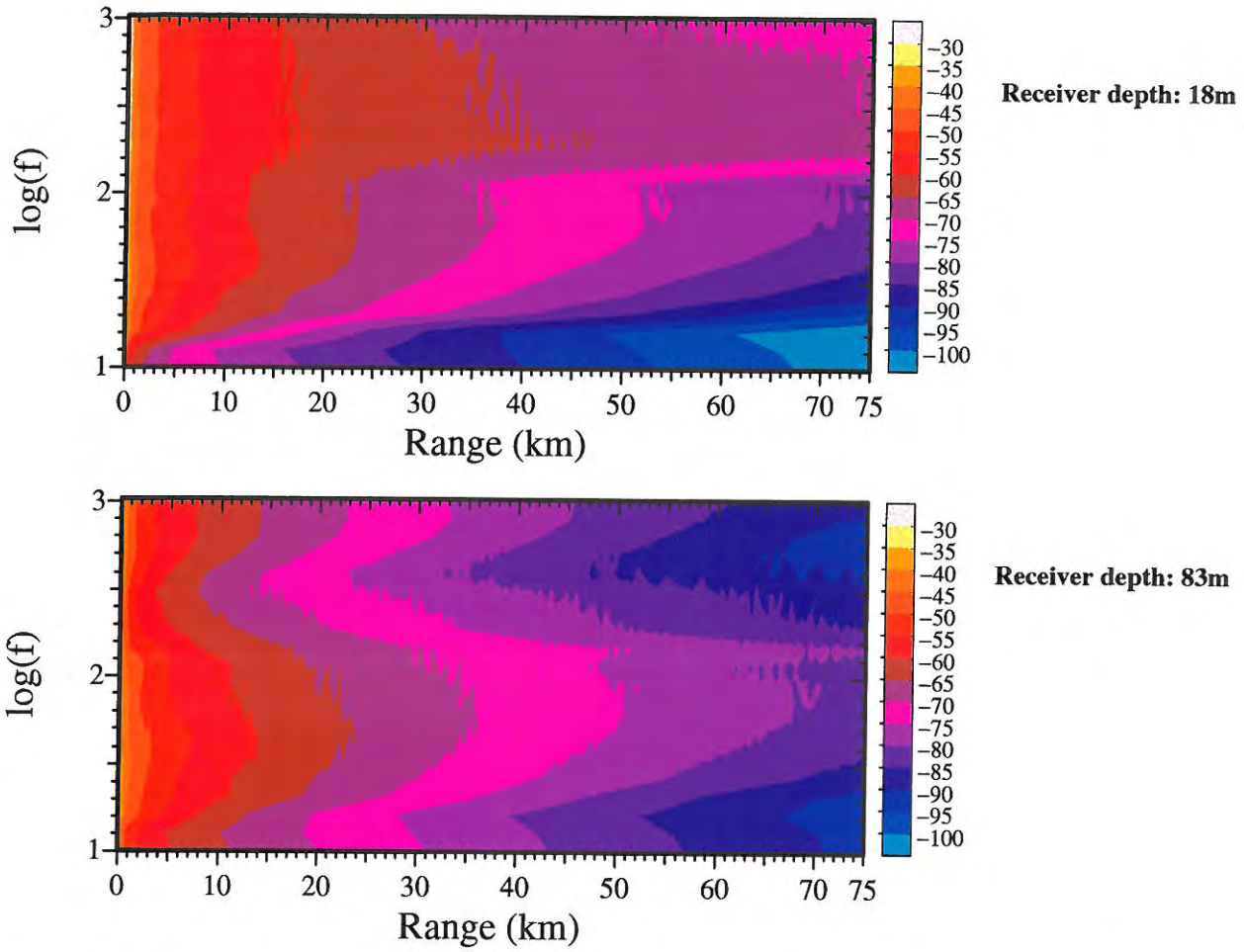

Figure 9.3. Tranmission loss as a function of frequency and range a) within the surface duct and b) close to the bottom. The source is positioned 18 m below a 1 cm thick cover with ice within a 40 m deep surface duct.

10. Summary, Recommendations, Application.

10.1 Summary.

Broad band ambient noise and broad band acoustic propagation in the marginal ice zone have analyzed in order to meet the overall objective of this study

Improve the understanding of the acoustic propagation and ambient noise generation in the MIZ.

Averaged levels, time series at selected frequencies, frequency spectra and sonogram have been used to characterize the ambient noise at 169 different locations. Acoustic propagation loss have been studied using propagation loss data and the numerical model OASES.

The main results of the six specific objectives are as follows:

Investigate broad band sound propagation in shallow water MIZ. (Chapter 5).

Experiment show

- a stronger transmission loss pr kilometer in the shallow MIZ than in open ocean or in the interior Arctic.
- that the optimum frequency domain of propagation is between 100 and 400 Hz for long range propagation.

Numerical simulations show that

- the reflection coefficient as a function of frequency and grazing angle is very sensitive to ice thickness.
- sound above 100 Hz is generally trapped in the surface duct where it is strongly exposed to reflection losses from the ice- water interface.
- optimum frequency domain is regulated by bottom interaction, ice thickness and the position of the receiver relative to the surface duct.

Investigate the hypothesis that hotspots along the ice edge are due to ice edge eddies. (Chapter 6)

- analysis of ambient noise data has verified that hotspots are generated by eddies, but other processes such as on ice wind and wave conditions produce hotspots too.

Investigate the hypothesis that icebergs causes hotspots in ambient noise. (Chapter 6)

• Ambient noise data have shown that hotspots can occur close to icebergs surrounded by dense sea ice exposed to swell in the Barents sea.

Investigate the effect of sound propagation on the broad band ambient noise. (Chapter 7)

• The maximum lobe of the frequency spectrum reflects the averaged optimum frequency domain of sound propagation.

• Kinks and slopes in frequency spectra are related to ice parameters through the reflection coefficients and the scattering from the ice.

Investigate the effect of swell on ambient noise. (Chapter 6 and 8)

• Ambient noise in cases of swell) is 9 dB higher along the ice edge compared to a case with insignificant swell.

• The period of swell propagating into the ice pack, can be derived from simple ambient noise measurements using omnidirectional hydrophones and simple processing of the data.

• A scheme for inversion of swell period and wavelength, is developed to retrieve ice thickness using elastic plate dispersion relation.

Investigate the effect of grease ice formation on ambient noise characteristics. (Chapter 9).

• Both the surface duct prior to freezing process and wave dampening effect of grease ice cause reduction of ambient noise above 100 Hz for a receiver located close to the sea floor.

10.2 Recommendations and Future work.

10.2.1 Future acoustic propagation modeling in the MIZ.

As was pointed out in Chapter 3 very little modeling of acoustic propagation in the MIZ have been done. This is due to the very complicated environmental conditions in the MIZ. The MIZ is an area partly covered with ice, which makes it different from the open ocean and the interior Arctic. Within the MIZ the ice conditions vary considerably in concentration (0-95%), floe size (0.5-100 m), ice type (grease ice, first year ice and multi year ice) and thickness (a few millimeters to 3 meters). The strong horizontal gradients in ice properties requires a range dependent ice scattering function and reflection/transmission coefficient. Generally, the scattering function from the ice cover will be dominated by scattering from edges instead of scattering from ridges as was the case in the Arctic Basin. In addition to the roughness introduced by the ice there is also roughness caused by the long surface waves that propagate

across the ice-water boundary into the MIZ from the adjacent oceans. This effect can readily be accounted for in models including ice roughness. Another complicating factor is the location of the ice/ocean boundary mainly at the continental shelf causing propagation in regions of shallow water and wedge shaped environments.

In Chapter 5 the range independent version of OASES was used to investigate the sensitivity of selected parameters, ice thickness and surface duct depth, on acoustic propagation. In forthcoming studies the range independent version of OASES will be used and the complexity of the environmental model will be extended. Special attention will be given to variable ice conditions, including roughness and layering, and range dependent variation in ocean stratification.

Another approach is to use ray trace models. Ray trace models are numerically efficient, have simple physical interpretation and they can handle relatively strong horizontal variations in the ocean stratification. The models have been relatively little used for forward modeling in for example shallow water regions due to its high frequency approximation. However, ray calculations in shallow water can be improved and made valid down to low frequency if beam displacement at the reflecting interfaces are accounted for (Tindle and Bould, J. Acoust. Soc. Am. 70, 813-819 (1981)). Generalized ray theory methods have been used to study the effect of ice cover on travel times (Jin et al., 1993).

The flexibility in the ray trace model offers an efficient method to handle the varying bottom and surface conditions in addition to variation in sound speed profiles. The possibility to include different reflection coefficients for different regions in the model makes it very useful in the MIZ. We suggest to provide the ray trace model with angle and frequency dependent reflection coefficients and scattering functions according to the different ice/bottom conditions along the propagation track. The reflection and transmission coefficients for the different media can be obtained from other models such as the OASES model, which also includes the material roughness and elastic properties.

The environmental input to the model will be (1) ice statistics of the region using satellite data and upward looking sonar data, (2) sound velocity profiles, (3) current velocity profiles (4) topography and geo-acoustic information from databases or maps. Due to little information about the oceanographical fields, apriori knowledge has to be used. Remote sensing data can be used to localize mesoscale structures such as eddies and fronts causing propagation anomalies.

A concept as outlined above would be an important contribution to understand the sound propagation in the MIZ, and would represent an useful tool in an operational acoustic monitoring system.

10.2.2 Proposed work in ambient noise.

One approach in acoustic ambient noise modeling is to find cross-spectral density of the ambient noise defined as the Fourier Transform of the cross correlation function of the acoustic field at two locations. Sound intensity at a point is similarly given by the Fourier Transform of the auto correlation of the acoustic field. In order to model the ambient noise, the acoustic field has to be found by solving the corresponding acoustic propagation loss problem. The propagation problem for the MIZ is far from solved, therefore no ambient noise model exists for the MIZ.

In order to perform an accurate inversion from ambient noise to sea ice parameters and ocean parameters a better knowledge of the reflectivity from ice and the effect ocean stratification in Arctic on the acoustic propagation and thereby on acoustic ambient noise is needed. The sensitivity of ocean temperature and sea ice parameters, including range dependence, on acoustic propagation will be studied in a new project using numerical models. If future investigations make it possible to invert broad band ambient noise observations to averaged ice parameters and ocean parameters, as described in Chapter 7, it will represent a new and important contribution to the long term acoustic monitoring concept of the Arctic regions.

10.3 "Listen to the Climate Change".

The possibility to monitor climate change in the Arctic ocean using underwater acoustic is a new concept which is studied in "Acoustic Monitoring of Ocean Climate" (AMOC) (Johannessen et al., 1997). The TransArctic Propagation experiment was the first study of basin wide propagation in the Arctic Basin (Mikhalevsky, 1994). This experiment showed that sound may propagate across the basin, and that travel time changes can potentially be used to monitor averaged ocean temperature in the Arctic. Laible and Rajan (1996) studied the temporal variation of the under ice reflectivity, and attributes the seasonal changes to the combined effect of mechanisms that affect the water column properties, wave speed structure in the ice as well as the roughness at the ice water interface.

AMOC is a three year international project founded by the European Commission Environment and Climate Programme 1994-1998 and the Norwegian Research Council. The overall objective of AMOC is to develop and design an acoustic system for long-term monitoring of the ocean temperature and ice thickness in the Arctic Ocean, including the Fram Strait, for climate variability studies and global warming detection.

The proposed monitoring concept, requires both source and receiver configurations. Results from our study suggests that ambient noise could be part of such an monitoring system. Ambient noise measurements have several benefits. First of all it produces no additional man-made noise in the Arctic ocean. Secondly, receiver arrays are much cheaper than configurations using large, low frequency acoustic sources. Thirdly, ambient noise recording systems needs much less energy supply and can also

easily be mounted at the sea bottom or under the ice. Finally, the ambient noise can be used in a variety of ways both to identify dynamic processes causing break up, swell, ridging and to retrieve changes in averaged ice parameters and ocean stratification.

This makes the monitoring of changes in broad band ambient noise characteristics very interesting as a component in future Acoustic Monitoring System concepts in the Arctic Ocean.

References.

Aagaard, K., E.C. Carmack (1994). The Arctic Ocean and Climate: Perspective. in *The polar oceans and their role in shaping the global environment, Nansen Centennial Volume, Geophysical Monograph 85,* edited by O.M. Johannessen, R.D.Muench and J.E. Overland, (American Geophysical Union, United States of America, 1994) pp. 5-20.

Anderson, L.G., G. Bjørk, O. Holby, E.P.Jones, G. Kattner, K.P. Koltermann, B. Liljeblad, R. Lindegren, B. Rudels, and J. H. Swift, (**1994**), Water masses and circulation in the Eurasian Basin: Results from the Oden 91 expedition", J. Geophys. Res. Vol 99 (C2), pp.3273-3283.

Buckingham, M.J., S.A.S. Jones, (**1987**). A new shallow-ocean technique for determining the critical angle of the sea bed from vertical directionality of the ambient noise in the water column. J. Acoust. Soc. Am. 81 (4), 938-946.

Buckingham, M.J., C. Cheng (**1988**). "Acoustic ambient noise in the Arctic ocean below the marginal ice zone" in *Natural mechanisms of surface generated noise in the ocean,* Edited by B.R. Kerman, (Kluwer Academic Publishers, Netherlands, 1988), 583-598.

Buckingham, M.J., (**1990**). "Ocean acoustic propagation and ambient noise in a surface duct," in *Natural Physical Sources of underwater sound,* edited by B.R. Kerman (Kluwer Academic Publishers, Netherlands, 1993) p. 1-15.

Buckingham, M.J., (**1991**). "On acoustic transmission in ocean surface waveguides" Phil. Trans. R. Soc. London. A 335, 513-555.

Buckingham, M.J., (**1992**). "Ocean acoustic propagation models" J. Acoustique, 223-287.

Buckingham, M.J., B. V. Berkhout, S.A.L. Glegg, (**1992**). "Imaging the ocean with ambient noise". Nature Vol 356.

Buckingham, M.J., (**1993**). On surface generated ambient noise in an upward refracting ocean. Lecture notes, Advanced course on acoustical oceanography, Crete.

Buckingham, M.J. ,G.B. Deane, N.M. Carbone (**1994 c**). "Determination of elastic sea floor parameters from shallow water ambient noise," in proceeding of The 2nd European Conference on Underwater Acoustics, edited by L. Bjørnø, (European Commission, Belgium, 1994) pp. 33-38.

Bourke, R.H., A.R. Parsons. (**1993**). Ambien tnoise characteristics of the northwestern Barents Sea. J. Acoust. Soc. Am. 94 (5), 2799-2808.

Brekhovskikh, L.M., (**1980**) Waves in layered media. (Sec. Ed.) Applied mathematics and Mechanics 16. Academic Press, Inc.

Chapman, NCR.,(**1988**), Source levels of shallow Explosive Charges, J.Acoust. Soc. of Am. 84(2).

Dahl, P.H., (**1989**), "Acoustic Diffraction from a Semi-Infinite Elastic Plate Under Arbitary Fluid Loading with Application to Scattering from Arctic Ice Leads", Doctoral Dissertation, WHOI-89-28.

Diachok, O.J., Winokur, R.S., (**1974**). "Spatial variability of underwater ambient noise at the Arctic ice-water boundary," J. Acoust. Soc. Am., **55**, 750 - 753.

Diachoke, O.I., (**1976**) "Effects of sea -ice ridges on sound propagation in the Arctic Ocean", J.Acoust.Soc.Am., Vol.59 (5), 1110-1120.

Diachoke, O.J., (**1980**). "Arctic Hydroacoustic," in Cold Regions Science and Technology, Vol.2, pp. 185-201.

Dyer I., P.H. Dahl, A.B. Baggeroer, P.N. Mikhalevsky (**1987**). Ocean Dynamics and Acoustic Fluctuations in the Fram Strait Marginal Ice Zone. Science, Volume 236, 435-436.

Elverhøi, A., A. Solheim (1983). Surface sediment distribution. Norsk Polarinstitutt Skrifter, Nr. 179A.

Engelsen, I., (**1990**). "SIZEX 89 - Sonobuoy ambient noise data report", Norwegian Defence Research Establishment, NOTAT-90/2007.

Engelsen, I., (**1993a**). "SIZEX 92 - Propagation loss studies-data report", Norwegian Defence Research Establishment, FFI/RAPPORT-93/2002.

Engelsen, I (**1993b**). SIZEX 92- Ambient noise measurements- Data report, FFI/Rapport-93/2006.

Farmer, D., S. Vagle (**1988**), On the determination of breaking surface wave distributions using ambient sound. J. Geophys. Res., 938 (**C4**), 3591-3600.

Fricke, J.R., (**1991**). "Acoustic scattering from elastic ice, A finite difference solution", Doctoral dissertation, WHOI-91-10.

Fricke, J. R. (**1993**), "Acoustic scattering from elemental Arctic ice features: Numerical modelling results.", J.Acoust. Soc.Am. 93 (4), 1784-1796.

Fricke, J. R. and G.L. Unger (**1995**), "Acoustic scattering from elemental Arctic ice features: Experimental results.", J.Acoust. Soc.Am. 97 (1), 192 - 198.

Focke, K. C., M.S. Bennett, N.R. Bedford. (**1993**). Ambient noise and Acoustic Propagation Loss at CEAREX/SIZEX 89 Barents Sea Sites. Technical Report ARL-TR-93-22. Applied Research Laboratories, The University of Texas at Austin.

Fox, C. and V. A Squire. (**1991**). Strain in Shore Fast Ice Due to Incoming Ocean Waves and Swell, J. Geophys. Res. Vol.96, (C3), 4531-4547.

Fox, C., V.A. Squire. (**1994**). On the oblique reflexion and transmisson of ocean waves at shore fast ice. Phil. Trans. R. Soc. London. A **347**, 185-218.

Gaspin, J.B., V.K. Schuler (**1971**), Source levels of Shallow Underwater Explosives. NOLTR 71-160, Naval Ordnance Laboratory.

Gerstoft, P., H. Schmidt (**1991**). A boundary element approach to ocean seismoacoustic facet reverberation. J. Acoust. Soc. Am. **89** (4), 1629-1642.

Gjevik, B., E.Nøst, T.Straume,. (1990). Atlas of tides on the shelfs of the Norwegian and the Barents Sea. Department of Mathematics, University of Oslo, P.O. Box 1053 Olso, Norway.

Goh, J. T., H. Schmidt (**1994**), "Validity of spectral theories for weakly range dependent ocean environments-Numerical results", J. Acoust. Soc. **95** (2), 727-732 .

Goh, J.T., H. Schmidt, (**1995**) "Spectral super element approach to range dependent ocean acoustic modelling", J.Acoust. Soc. Am. **98** (2) **100**, 465-472.

Goh, J.T., H. Schmidt, (**1996**) "A hybrid couples wave-number integration approach to range-dependent seismoacoustic modelling", J.Acoust. Soc. **100** (3), 1409-1420.

Goh, J.T., H. Schmidt, P. Gerstoft, Woojae Seong, (**1997**)"Benchmarks for validating range -dependent seismo-acoustic propagation codes", IEEE Journal of oceanic engineering, Vol.XX, NO.Y.

Goodman, D.J., P.Wadhams and V.A. Squire (1980), "The Flexural Response of a Tabular Ice Island to Ocan Swell", Annals of Glaciology.Hunter, S.C. (1983). "Mechanics of contineous media. Second edition.", (Ellis Horwood).

Jensen, F.B., W.A. Kupermann, M.B. Porter, H. Schmidt, (**1994**). *Computional ocean Acoustics*, (American Institute of Physics, New York, 1994) pp. 121-129.

Jin, G., J.F.Lynch, R.Pawlowicz, P. Wadhams. (**1993**). Effects of sea ice cover on acoustic ray travel times, with applications to the Greenland Sea tomography experiment. J.Acoust. Soc. Am. 94 (2), 1044-1057.

Jin, G., J.F.Lynch, R.Pawlowicz, P. Worcester. (**1994**). Acoustic scattering losses in the Greenland Sea marginal ice zone during the 1988-89 tomography experiment. J.Acoust. Soc. Am. 96 (5), 3045-3053.

Johannessen, O.M., and L.A. Foster (**1978**). A note on the topographically controlled Oceanic Polar Front in the Barents Sea. Journal of Geophysical Research, Ocean Front Issue, vol. 83, no. C9, Ser. 30.

Johannessen, O.M., J.A. Johannessen, B. Farrelly, and E.A. Svendsen (**1983**). Oceanographic conditions in the marginal ice zone noth of Svalbard in early fall 1979 with an emphasis on mesoscale processes. J. Geophys. Res., 88, 2755-2769.

Johannessen, O.M, J.A. Johannessen, E. Svendsen, R.A. Shuchman, W.J. Campbell, E.G. Josberger (**1987a**). "Ice- Edge Eddies in the Fram Strait Marginal Ice Zone," SCIENCE, Volume 236, 427-429.

Johannessen, J. A. , O.M. Johannessen, E. Svendsen, R. Shuchman, T. Manley, W.J. Campbell, E.G. Josberger, S. Sandven, J. C. Gascard, T. Olaussen, K. Davidson, J. Van

Leer, (**1987b**). "Mesoscale eddies in the Fram Strait marginal ice Zone during the 1983 and 1984 marginal ice zone experiments," J. Geophys. Res. **92**, 6754 - 6772.

Johannessen, O.M., Payne, S., Starke, K.V., Gotthardt, G.A. and Dyer, I., (**1988 a**). "Ice edge ambient noise," in *Natural mechanisms of surface generated noise in the ocean*, Edited by B.R. Kerman, (Kluwer Academic Publishers, Netherlands, 1988), pp. 599-605.

Johannessen, O.M., Starke, K.V., Payne, S., Sagen, H., (**1988 b**). *Ambient noise in the Marginal Ice Zone.* The Nansen Environmental and Remote Sensing Center Technical Report, no 14.

Johannessen, O.M., Sagen, H., Sandven, S, Starke, K.V., Payne, S.G., Engelsen, I., (**1990**). *Ambient noise in the Marginal Ice Zone*, The Nansen Remote Environmental and Sensing Center series of Technical reports, No 32.

Johannessen, O.M., Ø. Nesse and I. Engelsen (**1992a**) Correlation between ambient noise and environmental variables in the MIZ of the Barents Sea. NERSC Technical Report no. 52.

Johannessen, O. M., H. Sagen, Ø. Nesse, I. Engelsen and S. Sandven (**1992b**). "Ambient noise generated by ice-ocean jets, eddies and tidal current in the marginal ice zone," in *Proceeding of European Conference on Underwater Acoustics,* edited by M. Weydert (Elsevier Applied Science, 1992), pp. 28 - 38 .

Johannessen, O.M., W.J. Campbell, R. Schuchman, S. Sandven, P. Gloersen, J.A. Johannessen, E. G. Josberger, P.M. Haugan (**1992c**). Microwave study programs of air-ice-ocean interactive processes in the seasonal ice zone of the Greenland and Barents Seas. Microwave Remote Sensing of Sea Ice, Geophysical Monograph 68, American Geophysical Union.

Johannessen, O. M., H. Sagen, S. Sandven, K. V. Starke, S. Payne and I. Engelsen, (**1993a**). "Spatial variation in ambient sound level within ice edge eddies," in *Natural Physical Sources of Underwater Sound (2),* edited by B. R. Kerman, (Kluwer Academic Publishers, Netherlands,1993), pp. 563 - 572, .

Johannessen, O. M., I. Engelsen, H. Sagen, S. Sandven and Ø. Nesse. (**1993b**). Acoustic Experiment Report from the Seasonal Ice Zone Experiment in the Barents Sea in March 1992. NERSC Techn. Rep. no. 68.

Johannessen, O. M., H. Sagen, S. Sandven, I. Engelsen. (**1994a**). "The influence of grease ice, swell and icebergs on ambient noise," in proceeding of The 2nd European Conference on Underwater Acoustics, edited by L. Bjørnø, (European Commission, Belgium, 1994) pp. 33-38.

Johannessen, O. M., S. Sandven, W. P. Budgell and J. A. Johannessen (**1994b**). "Observation and simulation of ice tongues and vortex pairs in the marginal ice zone," in *The polar oceans and their role in shaping the global environment, Nansen Centennial Volume, Geophysical Monograph 85,* edited by O.M. Johannessen, R.D.Muench and J.E. Overland, (American Geophysical Union, United States of America, 1994) pp. 109-136.

Johannessen, O.M, et al., (**1997**). Acoustic Monitoring of the Ocean Climate in the Arctic Ocean (AMOC). A proposal to the European Commision Environment and Climate Programme, 1994-1998.

Kerman, B.R. (Ed.) (**1988**). Sea surface sound. Natural mechanisms of surface generated noise in the ocean. Kluwer Academic Publishers, Netherlands, 1988.

Kerman, B.R. (Ed.) (**1990**) Sea surface sound (II). Natural Physical Sources of Underwater Sound. Kluwer Academic Publishers, Netherlands, 1993.

Kloster, K., W. Spring (**1993**). Iceberg and glacier mapping using satellite optical imagery during the Barents Sea Ice Data Aquisition Program (IDAP). Proceeding of "the 12th international Conference on Port and Ocean Engineering under Arctic Conditions", Vol. 1., Hamburg.

Kowalik and Proshutinsk (1994). "The Arctic Ocean Tides." in *The polar oceans and their role in shaping the global environment, Nansen Centennial Volume, Geophysical Monograph 85,* edited by O.M. Johannessen, R.D.Muench and J.E. Overland, (American Geophysical Union, United States of America, 1994) pp. 137-158

Kupermann, W.A., H. Schmidt (**1989**). Self-consistent perturbation approach to rough surface scattering in stratified elastic media. J.Acoust. Soc. Am. **86** (4), 1511-1522.

Laible, H.A., S. D. Rajan. (1996). Temporal evolution of ice reflectivity. J. Acoust. Soc. Am., **99** (2), 851-865

Leighton,T.G. (**1994**). The Acoustic bubble. (Academic Press, London, 1994).

LePage, K. and H. Schmidt (**1994**), Modelling of low frequency transmission loss in the central Arctic", J.Acoust. Soc. Am **96** (3), 1783-1795.

Lu, I.T. and L.B. Felsen, (1987). Adiabatic transforms for spectral analysis and synthesis of weakly range-dependent shallow ocean Grens functions. J. Acoust. Soc. Am. **81**, 897-911.

Lynch, J.F., R.C. Spindel, C.-S Chiu, J.H. Miller, T.G. Birdsall (**1987**). Results from the Marginal Ice Zone Experiment Preliminary Tomography Transmissions: Implications for Marginal Ice Zone, Arctic and Surface Wave Tomography. J. Geophys. Res., Vol.92, No. C7, 6869-6885.

Lynch, J.F., H.X. Wu, R. Pawlowicz, P. Worcester, R. Keenan, H. Graber, P. Wadhams, O.M. Johannessen , (**1993**). "Ambient noise measurements in the 200-300 Hz band from the Greenland Sea tomography experiment," J. Acoust. Soc. Am., **94**, 1015-1033.

Lynch, J.F., G. Jin, R. Pawlowicz, D. Ray, A. J. Plueddemann, C.-S. Chiu, J.H. Miller, R.H. Bourke, A.R.Parsons, R. Muench (**1996**). Acoustic travel-time perturbations due to shallow-water internal waves and internal tides in the Barents Sea Polar Front: Theory and experiment. J. Acoust. Soc. Am.99 (2), 803-821.

Løset, S., T. Carstens (**1993**). Production of icebergs and observed extreme drift speeds in the Barents Sea. Proceeding of "the 12th international Conference on Port and Ocean Engineering under Arctic Conditions", Vol. 1., Hamburg.

Makris, N.C. , Dyer, I., (**1991**). "Environmental correlates of Arctic ice edge noise," J. Acoust. Soc. Am. **90**, 3288-3298.

Martin, S., P. Kauffman. (**1981**). A field and laboratory study of wave damping by grease ice. J. Glaciology, Vol. 27, No. 96. 283-313.

Mellberg, L. E, O. M. Johannessen, D. Connors, G. Botseas and D. Browning (**1987**). Modeled acoustic propagation through an ice edge eddy in the East Greenland Sea marginal ice zone. J. Geophys. Res. **92**. , 6857 - 6868.

Mellberg, L. E., O. M. Johannessen, D. Connors, G. Botseas and D. Browing (**1991**). "Acoustic propagation in the western Greenland Sea frontal zone," J. Acoust. Soc. **89**, 2144 - 2156.

Melville, W.K. (**1994**). "Oceanographic Applications of Natural Sea Surface Sound". In the proceeding Sea surface sound. Proceeding of the III meeting on Natural Physical Processes related to Sea surface sound. California.

Meylan, M., V.A. Squire. (**1994**). The response of ice floes to ocean waves. J. Geophys. Res. **99**. , 891 - 900

Mikhalevsky, P., A.B. Baggeroer, H. Schmidt, K. von der Heydt, E.K. Scheer, A. Gavrilov (1995). Transarctic Acoustic Propagation. Sea Ice Mechanics and Arctic Modelling Workshop, Volume I, Anchorage, Alaska.

Munk, W., P. Worcester, C. Wunsch (**1995**). Ocean Acoustic Tomography. Cambridge Monographs on Mechanics.

Nesse, Ø., O.M. Johannessen and I. Engelsen (**1992**). A note on the mid frequency ambient noise in the MIZ. NERSC progress report.

Noble, B..(**1958**). Methods based on the Wiener-Hopf Technique. Chelsea Publishing Company, New York.

Pawlowicz, R., D. Farmer, B. Sotirin, S. Ozard (**1996**). Shallow-water receptions from the transarctic acoustic propagation experiment. J. Acoust. Soc.Am. **100** (3), 1482-1491.

Pfirman, S.L., D Bauch, and T. Gammelsrød, (**1994**) The Northern Barents Sea: Water Mass Distribution and Modification, in*The Polar Ocean and Their Role in Shaping the Global Environment* edited by O.M.Johannessen, R.D. Muench, J.E. Overland (Geophysical Monograph Series, 85, American Geophysical Union, United States of America, 1994), pp. 77-94.

Pritchard, R.S, (**1990**). "Sea ice noise generating mechanisms." J. Acoust. Soc. Am. **88**, 2830-2842.

Rhor, J., R. Detsch (**1992**). Low sea-state study of the quieting effect of monomolecular films on the underlying ambient noise field. J. Acoust. Soc.Am. 92 (1), 365-383.

Rottier, P. J., (**1990**), *Wave/Ice interactions in the marginal ice zone and the generation of ocean noise.* Ph. D. thesis. University of Cambridge.

Sagen, H., O.M. Johannessen, S. Sandven. (**1990**). The influence of sea ice on ocean ambient noise. "Ice Technology for Polar Operation". Edited by T.K.S.Murthy, J.G. Paren, W.M. Sackinger, P. Wadhams. Computational Publications, 309-320.

Sandven, S., and O.M. Johannessen (**1987**). High-frequency internal wave observations in the Marginal Ice Zone. Journal of Geophysical Research, Vol. 92, June, 1987, pp6911 - 6920.

Sandven, S., O.M.Johannessen. (**1990**) Seasonal Ice Zone Studies. The Sea. Ocean Engineering Science. Volume 9. John Wiley&Sons, Inc., 567-592.

Sandven, S., O.M. Johannessen. (**1993a**). The use of microwave remote sensing for sea ice studies in the Barents Sea. ISPRS Journal of Photogrammetry and Remote Sensing, 48(1), 2-18.

Sandven, S., K. Kloster, O.M.Johannessen, M.Miles (**1993**). SIZEX 92. ERS-1 SAR Ice Validation Experiment. Final Report. NERSC Technical Report no.69.

Sandven, S., O.M. Johannessen, M.W. Miles, L.H. Petterson and Kjell Kloster. (**1998**). Barents Sea seasonal ice zone features and processes from ERS-1 SAR: SIZEX 92. Inpreparation.

Schmidt, H. (**1988**). SAFARI. Seismo Acoustic Fast field Algorithm for Range-Independent environments. User´s guide. Saclant Undersea Research Centre. Report.

Schmidt, H. (**1994**). "Seismo-Acoustics of the Arctic Ice Cover," in *Proceedings of the second European conference on Underwater Acoustics, Volume 1*, edited by L. Bjørnø, (European Commission, Belgium, 1994), pp. 3-14.

Schmidt, H., W.Seong and J.T. Goh (**1995**). "Spectral super-element approach to range dependent ocean acoustic modelling", J.Acoust. Soc. **98** (1), 465-472.

Schmidt, H.. (**1997**). OASES Version 2.1 User Guide and Reference Manual. Department of Ocean Engineering. Massachusetts Institute of Technology.

Shuchman, R.A., C.L. Rufenach, O.M. Johannessen (**1994**). Extraction of Marginal ice zone thickness using gravity wave imagery. J.Geopys.Res. 96, (C5), 901-918.

Solheim, A., Y. Kristoffersen (**1984**). Sediments above the upper regional uncomformity: thickness, seismic stratigraphy and outline of the glacial history. Norsk Polarinstitutt Skrifter, Nr. 179B.

Squire, V.A.. (**1993 a**). The break up of shore fast sea ice. Cold Regions Science and Technology, 21, 211-218.

Squire, V. A. .(**1993 b**). A comparison of the mass-loading and elastic plate models of an ice field, Cold Regions Science and Technology, 21, 219-229.

Squire, V.A.. (**1993 c**). Marginal ice zone parameterization from ocean wave refraction. Cold Regions Science and Technology, 22. 235-241.

Squire, V. A.(**1994**) . The Marginal Ice Zone, Lecture Notes, Finland.

Sutton, P.J., P.F. Worcester, G. Masters, B.D. Cornuelle, J.F. Lynch, (**1993**). Ocean mixed layers and acoustic propagation in the Greenland Sea. J.Acoust. Soc. Am. **94**(3), 1517-1526.

Turner, T., R.E. Jones. (**1993**). Fleet trial 26/90 Ambient noise report. EASAMS Limited. Ref. No.: 3879/005.

Updegraaf and V.C. Anderson. (**1989**). "Insitu acoustic signature of low sea state microbreaking. J. Acoust. Soc. Am. (85) suppl. 1,p S146, May .

Vinje, T., (1985). Drift, Composition, Morphology and Distribution of Sea Ice Fields in the Barents Sea. Norsk Polarinstitutt Skrifter, Nr. 179C.

Wadhams, P., (**1973**). The Attenuation of Swell by Sea Ice. J. Geophys. Res., 78 (**18**), 3552-3563.

Wadhams, P., M. Kristensen and O. Orheim, (**1983**). The response of Antarctic icebergs to ocean waves. J. Geophys. Res., 88(C10), 6053-6065.

Wadhams, P. (**1986**). "The seasonal ice zone" in The geophysics of sea ice. Edited by N. Untersteiner, NATO ASI Ser. B. 146, 825-991.

Wadhams, P., V.A. Squire, D.J. Goodman, A.M.Cowan, S.C. Moore (**1988**). The attenuation Rates of ocean Waves in the Marginal Ice Zone. J. Geophys. Res. Vol.93, No. C6, 6799-6818.

Wadhams, P., B. Holt(**1991**). Waves in Frazil and Pancake Ice and Their Detection in Seasat Syntehetic Aperture Radar Imagery. J.Geopys.Res. **96**, (C5), 8835-8852.

Wadhams, P. (**1994**). Sea ice thickness changes and their relation to climate. In *Nansen Centennial Volume on the Role of the Polar Oceans in Shaping the Global Environment*, (Editors: Johannessen, O.M., R. Muench and J.E. Overland). American Geophysical Union Monograph, No 85 - 572 pp337 - 362.

Wenz, G.M., (**1962**). Acoustic Ambient Noise in the Ocean: Spectra and Sources. J. Acoust. Soc. Am. 34 (12), 1936-1956.

Worcester, P.F., J.F. Lynch, W.M.L. Morawitz, R.Pawlowicz, P.J. Sutton, B.D. Cournuelle, O.M. Johannessen, W.H. Munk, W.B. Owens, R. Shuchman and R.C.Spindel (**1993**). Evolution of the large scale temperature field in the Greenland Sea during 1988-89 from tomographic measurements. Geophys. Res. Letter, Vol. 20, No. 20, 2211-2214.

Yang, T.C., G.R. Giellis, C.W. Votaw, O.I. Diachok, (**1987**). "Acoustic properties of ice edge noise in the Greenland Sea," J. Acoust.Soc. Am. **82**,1034-1038. .

Appendix A Description of broad band data processing

In order to study broad banded short term variations a new data processing system for acoustic data was developed at NERSC, in 1992 - 1993. The system is based on the possibility to take digital data from a DAT tape into a Silicon Graphic Workstation. Due to a software problem it was not possible to insert the analog data directly from the tape recorder to the Silicon Graphic workstation. To make the acoustic data available for the Silicon Graphics an AIWA DAT recorder was used as a digitizer. This DAT recorder has a maximum sampling frequency of 48 kHz. The data calibration and processing algorithm briefly described.

Calibration of data

The calibration of the acoustic data is done according to the algorithm used at NDRE (Engelsen, 1993). During the monitoring each buoy have been recorded on a certain channel which needs to be calibrated. A calibration signal of $1V_{RMS}$ at 100 Hz is recorded at all channels. This input signal will be modified by the total receiving system and produce an output signal (D) at the workstation which is some dB below 1 V. The deviation from 1 V_{RMS} will vary from channel to channel it will also depend on carrier frequency. A RF signal was transmitted simultaneously on all RF channels at 3 different levels (10, 19, 75 kHz carrier deviation) at a signal frequency of 100 Hz. This calibration signal is recorded on all sonotracks of the recorder. Based on tests made by NDRE the carrier frequency dependency is neglected from this work. The receiving system was calibrated after the P3 aircraft returned to base. Instead of doing the three step calibration of the [buoy - analog recorder], [the analog-DAT] and [DAT to Silicon Graphics], the calibration is done by only one step. The recorded 100 Hz calibration signal on the analog tapes is simply recorded into the DAT tape at the same input level as the data signal on the same channel. The calibration signal is now used to characterize the total system, and only one calibration factor is calculated for each channel:

$$C_d = \frac{1V_{rms}}{D}$$

where C_d is the calibrated signal, D is the signal level measured on the DAT tape by the Silicon Graphics.

It is important to note that the calibration factor strongly depends on the input level on the DAT recorder. So the input level must be constant during recording of both the calibration signal and the data. The calibration factor also depends on which channel is operated.

Buoy Sensitivity

The SSQ 57 buoy sensitivity at 100 Hz is 116 dB relative 1 μPa at Carrier frequency 19kHZ. This means that using a perfect recording system a sound pressure (P) of 116 dB relative 1 μPa is needed to produce a $1V_{RMS}$ electric signal at 100 Hz at the buoy.

Since 100 Hz is the reference frequency for buoy 57 A,B and 41 and the sensitivity is set to be 116 dB // 1 micro Pa using a 100 Hz 1 V_{RMS} signal the sensitivity factors are:

$$S_{f57} = S_{f41} = 10^{\frac{116}{20}}$$

The reference for 905 buoys the sensitivity is 106 dB // 1 micro Pa at 450 Hz. According the sensitivity graph the buoy sensitivity is 13 dB lower at 100 Hz. Therefore the buoy sensitivity is 119 dB // 1 micro Pa at 100 Hz.

This gives

$$S_{f905} = 10^{\frac{119}{20}}$$

The conversion factor S is kept constant for buoys of the same buoy type.

The total calibration/conversion factor is:

$C=S_fC_d$

The C factor is found for all buoys and used as input value to the signal processing program.

Generic frequency response curves

After multiplying the data by the conversion factor C the data is calibrated and correctly converted to μPa at 100 Hz, but due to the frequency dependent buoy sensitivity curves, the data needs to be corrected at all the other frequencies by using the frequency response curves. Three different types of sonobuoys were used SSQ 57, SSQ 41N, and SSQ 905. Generic frequency response curves of these sonobuoys are shown in Figure A.1.

There is a sensitivity curve for each sonobuoy which is assumed to be the same for all buoys of same type, because the individual sensitivity curves are not available. The errors introduced by this assumption has been shown to be negligible for this work (Engelsen, pers. comm.).

The correction may be done in two ways:

1) By using filters, corresponding to the frequency response functions, in the frequency domain. Those filters is designed for each buoy.

$$P(f) = 20 \cdot Log((Cp(f)) - S(f)$$

where Cp (f) represent spectrum component at f frequency in μPa, S(f) is the frequency response function, P(f) is the corrected spectrum component in dB.

2) By using an equalizer unit during the recording from analog tape to DAT, imposing an -15logf function on the data.

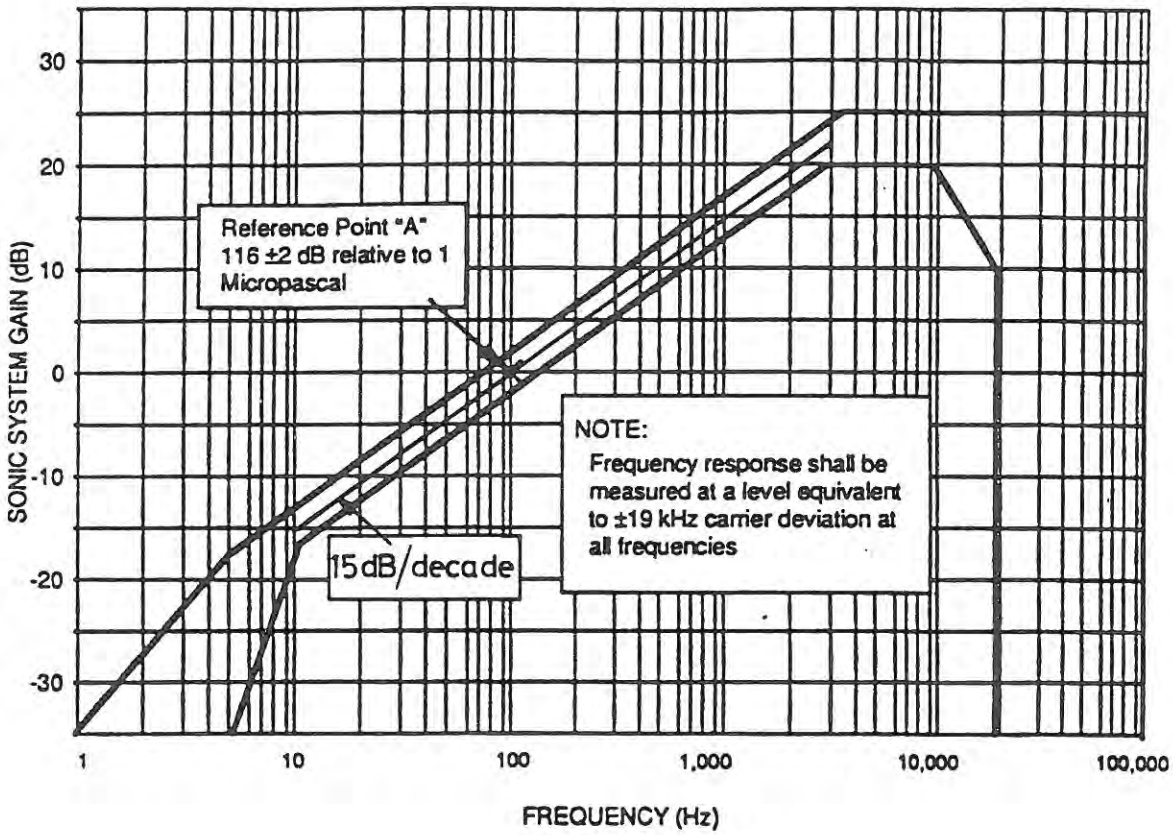

Figure A.1 Generic frequency response curves for the 57-B buoy (Engelsen, 1993)

$$P(f) = \underbrace{20 \cdot \mathrm{Log}((\mathrm{Cp}(f)) - 15 \cdot \mathrm{Log}(f)}_{\text{Pressure correct up to 3kHz}} + \underbrace{(15 \cdot \mathrm{Log}(f) - \mathrm{S}(f))}_{\text{Correction term above 3kHz}}$$

During our recording the equalizer was used during the entire data processing. After the filtering the "57" buoys have a flat response curve from 10-3000 Hz, above this the value subtracted was to large, so the data has to be corrected by a function

$$CORR57 = \begin{cases} 0 \text{ for } 10 \le f \le 3000 \\ \text{interpolation between } (3000,0) \\ \text{and } (10000,7) \text{ for } 3000 \le f \le 10000 \end{cases}$$

Similarly the frequency spectra obtained by the "41-N" buoys have to be corrected by adding the following function to the data:

$$CORR41 = \begin{cases} 0 \text{ for } 10 \le f \le 1000 \\ \text{interpolation between } (1000,0) \\ \text{and } (2000,2) \text{ for } 1000 \le f \le 2000 \end{cases}$$

By considering the frequency response curve for 905 buoys it is seen that the frequency dependence is 20logf rather then 15 logf. Therefore the data, which has been exposed for the function -15logf has to be added a function 15logf and then subtracted a function which corresponds to the actual frequency response.

$$P(f) = \underbrace{20 \cdot \mathrm{Log}((\mathrm{C}p(f)) - 15 \cdot \mathrm{Log}(f)}_{\text{Pressure uncorrect}} + \underbrace{15 \cdot \mathrm{Log}(f) - \mathrm{S}(f)}_{\text{Correction terms.}}$$

The frequency response function is established by interpolation routine and stored on a file. This procedure can also be used by the other buoys. If the equalizer had not been used during the recordings the only thing to do was to construct the canceling function of the frequency response function.

Finally, the frequency spectra components are normalized to 1 Hz instead of to the bandwidth (11.6 Hz) by subtracting 10 log (bandwidth) from the data.

Details of the frequency analysis

The sample frequency at the DAT is 48 kHz. Each FFT is performed on a 4096 sample time section in μPa.

Duration of each time section: T=4096/48000 s.

Step in frequency: 1/T=11.71 Hz.

Maximum frequency: 2047*1/T=23988 Hz.

Sonograms are produced by taking FFT of 46 successive time sections which are averaged. Each frequency spectra in the sonogram is therefore averaged over 4 s, which makes the frequency spectra statistically stable.